Effect of Nozzle Geometry on the Stability of a Turbulent Jet Flame With and Without Swirling Co-Flow

by

Christopher Omokhowa Iyogun

A Thesis submitted to the Faculty of Graduate Studies of

The University of Manitoba

in partial fulfilment of the requirements of the degree of

Doctor of Philosophy

Department of Mechanical Engineering

University of Manitoba

Winnipeg, Manitoba, Canada

THE UNIVERSITY OF MANITOBA

FACULTY OF GRADUATE STUDIES

*****

COPYRIGHT PERMISSION

Effect of Nozzle Geometry on the Stability of a Turbulent Jet Flame With and Without Swirling Co-Flow

By

Christopher Omokhowa Iyogun

A Thesis/Practicum submitted to the Faculty of Graduate Studies of The University of Manitoba in partial fulfillment of the requirement of the degree

Of

Doctor of Philosophy

ABSTRACT

An experimental investigation of the effect of fuel nozzle geometry with and without a sudden expansion on some of the stability features of a turbulent diffusion methane flame with and without swirling co-airflow has been conducted. The study is divided into two major parts. The first one concerned an examination of the effect of nozzle geometry with and without sudden expansion on the entrainment and spreading rates of non-reacting turbulent air jets. The second part was devoted to an assessment of the effect of nozzle geometry with and without sudden expansion on some of the main stability features of a jet (diffusion) methane flame as well as swirling non-premixed methane flame.

Five different nozzles were employed. They have the same external geometry (outer diameter of 14.9 mm) but all have different shape/geometry of the nozzle internal constriction section, which are a straight tube/pipe, a triangle, a rectangle, a square, and a contracted circular. The equivalent internal diameter of constriction is approximately 4.50 mm. The sudden expansion is a 12 mm long cylindrical pipe with 12 mm internal diameter. For the co-airflow, four different swirl numbers were tested, which are 0, 0.31, 0.79 and 1.15.

Two measurement techniques were employed. 2D laser Doppler velocimeter (LDV) was used for velocity measurements, and a high speed imaging system was employed for determining some of the stability features (such as liftoff height and flame length) of methane flame.

The main results of the effect of sudden expansion on the entrainment and spreading of a turbulent jet (with zero co-flow) show that the jet flow with the presence of sudden expansion exhibits higher rates of entrainment and spreading than without sudden expansion. In addition,

these results reveal that an increase in jet exit velocity reduces jet entrainment and spreading rates for all nozzles with and without sudden expansion.

The results of the effect of asymmetric fuel nozzles on the stability of turbulent jet methane flame (with zero-coflow) reveal that asymmetric nozzles reduce the jet flame liftoff height, and hence stabilizes the flame base closer to the nozzle compared with conventional circular nozzles. Furthermore, the study reveals that the jet flame liftoff height is reduced further when sudden expansion is attached to the exit of the nozzle. Consequently, the stability range of the lifted flame is found to increase when sudden expansion is attached to the nozzle.

Finally, the experimental investigation on the effect of nozzle geometry in conjunction with swirling and non-swirling co-flow on the stability of turbulent jet methane flame issuing from a rectangular or a contracted circular nozzle show that the jet flame blowout of the rectangular nozzle is higher than that of the contracted circular nozzle for identical swirl number. This is related to the higher entrainment which results in a better mixing engendered by the use of the rectangular nozzle compared with the contracted circular nozzle. In addition, for both nozzle geometries as the swirl intensity increases the blowout initially reduces especially for low co-flow velocity, but as the co-flow velocity increases the blowout suddenly increases noticeably. However, for low intensity swirl, as the co-flow velocity is increased, the flame blowout reduces considerably until it blows out at very low velocity while still attached. Furthermore, the flame liftoff velocity decreases as the co-flow velocity at low swirl number (intensity) increases, while it increases at high swirl number. In addition, the liftoff velocity of the contracted circular nozzle is found slightly higher than that of the rectangular nozzle for identical test conditions.

ACKNOWLEDGEMENTS

I want to first and foremost appreciate God for this opportunity. The profound effort of Dr. M. Birouk in supervising this work is greatly appreciated. His unending concern for a thorough job and sustained guidance and encouragements are acknowledged.

The examination committee's (Dr. S. Ormiston, Dr. G. Thomas, and Dr. I. Wierzba) time and input in this thesis is greatly appreciated. Their constructive comments and guidance only served to make the thesis better. Manitoba Hydro (N. Read, Project Monitor) deserves all the appreciation for making this work a reality. Without their funding of this project, this thesis may have been unrealized.

My wife, Beverly Iyogun and my sons, Jeffrey and Jadon Iyogun are very much appreciated. I could not have done this work without their full support and cooperation. My wife stood behind me like a pillar and my sons understood the demands of my program. I drew strength from the knowledge that if everything falls apart my family is always there for me to lean on. I appreciate the RCCG members and Pastors: Pastor T. Okunnu, Pastor A. Odeshi, Pastor G. Nekou, Sister R. Adegbamigbe, Bro. Femi Olumofin, Bro. Dave Allenotor, Pastor and Mrs. Adeleye-Olusae, Bro. John Akinyemi, and so on. My parents and siblings back in Nigeria are also acknowledged as well as my cousin Prof. Paul Iyogun and his wife.

My research group is acknowledged-Todd Phillips, Maher Abou-Al-Sood, and Sean Fabbro who worked with me every time I needed their help. Prof. Gabriel Thomas of the Department of Electrical and Computer Engineering, Ian, and Collins Gilmore who spent considerable time helping me with the MATLAB code are very much appreciated. My very good friends who have been very helpful in this pursuit are greatly acknowledged-Elder Samuel Paul, Sola Adeyinka, Martin Agenlichaab, Mohammed Khalid Shah, Lanre Ojo, James Arthur, Jonathan Tsikata, Kujo, Godwin, and others too numerous to mention. The technical and friendly support of John Finken, Irwin, and Dan are greatly appreciated.

DEDICATION

This thesis is dedicated to the almighty God who opened this door of opportunity and sustained me throughout this challenging area of research.

TABLE OF CONTENTS

LIST OF TABLES

LIST OF FIGURES

CHAPTER 1: INTRODUCTION

This thesis is concerned with an experimental investigation of turbulent jet flows with and without chemical reactions. One aspect of the work assesses the effect of nozzle geometry on the entrainment and spreading of turbulent non-reacting jets. While the other evaluates some of the diffusion flame characteristics as a function of nozzle geometry and co-airflow swirl strength. There are similarities between turbulent jets with chemical reactions and those without. Therefore, laser Doppler Velocimeter (LDV) results on non-reacting jets have been used to help explain their corresponding reacting jets (e.g. Gollahalli *et al.*, 1986; Gutmark and co-workers, 1989a, 1989b, 1991; Langman *et al.*, 2007). Consequently, the present thesis adopted in some flow cases this strategy in order to lower the cost of the experiment as well as to avoid the complexity of dealing with reacting jets. Nevertheless, LDV measurements were also obtained in some other reacting jet flow cases.

Turbulent jet flows with and without chemical reactions have several applications which include, for example, gas turbine engines and industrial burners. In these systems, the gaseous fuel and air are separately supplied to the combustion chamber. The rate of mixing of fuel with the oxidant is a determining factor in the combustion process. Among the combustion performance parameters that can be influenced by burner aerodynamics are flame stability and emissions (e.g. NOx, soot).

A wide range of burner configurations have been developed and assessed with the aim of enhancing flame stability and also to minimize combustion emissions (e.g. Nathan *et al.*, 2006). Examples include the use of swirl in the case of non-negligible co-airflow momentum, and non-conventional fuel nozzles in the case of turbulent free reacting jets. Swirling co-airflow has been demonstrated to drastically enhance flame stability as well as reduce emissions (e.g. Birouk and Gupta, 2001). Non-conventional (asymmetric) fuel nozzles are also believed to have an impact on the overall reacting and non-reacting jets characteristics (e.g. Gutmark *et al.*, 1989a, 1989b, 1991; Quinn, 1994, 1995, 2005; Mi *et al.*, 2000; Langman *et al.*, 2007; Ho and Gutmark, 1987).

It has been shown that using non-conventional nozzles such as a rectangular configuration, may tend to form a more uniform mixture that would reduce NOx and at the same time increase combustion efficiency. For instance, Yap and Pourkashanian (1996) reported that rectangular burners produced flames with increased flame stability, low NOx emissions, and high luminosity. In addition, Kamal and Gollahalli (2001) found a significant reduction in NOx emissions for some elliptic nozzles depending on their aspect ratio while in the worst case scenarios there were no significant differences between the NOx emissions from an elliptic nozzle and a contracted circular nozzle. This indicates that the worst scenario is there is no reduction in NOx but combustion efficiency increases as a result of increased mixing of fuel and oxidant by using asymmetric nozzles.

The present research is aimed at contributing to the global effort on the development of "enhanced mixing" burners, which increase the mixing of fuel and oxidant. The present effort builds upon previous published research which uses passive means of controlling entrainment and spreading of a jet. In the present study, asymmetric nozzles with sudden expansion are used to examine their effect on jet entrainment and spreading rates, and consequently their overall effect on non-premixed flame stability. To accomplish the goal of the present study, first, a non-reacting jet issuing from a non-axisymmetric nozzle with and without a sudden expansion is evaluated to quantify nozzle geometry effect on jet entrainment and spreading rates. Jet entrainment and spreading rates are good indicators of the level of fuel-oxidant mixing and hence the molecular mixture of the fuel and oxidant which provides insight into the combustion efficiency and pollutant emissions.

One other very good indicator of combustion efficiency is the flame stability. Flame stability is a term that can be measured (not in value) by its blowout and liftoff velocities, flame length, liftoff height, and reattachment velocities. The knowledge of these variables for a particular flame gives an indicator of the flame stability. Note that flame stability gives the overall working range of the fuel and oxidant. Consequently, increasing the stability limit would stretch the working range of the combustion system which implies higher efficiency. Therefore, the second objective of the present study is to examine the effect of nozzle geometry (non-axisymmetric fuel nozzles) on jet (diffusion) flame stability. Finally, the effect of fuel nozzle geometry in the presence of a swirling/non-swirling co-flow is assessed to determine some of the stability features of non-premixed methane flame.

The thesis is organized as follows. Chapter 2 expands upon the introduction presented above to provide a comprehensive review of previous research related to turbulent free jets issuing from axisymmetric or asymmetric nozzles. This chapter will also include review of pertinent literature on reacting jets with and without swirling co-airflow. Chapter 3 describes the experimental facilities, measurement techniques, uncertainty analysis, and experimental conditions employed in the present work. Chapter 4 presents and discusses the experimental results on reacting and non-reacting jet flows. Finally, Chapter 5 summarizes the conclusions reached from the experimental results and outlines some suggestions for further work.

CHAPTER 2: LITERATURE REVIEW

The literature review is divided into two main sub-headings namely: non-reacting turbulent free jets and turbulent diffusion flames. The non-reacting free jets review covers advances made on turbulent free jets with particular focus on asymmetric nozzles used for conveying the fluid before discharging into a quiescent environment. The review of turbulent diffusion flames, on the other hand, provides a fairly detailed account of diffusion flame characteristics with great attention paid to flame stability analysis.

2.1 Non-Reacting Turbulent Free Jet

Turbulent jets are used in several applications, such as air-conditioning and more specifically in combustion power systems. In fact, the entrainment and spreading rates of turbulent jets are controlling factors for the combustion performance as well as the level of pollutants emissions. Consequently, the configuration of a turbulent free jet provides a unique opportunity for evaluating the relationship between, for example, nozzle geometry as well as inlet conditions, and the jet characteristics such as spreading and entrainment. The jet entrainment and spreading rates can, in fact, be assessed via the centerline mean velocity decay and the jet half-velocity width profiles (e.g. Antonia *et al.*, 1980; Boersma *et al.*, 1998; Capp *et al.*, 1990). Note that the jet half-velocity width is defined as the distance from the centerline to the radial location (i.e. y-location) where the mean streamwise velocity becomes half of the centerline velocity. In fact, the centerline mean velocity decay and jet half-velocity width are, respectively, indicators of fluid entrainment rate and the level of jet spreading.

2.1.1 Turbulent Free Jets Issuing from Axisymmetric Nozzles

In a turbulent free jet configuration, it was customary to use an axisymmetric nozzle (e.g., Antonia *et al.*, 1980; Hussein *et al.*, 1994; Hussein and Zedan, 1978; Mi *et al.*, 2001a, 2001b; Xu and Antonia, 2002). A conventional axisymmetric nozzle consists of a smooth circular pipe or a contracted circular nozzle, which are characterized by fully developed velocity profiles, and top-hat velocity profiles, respectively. An orifice plate has sometimes also been investigated (see for example, Mi *et al.*, 2001b).

Early measurements of the mean velocity profiles of an axisymmetric jet were summarized by Hinze (1959) and turbulent quantities were presented in Corrsin (1943), Corrsin and Uberoi (1949, 1951), and Corrsin and Kistler (1955). Hinze summaries were for measurements undertaken with pitot tubes but with the advent of hot-wire anemometry and presently non-invasive measurement techniques such as laser Doppler velocimeter (LDV) and particle image velocimeter (PIV), turbulence fluctuations are now easily measured.

Nevertheless, a common denominator for most investigators of axisymmetric turbulent free jets in the 1960s is the issue of self-similarity of the mean velocity profiles, and sometimes the turbulence intensities. Wygnanski and Fiedler (1969) made a detailed investigation of the mean velocity and fluctuating components of a contracted circular nozzle using hot-wires. The measurements covered 40 to 100 diameters downstream from the nozzle exit. From the mean velocity and turbulence intensities; turbulence stresses, intermittency, skewness and flatness factors, correlations, and scales, were extracted. The major finding was that the mean velocity becomes self-similar at downstream distance less than when the turbulence intensities achieve self-similarity. Consequently, Wygnanski and Fiedler (1969) concluded that the jet truly becomes self-preserving at about 70 diameters downstream from the nozzle exit which is the distance at which turbulence intensities achieve self-similarity.

In the 1990s, however, due to the introduction of new velocity measurement tools such as LDV and particle image velocimeter (PIV) and the improvements of early velocity measurement tools such as hot-wires, new research work took place. These activities used different velocity measurement tools and identified the differences in the velocity profiles. For example, Panchapakesan and Lumley (1993) continued the investigation of a turbulent free jet discharging from a contracted circular nozzle into a quiescent air. Different modifications were made to the hot-wire used in order to eliminate some errors common with the use of a hot-wire, such as rectification errors (i.e. inability to resolve flow reversal). Streamwise centerline mean velocity decay were provided and compared with previous authors as well as the mean velocities and fluctuating components. Overall, major differences were observed in most quantities compared with other authors. Panchapakesan and Lumley (1993) attributed these differences to the disparate measurement tools employed by each group of investigators. In addition, Hussein *et al.* (1994) explored the differences inherent in the use of different measurement tools for mean velocity and fluctuating components of a turbulent free jet issuing from a contracted circular nozzle and discharging into a large room. As a result, they used flying and stationary hot-wire and LDV for their measurements. The results presented once again differ significantly from those of other investigators both in the magnitude and shape of the profiles. The authors attributed these differences to the dissimilar size of enclosure the jet discharges into. In addition, the results of the LDV and flying hot-wire used by Hussein *et al.* (1994) differ from the values obtained using stationary hot-wire from the same study. This was attributed to the cross-flow and rectification errors inherent in the stationary hot-wire when used to measure high turbulence intensities.

Starting in 2000, there were several investigations to distinguish between the entrainment and spreading rates of a jet issuing from a contracted circular nozzle and a straight pipe (e.g. Mi *et al.*, 2001a, 2001b; Xu and Antonia, 2002). For example, Xu and Antonia (2002) examined both of these nozzles' jet flow configurations and observed that there was improvement in fluid entrainment and jet spreading rates of the contoured circular nozzle compared with the fully developed turbulent pipe jet flow. This is in accordance with the findings of Mi *et al.* (2001a, 2001b). Xu and Antonia (2002) concluded that for the pipe jet, the streamwise vortices, which enhance entrainment and turbulent mixing, are absent in the shear layer of the pipe jet whereas they are present in the contracted circular jet. This is also in agreement with the findings of Mi *et al.* (2001a). Langman *et al.* (2007) in their diffusion flame study basically agreed with the findings of Xu and Antonia (2002), Mi *et al.* (2001a), and a host of other investigators of non-reacting turbulent free jet. They observed that the flame liftoff height issuing from a cylindrical pipe is different from that of a contoured circular nozzle. However, Coats and Zhao (1989) noticed no difference in the combustion characteristics, such as the flame liftoff height, between the two different nozzles. In addition, Antonia and Zhao (2001) found that the pipe and the contracted circular nozzle achieved self-similarity at approximately the same downstream location.

Mi *et al.* (2001b) in their investigation of the mixing characteristics of a turbulent free jet examined an orifice plate jet in addition to the contracted circular nozzle and long straight pipe jets. The findings were consistent with previous investigators concerning the increase of jet entrainment rate as a consequence of using a contracted circular nozzle instead of a pipe.

Nevertheless, the orifice plate was found to have the highest mixing with the ambient. They also observed that there were coherent large-scale structures in both the orifice and contracted circular jets. Finally, they noted that even though the pipe jet has some large scale structures, they were poorly correlated and do not occur regularly. Consequently, the pipe jet has a weaker entrainment of the ambient fluid.

In addition, Ferdman *et al.* (2000) investigated the effect of initial velocity profile on the development of round jets. They used a long straight pipe and another pipe that had a 90-deg bend upstream of the exit, thus preventing a fully developed velocity profile and instead giving an asymmetric profile. The finding showed that the bend has an effect only in the near-field (i.e. $x/D_e < 15$) after which the profiles of the two jets become similar. Nevertheless, in the near-field where there are differences, turbulence intensities and spreading rates of the bent pipe are larger than those of the long straight pipe. When these two jets results were compared with the initial results of a contracted circular jet it was observed that their turbulence intensities were smaller.

2.1.2 Turbulent Free Jets Issuing from Asymmetric Nozzles

The level of mixing between a jet and its surrounding fluid can be enhanced by using, for example, passive means such as asymmetric nozzles. They have been found to enhance jet entrainment and spreading, which in turn increases mixing, relative to their corresponding axisymmetric counterparts. For instance, it has been reported that asymmetric nozzles promote higher entrainment and jet spreading compared with their circular (i.e. axisymmetric) counterparts (e.g., Gutmark *et al.*, 1989a, 1989b, 1991; Quinn, 1994, 1995, 2005; Mi *et al.*, 2000).

This difference in entrainment and spreading rates of the asymmetric jets compared with their axisymmetric counterparts has been widely researched, and most investigators found that 'axis-switching' was the main cause. Axis switching is a phenomenon that occurs when the jet half-velocity width in the minor axis of an asymmetric nozzle jet which was initially lower than that of the major axis suddenly becomes higher downstream. It is also a re-orientation of the axes such that the initial orientation of the axis changes in the downstream field of the jet. This phenomenon was observed to be a major reason why asymmetric nozzles have higher rate of mixing relative to their axisymmetric counterparts (e.g. Ho and Gutmark, 1987; Gutmark *et al.*, 1989a, 1989b, 1989c, etc). For example, Ho and Gutmark (1987) used a small-aspect-ratio elliptic nozzle as a passive means of increasing jet entrainment compared with the same flow in an axisymmetric nozzle. Ho and Gutmark (1987) concluded that the mass entrainment of a small aspect ratio (2:1) elliptic jet is several times higher than that of a circular or a two-dimensional jet. In addition, they found that axis switching was prevalent in the elliptic jet but absent in the circular jet. The same conclusion about axis switching was reached by Gutmark *et al.* (1989a, 1989b, and 1989c), Hussain and Husain (1989), Koshigoe *et al.* (1989), Quinn (1994), and Zaman (1996). Hussain and Husain (1989) observed jet axis switching for different elliptic nozzles of varying aspect ratios and internal geometries and concluded that this phenomenon of axis switching enhances large-scale mixing. In addition, they attributed the source of the axis switching to the vortical structures caused by self-induction which is in accordance with the findings of Ho and Gutmark (1987). The frequency of axis switching has been credited to directly affect the rate of entrainment and mixing (e.g., Quinn, 2005).

Free jets issuing from other types of asymmetric nozzles with more complex geometries such as rectangle, square, triangles, star-shaped, cross-shaped (e.g. Gutmark *et al.*, 1989a, 1989b, and

1989c; Quinn, 1991, 1994; Mi *et al.*, 2000; Koshigoe *et al.*, 1989) were investigated. For example, Gutmark *et al.* (1989a) used an elliptic nozzle with aspect ratio (i.e. AR) of 3, contracted circular nozzle, and a rectangular nozzle of AR = 3 to investigate the non-reacting air flow dynamics using hot-wire anemometry. They found that both the rectangular and elliptic jets had remarkably higher entrainment and mixing with the ambient fluid compared with the circular jet as manifested by the increase in the jet streamwise centerline mean velocity decay. This increase was also attributed to the self-induction process of the jet's vortices in the near-field. However, they found the elliptic nozzle had a slightly higher rate of spreading compared with the rectangular jet. This scenario was attributed to the impact of the vertices of the rectangular nozzle which reduces the coherence of the jet's large-scale structures, thereby weakening the self-induction process which ultimately leads to a slightly reduced spreading rate. However, the elliptic vortices produced as a result of jet instability in the near-field were found to deform. This deformation was claimed to be caused by the different convection velocities at different azimuthal locations. Consequently, as a result of this deformation a self-induction process was initiated, which increased the spreading rate.

Gutmark *et al.* (1989b, 1989c) investigated the influence of nozzle vertex angle on a non-reacting turbulent free jet. These authors concluded that different turbulence dynamics occurs in the nozzle flat side and the corners. It was shown that highly coherent structures were shed from the flat sides of the nozzle while small-scale turbulent flow emanated from the vertex. This interplay of different structures is claimed by these authors to be beneficial to mixing. In addition, these authors found that the initial turbulence level at the vertices were considerably higher than those found at the center of the flat sides with the isosceles triangle having three times more while the equilateral triangle was doubled. However, the amplification rate of the turbulence intensity was higher at the flat sides compared with the vertices in the downstream region of the jet. Finally, they found that as the corner angle increases the differences in the streamwise development of the turbulence intensity between the vertices and the flat side reduces. As a result, for a corner angle of 90° (i.e. a square) there is almost no significant difference between the flat sides and the vertices in the amplification of the turbulence intensity as the jet develops further downstream.

However, the most complicated asymmetric nozzle used to date seems to be that of a 'lobed' nozzle designed primarily to increase mixing (see for example, McCormick and Bennett, 1993; Belovich *et al.*, 1996). The concept was to stretch the perimeter of the shear layer exposed to the ambient fluid so that entrainment could be increased. However, as a result of this shear layer stretching, streamwise vorticity was found to be introduced as a result of the asymmetry of the nozzle (e.g. Zaman, 1999). This increase in streamwise vorticity contributed to enhanced entrainment (Ho and Gutmark, 1987) relative to a round jet.

An attempt to further increase entrainment by using 'tabs', which are also passive means of controlling entrainment, has been explored (e.g. Ahuja and Brown, 1989; Zaman *et al.*, 1994; Reeder and Samimy, 1996; Reeder and Zaman, 1996; Zaman, 1996, 1997, 1999; Foss and Zaman, 1999; Sau, 2002, 2004). Zaman (1999) defined a tab as "a small protrusion placed at the jet nozzle exit that produces a pair of counter-rotating vortices". Sau (2002) studied numerically jets issuing from a rectangular channel with a suddenly expanded and contracted part to assess the effect of sudden expansion/contraction on vortex dynamics. Tabs were used to generate the strong streamwise vortices in order to enhance further the rate of entrainment in accordance with previous studies. Sau (2002) studied the source and type of the streamwise vortices present in the flow field. Sau (2002) agreed with the findings of Zaman (1996, 1997, 1999) concerning the introduction of inflow pairs of vortices by the tabs. However, the source of generation of streamwise vortices was attributed to the evolution of the jet from the developed high pressure regions to the surrounding low pressure regions inside the channel. Sau (2002) further extended his work to a jet flow issuing from a square nozzle with a sudden expansion (Sau, 2004). This work of Sau (2004) is similar to the study of Nakao (1986) who experimentally examined square sudden expansion flows and observed the presence of weak streamwise vortices, which fail to persist downstream. It was found in both numerical studies (Sau, 2002, 2004) that the developed transverse pressure gradient skewing controls the generation of streamwise vortices.

Another attempt to increase entrainment and jet spreading rate was investigated by New *et al.* (2007). They varied the sudden expansion (called collar by these authors) from a simple circular geometry to triangular as well as square while also changing the expansion-ratio. One of the major findings was that using a triangular collar produced the highest spreading rate compared with other collar geometries of square and circle.

Among the studies on asymmetric nozzles, there have been several discrepancies in the results reported by different authors. For example, results of fluid entrainment rate indicated by the centerline velocity decay of isosceles and equilateral triangles nozzles as reported by Mi *et al.* (2000) differ from those of Quinn (2005). While Mi *et al.* (2000), who used nine different nozzle geometries, found that their isosceles triangular jet induced a better entrainment rate than its counterpart equilateral triangular jet; Quinn (2005) reported the opposite scenario. Furthermore, Zaman (1999) and Gutmark *et al.* (1989a, 1989c, 1991) reported discrepancies concerning the extent of the increase in jet spreading and entrainment of rectangular nozzles as opposed to circular nozzles. Indeed, while Gutmark *et al.* (1989a, 1989c, 1991) observed considerable increase in jet spreading and entrainment of the rectangular nozzles (with an aspect ratio of 2:1) compared to their circular nozzle counterpart, Zaman (1999), who performed an experiment at a much higher Reynolds number (i.e. compressible flow) observed only slight increase for the same geometry. Zaman (1999) attributed this discrepancy to the different Reynolds numbers employed in both studies. The difference in the entrainment rates of identical nozzle geometries employed by Mi *et al.* (2000) and Quinn (2005) was also attributed to the different Reynolds number employed by both research groups.

As a result of these several discrepancies in the open literature, there have been attempts to discern their causes. For example, Riopelle *et al.* (1994) studied the effect of ambient pressure field on the entrainment rate of plane jets and axisymmetric jets and reported that the pressure field can in fact cause discrepancies. In addition, a different aspect ratio (AR) for the same nozzle geometry may cause some discrepancies. For example, Zaman (1997, 1999) reported that for a rectangular nozzle, varying the aspect ratio does not have any effect on the spreading and entrainment rates until a threshold is passed before any significant change can be noticed. This threshold varied from AR = 10 to AR = 16. However, Quinn (1991) observed significant change in entrainment and spreading rates for a rectangular slot with AR = 10 compared with the same geometry but AR = 2. This seems to contradict the findings of Zaman (1997, 1999).

However, the assertion of Reynolds number causing discrepancies had not been thoroughly investigated for the asymmetric nozzles, especially triangular and rectangular nozzles. Nevertheless, there have been studies which dealt with the effect of exit velocities on the ensuing entrainment and jet spreading of axisymmetric jet (e.g. Malmstrom *et al.*, 1997; Warda *et al.*, 1999). For example, Warda *et al.* (1999) showed that the far stream centerline mean velocity decay of an axisymmetric jet decreases with an increase in exit velocity. However, the same study found that there is no significant change in the near-field mean streamwise centerline velocity decay except that the length of the potential core increases for the higher exit velocity. This reduction in centerline mean velocity decay as exit velocity increases was attributed to the reduced turbulence intensity at the exit of the nozzle as a result of increased exit velocity (e.g. Warda *et al.,* 1999).

2.1.3 Motivations and Objectives

Although, literature reviewed above showed that there is substantial published data on the effect of nozzle geometry on the ensuing turbulent jet, there are still great deal of inconsistencies in the conclusions reached for the same nozzle geometry. In addition, some characteristics of free jets issuing from other different asymmetric nozzles than those reviewed above are yet to be investigated.

The present study, which builds upon the literature surveyed above, is a modest contribution to the understanding of the relationship between nozzle geometry and the characteristics of the ensuing jet discharging in quiescent atmosphere. The main focus of the present experimental study is to assess:

i) The effect of an axisymmetric sudden expansion on the entrainment and spreading rates of a non-reacting jet issuing from asymmetric nozzles. Detailed investigations of the effect of sudden expansion on asymmetric nozzle flow characteristics are still not available in the open literature.

ii) The effect of exit velocity on the entrainment and spreading rates of a non-reacting turbulent free jet issuing from a rectangular, a triangular, a circular, and a square nozzle with and without sudden expansion. This part of the study is expected to shed light on the discrepancies discussed above concerning the main features of a jet issuing from the same nozzle geometry.

2.2 Reacting (Non-Premixed) Turbulent Jets

2.2.1 Turbulent Jet (Diffusion) Flames

Turbulent jet diffusion flames and particularly its flame stability mechanisms have been an attractive topic for many decades and are still receiving considerable attention due to their practical importance. The stability limit of turbulent diffusion flame encompasses the liftoff height and velocity, flame length, reattachment velocity, and blowout velocity. These terms will be defined later on in Chapters 3 and 4.

Of prime importance is the liftoff height which has been studied extensively. Several theories have been proposed to explain the liftoff height stabilization mechanism of a turbulent jet diffusion flame. The first stabilization mechanism theory is conceived by Wohl *et al.* (1949) and has been the most commonly accepted theory. It states that the local flow velocity at the liftoff height matches the turbulent burning velocity of a premixed flame. This is the same theory which was further pursued by Vanquickenborne and Van Tiggelen (1966). Their main finding is that a lifted diffusion flame stabilizes at a height above the burner where stoichiometry is reached. They also concluded that the flame base is a form of a 'premixed' flame as the gas entrains air until it reaches this point. Following the same thought, Kalghathi (1984) determined that the turbulent jet diffusion flame liftoff height increases linearly with the jet exit velocity independently of the nozzle diameter.

The second theory has its origins with Peters (1983) which was later expanded by Peters and Williams (1983). Peters' (1983) theory suggests that the flame lifts off when the mixture of air and fuel in the combustion zone near the burner exit stretches faster than the mixture can ignite itself. As a result, the flame extinguishes or becomes extinct. The liftoff height is scaled in terms of a non-dimensional average scalar dissipation at extinction.

The third theory, which is proposed by Broadwell *et al.* (1984), states that the time available for backmixing by large-scale flow structures of hot products with fresh mixtures is less than a critical chemical time required for ignition. A blowout criterion was then proposed which is expressed as a ratio of the local mixing time to a characteristic chemical time.

In a review of the aforementioned theories, Pitts (1988) reported that the implicit assumption is that the base (i.e. the most upstream position) of a lifted jet diffusion flame is the stabilization point. In addition, Pitts (1988) pointed out that all the theories are based on the turbulent flow-field of the unignited regions close to the flame base. Pitts (1988), however, concluded that the stabilization mechanism of turbulent diffusion flame is still poorly understood.

A relatively recent theory, called triple flame, has been developed to describe the stabilization mechanism of lifted jet diffusion flame (Dold, 1989; Veynante *et al.*, 1994; Ruetsch *et al.*, 1995), although an observation of the triple flame has been reported several decades ago (Phillips, 1965). The triple flame theory presupposes that the base of the diffusion flame (i.e. stoichiometry point) is a confluence of three types of flames. At the edges are fuel-lean and fuel-rich flames which essentially are premixed flames and a diffusion flame aligned with the stoichiometry line. This assumption of triple flame, therefore, presupposes that the base of a lifted diffusion flame is a partially premixed flame. This theory has recently been pursued vigorously though it is still in its infancy. Upatnieks *et al.* (2004) applied cinema-PIV in an attempt to better understand the liftoff of turbulent jet diffusion flames and to further examine some of published theories developed to explain the stabilization mechanisms. They assessed the turbulence intensity theory proposed by Kalghatgi (1984), the edge-flame or triple flame concept as reported by Buckmaster and Webber (1996) and Boulanger *et al.* (2003), and the large-eddy theory reported by Miake-Lye and Hammer (1988). Upatnieks *et al.* (2004) concluded that the propagation speed of the base does not correlate well with the local turbulence intensity or passage of large eddies. Consequently, they concluded that the edge flame at the flame base propagates at the stoichiometric laminar burning velocity.

A thorough analysis of an up to date published work on the issue of lifted jet diffusion flame and all related theories was recently proposed by Lyons (2007). Lyons (2007) reviewed all the aforementioned theories, with more emphasis on work published since Pitts's review in 1988. Lyons concludes that there is still lack of complete understanding of the stabilization mechanisms of a lifted jet diffusion flame issuing from axisymmetric nozzles.

The reattachment and blowout phenomena as well as the liftoff velocity, which are also vital elements in the stabilization of a lifted jet diffusion flame, have not received equal treatment as the liftoff height. Scholefield and Garside (1949) studied the full stability range of a jet diffusion flame, such as the liftoff, reattachment and blowout velocities and their mechanisms. Scholefield and Garside (1949) attributed the reattachment and blowout phenomena to the effect of the turbulent flow-field of the unignited gas stream while they reported that the liftoff may be explained in terms of diffusion, velocity distribution, and thermal effect theories. However, Scholefield and Garside (1949) did not believe that the flame liftoff phenomenon can be explained by only one of these theories.

After the work of Scholefield and Garside (1949), further investigations of the diffusion flame liftoff, reattachment, and blowout mechanisms have been reported by several investigators (Coats and Zhao, 1989; Langman *et al.*, 2007; Eickhoff *et al.*, 1984; Gollahalli *et al.*, 1986; Takahashi *et al.*, 1984; Wu *et al.*, 2006; Dahm and Mayman, 1990). All these studies agree about the occurrence of hysteresis in which the liftoff velocity is higher than the reattachment velocity.

However, some of these studies reported different mechanisms as being responsible for the different stability phenomena. For example, Gollahalli *et al.* (1986) reported that the liftoff (i.e. the flame transition from attached to lifted) is governed by diffusion and flow structures while the reattachment is governed primarily by the dynamics of the organized flow structures. Nevertheless, Eickhoff *et al.* (1984), Coats and Zhao (1989), and recently Langman *et al.* (2007) all agreed that the flame liftoff is caused by the invasion of the laminar flame base by the unignited gas turbulence. The blowout phenomenon, according to Dahm and Mayman (1990), is governed primarily by the molecular mixing rate while the liftoff is controlled by the straining out of flame front, which is in line with the theory of Peters (1983).

2.2.2 Turbulent Jet (Diffusion) Flame Exposed to a Swirling or Non-Swirling Co-Airflow

Stability of jet (diffusion) flames without co-flow is better understood, as evidenced by the large amount of published works which have resulted; for instance, in several correlations intended to describe some of the flame stability aspects such as liftoff height, flame length, and blowout (e.g. Kalghatgi, 1981, 1984; Peters and Williams, 1983). Introducing co-airflow to a jet flame would change the whole dynamics of the flowfield and thereby makes the control of the resulting flow more complicated.

Nevertheless, there exist several studies devoted to examining the influence of co-flow on the stability of a jet flame issuing from axisymmetric nozzles (e.g. Wierzba and Oladipo, 1994; Karbasi and Wierzba, 1995; Takahashi and Schmoll, 1990). Takahashi and Schmoll (1990) classified four different types of lifting criteria based on observations of diffusion flames issuing from axisymmetric nozzles, with small diameters, surrounded by co-flow of air having a maximum exit velocity of 4.5 m/s. Wierzba and Oladipo (1994), who examined jet flame with co-flow of air having an exit velocity in the range below 10 m/s, proposed an empirical correlation for the blowout of attached and lifted flames.

The effect of swirling co-flow on the stability of a diffusion flame has also been studied quite extensively but it is still less understood due to the complexity caused by the flow's swirl. However, most studies of swirling flames agree that swirl enhances flame stability by generating a recirculating vortex, which then controls the size and shape of the flame, and enhances combustion intensity (e.g. Chigier and Chervinsky, 1967; Aref and Gollahalli, 1995; Al-Abdeli and Masri, 2007). Several studies in the literature reported that there is a strong correlation between swirling flame stability and mixing. For example, Sheen *et al.* (1996) noted that swirl increases the rate of fluid entrainment and mixing. This is a confirmation of the results of Panda and McLaughlin (1994) who found that spreading and mass entrainment rates increases for swirling jets compared to non-swirling jets. Wu and Fricker (1976) and also Syred and Beer (1974) reported that swirl strength influences the growth rate of the recirculation size and strength.

The effect of swirl strength on flame stability dynamics has also been investigated (e.g., Masri and Dally, 1999; Feikema *et al.*, 1991; Fricker and Leuckel, 1976; Tangirala *et al.*, 1987) and it was reported that swirl strength does not always enhance flame stability. For instance, Masri and

Dally (1999) found that using low swirl strength does not necessarily increase flame stability. Consistent with this finding, Feikema *et al.* (1991) showed that weak swirl strengths tend to produce flames with blowout similar to those without swirl. In addition, swirl strengths above unity have been shown to play conflicting roles on flames stability (e.g. Fricker and Leuckel, 1976; Tangirala *et al.*, 1987). For example, Tangirala *et al.* (1987) observed no increase in the recirculation zone or turbulence levels as swirl number was increased from 1.0 to 4.0. Because of significantly increased tangential velocity as a consequence of using very high swirl number, the flame becomes even leaner and less stable. Furthermore, this may also result in damaging burner material because of the strong recirculation of the hot products.

It is generally believed that using a swirl automatically shortens the flame length. However, recent study reported that this is not always the case (Al-Abdeli and Masri, 2007). Al-Abdeli and Masri (2007) found that irrespective of the co-flow exit velocity, flame length increases as swirl strength increases until a critical swirl number of around 0.2 after which the flame length starts decreasing. In addition, they found that flame length increases as the jet exit velocity increases which Al-Abdeli and Masri (2007) attributed to increased jet momentum. However, it is important to mention here that this finding was based on only a very limited jet exit velocity range; i.e. 40 m/s and 60 m/s. They also found that the flame becomes shorter as the co-flow exit velocity increases for swirl strength higher than 0.2. There were several attempts to explain this apparent effectiveness of swirl to shorten the flame length. For example, Fricker and Leuckel (1976) stated that the primary effect of swirl is to increase mixing of gaseous fuel and surrounding ambient air. However, Feikema *et al.* (1991) attributed this improvement in flame stability to the ability of the swirl to form localized flow regions with reduced flow velocity and hence reduced local strain rates. Tangirala *et al.* (1987) on the other hand, found that heat release is the major driving force of recirculation whereby it enforces the recirculation zone downstream of the nozzle exit and it also helps to increase turbulence levels. They found, however, that the effect of heat release was more pronounced for highly swirling flames.

2.2.3 Motivations and Objectives

Based on the literature review above concerning turbulent jet (diffusion) flames, it can be seen that jet flames issuing from axisymmetric nozzles have been extensively examined. However, studies on jet flames issuing from asymmetric geometries are very limited and not detailed enough. The stability studies of asymmetric nozzle flames are perfunctory at best and limited to very few asymmetric nozzles, despite the significant effect a nozzle geometry has on the overall jet dynamics (i.e. increase in jet entrainment and spreading which therefore leads to increased mixing).

The only stability investigations to the author's knowledge that were carried out on diffusion flames issuing from asymmetric nozzles are those from elliptic nozzles (Gollahalli *et al.*, 1992). Though, there are some other studies which examined diffusion flame issuing from asymmetric geometries, their focus was more on determining temperature and pressure fields (e.g. Gutmark *et al.*, 1989a, 1989b, 1991). Nonetheless, it was found that the geometry (e.g. elliptic) of the nozzle has an influence on the liftoff and reattachment velocities (Gollahalli *et al.*, 1992).

In this thesis, for the flame without co-flow investigation, one objective is to expand upon previous studies of axisymmetric nozzles by examining specifically the effect of nozzle geometry on the stability phenomena of a jet diffusion flame. In addition, this study seeks to obtain additional experimental data that would help shed more light on the mechanisms governing the liftoff height and associated liftoff and blowout phenomena. However, some of these published stabilization height theories will be appraised with a view to unravelling the more relevant one that describes best the present experimental data.

Furthermore, a review of the literature showed that several nozzle's geometries were developed with the goal of enhancing further fluid entrainment and mixing very close to the nozzle exit (e.g. Nakao, 1986; Zaman, 1999; Sau, 2002 and 2004). Therefore, the present investigation will examine the effect of a sudden expansion on the stability of a turbulent jet diffusion methane flame.

As for jet flame with swirling/non-swirling co-flow, it is well known that swirl introduces large scales which are important for mixing. However, small scales are important for chemical reactions. To the best knowledge of the author, all published literature dealt with a central jet issuing from a circular pipe surrounded by an annulus of swirling air. Recent studies surveyed in the previous two sub-sections have shown that asymmetric fuel nozzles have the potential of inducing various turbulent structures compared to a simple pipe counterpart. Therefore, the main purpose of the present part of the study is to examine some of the stability features of non-premixed swirling flame as subjected to both large scales induced by the swirl and relatively smaller scales generated by the asymmetric fuel nozzle. Specifically, this present study will report on the blowout and liftoff velocities as well as the liftoff height and length of a swirling non-premixed methane flame.

CHAPTER 3: EXPERIMENTAL FACILITY, MEASUREMENT TECHNIQUES, AND TEST CONDITIONS

This chapter gives a description of the experimental test rig which consists mainly of the burner configuration, flow control, and seeding system as shown in Fig. 3.1. The measurement techniques employed here, which are mainly a high speed camera and a two-component TSI laser Doppler velocimeter (LDV) are presented. In addition, test conditions for both reacting and non-reacting jets, as well as measurement uncertainties are also provided.

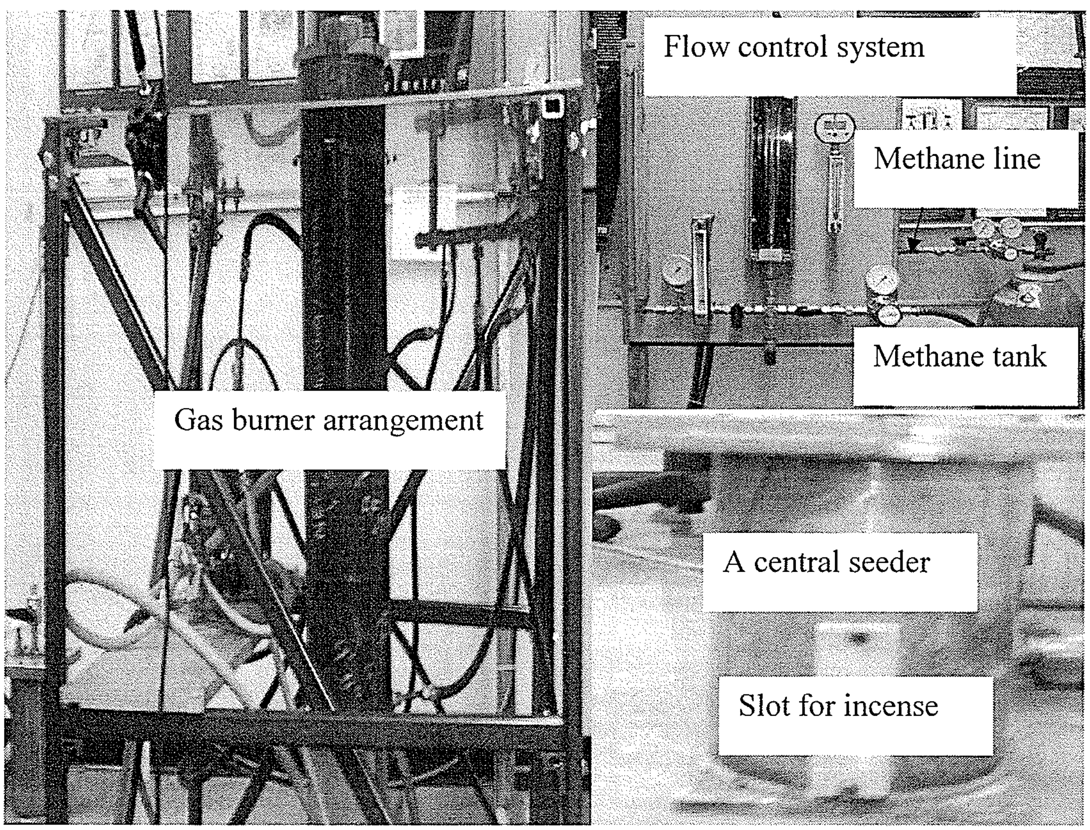

Figure 3.1: A picture of the gas burner as well as the flow control system.

3.1 Flow Control System

A schematic representation of the flow system, as shown in Fig. 3.2, comprises of a series of flowmeters, pressure gauges, valves, regulators, and cylindrical pipes which convey the gas to the burner. The gas was either methane from a compressed cylinder or air from a compressed supply line.

For reacting jets investigations, methane was supplied from a compressed cylinder as shown in Fig. 3.2. The supply line pressure of methane from the cylinder was initially regulated by a two-stage Prostar regulator before it passed through a pressure gauge and then into a Matheson FM-1050 series flowmeter. The regulator has an outlet pressure range of 0 – 200 *psi.* A pressure gauge installed downstream of the flowmeter, which had an operating range of 0 – 60 *psi,* is intended to give an accurate reading of the pressure of the gas flowing through the flowmeter. The flowmeter was designed to have interchangeable tubes so that a variety of flow rates can be used. In the present experiment two tubes were used; i.e. the low flow tube has a range of 1.26 to 22.6 *LPM* of methane (or 0.88 to 16 LPM of air) while the high flow tube has a range of 3.51 to 59.3 *LPM* of methane (or 2.4 to 44 LPM of air). The flowmeter has a 6 turn utility valve at the outlet to control the flow supplied to the central seeder and finally the nozzle exit. Most of the reacting and non-reacting flow experiments were run at a pressure of 40 *psi* in the flowmeter. The flowmeter was calibrated at atmospheric pressure, therefore, a correction factor must be used when running at higher pressures, which is given as

$$Q_{act} = Q_{read}\sqrt{P_{act}/P_{atm}} \qquad (3.1)$$

where Q_{act} is the actual flow rate, Q_{read} is the flow rate read from the flowmeter, P_{act} is the pressure at the inlet of the flow meter and P_{atm} the room atmospheric pressure. The accuracy of the flowmeter is ±1% full scale.

The air was supplied from the University of Manitoba's compressed air system. The inlet maximum pressure was 90 *psi*. As shown in Fig. 3.2, the experimental air was regulated by a one-stage Prostar regulator having an operating range between 0 and 200 *psi*. A 0 – 60 *psi* pressure gauge was employed to ensure greater accuracy.

For some measurements where co-flow was required, two flowmeters were installed based on the co-flow velocity demands. A Brooks Model 1000 flowmeter with a range of air flowrates from 159 *LPM* to 1589 *LPM* at 30 *psi* (which is the pressure at which this flowmeter is calibrated), with an accuracy of ±1% full scale is used for relatively high exit velocities. A Cole-Parmer acrylic flowmeter for low velocity air flow, which is capable of a flow range between 30 to 280 *LPM*, and it is calibrated at standard conditions, was installed in parallel with the Brooks Model 1000 flow meter.

The maximum air flow attainable from the University compressed air line was 600 *LPM* at 30 *psi*. The exit airflow velocity range achievable using these two flowmeters ranges between 0.56 *m/s* and 11.41 *m/s*. The flow system has a valve connecting the air and fuel line to enable using air instead of methane. Note that all the three flowmeters have safety valves that open up when the pressure exceeds the value that the flowmeter tubes can withstand.

The flowmeters were supplied with calibration charts from the manufacturers. To confirm if the manufacturer's calibration charts are accurate, LDV velocity measurements at the exit of a pipe flow was undertaken. After the LDV measurements were taken, the average velocity at the nozzle exit was also determined from the flow field. This was used with the cross sectional area to determine the flow rate. This flow rate matched very closely with the manufacturer's calibration data (i.e. difference of $< \pm 1\%$).

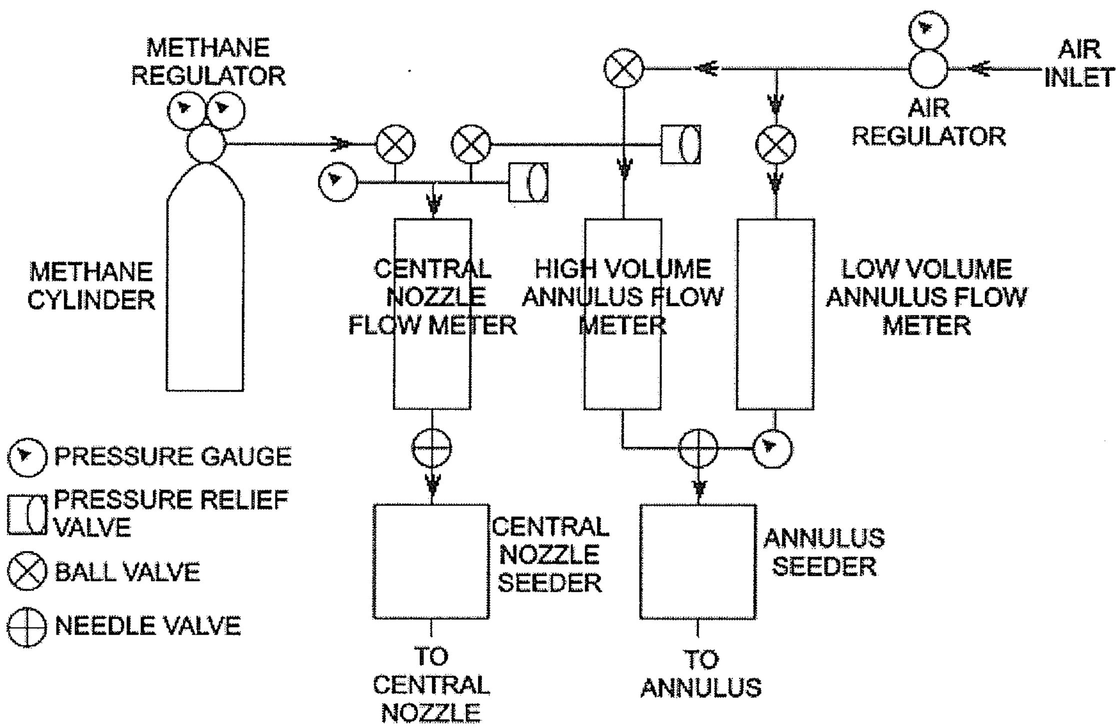

Fig. 3.2: Schematic diagram of flow control system.

3.2 Flow Seeding System

The seeding system was used to add light scattering particles (referred to as tracers) to the gas flow in order to facilitate LDV measurements. See Section 3.4.2 for more details about the operating principles of LDV. The seeding system consists of two settling chambers in which solid particles or incense smoke can be deposited and then picked up by the methane or air before flowing out of the burner. One seeder is used for the air flow through the annulus and another for the central nozzle. The settling chambers (or seeding chambers) are cylinders made from mild steel and have a welded plate on the bottom and a welded flange on the top. A top plate was then bolted to the flange. Three ports were machined on the top for the air or fuel in and out, as well as for particles supply. One port on the sides (close to the bottom) of the central nozzle seeder has an air tight slot fitted with an aluminum piece. It is used to house series of incense for seeding the air flow for non-reacting flow studies (see Fig. 3.1).

Three types of seedings were employed. Titanium oxide with a mean diameter of 0.2 μm was used for the combustion experiments because of its ability to survive in high temperature environment. It is important to mention that the titanium oxide particles must be kept very dry as moisture can cause them to bond together rendering them large and hence useless. However, incense smoke was introduced through the central nozzle seeder for the non-reacting flow investigations while simultaneously introducing into the annulus a low-momentum co-flow seeded with Di-Ethyl-Hexyl-Sebacat (DEHS) particles produced by a 10-bar LaVision droplet generator. It is important to mention here that the incense smoke's (mass median aerodynamic) diameter was estimated to be around 0.3 μm based on the findings of Cheng *et al.* (1995) and Chang *et al.* (2007) while the DEHS had an average diameter much less than 1 μm (the DEHS particles bimodal diameter provided by the droplet generator manufacturer is 0.25 μm). Following the method of Melling (1997), the frequency response of the incense smoke was determined (See Appendix A) to be about 76 kHz, that of titanium oxide particles was 43 kHz while that of DEHS particles was 126 kHz (based on an average diameter of 0.25 μm).

3.3 Gas Burner

The burner which was designed, manufactured and assembled at the University of Manitoba consists of a central fuel nozzle surrounded by an annulus of air. A schematic of the burner arrangements along with its dimensions are shown in Fig. 3.3 and 3.4. The burner base plate, top plate, and the outer and inner chambers were machined from mild steel. The swirl pipe and throat were machined from stainless steel while the central pipe was a stainless steel piece of extruded pipe. Plastic swirl generators were first created from CAD images using a rapid prototyping machine. The plastic forms were then cast out of stainless steel. This was necessary due to the complexity of their machining. The asymmetric nozzles, as shown schematically in Fig. 3.5 were also made following the same fashion, while the contracted circular nozzle was machined from stainless steel. The quarl is a hollow cylindrical pipe made from stainless steel with an inner diameter of about 12 mm and a thickness of 1 mm. It is placed at a height of 12 mm above the nozzle exit (see Figure 3.4). Relatively different arrangements of the burner for different investigations were used, as described below.

3.3.1 Gas Burner Arrangement for Diffusion Flame without Co-Flow

The schematic diagram shown in Figure 3.3 was used for diffusion methane flame without co-flow. Methane with a purity of 99% is fed through the central pipe from a 6 foot tall compressed methane cylinder. The required flowrate (described in Section 3.1) enters the central nozzle settling chamber. Afterwards, the methane gas at the exit of the seeding/settling chamber flows through a pipe of 7.62 mm in diameter (called here as the central pipe), and exits through a nozzle, which is attached to the pipe, as shown in Fig. 3.3. To ensure a well-developed flow at the exit of the pipe, the ratio of the length, L to diameter, d of the pipe (i.e. L/d) is taken to be about 135. The nozzle, which is about 47 mm long and attaches to the central pipe through a nozzle holder, is interchangeable. Four interchangeable nozzles with different internal geometries, which are a rectangular, a triangular, a contracted circular and a square, were used (see Fig. 3.5).

The contracted circular nozzle has a diameter of 4.82 mm and the other three nozzles have similar equivalent diameter, D_e (i.e. the diameter of round slot with the same exit area as the geometry in question). The rectangular nozzle has D_e = 4.71 with an aspect ratio of 2:1, the equilateral triangle has D_e = 4.46 mm, and the square nozzle has a D_e = 4.56 mm. In addition, a straight pipe of diameter, d = 4.45 mm with $L/d \approx 180$ was also used as a reference for the present study so that comparisons with the existing data of pipe from previous investigators can be made.

Two different flow arrangements were tested; one with the presence of quarl (sudden expansion) which is attached to the exit of the nozzle, as shown in Fig. 3.3, and the other without quarl. These two arrangements were employed to assess the effect of quarl on the characteristics of a turbulent flame issuing from an axisymmetric or asymmetric nozzle. Note that all the five nozzles mentioned above were tested with quarl except for the pipe.

3.3.2 Gas Burner Arrangement for Diffusion Flame with Co-flow

The co-flow addition and the absence of quarl are the only major differences between the jet flame experiment with co-flow and without co-flow. Consequently, the same configuration shown in Fig. 3.3 was also used for investigating jet flame with co-flow except for the absence of quarl and the presence of co-flowing air. That is, methane was supplied through the central settling chamber which contains TiO_2 while co-flow air was supplied through the air annulus from the annulus seeder (see Fig. 3.2). Note that the co-flow used here was either swirling (i.e.

swirl generator vane angles greater than zero) or non-swirling (i.e. swirl generator vane angle of zero) co-flow.

The air co-flow was supplied from a laboratory compressed air line through a Brooks Instrument Flowmeter or a Cole-Parmer Flowmeter in the flow control system to measure the flowrate. The Cole Parmer Flowmeter is used for air flowrates that are below 110 LPM while the Brooks flowmeter handles higher flowrates. The Cole-Parmer flowmeter and the Brooks Instrument flowmeter have a full scale accuracy of ±3% and ±1%, respectively. However, the pressure of the air delivered to the flowmeter is measured by pressure gauges installed before and after the flowmeters.

Consequently, the desired air flowrate, $\underline{U}_a$, is then conveyed through high pressure hoses to the annulus settling chamber which contains titanium oxide particles of 0.2 μm average diameter. Thereafter, the seeded air is conveyed to a manifold where it is connected to four equally-spaced tangential ports in the burner's outer chamber. The air travels upwards in the space between the walls of the inner and outer chambers as shown in Fig. 3.3. The air first passes through a coarse screen fitted in the annulus close to the base of the burner to straighten the flow after which it enters a honey-comb to make the flow more uniform across the annulus. Further downstream, it passes through another screen but of finer pores before going through the swirl generators and exiting through an air annulus which has an inside and outside diameter of 14.9 mm and 36.6 mm, respectively. The four swirl generators used here as shown in Fig. 3.6(a) to (d) (also see Philips, 2006) have vane angles α, of 0°, 25°, 50°, and 60°, which corresponds to swirl numbers, S of 0, 0.31, 0.79, and 1.15. The swirl number is calculated as (Birouk and Gupta, 2001):

$$S \approx \frac{2}{3}\tan\alpha \tag{3.2}$$

Figure 3.7 shows the top-view of a typical vane swirler indicating how the vane angles were measured.

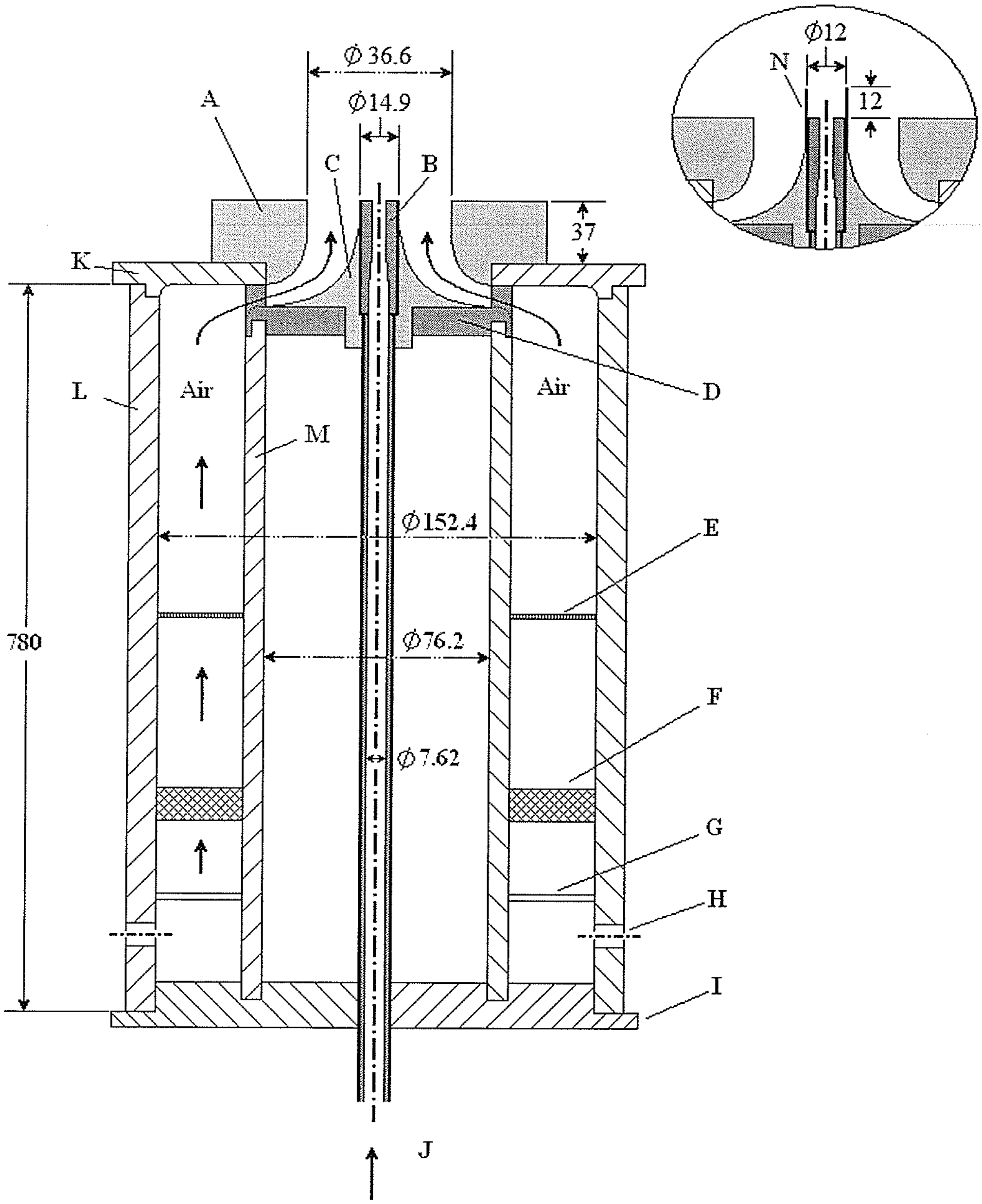

Figure 3.3: Schematic diagram of burner arrangement used for studying reacting jet (all dimensions are in mm). A-Swirl Pipe, B-Nozzle, C-Nozzle holder, D-Vane swirl generator, E-Fine screen, F-Honeycomb, G-Coarse screen, H-4 Equally-spaced tangential air ports where air seeded with TiO_2 or not seeded at all is introduced, I-Bottom plate, J-Methane either seeded with TiO_2 or not seeded at all in through the central pipe, K-Top plate, L-Outer chamber, M-Inner chamber, and N-Quarl (Sudden expansion).

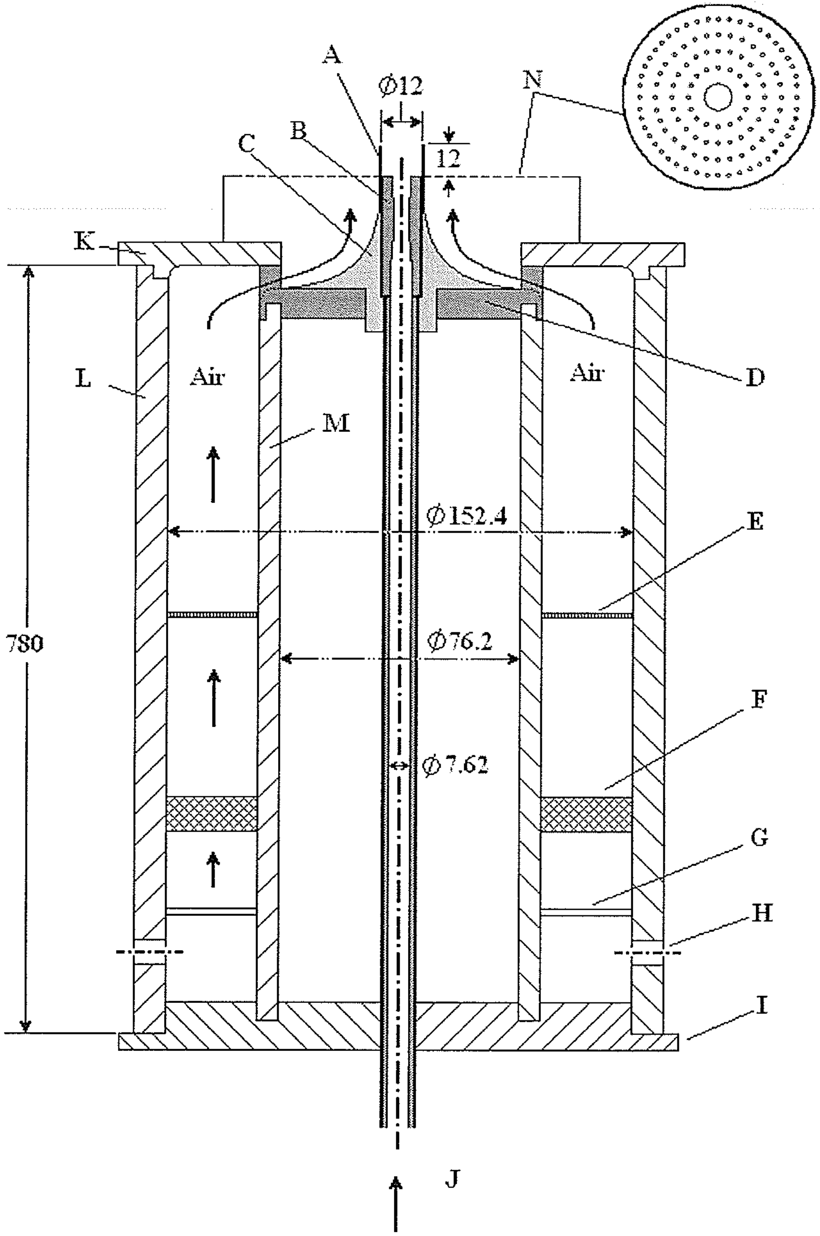

Figure 3.4: Schematic diagram of burner arrangement used for studying non-reacting jet (all dimensions are in mm). A- Sudden expansion (or quarl), B-Nozzle, C-Nozzle holder, D-0° Vane swirl generator, E-Fine screen, F-Honeycomb, G-Coarse screen, H-4 Equally-spaced tangential air ports where air seeded with DEHS is introduced, I-Bottom plate, J-Air seeded with incense particles in through the central pipe, K-Top plate, L-Outer chamber, M-Inner chamber, and N-Perforated cylindrical plate filled with equally spaced concentric holes of Ø2.0 mm.

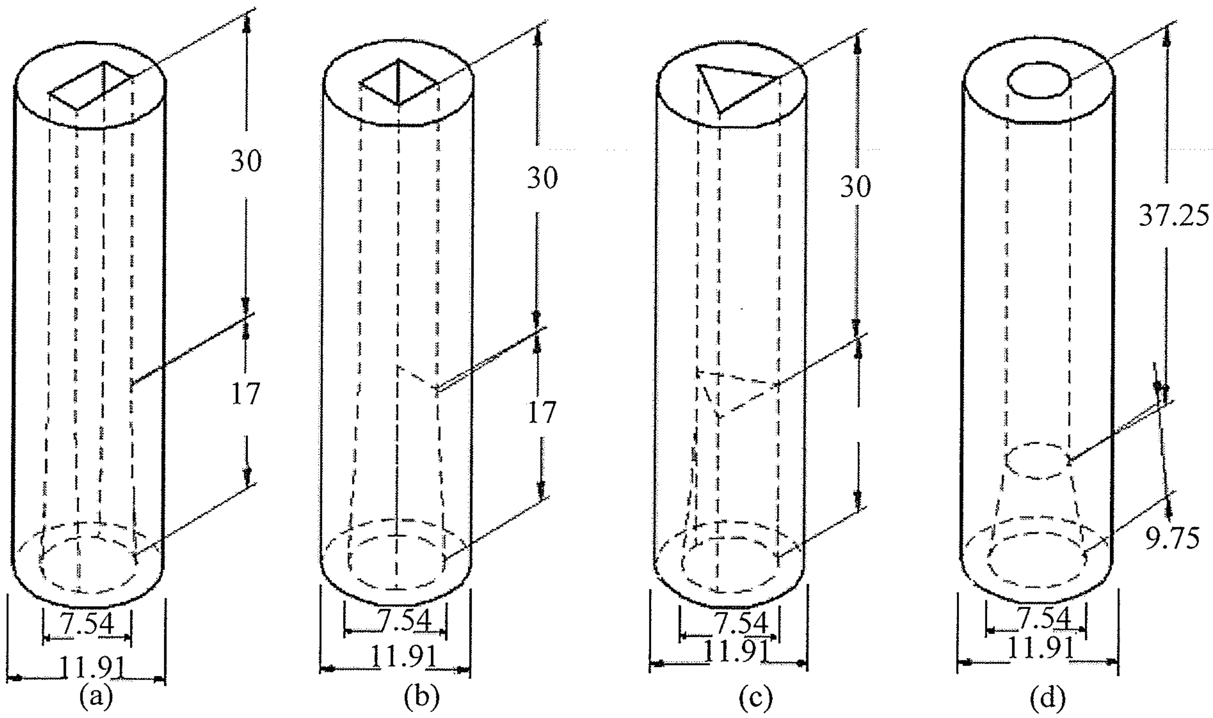

Figure 3.5: Nozzle shapes (all dimensions are in mm) - (a) Rectangular, (b) Square, (c) Equilateral triangle, and (d) Contracted circular.

3.3.3 Gas Burner Arrangement for Non-Reacting Jet Flow

Figure 3.4 shows a schematic of the flow arrangement used for the non-reacting jet. It is almost the same configuration used for jet flame (reacting flow) without co-flow. The only differences are that the swirl pipe in the reacting jet flow is replaced by a perforated cylindrical plate which has equally spaced Ø2 mm concentric holes on top and the presence of a very weak co-flow. This is intended to minimize the effect of seeding bias, which can be caused by not seeding the surroundings of the jet. Therefore, a similar method to that employed by Mi *et al.* (2007) for seeding the jets' ambient was used. This was recommended in order to approach an acceptable level of statistically uniform spatial seeding which is needed for bias-free LDV measurements (Hussein *et al.*, 1994). The seeded co-flow is a very low-momentum flow with a maximum exit velocity of less than 1% of the jet's bulk exit velocity of 30 m/s. Also in this burner configuration, the air supplied from a laboratory compressed supply line replaces the methane as shown in Fig. 3.4. A fraction of the air is passed through the annulus while the remaining flows through the central nozzle's flowmeter before entering the central pipe.

The same nozzles used for the reacting jet were also employed in this configuration for studying non-reacting jet. However, the smooth pipe was different. A larger pipe of Ø7.62 mm replaced the Ø4.45 mm pipe used for the flame experiments. This relatively large diameter of the smooth pipe was chosen because a smaller diameter pipe was found prone to misalignments and hence could cause error in the LDV velocity measurements.

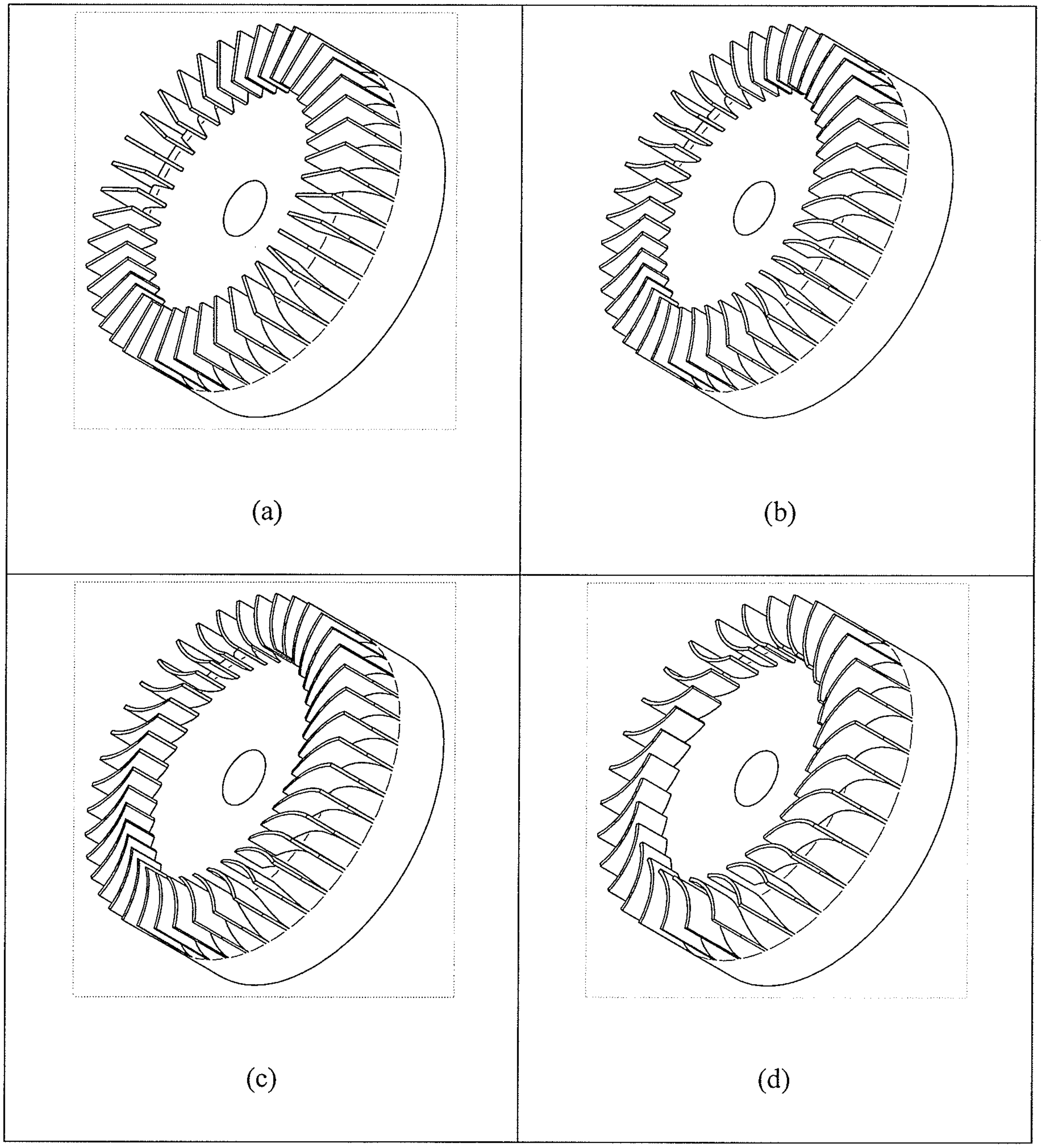

Figure 3.6: Different degrees of vane swirlers used with vane angles and number of vanes - (a) 0° (40 vanes), (b) 25° (40 vanes), (c) 50° (40 vanes), and (d) 60° (30 vanes).

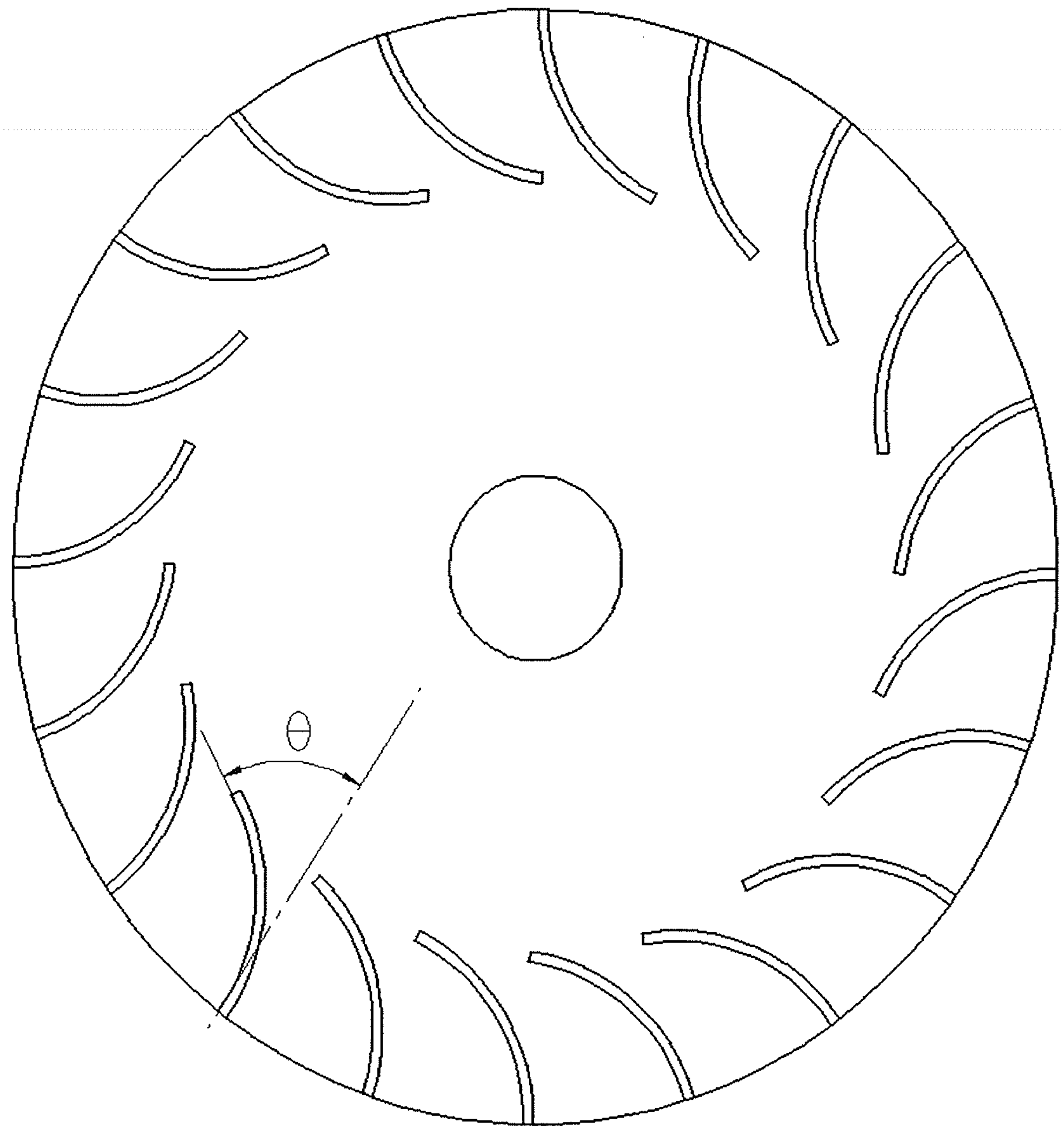

Figure 3.7: Top view of a typical vane swirler showing how vane angles in Fig. 3.6 were measured (θ represents the vane angle).

3.4 Measurement Techniques

The measurement techniques employed were based on the type of data needed. For the flame lift off height and the flame length, a high speed digital video camera was used whereas LDV was used for flow velocity measurements of the reacting and non-reacting jet flows. The following sub-sections present a brief overview of these measurement techniques.

3.4.1 Imaging Technique

The liftoff height, h, and flame length, l, are imaged by a NanoSense MKIII high-speed camera. The distance from the nozzle exit to the flame base (i.e. the lowest point of the flame) is the liftoff height while flame length is the distance from the nozzle exit to the visible flame tip (i.e. highest point of the flame). Figure 3.8 shows a typical definition of flame liftoff height and flame length.

The camera resolution of 1280×1024 pixel was used for all measurements. The camera frequency of 60 Hz was used for the jet flame with co-flow measurements while two different camera frequencies were employed for the jet flame experiments without co-flow; 60 Hz for exit velocities greater than 40 m/s, and 30 Hz for velocities below 40 m/s. For the flame experiments without co-flow, over 1600 images were taken for each set condition to determine the average flame liftoff height while a total of not less than 815 images were taken to determine the average liftoff height and length of flames with a co-flowing air stream. For the flame liftoff height measurements, the camera was set close to the flame, whereas it was set relatively farther away for the flame length in order to capture a larger field of view as the flame length fluctuates more than the liftoff height. The relatively high number of images was chosen to statistically improve the accuracy of the fluctuating flame liftoff height and flame length.

A ruler was first placed over the burner in order to calculate the height of a pixel, and thus calibrate the imaged field of view. The liftoff height and length of each flame was measured from the nozzle exit plane. An in-house developed MATLAB code (i.e. image processing code presented in Appendix B) was used to analyze the images and determine the flame base and peak based on the brightness of each pixel, and thus calculates the number of pixels between the nozzle exit and the flame base or tip. A threshold was applied to separate the background from the real flame image. The MATLAB code assigns each pixel a brightness level between 0 and 256, with 0 being black and 256 being white. The number of pixels between the flame base or tip and nozzle exit was then multiplied by a pixel height to determine the liftoff height or the flame length, respectively.

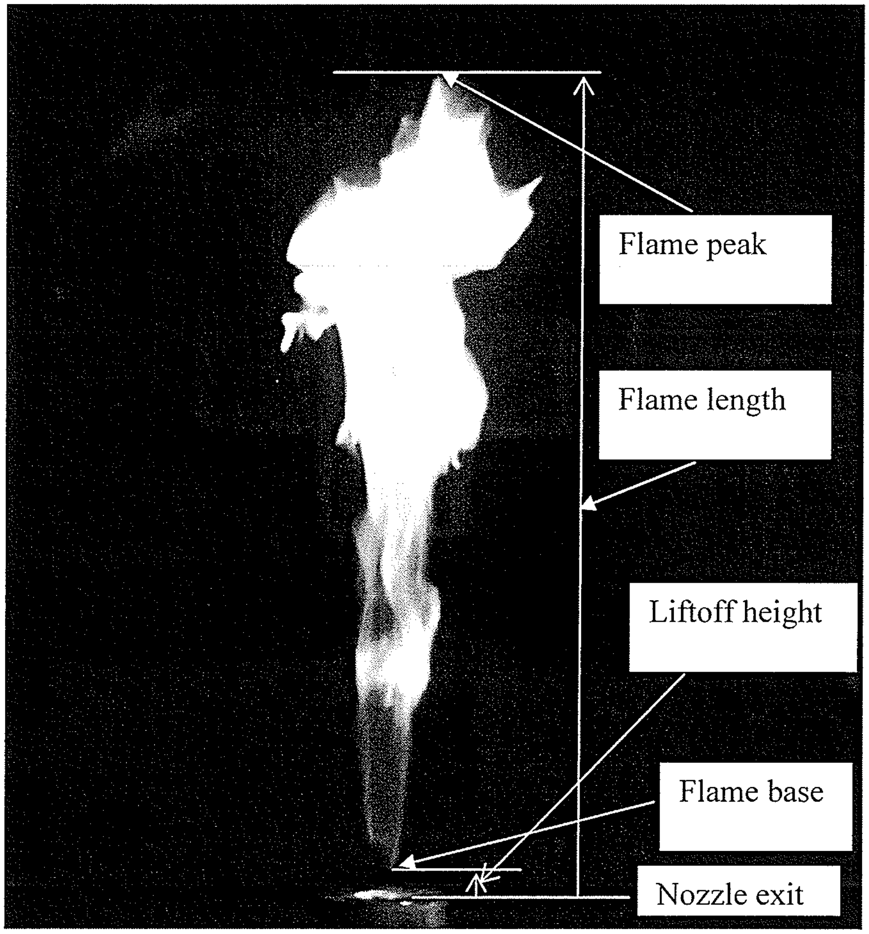

Figure 3.8: Definition of flame liftoff height and flame length.

3.4.2 Laser Doppler Velocimeter (LDV)

The main components of the LDV system used in the present study are shown in Fig. 3.9. This LDV is capable of two-dimensional flow velocity measurements capability. It is a non-intrusive technique for measuring the instantaneous velocity of a seeding particle assumed to be moving at the same speed as the carrier fluid, and it requires no calibration. The flow of interest is seeded with small tracer particles that follow the fluid motion faithfully. The seeding particles are illuminated by a coherent laser light causing them to scatter light which is picked up by the transmitter and sent to the analyser which determines the particle's frequency and velocity information. The transmitter/receiver is mounted on a traversing mechanism controlled by the Flowsizer software installed in the computer. The traversing mechanism is used to position the probe in *x-y-z* direction. The traversing mechanism cannot move below 0.01 mm in all directions. Note that it is only the *x* and *y* directions that could be automatically controlled by the computer but the *z* direction has to be manually adjusted via a micrometer. The operating principle of the laser used in this thesis is presented next.

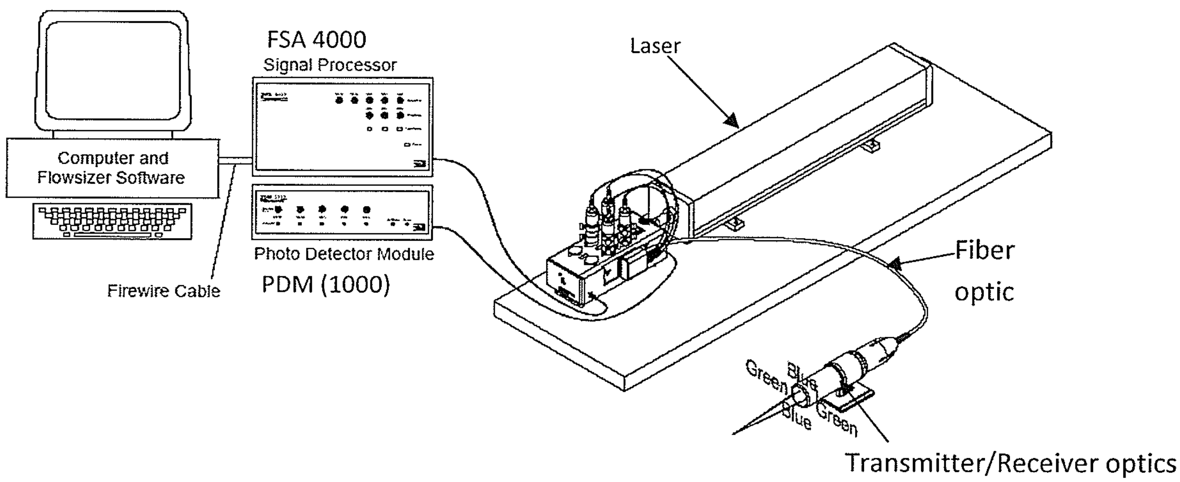

Figure 3.9: Schematic diagram of LDV (TSI, 2000).

3.4.2.1 Operating Principle of the LDV Used in the Present Study

Figure 3.10 shows a schematic layout of the LDV system used in this study. It operated in a back-scattering mode. Innova 70C series, 5 W (all modes included), argon-ion laser generates a coherent (fixed frequency) beam which illuminates the flow (i.e. seeding particles). The laser used in this experiment generates two green beams of equal intensity (having a 514.5 nm wavelength) and two blue beams with equal intensity (wavelength of 488 nm). These beams are transmitted through an optical fiber to the transmitting/receiving optic that uses a 363 mm focal length lens to intersect the beams. The intersection at the focal point of the lens forms a probe volume. The probe volume consists of a set of bright and dark fringes. The measurement volume has a Gaussian intensity distribution in all three-dimensions. The bright fringes increase in intensity as you move towards the center of the measuring volume. A particle scatters light as it crosses the bright fringes. The scattered light is collected by the transmitting/receiving optics and converted to electrical signals by Photomultiplier Tubes (PMTs) (i.e. the Photo Detector Module 1000 (PDM 1000)). The PDM 1000 sends the signal as an electrical signal to the TSI Flow Size Analyzer 4000 (FSA 4000) signal processor. The latter extracts the frequency at which the seeding particle crossed a bright fringe. This frequency is known as Doppler frequency, f_D, and because the fringe spacing, δ_f, is geometrically fixed, the Flowsizer can determine the particle's velocity, u_∞, as

$$u_\infty = \delta_f f_D. \tag{3.3}$$

The measurement (probe) volume is ellipsoidal in shape and its dimensions are tabulated in Table 3.1 (see Appendix C for the equations used in calculating the dimensions of the probe volume). Furthermore, the settings of the optics and the laser beams used are also tabulated in Table 3.1.

To maximize the data rate, the software called Flowsizer is optimized. This process is mostly iterative and it involves selecting the right PMT voltage, Burst threshold, Band pass filter, Signal-to-Noise Ratio, and downmix frequency.

Table 3.1: Characteristics of the laser optics set-up

	Channel 1 (Green Beams)	**Channel 2 (Blue Beams)**
Wavelength (nm)	514.5	488
Focal Length (mm)	363	363
Beam Separation (mm)	40.00	40.00
Laser Beam Diameter (mm)	2.80	2.80
Fringe Spacing (μm)	4.6762	4.4353
Probe Volume Width (μm)	84.93	80.55
Probe Volume Length (mm)	1.53	1.46
Probe Volume Height (μm)	85.06	80.67

Note that LDV was mainly used for the non-reacting turbulent jet and the reacting jet in the presence of swirling/non-swirling co-flow. For each flow location, 40,000 sample points are taken to determine the orthogonal mean velocities, U and V, and their mean fluctuating components.

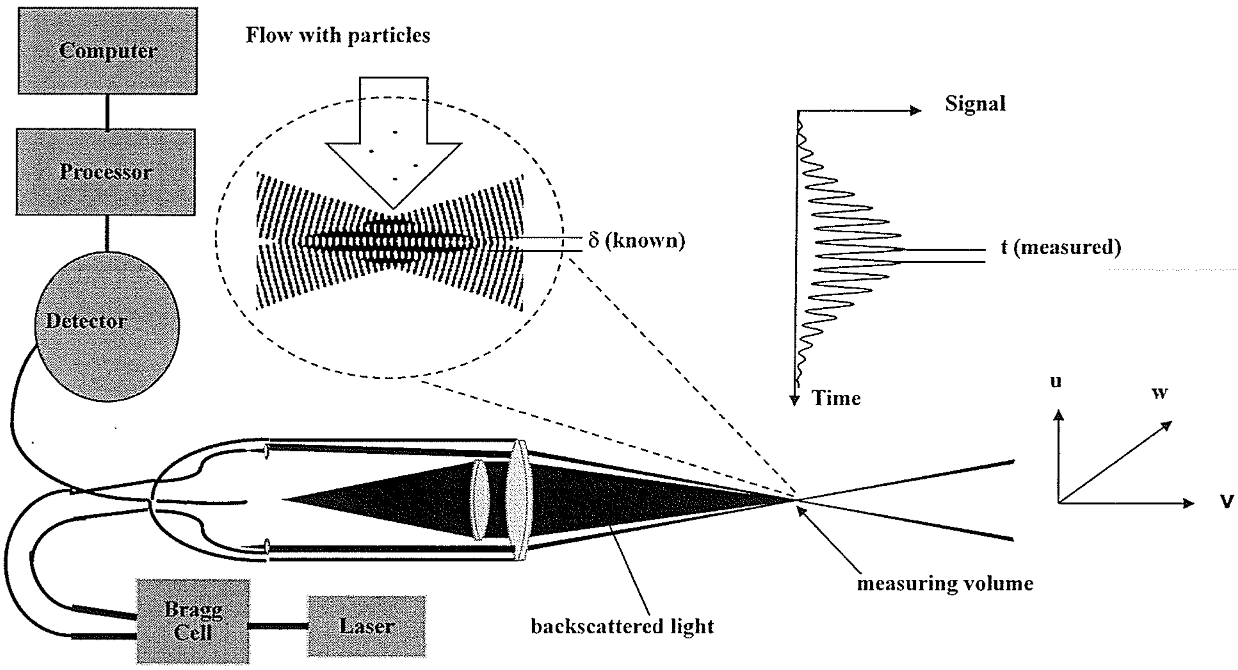

Figure 3.10: Schematic layout of the backscattering LDV used in the present study.

3.5 Uncertainty Estimates

This section treats separately the combined measurement uncertainties of the reacting and non-reacting jet flows. There are two broad sources of error in experimental measurements, namely bias and precision errors. Consequently, the total uncertainty can be found by combining precision and bias errors as: $\sigma_{total} = \pm(B+tP)$, where B is the bias error, P is the precision error, and t = 1.96 for a 95% confidence level.

3.5.1 Non-Reacting Jet Flow Uncertainty Estimates

The error analysis of the LDV data is based on the recommendations of Schwarz (1998) and relevant references cited therein. A 95% confidence interval for Gaussian (or nearly Gaussian) distribution was assumed (Moffat, 1988). The equations used for the uncertainty estimates are given in Appendix D.

Applying these uncertainty equations, it was found that close to the nozzle exit (i.e. $x = 2$ mm) and downstream, a typical error obtained for the mean velocities at the center of the jet are about ±0.4% while those at the shear-layer (i.e. at the jet edges) are about ±0.9%. The corresponding mean turbulence intensity uncertainties at the centerline and shear-layers are ±0.7 % for u and ±0.6% for v while the Reynolds shear stress uncertainty in the shear-layer is about ±10% at $x = 2$ *mm*. The Reynolds shear stress uncertainty in the far-field shear-layer reduces to about ±3.0% while those of the turbulence intensities remain nearly unchanged.

3.5.2 Reacting Jet Flow Uncertainty Estimates

The reacting jet flow combined uncertainty was quite difficult to quantify. In contrast to the precision errors, the bias errors were not very difficult to quantify. Consequently, the precision error of the measurements was estimated by using 95% confidence interval. The error estimated for the liftoff height measurements is about ±0.6% while that of the flame length is about ±1.0%. The maximum error estimated for the blowout and liftoff velocities are ±5.4% and ±3.4%, respectively. The relatively higher error of the flame blowout and liftoff velocities are mainly due to the limited number of samples taken (i.e., three measurements for each set condition). However, these three measurements for each set condition were very similar so, in order not to waste the methane gas, these measurements were deemed sufficient.

3.6 Test Conditions

Table 3.2 represent the test conditions employed in the study of non-reacting jet flow as well as reacting jet flow (with no co-flow). Table 3.3 represents the conditions tested for turbulent methane flame with swirling/non-swirling co-flow.

Table 3.2: Experimental test conditions for non-reacting turbulent jets with and without sudden expansion.

Nozzle	**D_e (mm)**	**U_j (m/s)**	**Re ($\times 10^{-3}$)**
Pipe	7.62	30	16.1
Contracted Circular	4.82	30, 65	10.2– 22.1
Rectangle	4.71	30, 65	9.9 – 21.6
Triangle	4.46	30, 65	9.4 – 20.4
Square	4.56	30, 65	9.6 – 20.9

Table 3.3: Experimental test conditions for turbulent jet flame without sudden expansion and no co-flow.

Nozzle geometry	Pipe	Contracted circular	Rectangle	Triangle	Square
D_e (mm)	4.45	4.81	4.71	4.46	4.56
Reacting jet's exit velocity (m/s)	27-68	27-68	27-78	27-68	27-68

Table 3.4: Experimental test conditions for turbulent jet flame with sudden expansion but without co-flow.

Nozzle geometry	**Pipe**	**Contracted circular**	**Rectangle**	**Triangle**	**Square**
D_e (mm)	4.45	4.81	4.71	4.46	4.56
Reacting jet's exit velocity (m/s)	27-67	27-88	27-88	27-88	27-88

Table 3.5: Experimental test conditions for turbulent jet flame with co-flow but without sudden expansion.

	Contracted Circular Nozzle (CCN)			**Rectangular Nozzle (RN)**		
Quantities Measured	U_j *(m/s)*	U_a *(m/s)*	S	U_j *(m/s)*	U_a *(m/s)*	S
Liftoff Height, h	35-90	0.58, 2.65	0, 1.15	35-90	0.58, 2.65	0, 1.15
Blowout	*	0.58-4.56	0-1.15	*	0.58-4.56	0-1.15
Flame Length	35-75	0.58, 3.02	0, 1.15	35-75	0.58, 3.02	0, 1.15
Liftoff Velocity	*	0.58-4.56	0-1.15	*	0.58-4.56	0-1.15
U, u, v, uv (LDV)	60	3.02	1.15	20, 60	1.84, 3.02	0, 1.15

*Denotes the quantity that is required to be measured.

CHAPTER 4: RESULTS AND DISCUSSIONS

This section is sub-divided into non-reacting and reacting jet flows. Non-reacting flow results on the effect of sudden expansion on the entrainment and spreading of a turbulent free jet issuing from asymmetric nozzles are presented first, followed by the effect of exit velocity on the jet centerline mean velocity decay and spreading. Reacting jet flow results, concerning the effect of asymmetric nozzles and sudden expansion on the stability of a turbulent methane jet flame issuing into a quiescent environment are presented next. Finally, this section will be concluded by results on swirling and non-swirling methane flames.

4.1 Non-Reacting Jet Flow

4.1.1 Effect of Sudden Expansion on Entrainment and Spreading of a Turbulent Free Jet

The results presented in this sub-section concern LDV profiles of the streamwise mean velocity decay, the streamwise development of the jet half-velocity width, the streamwise and radial mean velocity, turbulence intensity and Reynolds shear stresses of each nozzle's geometry with and without sudden expansion along the centerline plane as shown in Fig. 4.1. However, the sudden expansion (quarl) is not used for the pipe flow, as the current burner arrangement requires further complicated modifications to allow the use of quarl. The two-dimensional results presented below are deemed sufficient because the main focus of the present work is on studying the effect of a sudden expansion (i.e. quarl) on jet's entrainment and spreading, which can be determined via two-dimensional measurements. Furthermore, two-dimensional study can reveal largely the rate of entrainment because the most significant quantity needed to determine jet's entrainment is the mean centerline velocity decay. However, for a better understanding of the effect of the asymmetry of a nozzle on the spreading of the rectangular jet, the minor plane (*x*-*z*) of the rectangular nozzle was also explored to assess the development of the half- velocity width along this plane. Note that all results in this sub-section are for a 30 m/s air jet.

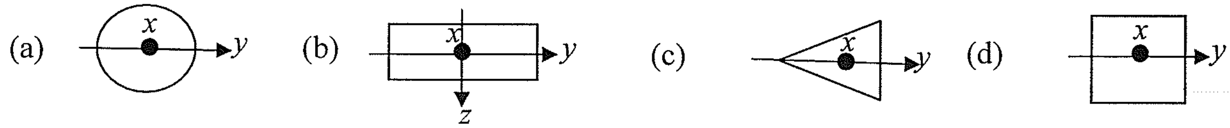

Figure 4.1: LDV measurement planes for-(a) Smooth pipe or contracted circular nozzle (b) Rectangular nozzle (c) Equilateral triangular nozzle, and (d) Square nozzle.

4.1.1.1 Mean Streamwise Centerline Velocity Decay Without Quarl

Figure 4.2 shows the effect of asymmetric nozzles on the streamwise centerline mean velocity decay without the presence of a quarl. For a self-preserving round jet, the centerline mean velocity decay is expressed as (Xu and Antonia, 2002)

$$\frac{U_{\max}}{U_{cl}} = \frac{(x - x_0)}{C_1 D_e}, \tag{4.1}$$

where x_0 is the virtual origin, C_1 is the decay constant, x is the centerline streamwise distance from the nozzle exit, U_{max} is the maximum centerline mean velocity, and U_{cl} is the centerline mean velocity. For a round jet, it is usually assumed that the self-preserving region is at $x/D_e \geq 20$ (e.g., Boersma *et al.*, 1998; Capp *et al.*, 1990; Xu and Antonia, 2002; Quinn, 2005; Panchapakesan and Lumley, 1993). Consequently, Eq. (4.1) is used to fit the measured data presented in Fig. 4.2 in the range between $x/D_e = 20 - 45$, where for the pipe jet, C_1 and x_0 are found to be approximately 5.82 and $2.76D_e$, respectively. The present value of C_1 is not in good agreement with published values reported in Table 4.1, however, the present x_0 seem to be in fair agreement with that of Xu and Antonia (2002). One may attribute this discrepancy in C_1 to the difference in the exit conditions of the pipe's jet (e.g., Reynolds number, orifice exit shape) or the technique employed by the different investigators to measure the jet velocity profiles. However, since the value of C_1 reported by Xu and Antonia (2002) is nearly similar to published results of Boersma *et al.* (1998) and Ferdman *et al.* (2000) which are obtained at two largely different Reynolds numbers, this rules out the possibility of Reynolds number difference being the cause of this disparity in the value of C_1. However, the published velocity measurements were obtained by using hot-wire anemometry (Boersma *et al.*, 1998; Xu and Antonia, 2002; Ferdman *et al.,* 2000) whereas LDV is used in the present study. It has been found that measurements of mean velocities and their fluctuating components obtained using hot-wire anemometry exhibit some differences compared to those obtained by using LDV (Hussein *et al.*, 1994; Panchapakesan and Lumley, 1993). In fact, the value of C_1 for a contracted circular nozzle obtained, with the same test conditions, by using hot-wire anemometry and LDV was quite different (Hussein *et al.*, 1994). Some of these discrepancies were assumed to be caused by the cross-flow and rectification errors present in stationary hot-wire measurements. However, even the flying hot-wire measurements were also found to differ from those acquired by using LDV (Hussein *et al.*, 1994). Therefore, the reason for the discrepancy in the values of C_1 between the present study and published studies may be attributed to the different techniques used for velocity measurement. It is believed that the co-flow is too weak to cause such a significant discrepancy in the value of C_1.

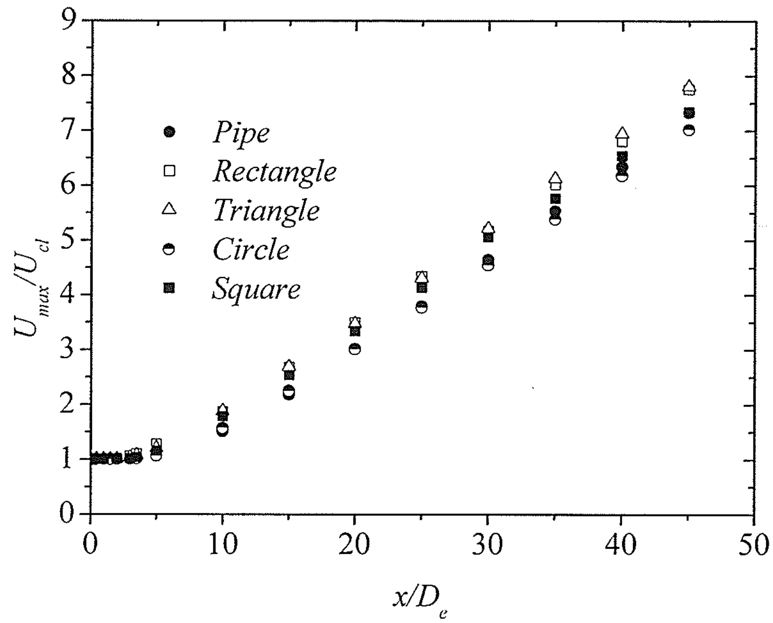

Figure 4.2: Centerline mean velocity decay for various nozzle geometries without quarl.

Table 4.1: Jet decay rate for the pipe flow

Ref.	***U* (m/s)**	***D_e* (mm)**	**Re × 10^{-3}**	***C_1***	***x_o***
Present Work	30	7.62	15	5.82	2.76D_e
Xu and Antonia (2002)	23.3	55	86	6.5	2.6D_e
Boersma *et al.* (1998)	N/A	N/A	2.4	6.3	N/A
Ferdman *et al.* (2000)	N/A	14.5 (far-field) and 25.4 (near-field)	24	6.7	N/A

Using Eq. (4.1) and the same x/D_e range reported above for the pipe, the corresponding values for the rectangular, triangular, contracted circular, and square jets are C_1 = 5.93, 5.74, 6.23, 6.26 while x_0 is -0.65D_e, 0.11D_e, 1.45D_e, and -1.01D_e, respectively (see Tables 4.2 and 4.3). The linear fit for all nozzle jets have almost perfect value of R^2 which is about 1. This value corresponds to a perfect fit. It has to be acknowledged that using the same self-similar region for computing C_1 and x_0 does not in any way imply that all nozzles achieve self-similarity at the same streamwise location.

The present measured value of C_1 for the contracted circular jet is not in good agreement with most published data, as shown in Table 4.2 though it is close to the value of 6.06 obtained by Panchapakesan and Lumley (1993). The difference in C_1 may be primarily due to the dissimilarity in the profile of the nozzle's orifice contraction, and could also be slightly caused in part by the low-momentum co-flow employed in the present study. In fact, the nozzle's orifice contraction ratio of the present contracted circular nozzle is quite low (i.e. 2.5:1) which may be the reason why the velocity profiles are not perfectly top-hat at the exit of the nozzle. The value of x_0 for the present contracted circular jet is also not in agreement with the values reported in Table 4.2. These discrepancies may be partly caused by the same reasons as for C_1. However, the value of x_0 can be different for different Reynolds numbers. In fact, it has been shown that an increase in Reynolds number can lead to a decrease in the streamwise mean velocity decay as a result of a decrease in the rate of jet entrainment, which in turn engenders an increase in the potential core of the jet (i.e. an increase in x_0) (Warda *et al.*, 1999). Furthermore, the values of C_1 and x_0 for the triangular jet are not in agreement with those of Quinn (2005) whose values are 5.10 and 0.389D_e, respectively, at a Reynolds number of 184,000. This difference could result from the Reynolds number, which is significantly different in both studies, the little difference in the nozzle's contraction geometry employed in the two studies, or it could be both. It has to be acknowledged that the nozzle employed by Quinn (2005) has very sharp-edges with a slightly different (larger) contraction compared to the nozzle's configuration employed here.

Table 4.2: Jet decay rate for the contracted circular nozzle without quarl

Reference	***U*** ***(m/s)***	**Measurement type**	D_e *(mm)*	**Re × 10^{-3}**	C_1	x_o
Present Work	30	LDV	4.82	9.4	6.23	$1.45D_e$
Xu and Antonia (2002)	23.3	Hot-wires	55	86	5.6	$3.7D_e$
Boersma *et al.* (1998)	N/A	DNS	N/A	2.4	5.9	N/A
Capp *et al.* (1990)	N/A	LDV	N/A	N/A	5.8	N/A
Capp *et al.* (1990)	N/A	Hot-wires	N/A	N/A	5.9	N/A
Rodi (1975)	101	Hot-wire	12	87	5.9	N/A
Panchapakesan and Lumley (1993)	27	Hot-wire	6.1	11	6.06	$-2.5D_e$

Figure 4.2 shows clearly that with a jet bulk exit velocity of 30 m/s, the jet decay is faster for the triangular nozzle, followed by the rectangular, with the pipe as the lowest. This trend confirms the findings reported in (Mi *et al.*, 2000; Quinn, 2005) amongst others. This is more evident when observing the centerline streamwise mean-velocity decay of the jet's near-field region (i.e. $x/D_e \leq 15$), as shown in Fig. 4.3.

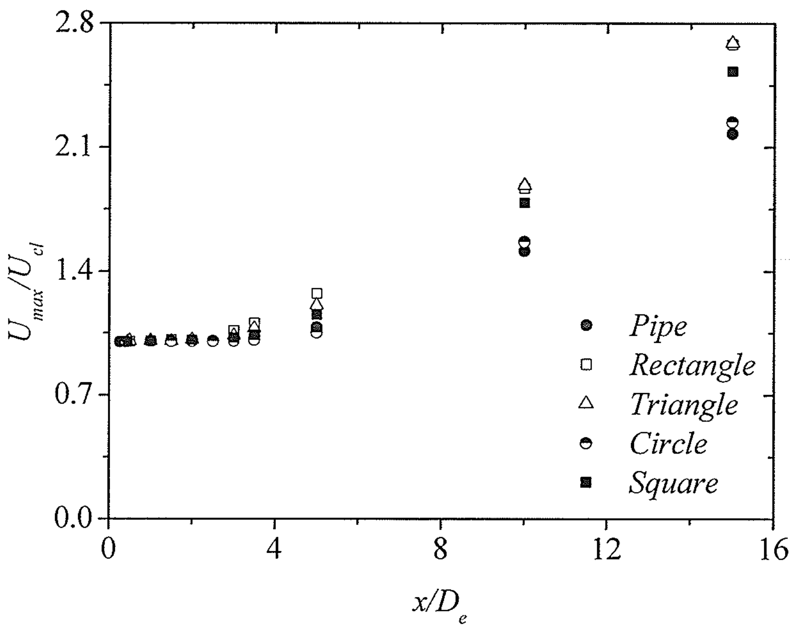

Figure 4.3: Near-field centerline mean velocity decay for various nozzle geometries without quarl.

What can be retained from the brief discussion above and from Fig. 4.2 to 4.3 is that the coefficient C_1 alone seems incapable of predicting the trend of the rate of jet entrainment for all nozzles' geometries as presented in Fig. 4.3. Also the values of x_o alone do not reflect this trend. It has been shown that the lower the C_1, the higher the rate of entrainment (Xu and Antonia, 2002). However, this concept fails when the pipe, which has the lowest entrainment rate and the square with the third highest rate of entrainment, are included. This failure is due to the differences in the decay rate of the pipe and square in the near-field (i.e. $x/D_e \leq 20$) and far-field (i.e. $x/D_e > 20$) relative to other nozzles. In the near-field, the pipe's streamwise centerline mean velocity decay is lower than all of the other nozzles but becomes similar to the square jet and even becomes higher than the contracted circular nozzle in the far-field when self-preservation of the jet is reached. Consequently, because C_1 is calculated in the far-field (i.e. $x/D_e \geq 20$), it does not give an accurate representation of the near-field which determines the extent of entrainment. This finding is consistent with that of Quinn (2005) who tested triangular jets and a sharp-edged circular nozzle. Quinn (2005) found that the value of C_1 for the round jet and isosceles triangular jet were lower than that of the equilateral triangular jet but the near-field clearly showed that the equilateral triangular jet had better entrainment. On the other hand, the x_o in the present study does not have any particular order/trend and no firm conclusion can, therefore, be obtained from it. This is also in accordance with the findings of Quinn (2005). However, if C_1 and x_0 of each individual nozzle, as presented in Tables 4.1 to 4.2, are combined then they can predict an overall pattern or order of the velocity decay rate (i.e. entrainment rate) shown by the tested nozzles. Consequently, C_1 and x_0 are sufficient to predict the nozzles' streamwise mean velocity decay in the far-stream.

4.1.1.2 Jet Centerline Mean Velocity Decay with Quarl

The streamwise mean velocity decay in the jet centerline is shown in Figure 4.4 for the rectangular, triangular, square, and contracted circular nozzles with and without quarl. Note that the measurements of the mean velocities and their fluctuating components with the presence of quarl were taken starting from $x/D_e = 3.5$ downstream of the nozzle exit. Consequently, to make a comparison between the quarl and no-quarl jet configurations, the results of the no-quarl configuration are only considered for $x/D_e \geq 3.5$. In addition, the U_{max} for the sudden expansion configuration is taken as the U_{max} of the corresponding geometries without sudden expansion (often taken at x = 2 *mm* or further downstream depending on the nozzle type). This practice is necessary in order to account for the effect of sudden expansion and exit velocity on the streamwise centerline mean velocity decay. Figure 4.4 compares the centerline mean velocity decay for the jet flow configurations with and without quarl. Utilizing the same Eq. (4.1) to fit the present quarl experimental data in the range $20 \leq x/D_e < 45$, we find the values of C_1 and x_0 as reported in Table 4.3.

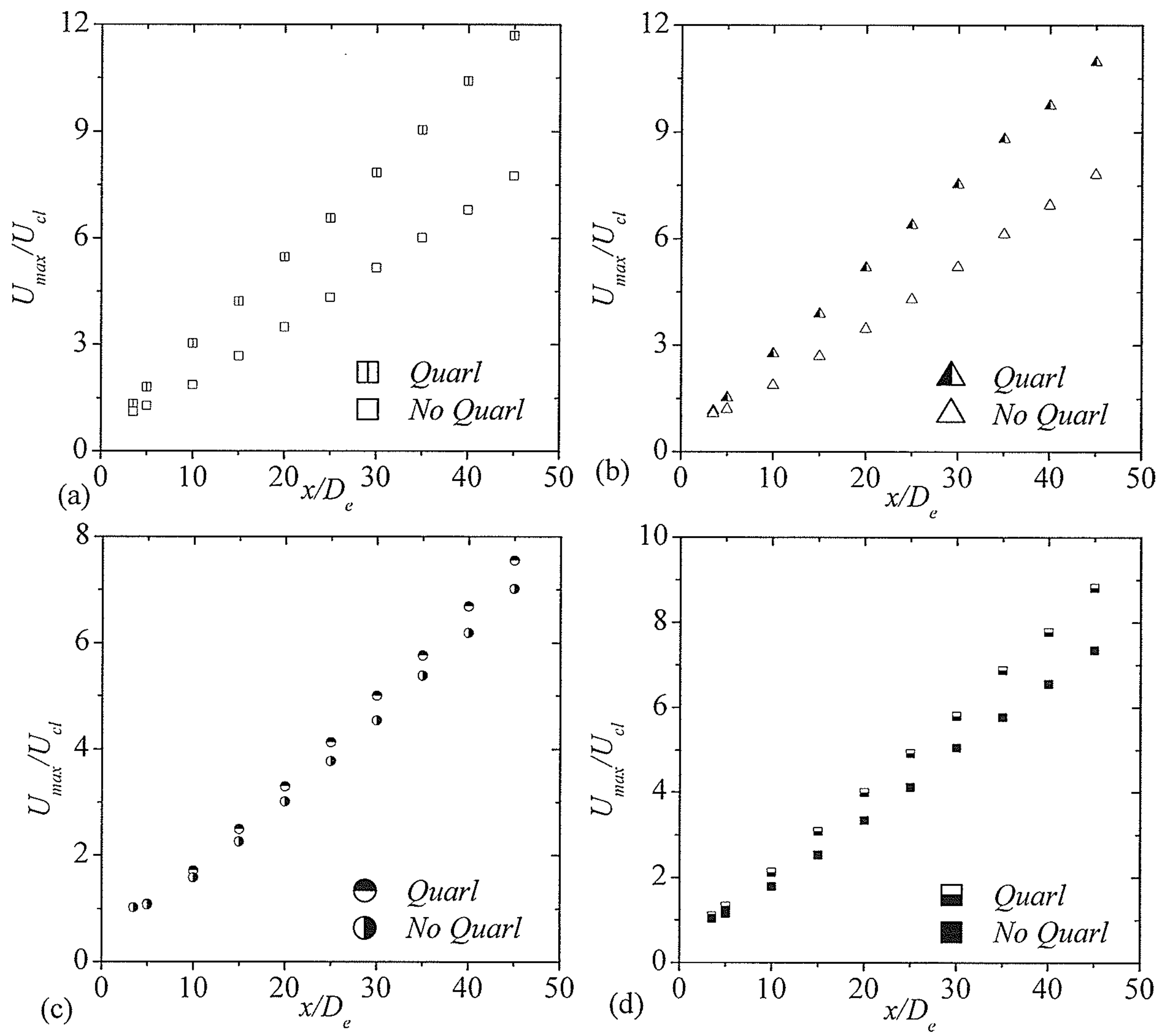

Figure 4.4: Centerline mean velocity decay for various nozzle geometries with and without quarl-(a) Rectangle, (b) Triangle, (c) Contracted circular, and (d) Square.

Table 4.3: Jet decay with and without quarl for different nozzle's geometries

Geometries	(U_{max} taken at $x = 2$ *mm* or the highest U_{cl}) U_j=30 m/s No Quarl		With Quarl	
	C_1	x_o	C_1	x_0
Rectangle	5.93	$-0.65D_e$	3.99	$-1.40D_e$
Triangle	5.74	$0.11D_e$	4.35	$-2.74D_e$
Circle	6.23	$1.45D_e$	5.90	$0.63D_e$
Square	6.26	$-1.01D_e$	5.19	$-0.52D_e$

Figure 4.4 clearly reveals that there is considerable improvement in the jet decay when quarl is used as opposed to without quarl. This increase in entrainment may be related to the jet flow changes induced by sudden expansion of the jet flow issuing from a relatively smaller diameter into a larger diameter. For example, studies of the effect of square and rectangle sudden expansion of jets issuing from a square and rectangular nozzle, respectively, showed that the rate of entrainment and spreading is controlled by the growth rate of the streamwise vortices, which are accelerated by the sudden expansion of the nozzle (e.g., Sau, 2002, 2004; Nakao, 1986). Consequently, the higher entrainment generated by the use of quarl may possibly be attributed to the higher growth rate of the streamwise vortices generated by the circular sudden expansion of the jet flow issuing from either an asymmetric nozzle or a contracted circular nozzle. In particular, the higher entrainment of the rectangular and triangular nozzles with quarl is also attributed to their much higher growth rate of their streamwise vortices compared to the other geometries with quarl, such as the square and contracted nozzles. For example, Nakao (1986) found that for a square duct followed by an expansion, the streamwise vortices were largely

weak and do not persist downstream which is an indication of a relatively low jet entrainment. However, Sau (2002) found that there were strong streamwise vortices that dominate the entire flow field of a rectangular sudden expansion jet. Sau (2002) reported that these strong streamwise vortices increase the relative rate of entrainment of the rectangle sudden expansion flow. This may explain why sudden expansion seem to influence the streamwise centerline velocity of the rectangular nozzle much more compared to all other nozzles used here.

4.1.1.3 Development of the Jet Half-Velocity Width without Quarl

The jet half-velocity width is a very good indicator of the jet spreading rate. Figure 4.5(a) presents the jet spreading as a function of x/D_e along the major plane (x-y) of the rectangular nozzle as well as the planes shown in Fig. 4.1 for the remaining four nozzle's geometries tested in the present study.

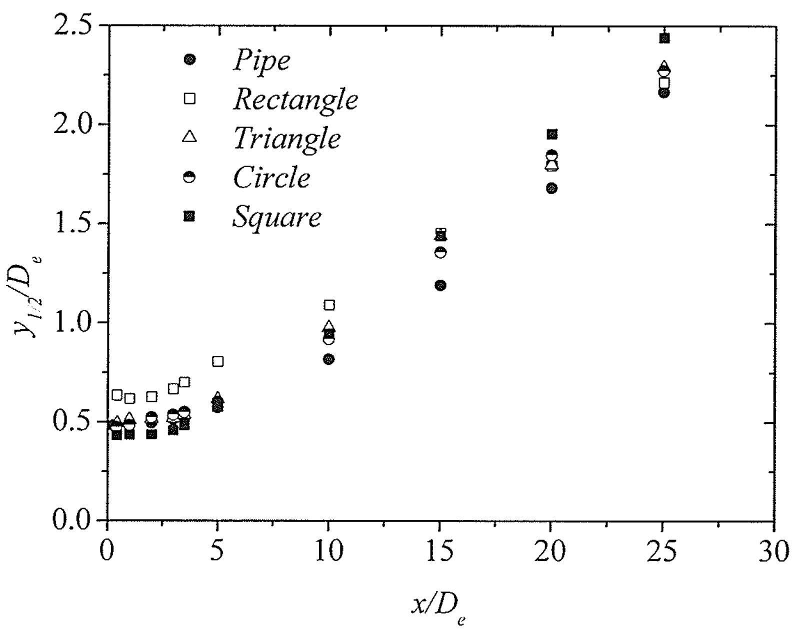

Figure 4.5(a): Jet half-velocity width for various nozzle geometries without quarl.

The requirement for self-preservation for a round jet, according to Xu and Antonia (2002), is given as

$$y_{1/2}/D_e = C_2(x - x_{02})/D_e \tag{4.2}$$

where $y_{1/2}$ is the jet half-velocity width, C_2 is a constant, and x_{02} is a virtual origin. However, the maximum streamwise location where the jet spread is measured for each nozzle is at $x/D_e = 25$ and therefore only two locations (i.e. x/D_e = 20 and 25) are used to compute C_2 and x_{02}. The experimental data for each nozzle's geometry, which is presented in Fig. 4.5(a), is used to fit Eq. (4.2). The value of C_2 for the pipe jet is found to be 0.097 (see Table 4.4), which is not in good agreement with the value of 0.086 found by Xu and Antonia (2002). The value of x_{02} for the pipe is found to be $2.65D_e$ in this study. While the values of C_2 and x_{02} are found to be 0.084 and -$1.28D_e$; 0.098 and $1.72D_e$; 0.085 and -$1.78D_e$; and 0.097 and -$0.11D_e$ for the rectangular, triangular, contracted circular, and square jet, respectively. The value of C_2 for the contracted circular jet is not in good agreement with the LDV measurements of Capp *et al.* (1990), the hot-wire measurement of Xu and Antonia (2002) and the hot-wire measurements of Panchapakesan and Lumley (1993) who obtained a value of C_2 equal to 0.094, 0.095 and 0.096, respectively, as shown in Table 4.5. However, the present value of C_2 is in fair agreement with those of Rodi (1975) and Wygnanski and Fieldler (1969) who both obtained a value of 0.086. These differences may, in part, be due to the variation of the nozzle's orifice contraction profile used by each investigator, and also possibly in part to the different measurement techniques employed. It has to be emphasized that the values of C_2 and x_{02} when used individually do not give a very clear indication of the trend of the spreading rate when comparing different nozzles especially the asymmetric nozzles. For example, the near-field of the triangular and rectangular nozzle gives the impression that they have higher rate of spread; however, the far-field shows that the square nozzle and the contracted circular nozzle become higher. This discrepancy is due to the fact that the pipe, contracted circular nozzle, and to some extent the square nozzle have symmetric mean velocity profiles across most of the planes whereas the rectangular and triangular nozzles are not.

Table 4.4: Jet spread rate for the pipe flow

Ref.	U *(m/s)*	D_e *(mm)*	**Re × 10^{-3}**	C_2	x_{02}
Present Work	30	7.62	15	0.097	$2.65D_e$
Xu and Antonia (2002)	23.3	55	86	0.086	N/A

Table 4.5: Jet spread rate for the contracted circular nozzle

Ref.	C_2	x_{02}
Present work	0.085	$-1.78D_e$
Capp *et al.* (1990)	0.094	N/A
Panchapakesan and Lumley (1993)	0.096	N/A
Xu and Antonia (2002)	0.095	N/A
Wygnanski and Fieldler (1969)	0.086	N/A
Rodi (1975)	0.086	N/A

Consequently, to put in perspective the effect of this asymmetry on jet spread, the measurement of the jet spread for the rectangular nozzle is also performed along the minor plane (x-z). This is represented in Figure 4.5(b) which shows the phenomenon of 'axis switching' that has been observed and described in the literature (e.g., Quinn, 1995, 2005; Zaman, 1996). In the near-field where the rectangular jet still retains its shape (see Quinn, 1995), the spread rate along the minor axis is seen to be lower than that of the major plane but at around $x/D_e = 10$, they become very similar until the jet spreading rate along the minor axis grows much faster than that along the major axis farther downstream. This phenomenon is termed as axis switching and it has been shown that as its frequency of occurrence increases, the rate of entrainment and subsequently mixing is increased. For example, it was observed by Quinn (2005) that axis switching occurs multiple times for the equilateral triangular jet, which may explain its apparent increase in entrainment and jet spreading compared to other nozzle geometries. Furthermore, the half-velocity width of the rectangular and triangular jets, as shown in Fig. 4.5(a), decreases initially or remains nearly constant in the very near-field *(i.e.* for $x/D_e < 2$), which Quinn (2005) attributes to the vena contracta effect of the triangular nozzles. However, for $x/D_e > 2$, the jet half-velocity width increases linearly with the streamwise distance. Nevertheless, the half-velocity width for the other nozzles remains nearly constant starting from the initial point of measurement (i.e. $x = 2$ *mm*) to about $x/D_e < 5$ before it increases linearly with the streamwise distance.

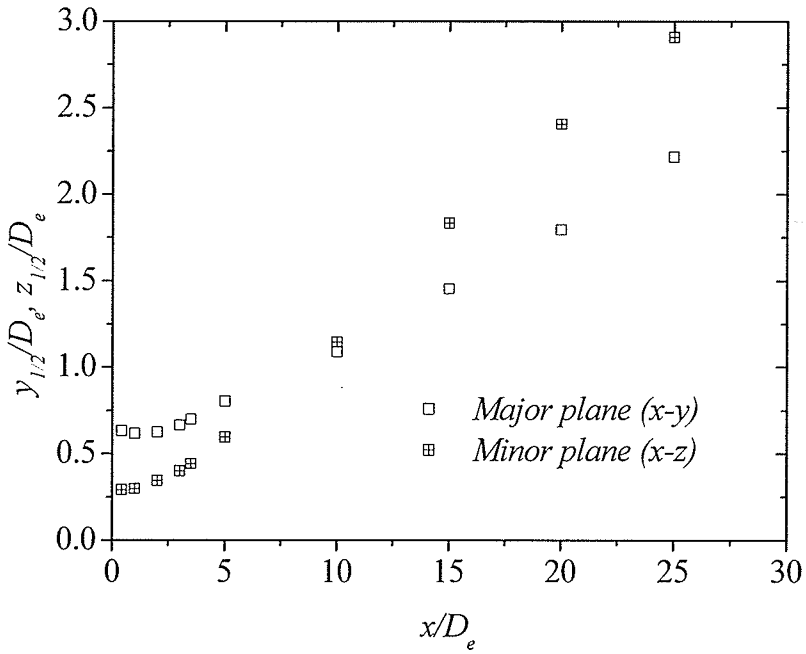

Figure 4.5(b): Comparison of the jet half-velocity width of the major and minor plane of the rectangular nozzle geometry without quarl.

4.1.1.4 Development of the Jet Half-Velocity Width with the Presence of Quarl

The use of quarl considerably increases jet spreading for all the nozzles tested here, as shown in Fig. 4.6. However, the effect of quarl is more predominant in the case of asymmetric nozzles compared with their axisymmetric counterpart (such as the contracted circular nozzle).

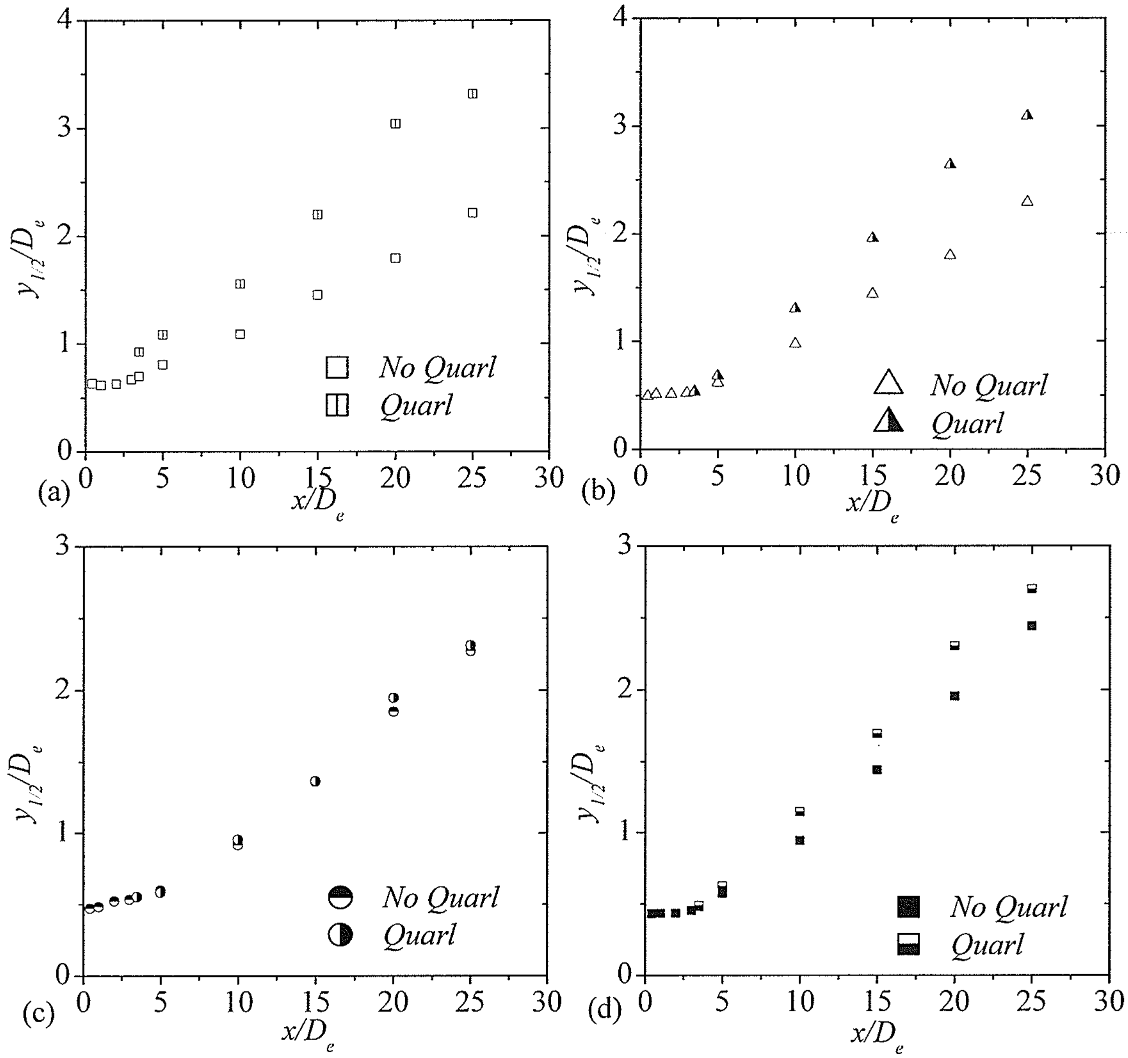

Figure 4.6: Jet half-velocity width for various nozzle geometries with and without quarl- (a) Rectangle, (b) Triangle, (c) Contracted circular, and (d) Square.

Eq. (4.2) is fitted to the data presented in Fig. 4.6 in order to determine the values of C_2 and x_{02} for the different nozzles' configuration. We find that C_2 and x_{02} for the quarl configurations are 0.056 and -34.63D_e; 0.091 and -9.06D_e; 0.073 and -6.80D_e; and 0.080 and -8.92D_e for the rectangular, triangular, contracted circular and square jets, respectively (see also Table 4.6).

Table 4.6: Jet spread rate with and without quarl for different nozzle geometries

Geometries	**No Quarl**		**With Quarl**	
	C_2	x_{02}	C_2	x_{02}
Rectangle	0.084	$-1.28D_e$	0.056	$-34.63D_e$;
Triangle	0.098	$1.72D_e$	0.091	$-9.06D_e$
Circle	0.085	$-1.78D_e$	0.073	$-6.80D_e$
Square	0.097	$-0.11D_e$	0.080	$-8.92D_e$

It has to be emphasized again, that the values of C_2 and x_{02} when considered individually are incapable of representing the trend of the jet spreading rate shown in Figure 4.6. This is because the determination of C_2 and x_{02} is only based on the self-similar region (which is assumed to range from $x/D_e \geq 20$); consequently, they do give an overall good representation of the self-similar regions. Each coefficient (i.e. C_2 or x_{02}) when taken individually, however, is not sufficient to indicate the overall trend of the rate of jet spreading as revealed in Figure 4.6. However, comparing the C_2 and x_{02} of the geometries with quarl and those without quarl, it can be seen that the virtual origins of the geometries with quarl become lower which is an indication of a shorter jet's potential core length and lower values of C_2. In addition, from Figure 4.6, one can easily notice that the rectangular nozzle has the highest overall spread rate followed by the triangular nozzle and thereafter the square nozzle which is in accordance with the trend of the corresponding streamwise centerline mean velocity decay.

4.1.1.5 Profiles of the Mean Velocities, Turbulence Intensities, and Reynolds Stresses with and without the Presence of Quarl

Figure 4.7 presents the centerline mean velocity profiles at a typical near-field region, i.e. $x = 2$ *mm* (which corresponds to the first streamwise location measured), for the five different nozzles tested in the present study.

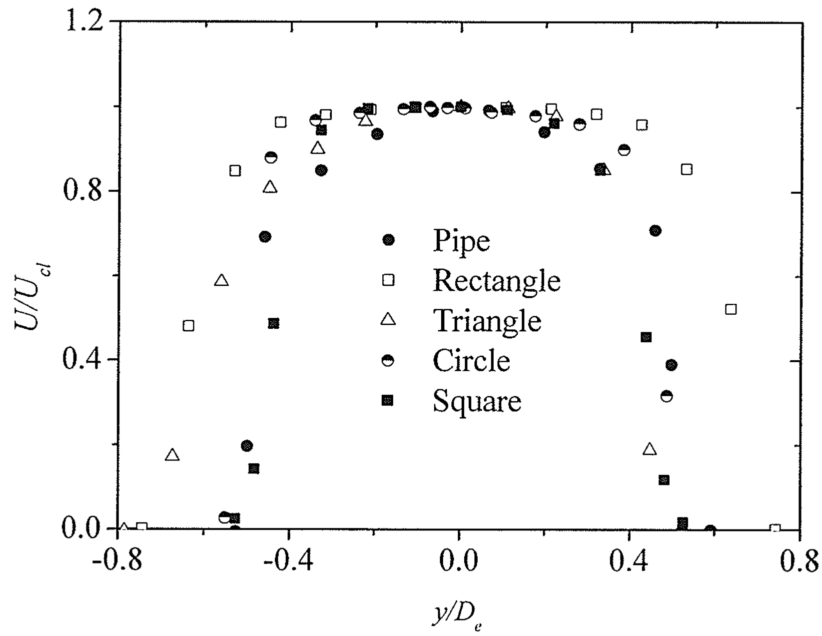

Figure 4.7: Radial profiles of the streamwise mean velocity for various nozzle geometries without quarl at $x = 2$ *mm*.

For the rectangular nozzle, the mean velocity profiles and their corresponding fluctuating components as well as Reynolds stresses are presented only for the major plane (x-y). This figure shows that apart from the pipe, most nozzles' velocity profile approaches a top-hat shape especially the rectangular nozzle's jet. The pipe's fully developed turbulent profile (U/U_{cl}) is fairly well described by the empirical power-law relation $(1\text{-}2y/D_e)^{1/n}$ with $n = 6$, which confirms that the flow upstream of the pipe exit is fully-developed turbulent pipe flow. At flow locations prior to $x/D_e = 3$, LDV measurements for the quarl configuration could not be made because the quarl extends beyond $x = 2$ mm and it is rather too close to $x/D_e = 3$. Consequently, the quarl measurements for the mean velocity profiles, turbulence intensities, and Reynolds stresses are made only for $x/D_e > 3$. Figure 4.8 shows the corresponding turbulence intensities at $x = 2$ mm.

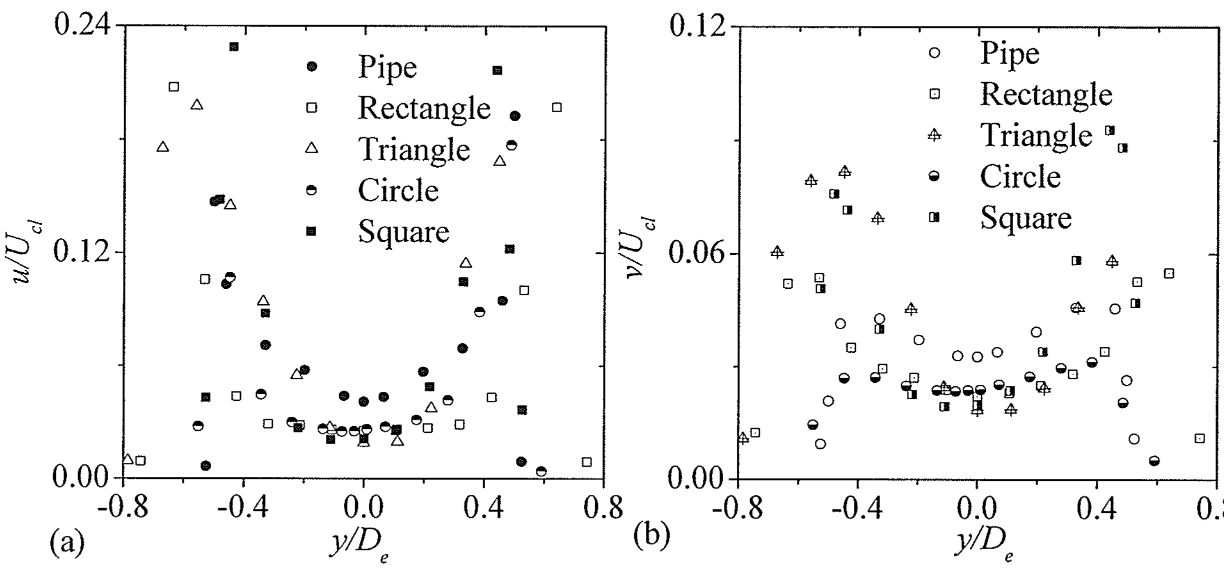

Figure 4.8: Radial profiles of the mean fluctuating velocity components for various nozzle geometries without quarl at $x = 2$ mm.

At this location, u/U_{cl} varies significantly from 4% at $y/D_e = 0$ to 19% at the jet edge for the pipe, while for the other nozzles u/U_{cl} spans between 1.9% and 23%. The asymmetric nozzles have the highest shear-layer turbulence intensities at this location. The superior centerline velocity decay rate and spreading rate of the asymmetric nozzles, which is shown above, could be attributed to their higher shear-layer turbulence intensities. The higher turbulence intensities at the corners of the triangular and rectangular nozzles have been shown by (Quinn, 2005) to produce a stronger vortex pair which enhances entrainment and spreading rates. There are different scales of turbulence for the asymmetric nozzles according to (Gutmark *et al.*, 1991). The small-scale structures occur at the nozzle corners and the large-scale structures at the flat sides (Gutmark *et al.*, 1991). It has also been established by Gutmark *et al.* (1991) that the coexistence of large-scale structures at the flat side and small-scale structures at the corners improve combustion as a result of improved mixing. Gutmark *et al.* (1991) also stated that as a result of the high level of turbulence at the corners, combustion reaction starts closer to the nozzle exit when compared to the axisymmetric nozzles with no corners. Consequently, according to (Gutmark *et al.*, 1991; Quinn, 2005) the improved entrainment and spreading of the asymmetric nozzles compared to their axisymmetric counterparts could be due to the influence of the corners which produce strong vortex rings due to high velocity gradients at these locations. Quinn (2005) and Sau (2002, 2004) reported that the counter-rotating vortex pairs have a drastic impact on mixing. It has also been remarked by (Gutmark *et al.*, 1991) that the smaller the corner angle, the higher the level of turbulence and subsequently, the higher the spreading. Consequently, the triangular nozzle with smaller corner angles (i.e. 60 degrees) compared to the rectangular and square nozzle (i.e. 90 degrees) could indicate why entrainment and spreading seems higher for the triangular nozzle as shown above. Furthermore, the thinner shear layers and the flat centers of the asymmetric nozzles compared to their axisymmetric counterparts could indicate why the vorticity may be concentrated at the edges of the jet. The thin shear layer has been known to be responsible for the formation of uniform azimuthal vortex rings in axisymmetric jets and non-uniform azimuthal vortex rings in asymmetric jets (e.g., Mi *et al.*, 2001; Sau, 2002). This vortex dynamics has been shown to be responsible for axis switching in elliptical, rectangular and triangular jets (e.g., Ho and Gutmark, 1987; Zaman, 1996, 1999; Sau, 2002, 2004). However, Xu and Antonia (2005) hypothesized that for a pipe jet, the turbulence is spread over a wide range of wavenumbers, thereby impeding vortex formation and pairing processes needed for mixing. This could also explain why asymmetric nozzles have better entrainment and spreading compared to the pipe jet.

The Reynolds shear stress distribution at the same location (i.e. $x = 2\ mm$) for all the nozzles used in this study is shown in Fig. 4.9.

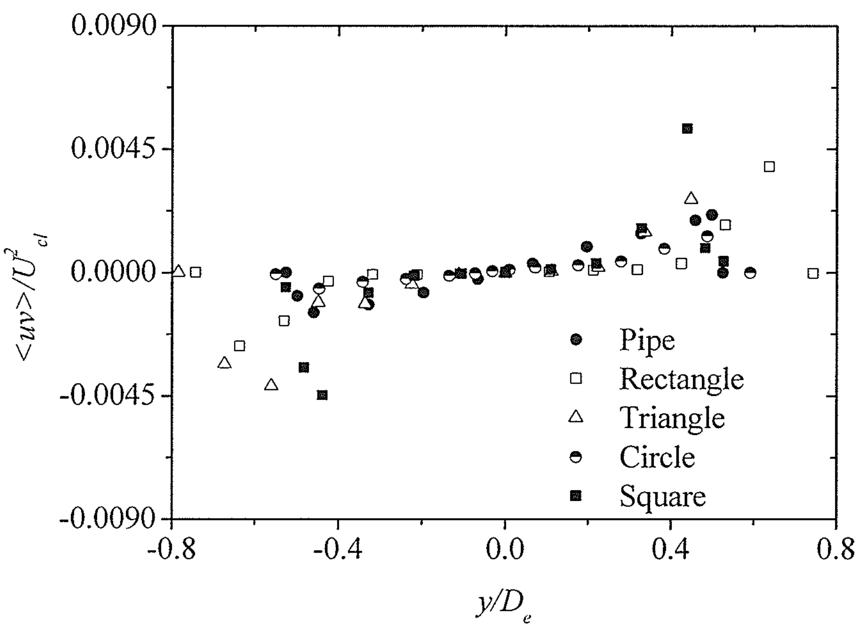

Figure 4.9: Radial profiles of Reynolds shear stresses for various nozzle geometries without quarl at $x = 2\ mm$.

This figure shows clearly that the Reynolds shear stresses are higher at the nozzle edges, which are the regions where high spanwise or radial velocity gradients are predominant. It, therefore, indicates that the Reynolds shear stresses correlate well with the mean spanwise velocity gradients (i.e. $\partial U/\partial y$). Consequently, the Reynolds shear stress is very flat in the center of the jets but increases significantly at the edges, though it is not symmetric as also shown in (e.g., Xu and Antonia, 2002; Quinn, 2005). This Reynolds shear stress flatness scenario is more predominant for the jets characterized by a top-hat velocity profile compared to the pipe with a fully developed turbulent pipe flow.

Figure 4.10 shows the mean velocity profiles at $x/D_e = 3$. This figure clearly shows the departure from the nearly top-hat velocity profile shape that is seen at $x = 2$ *mm*. This is an indication of the entrainment of the ambient fluid that has already taken place up to this flow location. Furthermore, this figure shows that the U/U_{cl} profile for the asymmetric nozzles is wider than that of the axisymmetric counterparts as a result of the higher spreading and entrainment of the asymmetric nozzles.

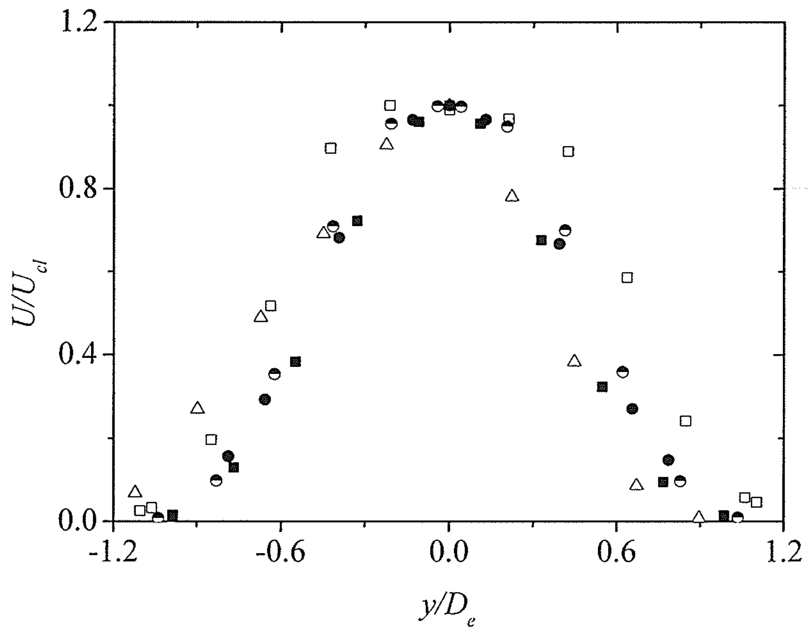

Figure 4.10: Radial profiles of the streamwise mean velocity for various nozzle geometries without quarl at $x/D_e = 3$ (Symbols are as in Figure 4.7).

Figure 4.11 shows the radial distribution of u/U_{cl} and v/U_{cl} for the different nozzles tested here. This figure demonstrates that the asymmetric nozzles have higher turbulence intensities at the nozzle edges compared to their axisymmetric counterparts. However, the rectangular jet seems to have a relatively flatter center compared to all other nozzles which is also a characteristic of the mean streamwise velocity distribution at this location, as shown in Fig. 4.10. This flatness of the turbulence intensity profile in the center of the rectangular jet is an indication that the turbulence intensities are concentrated at the edges of the asymmetric nozzles though not very obvious for the triangular nozzle because of the plane of measurement used and the configuration of the geometry. Consequently, this figure emphasizes again the influence of asymmetric nozzles on the rate of ambient air entrainment since the mean centerline velocity decay correlates well with the radial distributions of u/U_{cl} and v/U_{cl} at the nozzle edges.

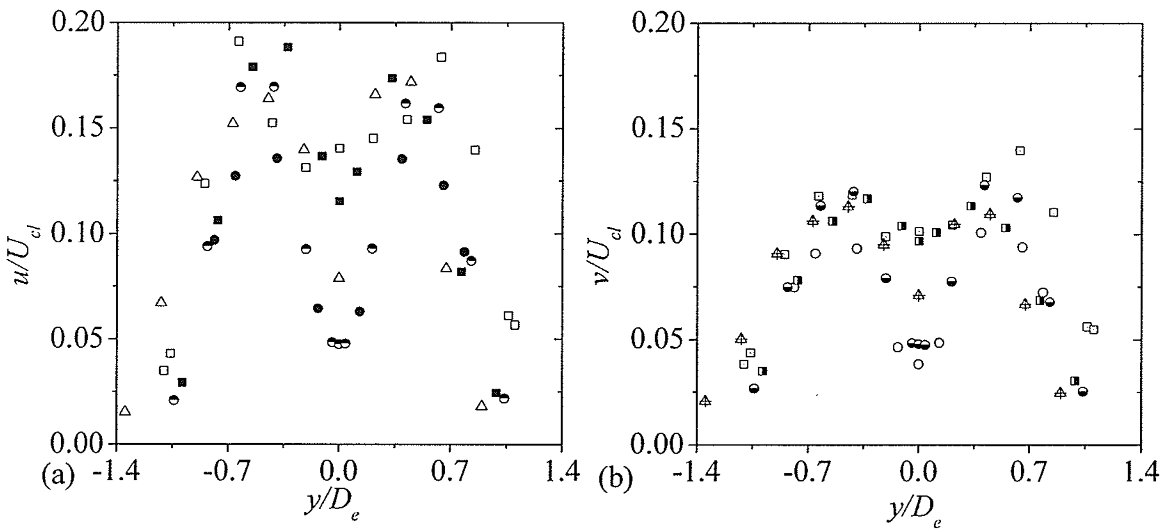

Figure 4.11: Radial profiles of the fluctuating velocity components for various nozzle geometries without quarl at $x/D_e = 3$ (Symbols are as in Figure 4.8).

Figure 4.12 shows the radial profiles of the Reynolds shear stress at $x/D_e = 3$. This figure shows very similar profiles to those measured at $x = 2$ *mm,* except that there is a reduction in the flatness at the center of the asymmetric nozzles as a result of entrainment. This reduction is due to a change in the velocity gradient as a result of the entrainment of more ambient fluid by the jet flow (i.e. $\partial U/\partial y$ changes). However, the asymmetric nozzles still have the highest Reynolds shear stresses at the edges compared to their axisymmetric counterparts. The higher Reynolds shear stresses of the asymmetric nozzles in the mixing layer indicates higher entrainment and spreading of the asymmetric nozzles compared to their axisymmetric counterparts.

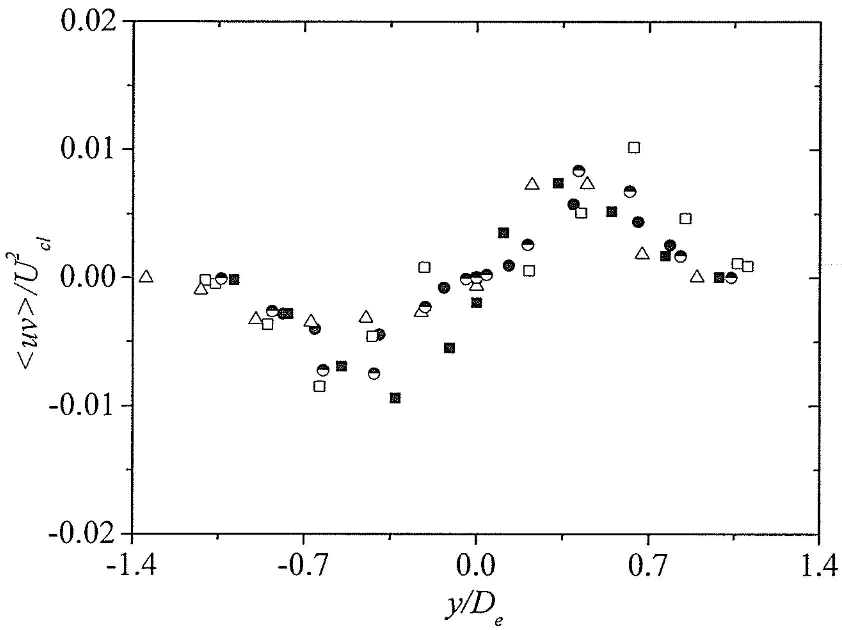

Figure 4.12: Radial profiles of Reynolds shear stress for various nozzle geometries without quarl at $x/D_e = 3$ (Symbols are as in Figure 4.9).

Figures 4.13 and 4.14 show the radial distribution of the normalized mean velocity profiles at $x/D_e = 5$ and 20, respectively, for both the quarl and no-quarl nozzles' configurations.

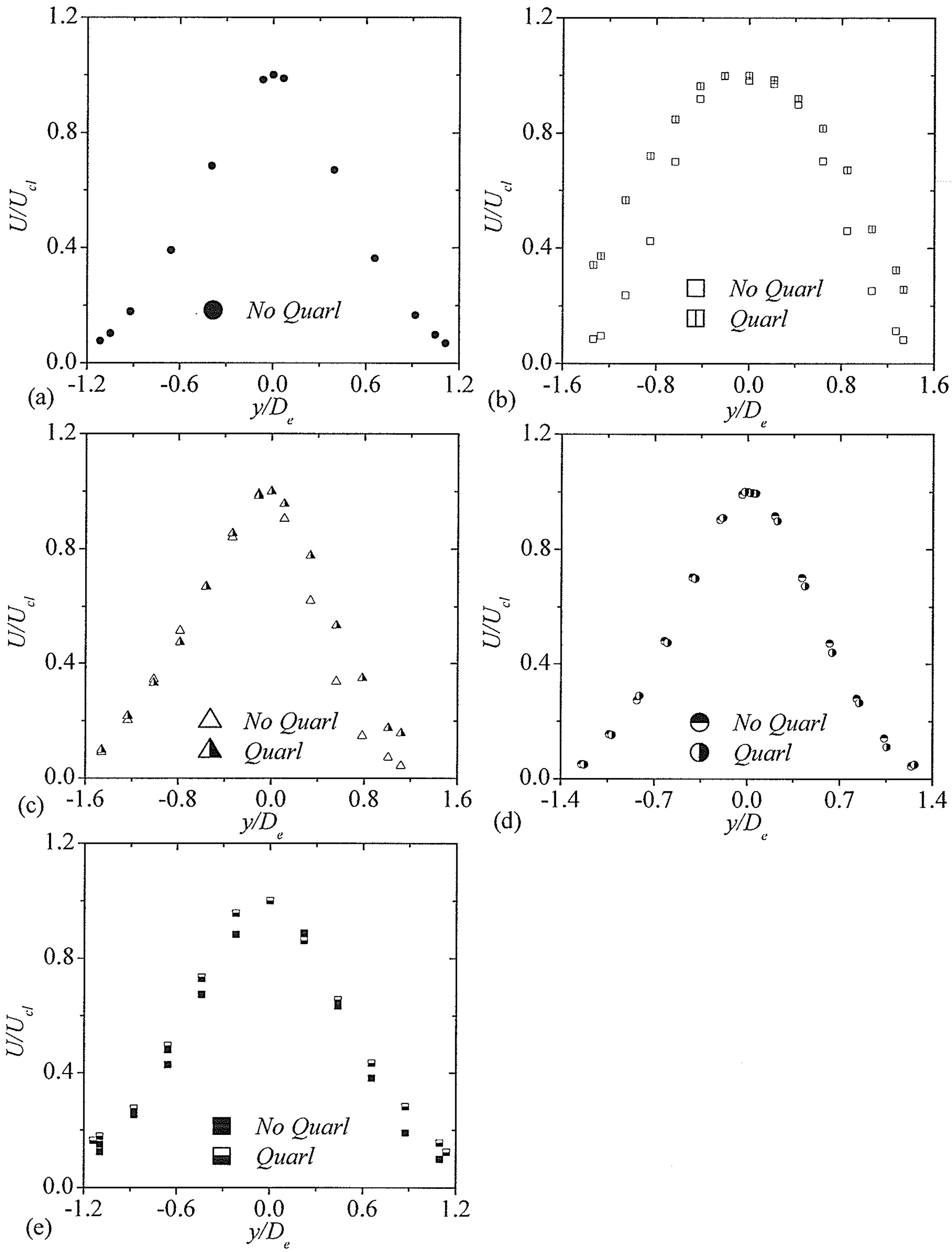

Figure 4.13: Radial profiles of the streamwise mean velocity for various nozzle geometries with and without quarl at $x / D_e = 5$- (a) Pipe, (b) Rectangle, (c) Triangle, (d) Circle, and (e) Square.

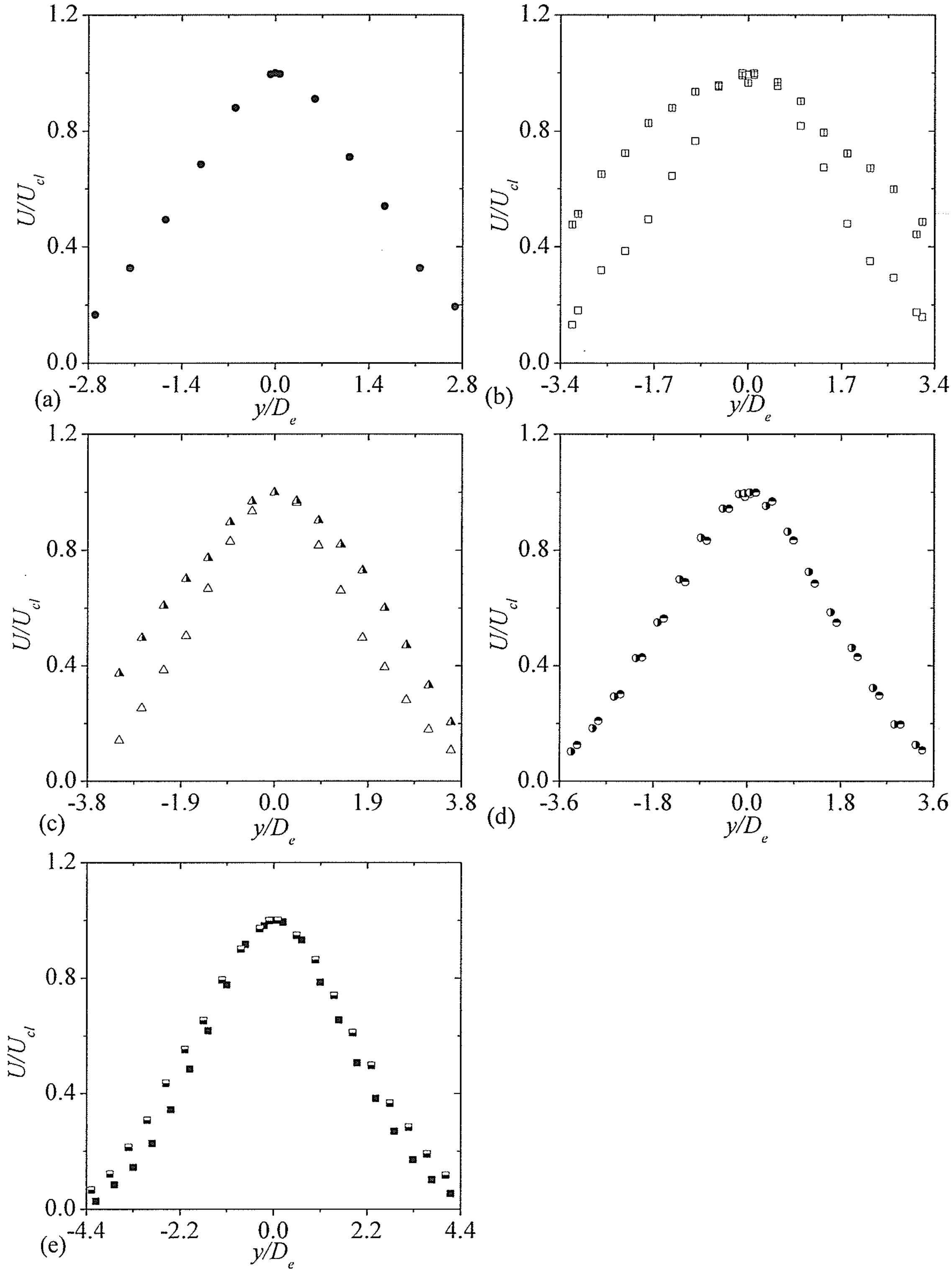

Figure 4.14: Radial profiles of the streamwise mean velocity for various nozzle geometries with and without quarl at $x/D_e = 20$ (Symbols are as in Figure 4.13).

The location x/D_e = 20 is chosen because it is assumed that downstream of this normalized streamwise location, the mean velocity profiles of an axisymmetric jet becomes self-similar. Furthermore, the effect of quarl is clearly evident from these figures. The profile of the quarl configuration is seen to be wider than the no-quarl configuration indicating a greater jet's spreading rate of the quarl configuration compared to the no-quarl configuration. However, while the quarl configurations of the asymmetric nozzles are seen to have much wider profiles compared to their no-quarl counterpart, only little change is observed for the quarl and no-quarl of the contracted circular nozzle.

Figures 4.15 and 4.16 show the radial distribution of u/U_{cl} and v/U_{cl} at x/D_e = 5 and 20, respectively, for the quarl and no-quarl configurations of the different nozzles tested here. Again, it is clearly shown in these figures that the turbulence intensity profiles of the quarl configurations are wider and much larger than the no-quarl configurations. This also confirms the initial stipulation that the rate of entrainment and spreading correlates well with the increase in turbulence intensities at the edges. Mixing is initiated at the edges or corners and the higher the turbulence at these edges and corners, the higher the entrainment and spreading rates. Consequently, the asymmetric nozzles with quarl, which have the highest turbulence intensities at the edges, have also higher jet entrainment and spreading compared to their no-quarl counterparts. In addition, Figure 4.16 which shows the profile of u/U_{cl} and v/U_{cl} at x/D_e = 20 gives the impression that the profiles of the mean fluctuating components have not reached self-similarity at this location. This is in accordance with the proposition by Boersma *et al.* (1998) that self-similarity for the velocity fluctuations can only occur at x/D_e > 35 for axisymmetric nozzles.

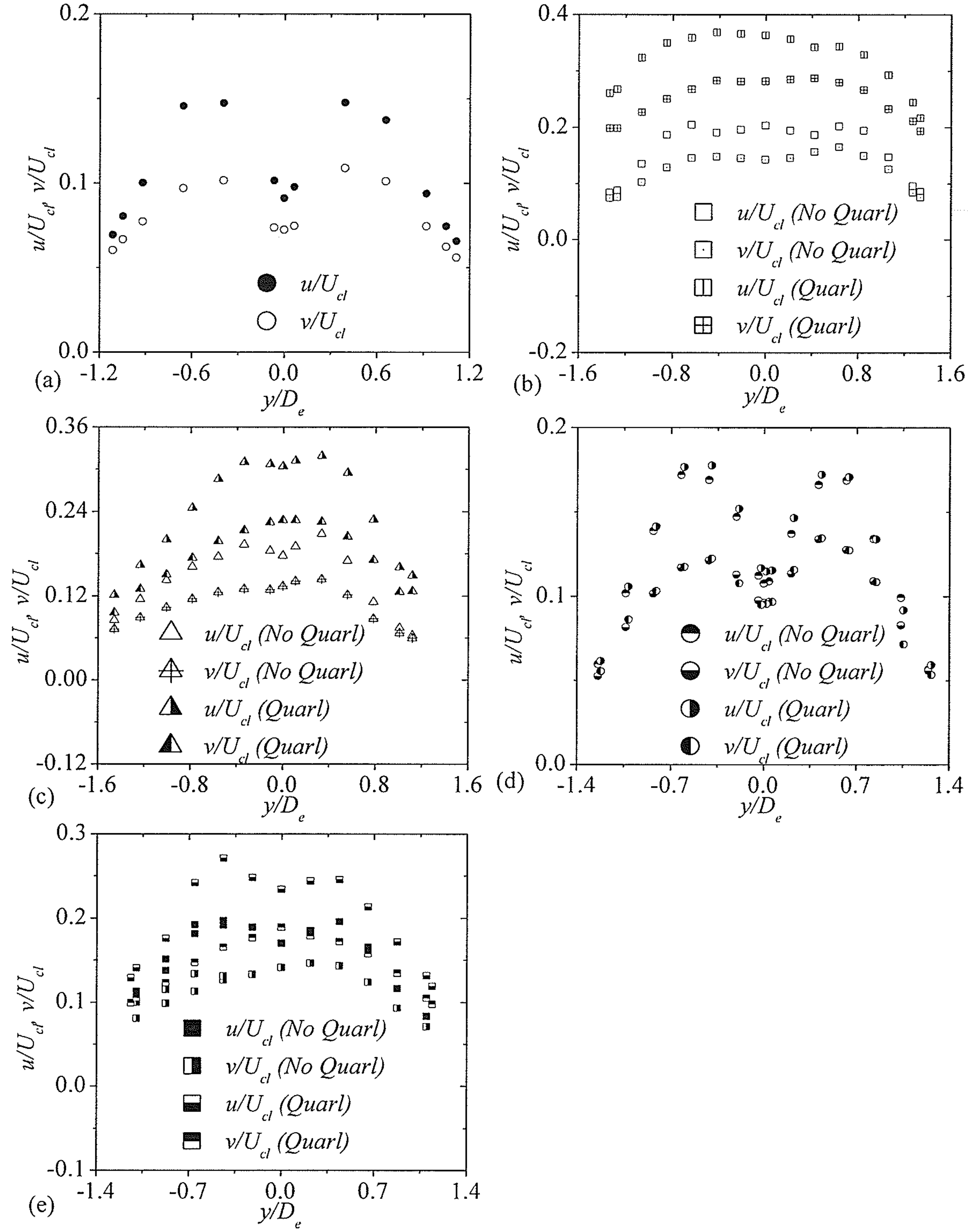

Figure 4.15: Radial profiles of the fluctuating velocity components for various nozzle geometries with and without quarl at $x/D_e = 5$- (a) Pipe, (b) Rectangle, (c) Triangle, (d) Circle, and (e) Square

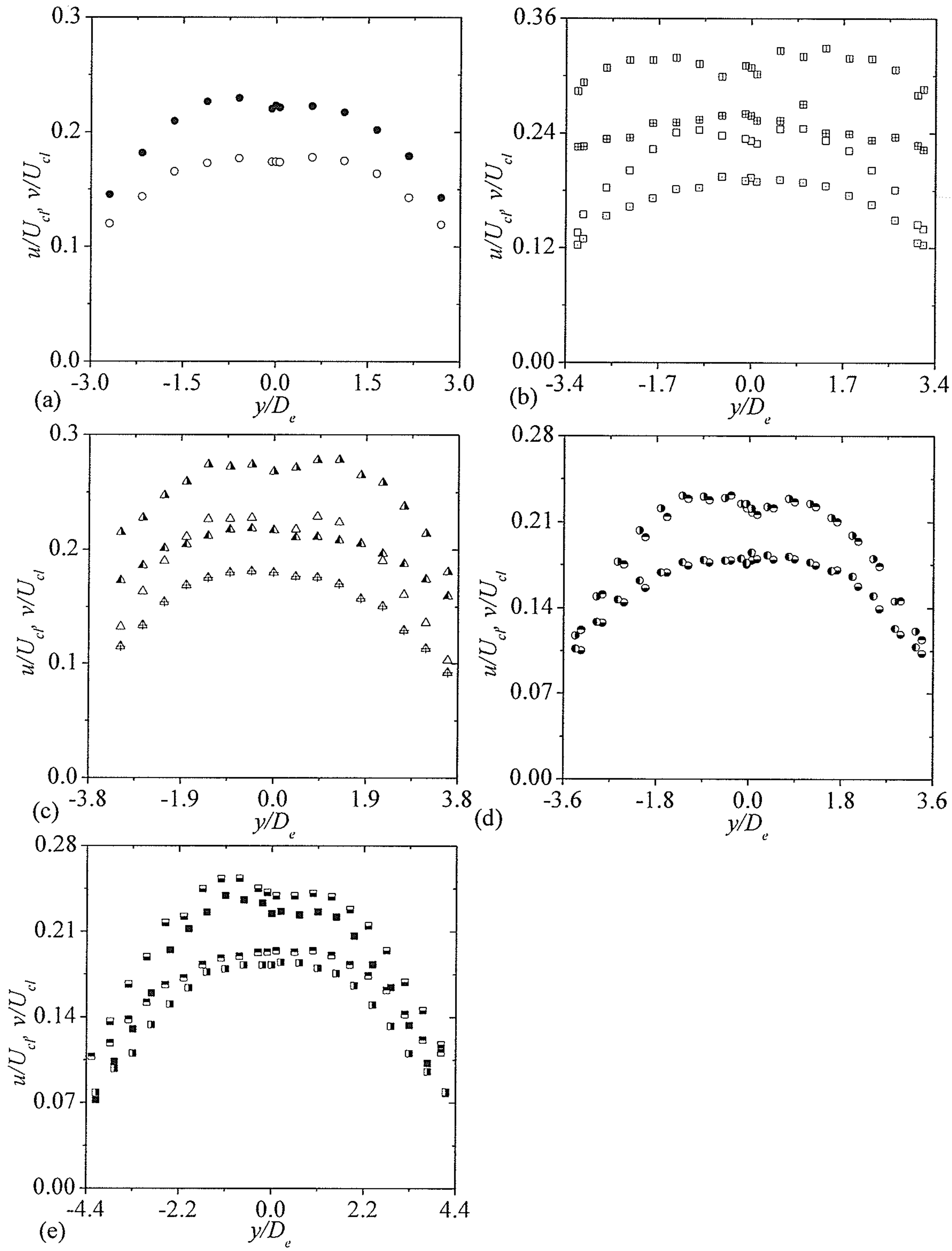

Figure 4.16: Radial profiles of the mean fluctuating velocity components for various nozzle geometries with and without quarl at $x/D_e = 20$ (Symbols are as in Figure 4.15).

Figures 4.17 and 4.18 show the Reynolds shear stresses of the different nozzle geometries with and without quarl at $x/D_e = 5$ and 20, respectively. These figures clearly reveal that the Reynolds shear stress distribution is higher for the quarl configuration compared to the no-quarl counterparts. This implies that the radial velocity gradient ($\partial U/\partial y$) is higher for the quarl configuration compared to the no-quarl configuration. Consequently, as a result of increased Reynolds shear stress for the quarl configuration over the no-quarl counterpart, jet's spreading and entrainment are improved.

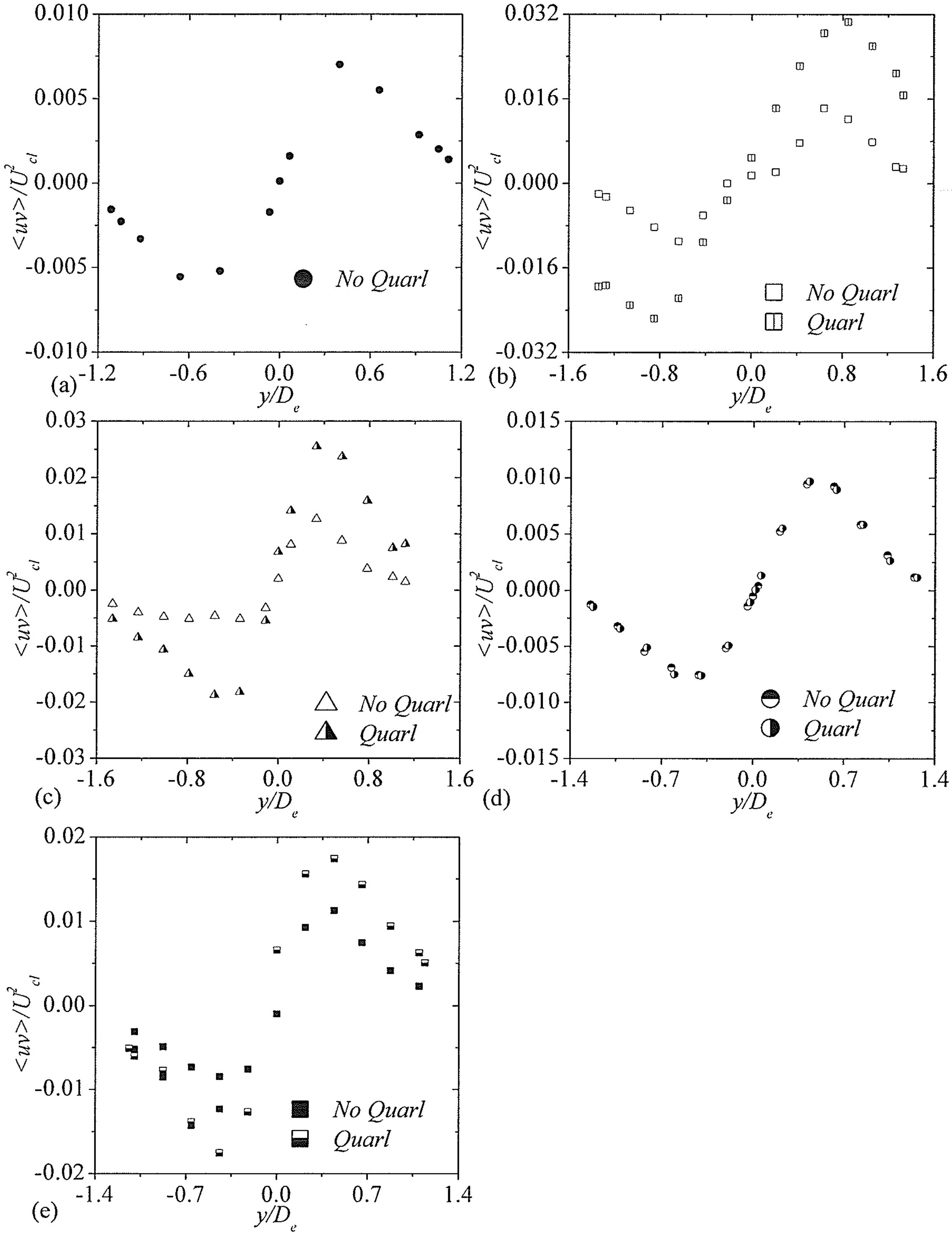

Figure 4.17: Radial profiles of Reynolds shear stress for various nozzle geometries with and without quarl at $x/D_e = 5$- (a) Pipe, (b) Rectangle, (c) Triangle, (d) Circle, and (e) Square.

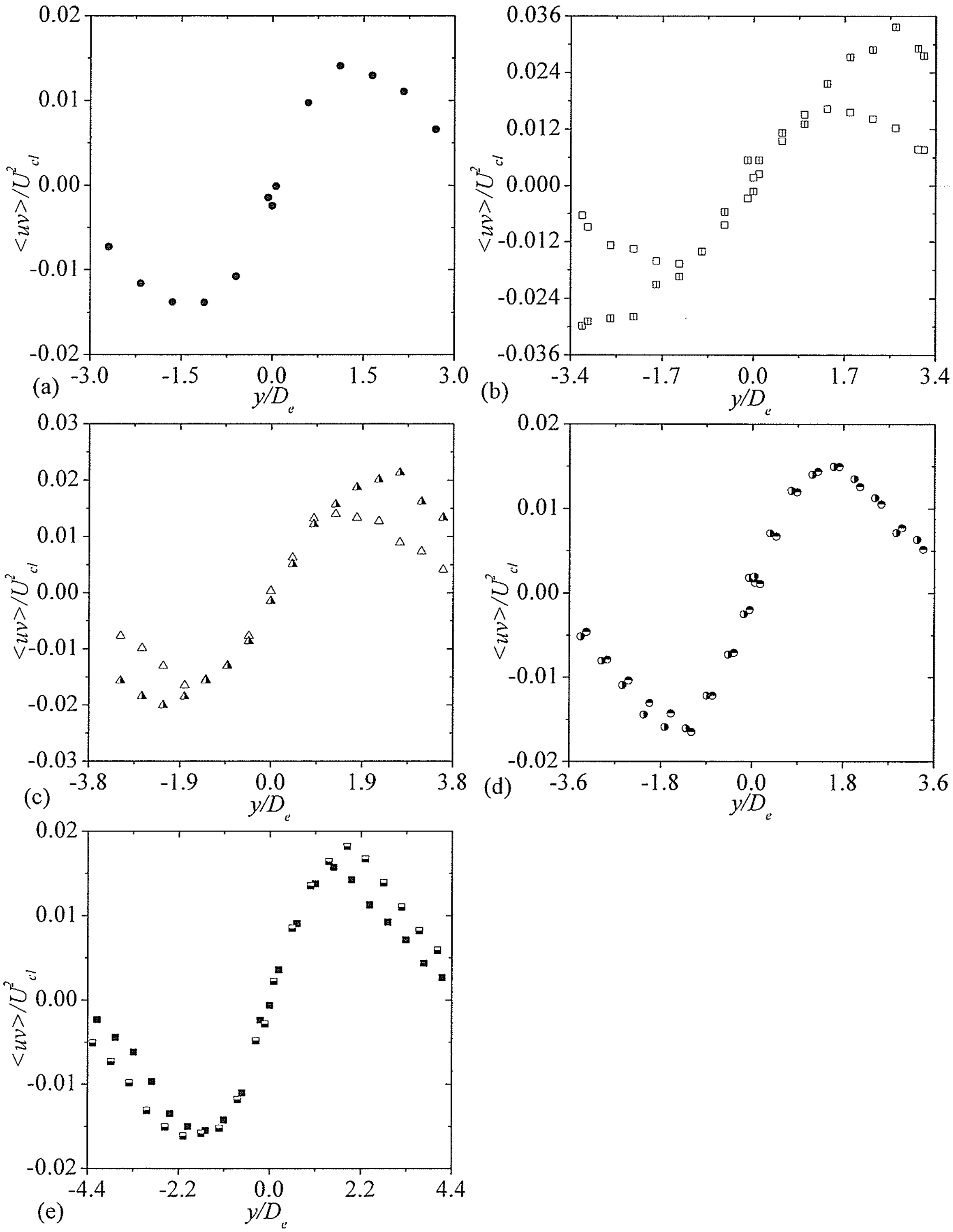

Figure 4.18: Radial profiles of Reynolds shear stress for various nozzle geometries with and without quarl at $x/D_e = 20$ (Symbols are as in Figure 4.17).

The normalized centerline mean fluctuating velocity profiles (i.e. u/U_{cl} and v/U_{cl}) are shown in Figure 4.19 for different nozzle geometries without quarl.

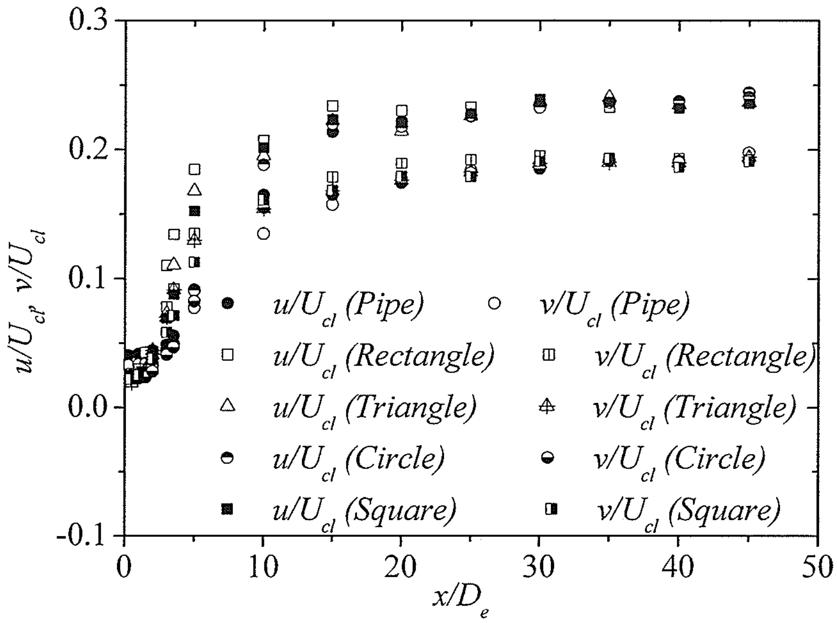

Figure 4.19: Axial profile of the normalized mean fluctuating velocity components for various nozzle geometries without quarl.

This figure shows that in the near-field, the values of u/U_{cl} and v/U_{cl} are higher for the asymmetric nozzles compared to their circular counterparts. Consequently, this increase in turbulence intensities could be responsible for the better entrainment and spreading of the asymmetric nozzles. The same figure shows also that the normalized mean fluctuating velocity (i.e. u/U_{cl}) for the pipe jet increases until it reaches a value of $u/U_{cl} \approx 0.24$ at $x/D_e \approx 30$. This is in fair agreement with the findings of Xu and Antonia (2002) who measured a maximum value of $u/U_{cl} = 0.25$ at $x/D_e \geq 40$. The corresponding maximum values for other nozzle jets is identical to that of the pipe; that is $u/U_{cl} \cong 0.24$. However, these maximum values occur at different x/D_e locations compared to the pipe's maximum u/U_{cl} location. This figure shows clearly that the asymmetric nozzles have much higher u/U_{cl} at the initial stage (i.e. near-field) of the jet development compared to their axisymmetric counterparts. Consequently, the higher turbulence in the near-field of the asymmetric nozzles enhances the jet's entrainment. This observation that asymmetric nozzles have higher fluctuating components compared to their axisymmetric counterpart confirms the findings of Mi *et al.* (2000). Overall, these observations strengthen the role of turbulence in jet entrainment and spreading.

Figure 4.20 underscores the influence of quarl on u/U_{cl} and v/U_{cl}; as it shows that, at any given streamwise flow location, u/U_{cl} and v/U_{cl} increases significantly for the quarl configurations of the asymmetric nozzles compared to their no-quarl configurations. However, the increase in the axisymmetric nozzles (i.e. contracted circular nozzle) is not as significant as that of the asymmetric nozzles. This increased turbulence which is more pronounced for the asymmetric nozzles with quarl over the axisymmetric nozzles with quarl partly explains why the asymmetric nozzles have higher rates of ambient fluid entrainment and jet spreading. Figure 4.19 shows that the hump observed by Mi *et al.* (2000) is not easily discernible in the present experiment for the triangular and rectangular jets. This could be due to the fact that no measurements were made in the region $5 < x/D_e < 10$, where Mi *et al.* (2000) observed the hump. However, this hump is easily discernible for both the triangular and rectangular jets with quarl at $x/D_e = 5$.

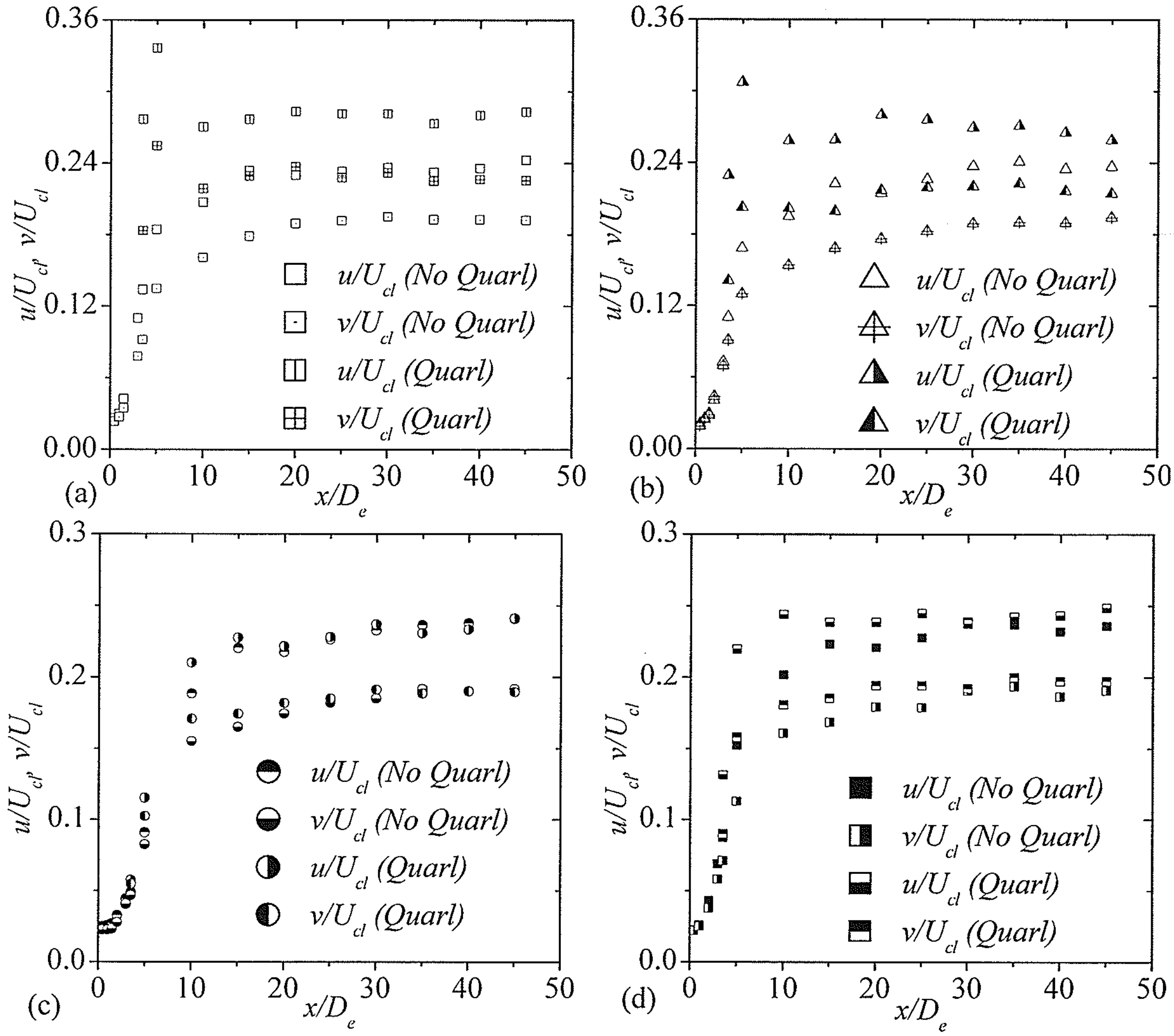

Figure 4.20: Axial profiles of the normalized mean fluctuating velocity components for various nozzle geometries with and without quarl-(a) Rectangle, (b) Triangle, (c) Circle, and (d) Square.

The foregoing shows, for instance, that just as the tabs in the rectangular nozzle of Zaman (1996, 1999) are found capable of increasing jet spreading and entrainment, the use of quarl, which is a cylindrical sudden expansion, is also found to promote higher rates of entrainment and spreading than without quarl. Furthermore, the effect of quarl is seen to be more predominant for the triangular jet and least for the contracted circular jet. It is shown that this phenomenon could be the result of increased vortical dynamics and increased turbulence intensity of the asymmetric nozzles with quarl compared to the axisymmetric nozzle (i.e. contracted circular nozzle) with quarl.

4.1.2 Effect of Exit Velocity on Entrainment and Spreading of a Turbulent Free Jet

The results presented below are an attempt to investigate the effect of exit velocity on the entrainment and spreading of a turbulent free jet. To accomplish this objective, 30 m/s (already reported above) and 65 m/s profiles of the mean-velocity decay and half-velocity width, as well as the radial and axial profiles of the mean-velocity, turbulence intensity and Reynolds shear stresses along the jet centreline plane are compared. These data are reported for each nozzle configuration with and without sudden expansion for two different jet exit velocities. The two-dimensional results presented here are deemed sufficient because the main focus of the present work is on studying the effect of initial flow conditions (e.g. jet exit velocity) on jet's entrainment and spreading, as these characteristics of a jet can be determined via two-dimensional measurements. However, for a better understanding of the effect of the asymmetry of a nozzle on the spreading of the rectangular jet, the minor plane (*x-z*) of the rectangular nozzle was also explored to assess the development of the half- velocity width along this plane. Note that, the present investigation employed all nozzles except the pipe jet. The nozzle planes measured with the LDV is as represented in Fig. 4.1.

4.1.2.1 Jet Streamwise Centerline Mean-Velocity Decay and Half-Velocity Width for Nozzles without Sudden Expansion

It should be noted that the nearest LDV measurement flow station was at $x = 2$ *mm* for the nozzle configurations without sudden expansion. Fig. 4.21 presents the effect of exit velocity on the streamwise centerline mean-velocity decay for the different nozzle's geometries without the presence of sudden expansion.

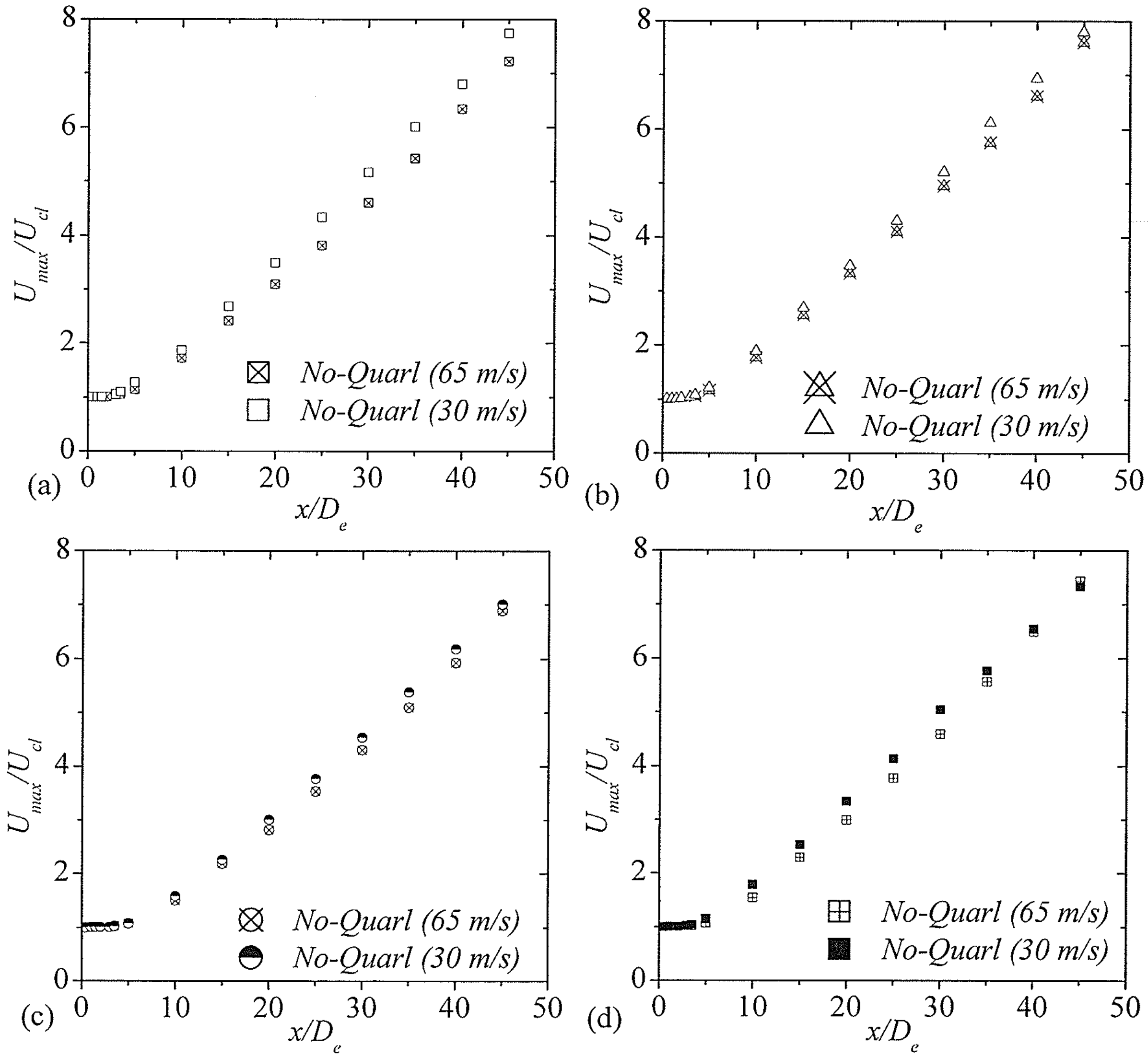

Figure 4.21: Streamwise centerline mean velocity decay of various nozzle geometries without quarl: (a) Rectangle, (b) Triangle, (c) Contracted circular, and (d) Square.

This figure shows that the exit velocity appears to affect similarly the streamwise centreline mean velocity decay of all the jets. That is, for these nozzles, the jet streamwise centerline mean velocity decay tends generally to decrease as the exit velocity increases. The near-field streamwise centerline mean velocity decay of the nozzles (i.e. the triangular and rectangular) with the highest rate of entrainment in the near-field shown in Fig. 4.22 emphasizes the effect of the exit velocity described above. That is, at the lower exit velocity of 30 m/s, the triangular nozzle has the highest decay rate followed by the rectangular nozzle. However, at the exit velocity of 65 m/s, the centerline mean velocity decay reduces but the triangular nozzle is still slightly higher than that of the rectangular nozzle. These trends confirm the findings reported in the literature (Mi *et al.*, 2000; Quinn, 2005, amongst others).

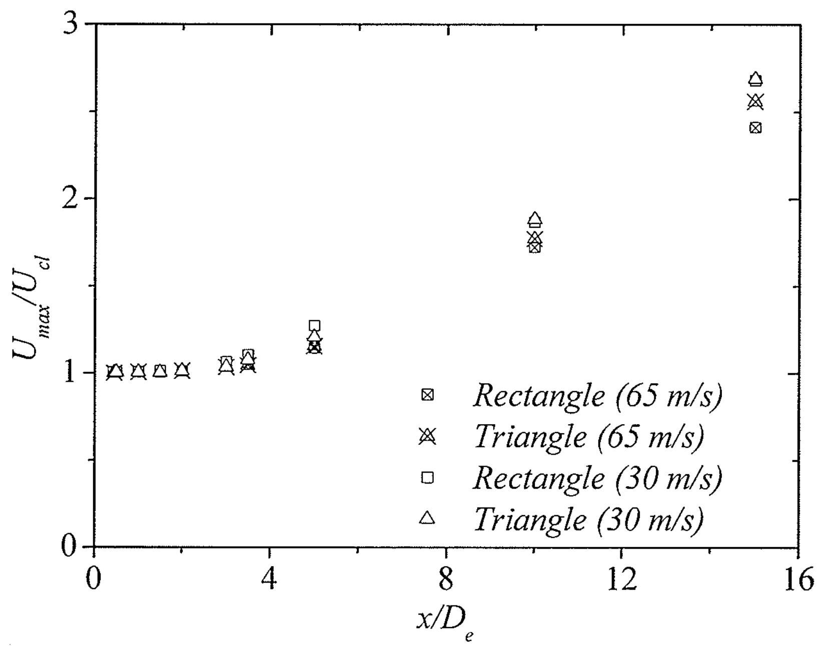

Figure 4.22: Streamwise near-field centerline mean velocity decay for rectangular and triangular nozzles without quarl at exit velocity of 30 m/s and 65 m/s.

However, the jet half-velocity width, shown in Fig. 4.23, which is also re-emphasized in the near-field for the triangular and rectangular nozzles in Fig. 4.24 have a slightly different trend compared to the streamwise centerline mean velocity decay. The contracted circular and square jets, however, still indicate that an increase in the jet exit velocity leads to a lesser jet spreading rates. As for the rectangular and triangular nozzles, the effect of exit velocity is not well noticeable especially in the mid-field. This scenario suggests that exit velocity affects the jet spreading rate of these two nozzles differently in the different planes of measurements as a result of their asymmetry.

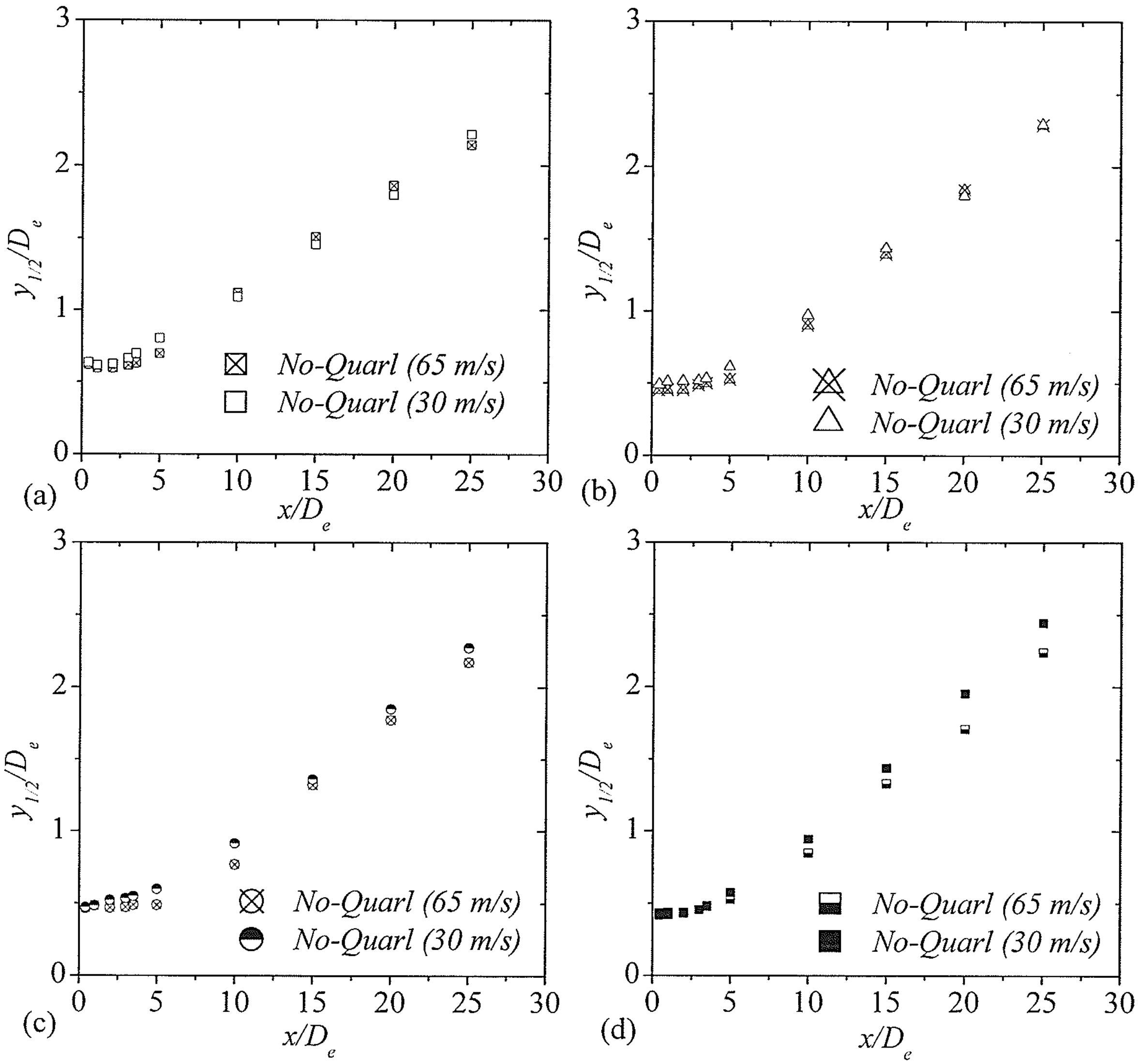

Figure 4.23: Jet half-velocity width for various nozzle geometries without quarl: (a) Rectangle, (b) Triangle, (c) Contracted circular, and (d) Square.

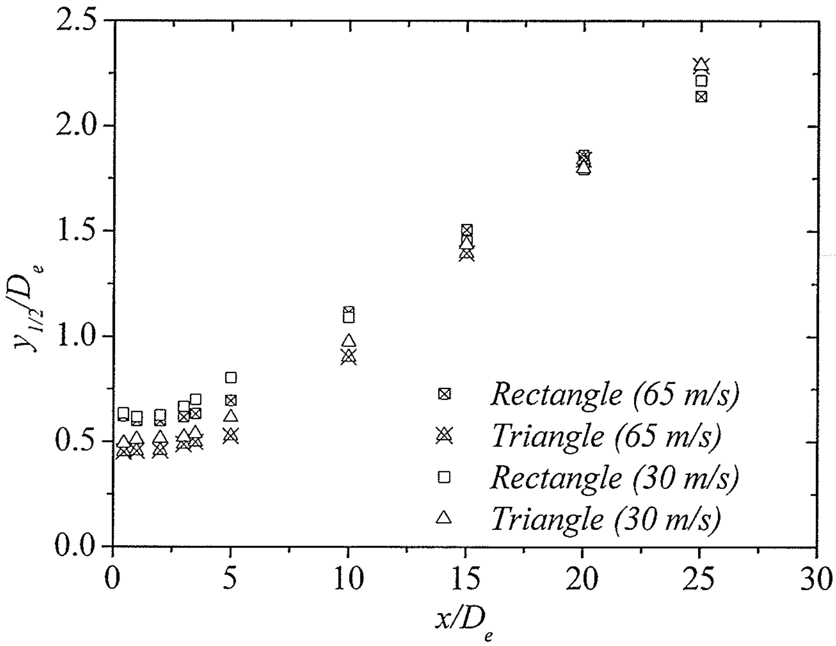

Figure 4.24: Jet half-velocity width for rectangular and triangular nozzles without quarl.

Consequently, Fig. 4.25 represents the streamwise development of the *x-y* and *x-z* jet half-velocity width of the rectangular nozzle for both exit velocities. What is clearly evident from this figure is that, at both exit velocities, the streamwise development of the jet half-velocity width in the major axis plane (*x-y*) is higher than that of the minor axis plane (*x-z*) in the near-field (say for $x/D_e < 10$), but it changes as the jet evolves progressively farther downstream. At the exit velocity of 30 m/s, the jet half-velocity width along the minor axis plane catches up with that of the major axis plane at about $x/D_e = 10$ and subsequently becomes higher. However, at the exit velocity of 65 m/s, the minor axis plane jet half-velocity width catches up with that of the major axis at around $x/D_e \sim 15$ and then becomes higher further downstream. This phenomenon is referred to as 'axis switching' which has been observed and described in the literature (Quinn, 1995, 2005; Zaman, 1996). Quinn (2005) stated that axis switching significantly increases entrainment, and the frequencies of the occurrence of 'axis switching' enhance further jet entrainment and spreading rate. For example, it was observed by Quinn (2005) that axis switching occurs multiple times for the equilateral triangular jet, which may explain why it has higher entrainment and jet spreading compared to other nozzle's geometries presented here. One pertinent point to emphasize from Fig. 4.25 is that the location where axis switching occurs is affected by the exit velocity. At lower exit velocity, axis switching occurs earlier, whereas it takes slightly longer for axis switching to develop at the higher exit velocity of 65 m/s. It has to be acknowledged that increasing the near-field entrainment could potentially increase molecular mixing. This may partly explain why the 30 m/s jet has a higher entrainment and jet spreading compared to the 65 m/s jet for both the triangular and rectangular jets.

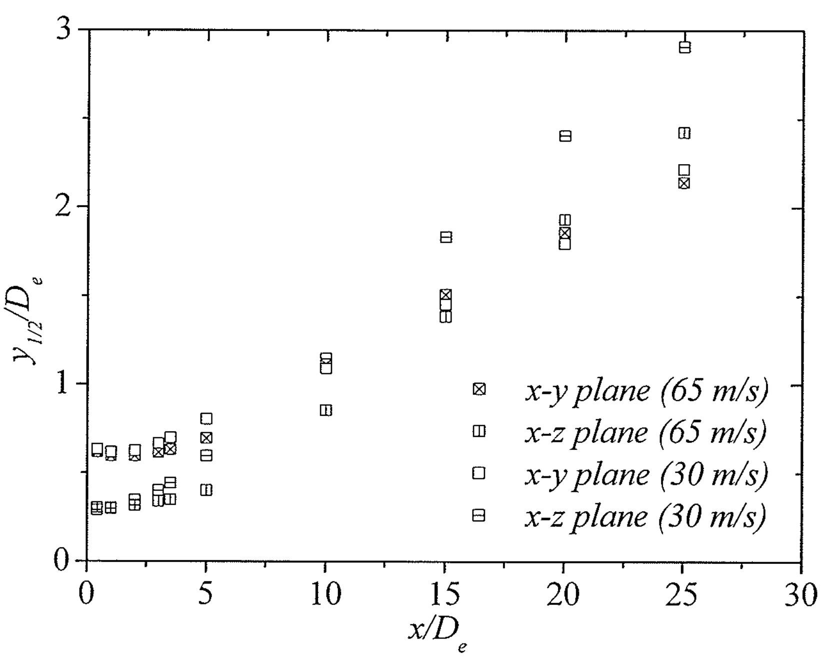

Figure 4.25: Comparison of the major (*x-y*) and minor (*x-z*) planes jet half-velocity width for the rectangular nozzle without quarl.

Eq. (4.1) is used to fit the measured data presented in Figure 4.21 in the range between $x/D_e = 20 - 45$. The decay constant, C_1, is found to be approximately 6.23 and 6.21, and the virtual origin, x_0, is equal to $1.45D_e$ and $3.10D_e$ for the contracted circular jet at the exit velocities of 30 m/s and 65 m/s, respectively. The present measured values of C_1 at both exit velocities for the contracted circular jet are not in good agreement with most published data, as shown in Table 4.7, though they are close to the value of 6.06 obtained by Panchapakesan and Lumley (1993).

Table 4.7: Comparison of the streamwise centerline mean velocity decay of the contracted circular jet without quarl with published results

Ref.	U *(m/s)*	**Measurement type**	D_e *(mm)*	**Re × 10^{-3}**	C_1	x_o
Present Work	30,65	LDV	4.82	9.4, 20	6.23, 6.21	$1.45D_e$, $3.10D_e$
Xu and Antonia (2002)	23.3	Hot-wires	55	86	5.6	$3.7D_e$
Boersma *et al.* (1998)	N/A	DNS	N/A	2.4	5.9	N/A
Capp *et al.* (1990)	N/A	LDV	N/A	N/A	5.8	N/A
Capp *et al.* (1990)	N/A	Hot-wires	N/A	N/A	5.9	N/A
Rodi (1975)	101	Hot-wire	12	87	5.9	N/A
Panchapakesan and Lumley (1993)	27	Hot-wire	6.1	11	6.06	$-2.5D_e$

The differences in C_1 may be primarily due to the dissimilarity in the profile of the nozzle's orifice contraction, and could also be slightly caused in part by the low-momentum co-flow employed in the present study. In fact, the nozzle's orifice contraction ratio of the present contracted circular nozzle is quite low (i.e. 2.5:1) which may be the reason why the velocity profile shape is not perfectly top-hat at the exit of the nozzle. However, one pertinent observation is that C_1 does not vary significantly with exit velocity which is attributed to the fact that the far-field differences in the streamwise centerline mean velocity decay between the two exit velocities remains almost the same at each streamwise location. That is, at higher exit velocity (i.e. 65 m/s), the decrease in the far-field streamwise centerline mean velocity decay is consistent from one streamwise location to another. This may explain why most studies seem to have very good agreement in the decay constant. However, the difference in exit velocities could be responsible for the disparity in published values of x_0. In addition, Fig.4.21 shows that though C_1 does not vary much as the exit velocity increases from 30 m/s to 65 m/s, the streamwise mean velocity decay of the contracted circular nozzle decreases which implies a reduction in entrainment and a change in x_0. This reduction as a result of increased exit velocity could be one reason why different investigators using different Reynolds numbers have dissimilar results. This is consistent with the findings of Warda *et al.* (1999) who noticed an increase in the length of the potential core as exit velocity is increased and, Malmstrom *et al.* (1997) who observed a decrease in the centerline mean velocity decay of an axisymmetric jet.

Using Eq. (4.1) and the same x/D_e range reported above for the contracted circular jet, the corresponding values of C_1 and x_0 for the rectangular, triangular, and square jets are reported in Table 4.8 for exit velocities of 30 m/s and 65 m/s, respectively. Comparison of C_1 and x_0 for the triangular, rectangular, and square nozzles tested here with published results will only be limited to that of the triangular nozzle because published data for the remainder of nozzle's geometries are currently unavailable. The values of C_1 and x_0 for the triangular jet at both exit velocities are not in perfect agreement with those of Quinn (2005) who reported, respectively, 5.10 and $0.389D_e$, at a Reynolds number of 184000. These differences could result from the Reynolds number, which is significantly different between both studies or from the differences in the nozzles' contractions. It has to be acknowledged that the nozzle employed by Quinn (2005) has very sharp-edges with a slightly different contraction.

Table 4.8: Streamwise mean velocity decay for various nozzle geometries with and without quarl

	(U_{max} taken at $x/D_e = 2$)							
	With Quarl				**No Quarl**			
	30 m/s		**65 m/s**		**30 m/s**		**65 m/s**	
Geometry	C_1	x_o	C_1	x_o	C_1	x_o	C_1	x_o
Rectangle	3.99	$-1.40D_e$	4.07	$-0.04D_e$	5.93	$-0.65D_e$	6.06	$1.90D_e$
Triangle	4.35	$-2.74D_e$	4.03	$1.44D_e$	5.74	$0.11D_e$	5.88	$0.86D_e$
Circle	5.90	$0.63D_e$	6.02	$2.52D_e$	6.23	$1.45D_e$	6.21	$3.10D_e$
Square	5.19	$-0.52D_e$	5.29	$1.77D_e$	6.26	$-1.01D_e$	5.59	$3.83D_e$

For the jet half-velocity width, the maximum streamwise location where the jet spread is measured for each nozzle is at $x/D_e = 25$ and therefore only two locations (i.e. $x/D_e = 20$ and 25) are used here to compute C_2 and x_{02}. Eq. (4.2) is used to fit the experimental data presented in Fig.4.23 for each nozzle's geometry without sudden expansion at exit velocities of 30 m/s and 65 m/s for x/D_e in the range from 20 to 25. The value of C_2 for the contracted circular jet is found to be 0.085 and 0.079 at 30 m/s and 65 m/s, respectively (also shown in Table 4.9). Though the values of C_2 are not very different at both exit velocities, they are mostly not in perfect agreement with published results (Iyogun and Birouk, 2009a). These dissimilarities could be caused by the same reasons mentioned above for the differences in C_1 obtained here compared to other studies. The values of x_{02} for the contracted circular jet in the present study are found to be $-1.78D_e$ and $2.27D_e$ for the 30 m/s and 65 m/s exit velocity, respectively. The differences in x_{02} also give a good indication of the effect of exit velocity. The corresponding values of C_2 and x_{02} at exit velocities of 30 m/s and 65 m/s for the rectangular, triangular, and square jets are shown in Table 4.9. Each geometry shows a unique value of C_2 and x_{02} which also reflects exit velocity effect.

Table 4.9: Jet half-velocity width for various nozzle geometries with and without quarl

	With Quarl				**No Quarl**			
	30 m/s		**65 m/s**		**30 m/s**		**65 m/s**	
Geometry	C_2	x_{02}	C_2	x_{02}	C_2	x_{02}	C_2	x_{02}
Rectangle	0.056	$-34.63D_e$	0.090	$-4.83D_e$	0.084	$-1.28D_e$	0.056	$-13.18D_e$
Triangle	0.091	$-9.06D_e$	0.120	$0.708D_e$	0.098	$1.72D_e$	0.089	$-0.69D_e$
Circle	0.073	$-6.80D_e$	0.077	$-3.18D_e$	0.085	$-1.78D_e$	0.079	$2.27D_e$
Square	0.080	$-8.92D_e$	0.115	$2.90D_e$	0.097	$-0.11D_e$	0.105	$3.89D_e$

4.1.2.2 Jet Streamwise Centerline Mean Velocity Decay and Half-Velocity Width for Nozzles with Sudden Expansion

The streamwise centerline mean velocity decay at 30 m/s and 65 m/s is shown in Fig.4.26 for the rectangular, triangular, square and the contracted circular nozzles with sudden expansion. Note that the nearest LDA measurement flow station for the sudden expansion configurations is x/D_e =

3.5. However, the U_{max} for the sudden expansion configuration is taken as the U_{max} of the corresponding configuration without sudden expansion (often taken at x = 2 *mm* or slightly downstream depending on the nozzle geometry). This practice is necessary in order to account for the effect of sudden expansion and exit velocity on the streamwise centerline mean velocity decay. Figure 4.26 shows that the effect of exit velocity on the trend of the streamwise centerline mean velocity decay of the nozzles is similar whether these nozzles have a sudden expansion or not as shown in Fig. 4.21. This is also confirmed by the jet half-velocity width shown in Fig. 4.27 which illustrates the same scenario. That is, an increase in exit velocity leads to a reduction in the jet decay and spreading.

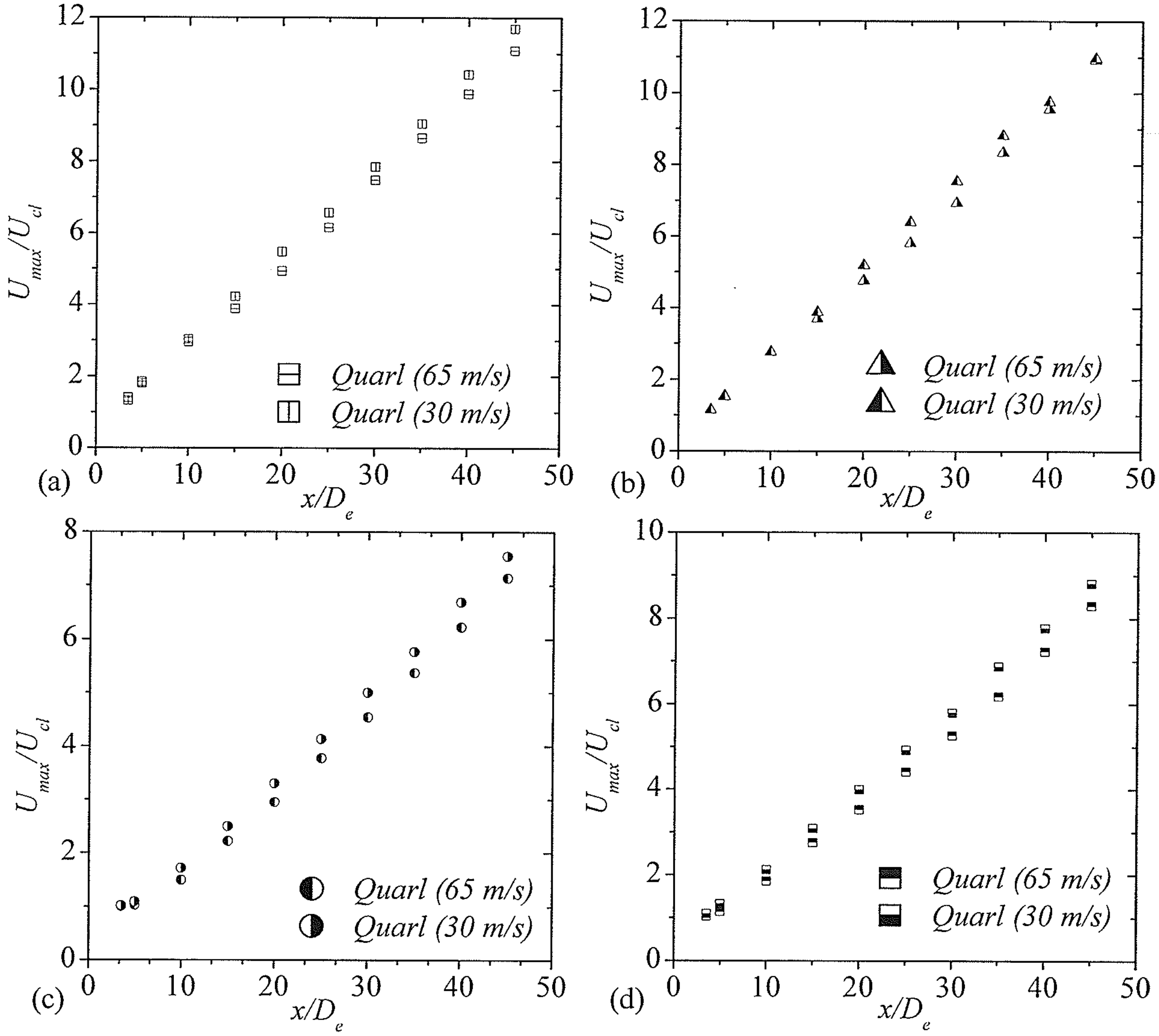

Figure 4.26: Streamwise centerline mean velocity decay for various nozzle geometries with quarl: (a) Rectangle, (b) Triangle, (c) Contracted circular, and (d) Square.

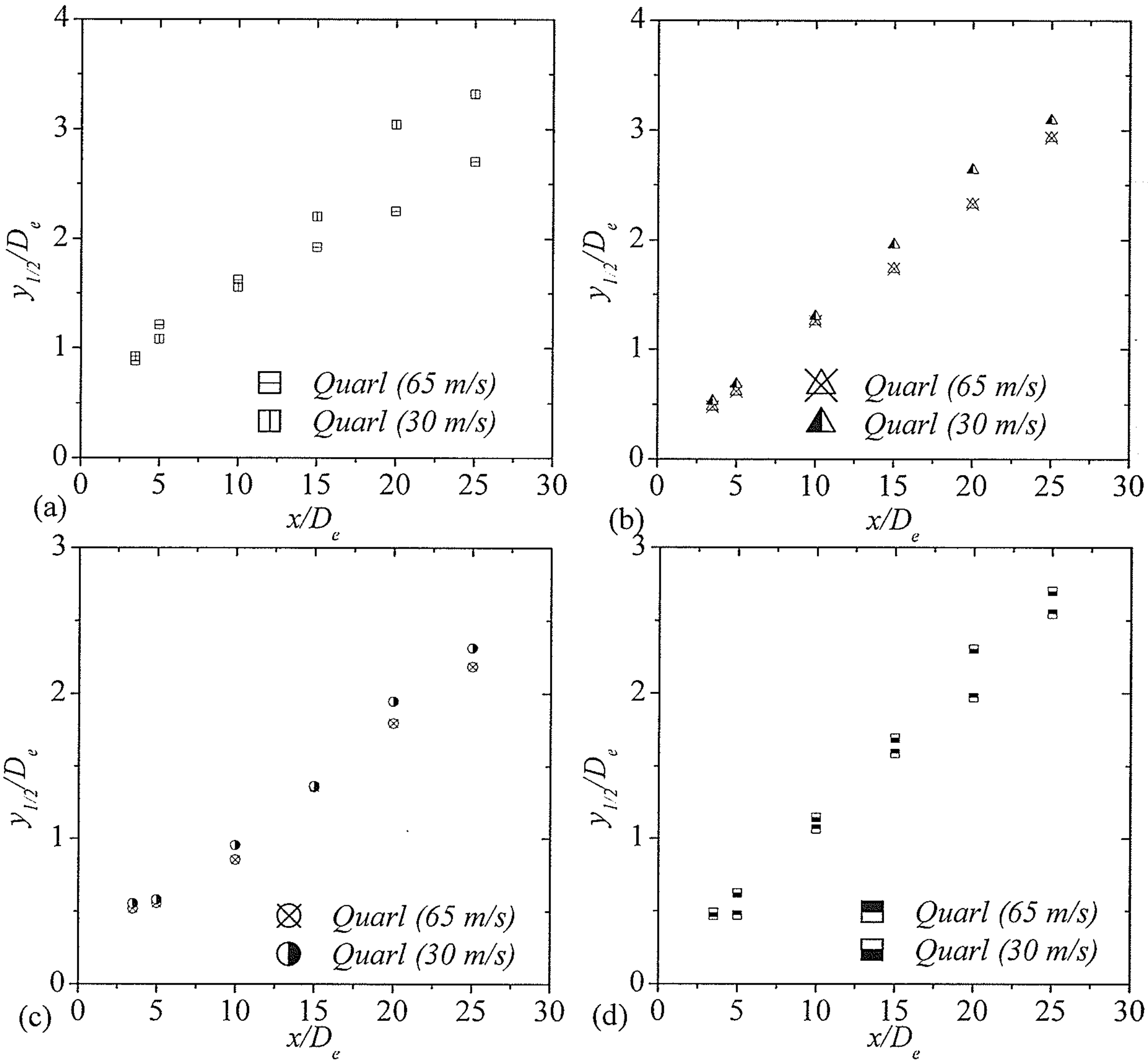

Figure 4.27: Jet half-velocity width for various nozzle geometries with quarl: (a) Rectangle, (b) Triangle, (c) Contracted circular, and (d) Square.

One other observation from Fig. 4.26 and 4.27 is that using sudden expansion generally improves the entrainment and spreading rates of all nozzles and especially that of the rectangular nozzle jet. Note that without sudden expansion, the triangular nozzle jet has a better entrainment (i.e. higher decay rate) and spreading rates compared with the rectangular nozzle jet. Comparing Fig. 4.21 and 4.23 with Fig. 4.26 and 4.27, respectively, reveal that the presence of sudden expansion for both exit velocities improves the streamwise centerline mean velocity decay of each nozzle for the 30 m/s jet (Iyogun and Birouk, 2009a). Furthermore, it has to be noted that this increase in entrainment and spreading rates are so significant, especially for the rectangular nozzle jet, that the phenomenon of axis switching does not make the 30 m/s jet half-velocity width lower than that of the 65 m/s jet in the far-field. Rather, the 30 m/s jet with sudden expansion has consistently higher half-velocity width compared to the 65 m/s jet at any streamwise location. This increase in the streamwise centerline velocity decay and half-velocity width of the nozzles with sudden expansion may be an indication of higher growth rate of streamwise vortices as reported by Sau (2002, 2004) and Nakao (1986).

Equation (4.1) is used to fit the present sudden expansion experimental data presented in Fig. 4.25 for the streamwise centerline mean velocity decay in the range $20 \leq x/D_e < 45$, and hence determine the values of C_1 and x_0 as reported in Table 4.8 for the various nozzles at exit velocities of 30 m/s and 65 m/s. On the other hand, Eq. (4. 2) is used to fit the half-velocity width data shown in Fig. 4.27 in order to determine the values of C_2 and x_{02} for the different nozzles with sudden expansion at the two exit velocities as reported in Table 4.9. The sudden expansion affects the decay and spreading rates, as well as the virtual origins for each nozzle's geometry at any exit velocity. Consequently, at both exit velocities examined here, the effect of the sudden expansion is seen to lower the values of C_1 and x_0 compared with their counterparts' values obtained without sudden expansion.

4.1.2.3 Profiles of the Streamwise Mean Velocity, Turbulence Intensities and Reynolds Stresses for Nozzles without Sudden Expansion

The radial and streamwise profiles of the mean velocities, turbulence intensities, and Reynolds stresses may give further insight into the effect of exit velocity on the streamwise centerline mean-velocity decay and jet half-velocity width of the various nozzles with and without sudden expansion. In addition, these profiles may also be helpful for CFD modeling. Figures 4.28 and 4.29 present the normalized centerline mean velocity radial profiles at a typical near-field region, i.e. $x = 2\ mm$ (corresponds to the first measured location) and $x/D_e = 3$ respectively, for all nozzles at the two exit velocities tested in the present study.

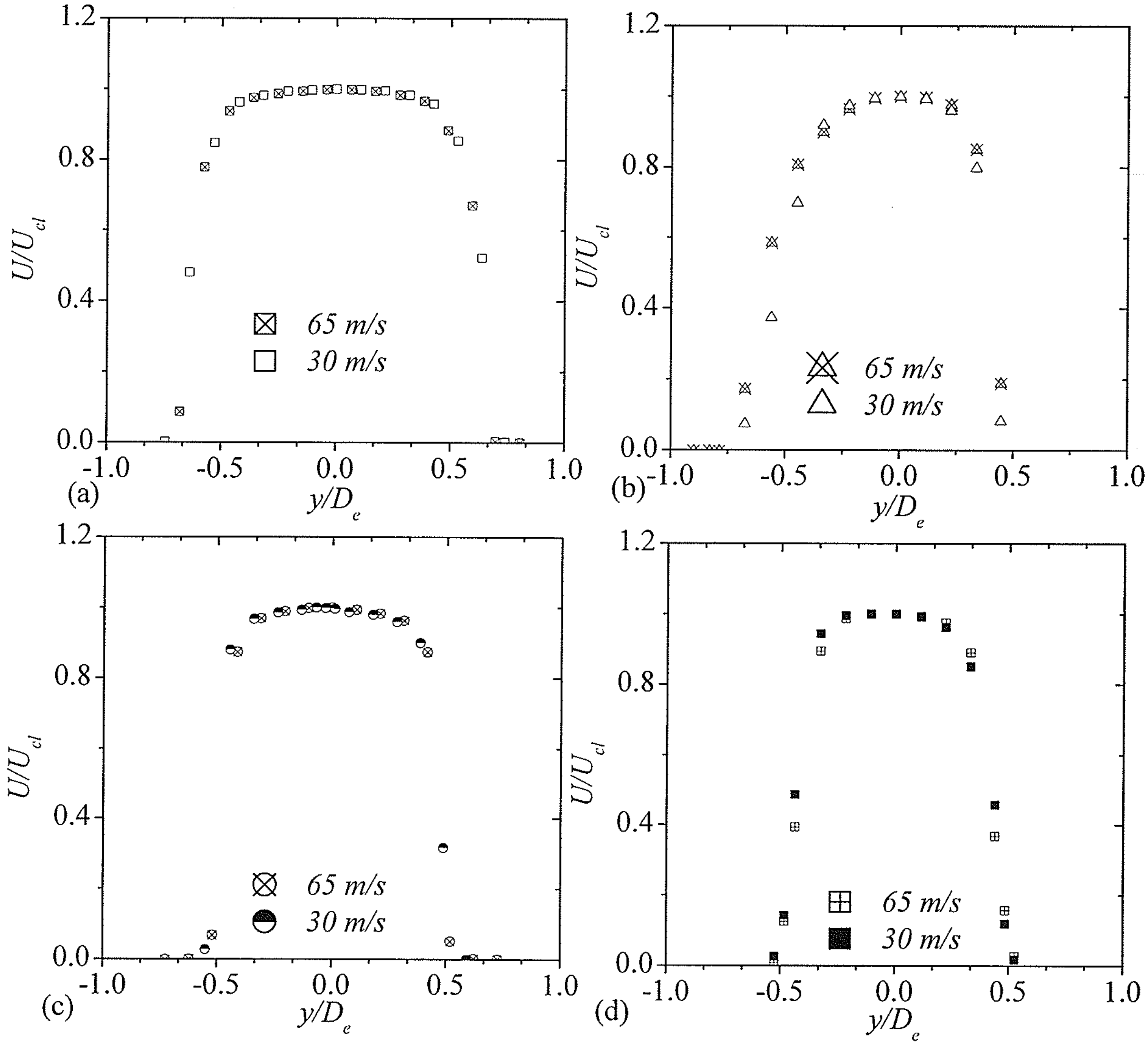

Figure 4.28: Radial profiles of mean velocity for various nozzle geometries without quarl at $x = 2$ *mm*: (a) Rectangle, (b) Triangle, (c) Contracted circular, and (d) Square.

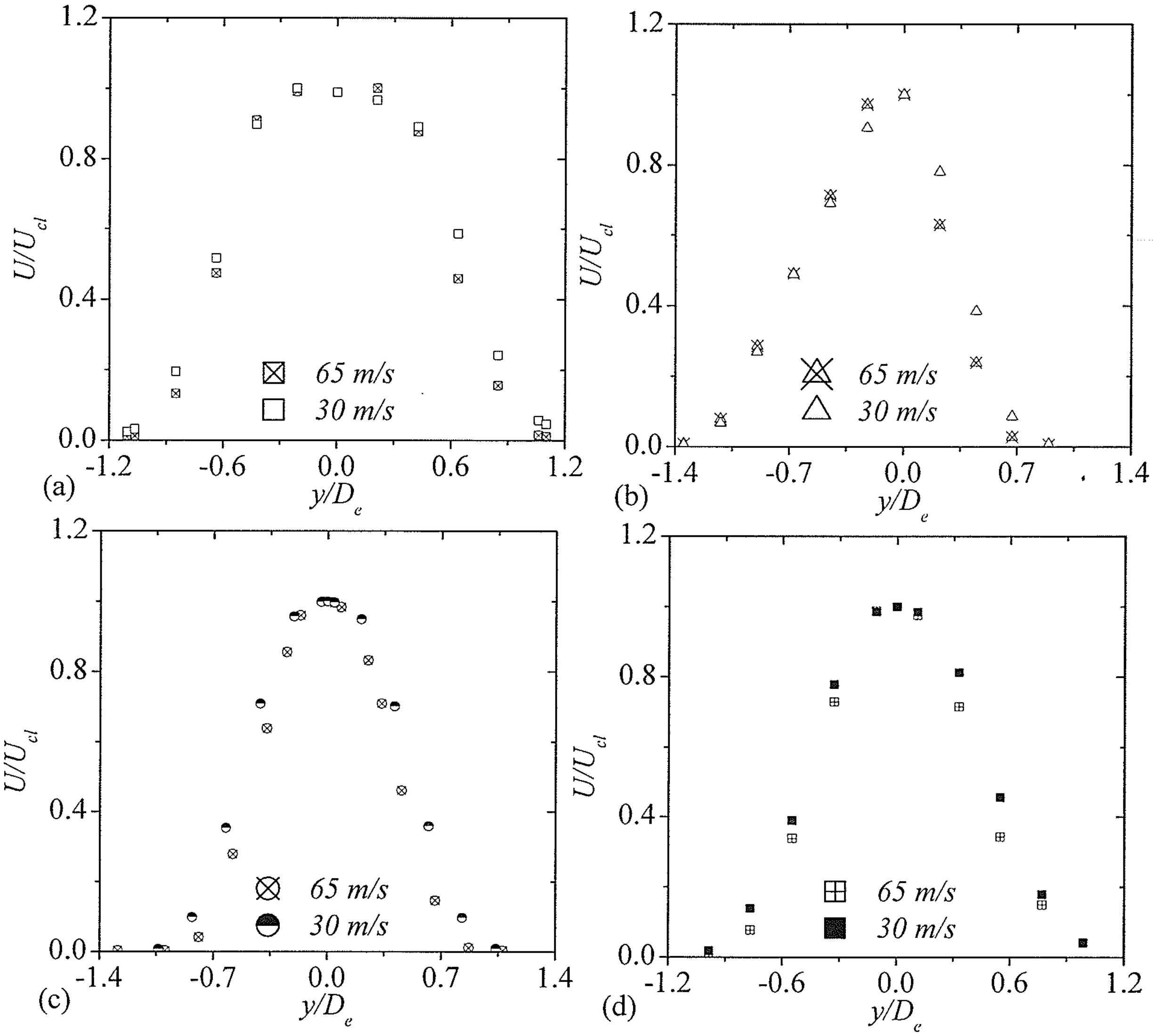

Figure 4.29: Radial profiles of mean velocity for various nozzle geometries without quarl at $x/D_e = 3$: (a) Rectangle, (b) Triangle, (c) Contracted circular, and (d) Square.

Figure 4.28 shows that at this location (x = 2 *mm*), the nozzles mean-velocity radial profiles are similar for both exit velocities. However, the radial profiles of the nozzles are slightly wider for the lower jet exit velocity. This is an indication of higher spreading of the jet at the lower exit velocity for all nozzles. This scenario occurs because the rate of entrainment of ambient fluid (as indicated by the jet decay) is higher at the jet lower exit velocity (i.e. 30 m/s) compared with that at the higher exit velocity (i.e. 65 m/s). Figure 4.28 also shows that the rectangular nozzle has a velocity profile shape that approximates top-hat at this location (x = 2 *mm*) for both exit velocities while the shape of the contracted circular nozzle and others deviates slightly from a top-hat velocity profile shape. This is caused by the small contraction ratio mentioned earlier for the contracted circular nozzle. However, Fig. 4.29 shows the complete departure from the top-hat velocity profile shape that is seen at x = 2 *mm* for the rectangular nozzle while the profiles of the other nozzles are gradually becoming more parabolic. In addition, Fig. 4.29 shows that the profiles of the 30 m/s jets are in general slightly wider than those of the 65 m/s jets compared with Fig. 4.28. This is an indication of the entrainment of the ambient fluid that has taken place up to this location and the fact that the 30 m/s jet appears to entrain higher rate of ambient fluid. Figures 4.30 and 4.31 present the corresponding radial distribution of u/U_{cl} and v/U_{cl} at x = 2 *mm* and $x/D_e = 3$, respectively, at the exit velocities of 30 m/s and 65 m/s. The turbulence profiles especially the shear-layer turbulence shed more light on the mixing that takes place between the jet and the ambient fluid. There is a good correlation between the shear-layer turbulence and the level of molecular mixing expected. It is therefore reasonable to suggest that entrainment of ambient air would also increase as the shear-layer turbulence increases. Figures 4.30 and 4.31 show that, for all nozzles, the 30 m/s jet has higher u/U_{cl} and v/U_{cl} at every identical streamwise location compared with the 65 m/s jet. Figure 4.30 shows that the square, rectangle, and triangular nozzles exhibit a u/U_{cl} in the order of 20% in the shear-layer, and that of the contracted circular nozzle is only about 18%. Figure 4.31 shows that there is a slight decrease in shear-layer, u/U_{cl}, for all nozzles further downstream, *e.g.* $x/D_e = 3$. Thus, it is clearly shown that turbulence intensity profiles correlate fairly well with the jet spreading, entrainment, and mean-velocity for the all nozzles. This affirms the initial postulation that the higher the level of shear-layer turbulence, the higher the tendency for both jet entrainment and spreading rates to increase.

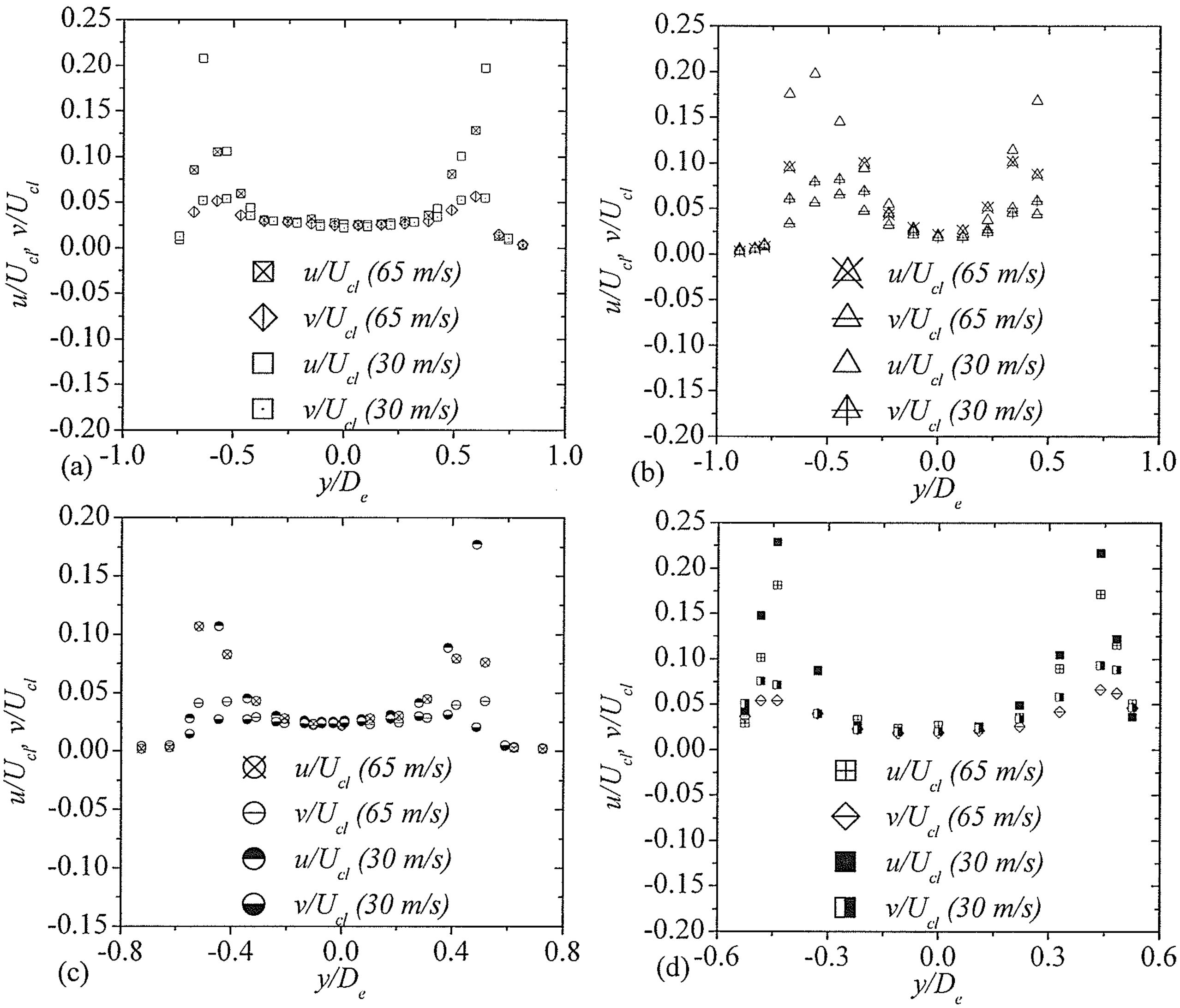

Figure 4.30: Radial profiles of mean turbulence intensities for various nozzle geometries without quarl at $x = 2$ *mm*- (a) Rectangle, (b) Triangle, (c) Contracted circular, and (d) Square.

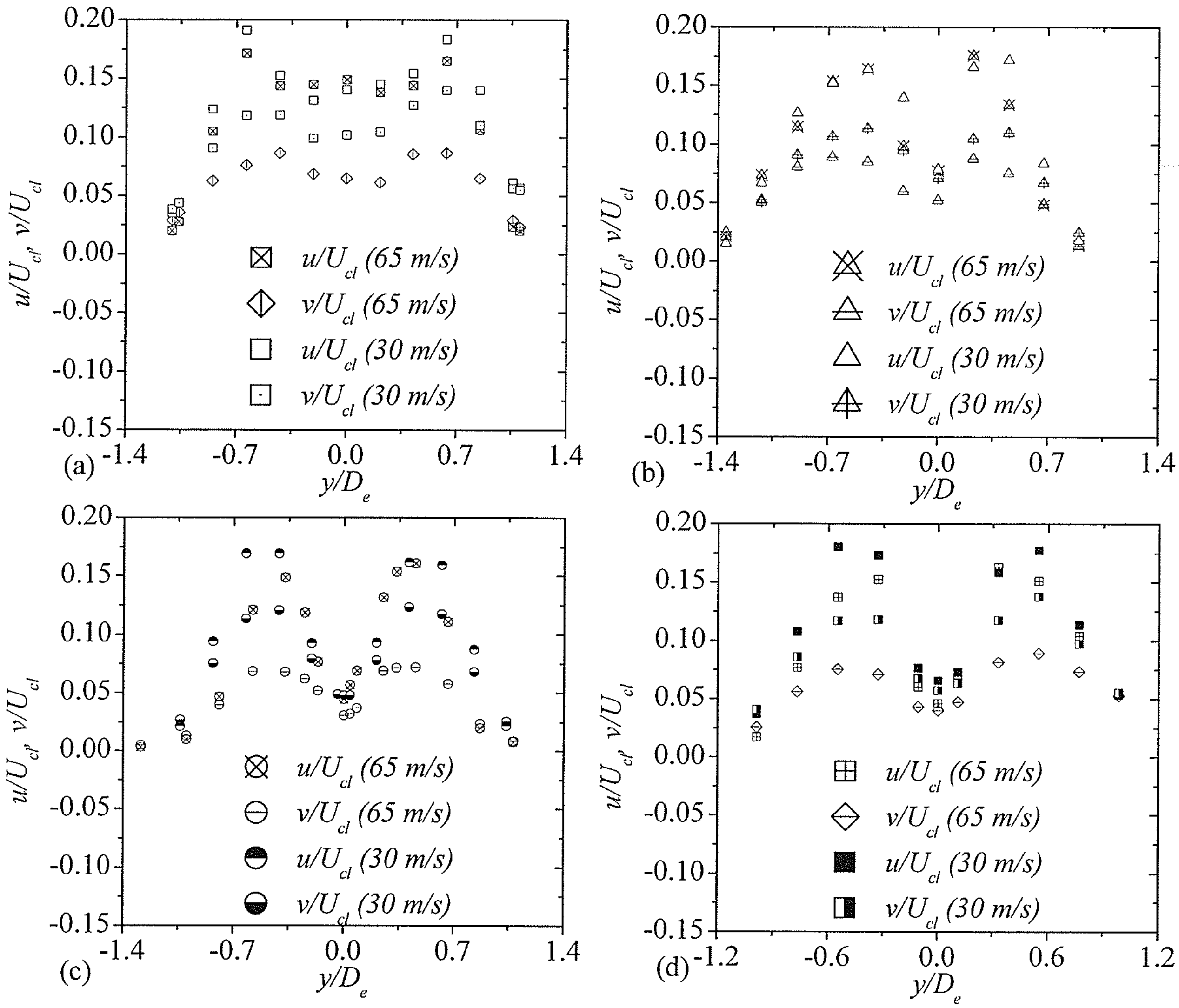

Figure 4.31: Radial profiles of mean turbulence intensities for various nozzle geometries without quarl at $x/D_e = 3$ - (a) Rectangle, (b) Triangle, (c) Contracted circular, and (d) Square.

Reynolds shear stress distribution of the jet at $x = 2$ *mm* and $x/D_e = 3$ for all nozzles at the two exit velocities tested in this study are shown in Fig. 4.32 and 4.33, respectively. These figures show that for all nozzles, the Reynolds shear stress profile is generally wider and has larger value at any identical location for exit velocity of 30 m/s compared with that of the 65 m/s.

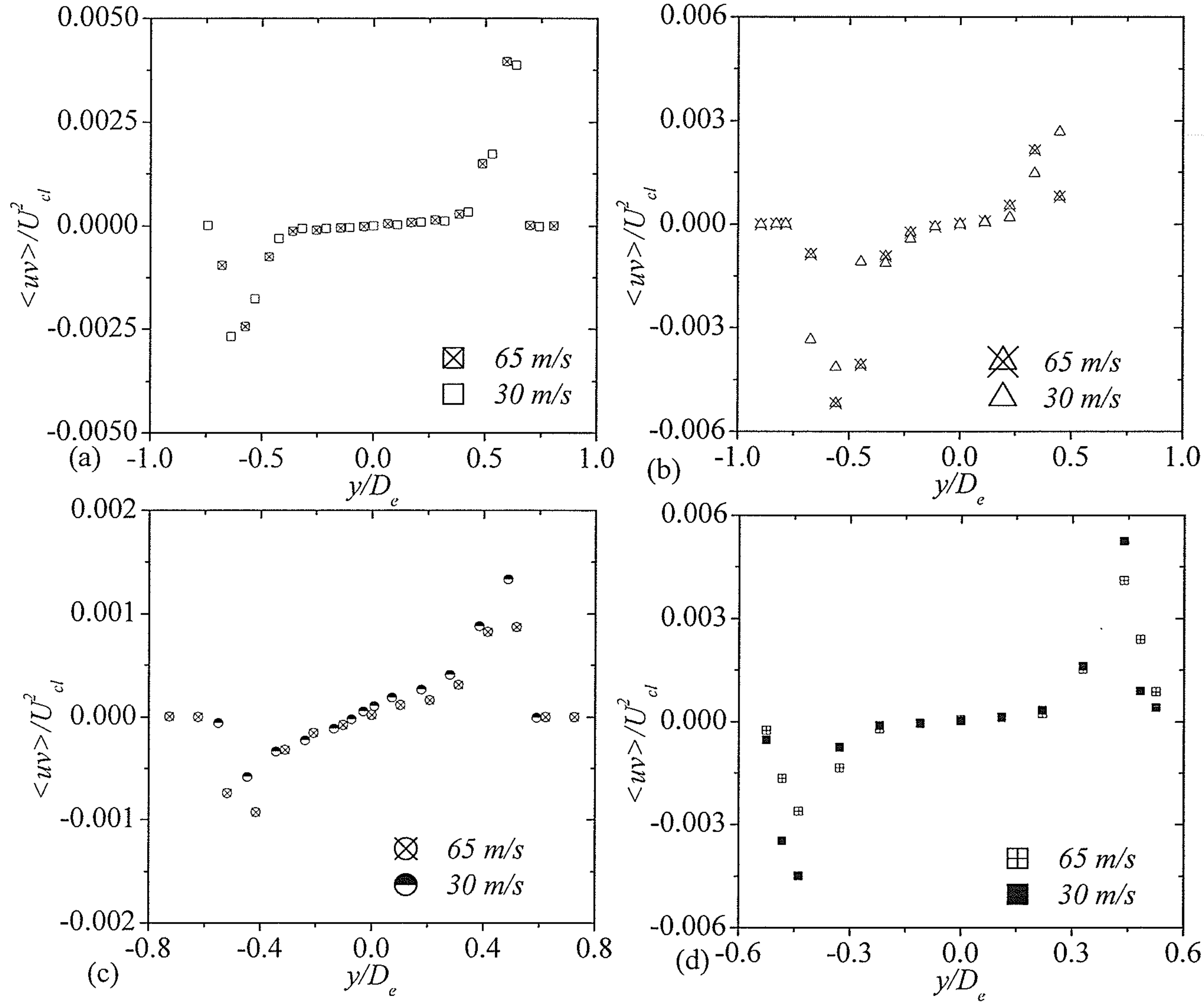

Figure 4.32: Radial distribution of Reynolds shear stress for various nozzle geometries without quarl at $x = 2$ *mm*- (a) Rectangle, (b) Triangle, (c) Contracted circular, and (d) Square.

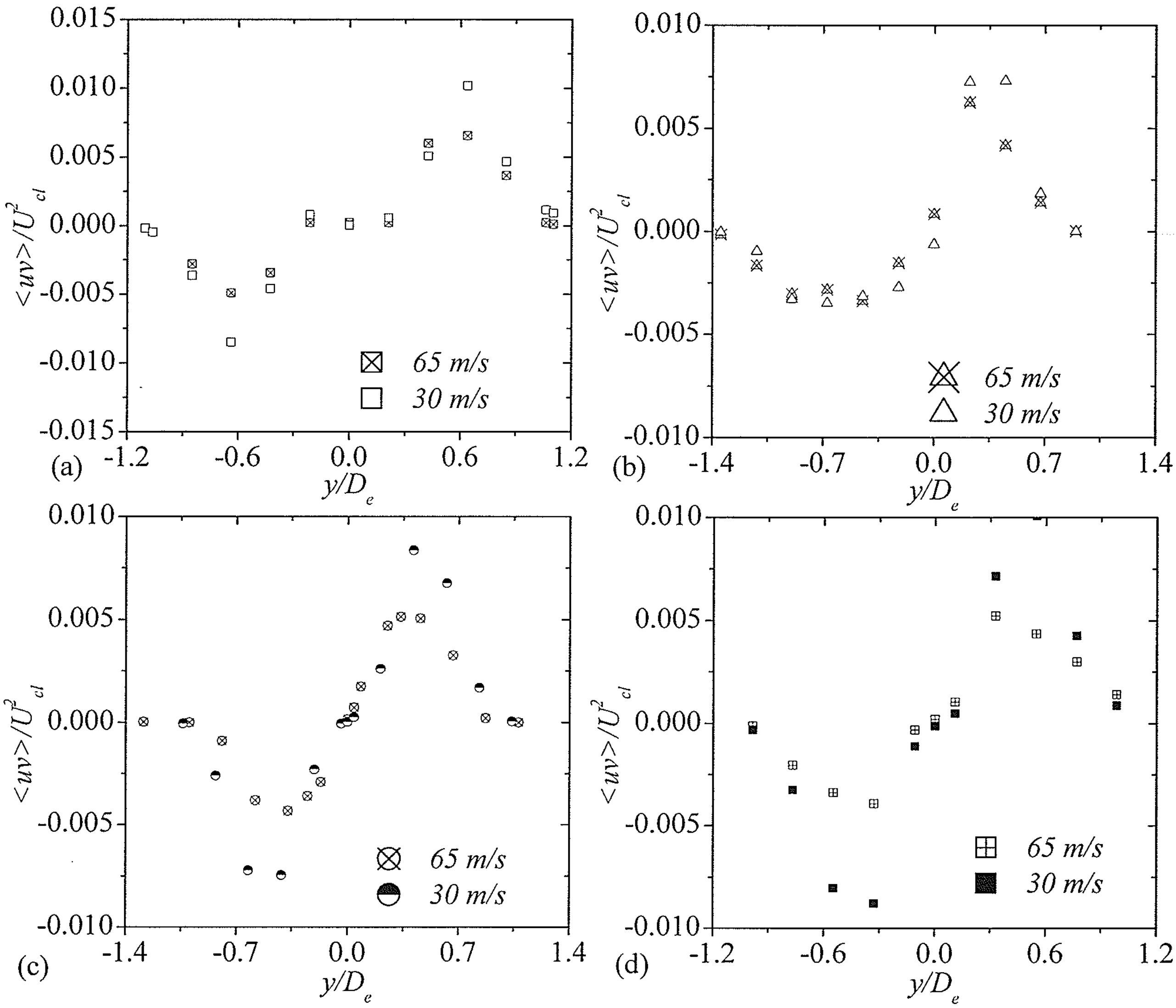

Figure 4.33: Radial distribution of Reynolds shear stress for various nozzle geometries without quarl at $x/D_e = 3$- (a) Rectangle, (b) Triangle, (c) Contracted circular, and (d) Square.

By observing Fig. 4.32 and 4.33, it can be seen that Reynolds shear stress values at the edges of the nozzle are higher at $x = 2$ *mm* compared with their corresponding values at $x/D_e = 3$, as a consequence of increased entrainment of ambient fluid. This results in a reduction of the spanwise mean velocity gradient (i.e. $\partial U/\partial y$) as the jet evolves further downstream. In addition, the 30 m/s jet's Reynolds shear stress profiles gradually becomes slightly wider than those of the

65 m/s as the jet develops downstream (e.g., $x/D_e = 3$). Whereas, for all nozzles, the difference in the profiles between the two exit velocities is not easily noticeable at the first streamwise location $x = 2$ *mm*. Similar scenario is also shown by the turbulence intensity and mean velocity profiles discussed above. Consequently, the dynamics of entrainment and spreading of the jet might be attributed to the large scale mixing by the mean flow, and the small scale mixing perpetuated by the fluctuating components of velocity and the Reynolds shear stresses. Moreover, Fig. 4.32 shows that for both exit velocities, Reynolds shear stresses are higher at the nozzle's edges, which are the regions where high spanwise or radial velocity gradients are pronounced. It, therefore, indicates that Reynolds shear stresses correlate well with the spanwise mean velocity gradients (i.e. $\partial U/\partial y$). Consequently, Reynolds shear stress is very flat at the center of the nozzles/jet at both exit velocities but increases significantly at the edges. Figure 4.33, on the other hand, shows very similar profiles to those measured at $x = 2$ *mm,* except that there is a reduction in the flatness at the center of the nozzles as a result of ambient fluid entrainment up to this location. This reduction causes a change in the velocity gradient as a result of entrainment of more ambient fluid by the jet flow (i.e. $\partial U/\partial y$ changes).

4.1.2.4 Profiles of the Streamwise Mean-Velocity, Turbulence Intensities and Reynolds Stresses for Nozzles with and without Sudden Expansion

Figures 4.34 and 4.35 present the radial distribution of the normalized mean velocity profiles at $x/D_e = 5$ for jet flows at 30 m/s and 65 m/s issuing from the nozzle's configurations without and with sudden expansion, respectively. The $x/D_e = 5$ location is chosen because comparison of the mean velocity and fluctuating component profiles can be made with and without sudden expansion at this position. Note that the sudden expansion made it impossible to measure the profiles upstream of x/D_e = 3.5. Furthermore, no other location beyond x/D_e = 5 was chosen because it has been reported that similar trend is observed beyond this streamwise location (Iyogun and Birouk, 2009a).

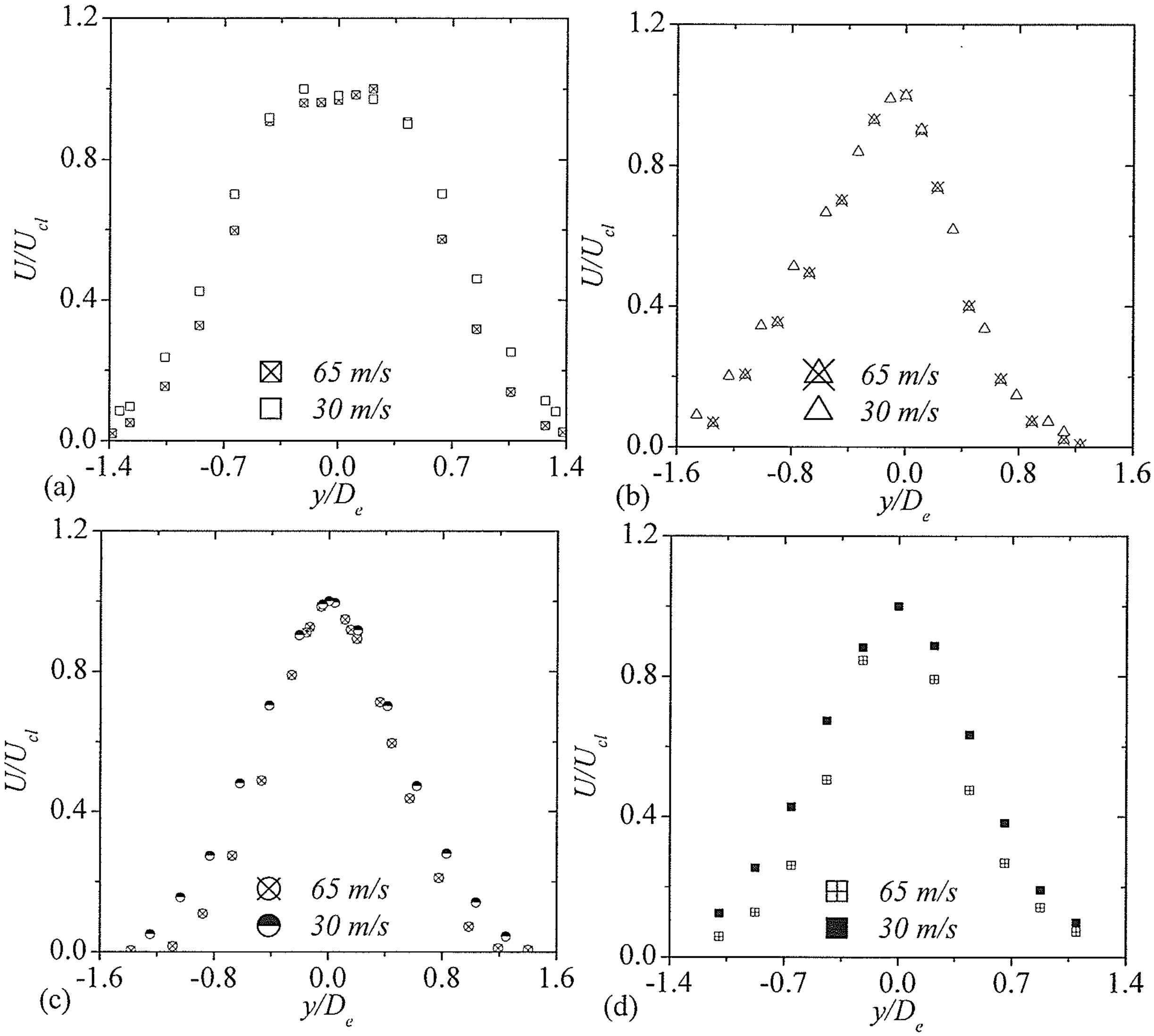

Figure 4.34: Radial profiles of mean velocity for various nozzle geometries without quarl at x/D_e = 5- (a) Rectangle, (b) Triangle, (c) Contracted circular, and (d) Square.

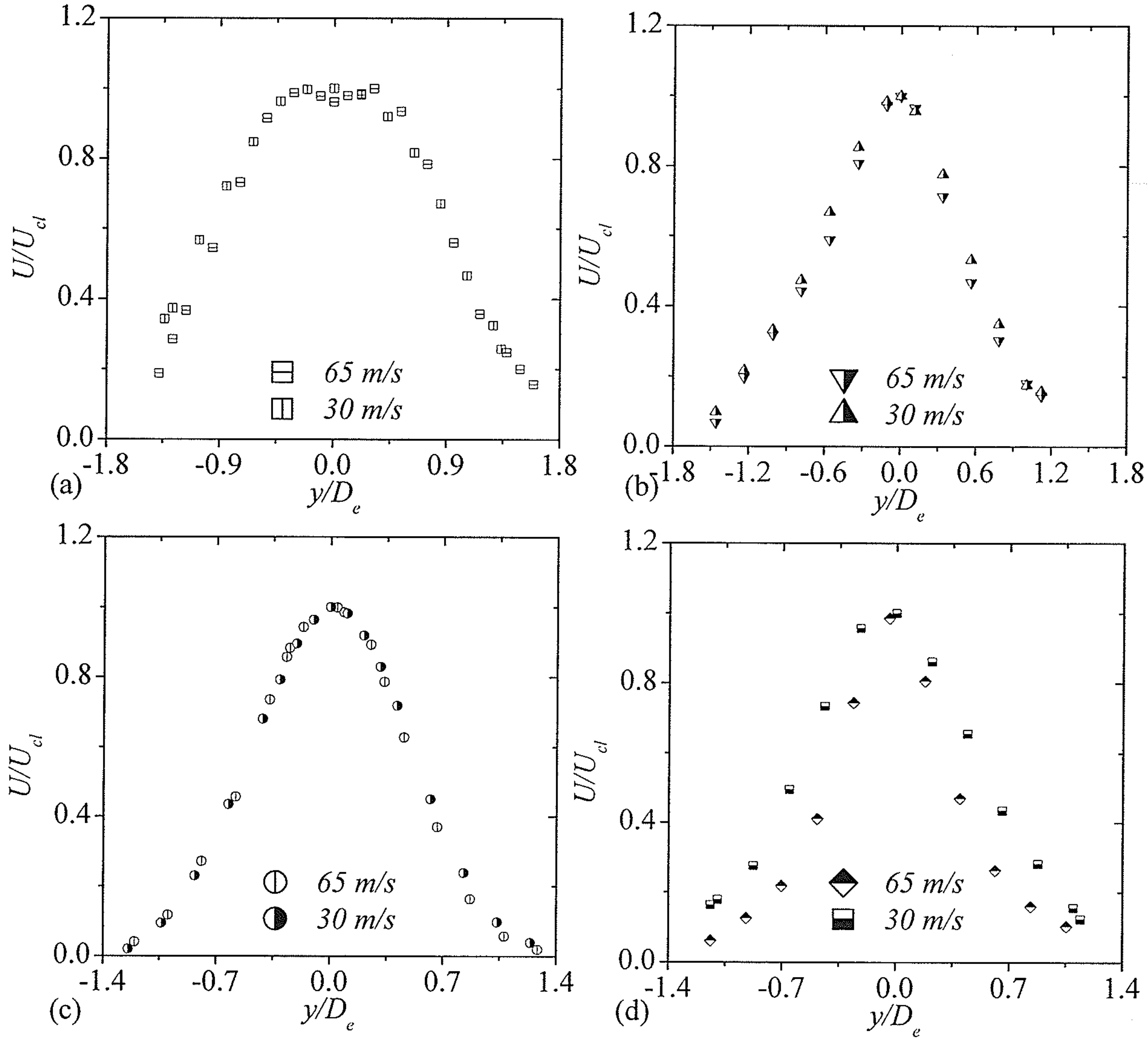

Figure 4.35: Radial profiles of mean velocity for various nozzle geometries with quarl at $x/D_e =$ 5- (a) Rectangle, (b) Triangle, (c) Contracted circular, and (d) Square.

Figures 4.34 and 4.35 both show that for all nozzles with and without sudden expansion, the jet normalized mean-velocity radial profiles in general shrink or becomes smaller as the exit velocity is increased from 30 m/s to 65 m/s. This is an indication of reduced jet spreading as exit velocity is increased which is consistent with previous locations reported above (see Fig. 4.27). Once again this demonstrates the effect of exit velocity on the large-scale mixing which controls in part the entrainment and spreading of the jet. Figures 4.36 and 4.37, on the other hand, show the corresponding radial distribution of u/U_{cl} and v/U_{cl} at $x/D_e = 5$ for all nozzles with and without sudden expansion, respectively. These figures demonstrate that the turbulence intensity profiles are higher and wider at the exit velocity of 30 m/s compared with that of 65 m/s for identical nozzle's configuration. This is a consistent pattern from $x = 2$ *mm* to further downstream locations of the jet. Consequently, the higher and wider the normalized turbulence intensity profile is, the higher the rates of entrainment and spreading of the jet. Another pertinent observation from these figures (compare Fig. 4.36 with Fig. 4.37) is the significant increase in the turbulence intensity especially the shear-layer turbulence for both cases of the exit velocity as sudden expansion is used for all nozzles except the contracted circular. This explains why there is significant increase in entrainment and spreading as a consequence of using sudden expansion for the asymmetrci nozzles while there is only a mild increase for the contracted circular nozzle. This is consistent with the findings reported in earlier sections for the 30 m/s jets, for all streamwise locations beyond $x/D_e = 5$ (Iyogun and Birouk, 2009a).

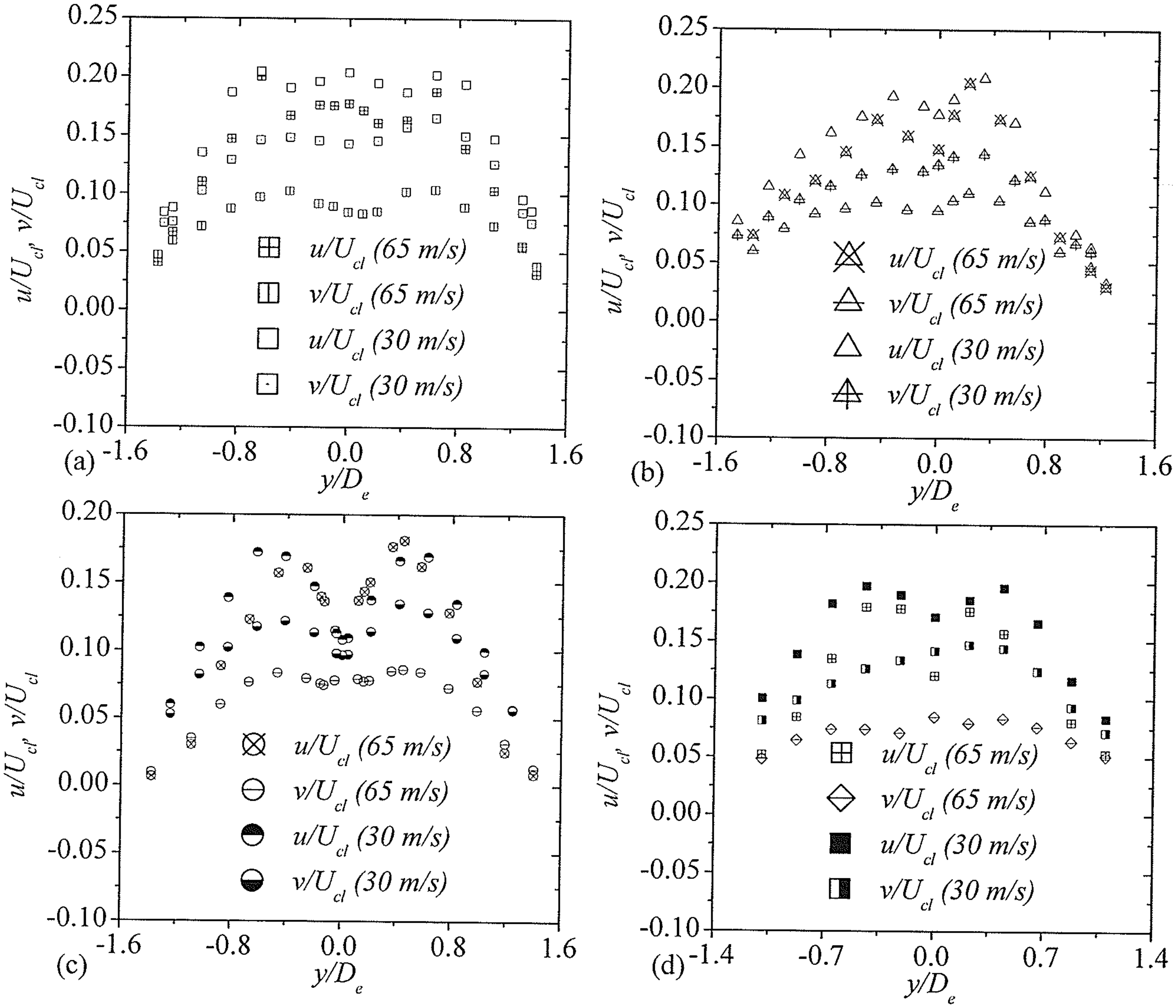

Figure 4.36: Radial profiles of mean turbulence intensities for various nozzle geometries without quarl at $x/D_e = 5$- (a) Rectangle, (b) Triangle, (c) Contracted circular, and (d) Square.

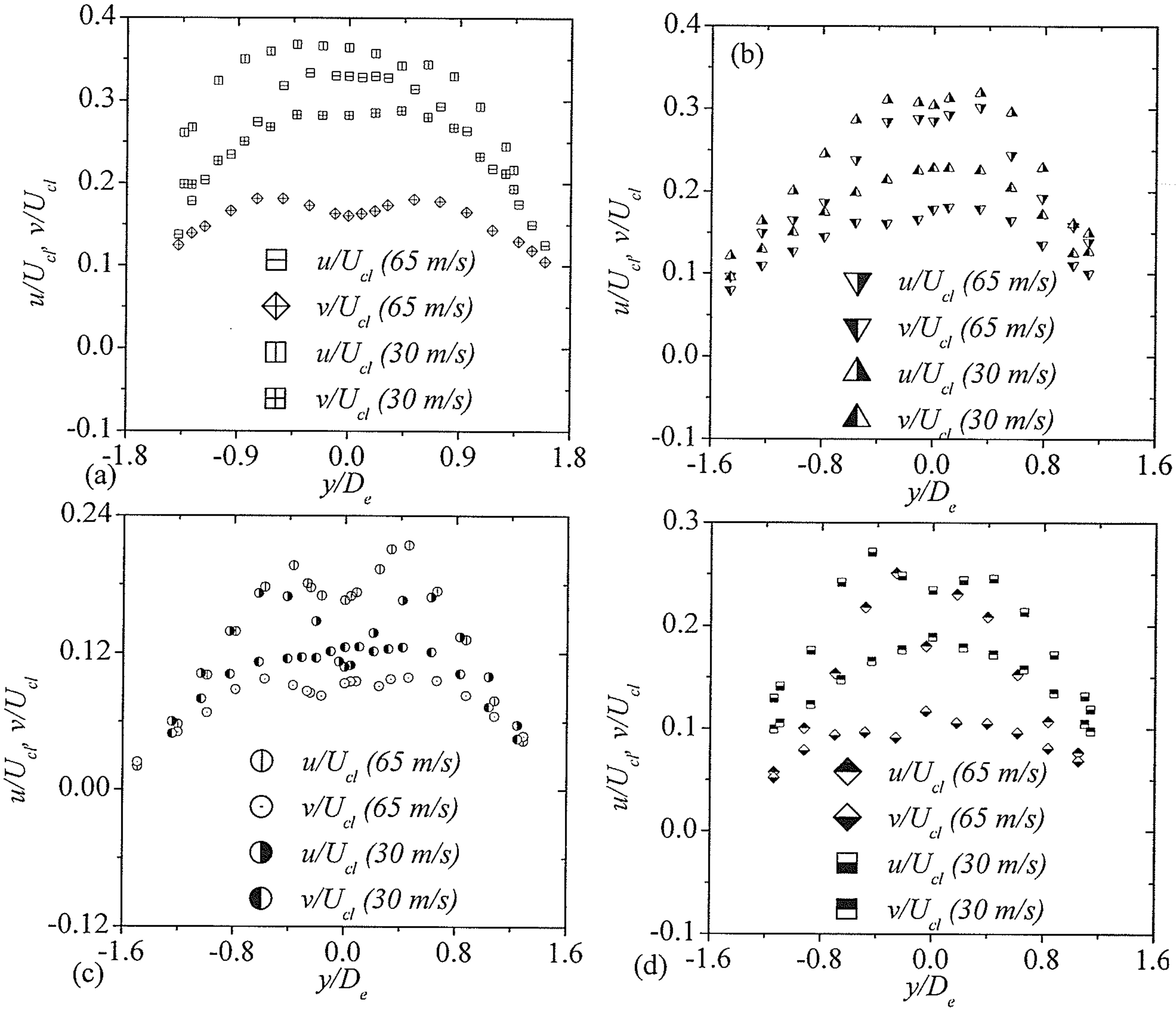

Figure 4.37: Radial profiles of mean turbulence intensities for various nozzle geometries with quarl at $x/D_e = 5$- (a) Rectangle, (b) Triangle, (c) Contracted circular, and (d) Square.

Figures 4.38 and 4.39 show the Reynolds shear stresses of the different nozzle geometries without and with sudden expansion at $x/D_e = 5$, respectively. These figures show consistently that the jet Reynolds shear stress profiles are generally higher and wider at 30 m/s compared with 65 m/s. This shows that the radial velocity gradient is higher for the 30 m/s compared with the 65 m/s. In addition, there is also noticeable increase in the Reynolds shear stresses especially in the shear-layer zone of the jet at both exit velocities as sudden expansion is used for all nozzles except the contracted circular which exhibits a mild increase. This also supports the reason why there is an apparent increase in the streamwise centerline mean velocity decay and jet half-velocity width as a consequence of using sudden expansion especially for the triangular and rectangular nozzles.

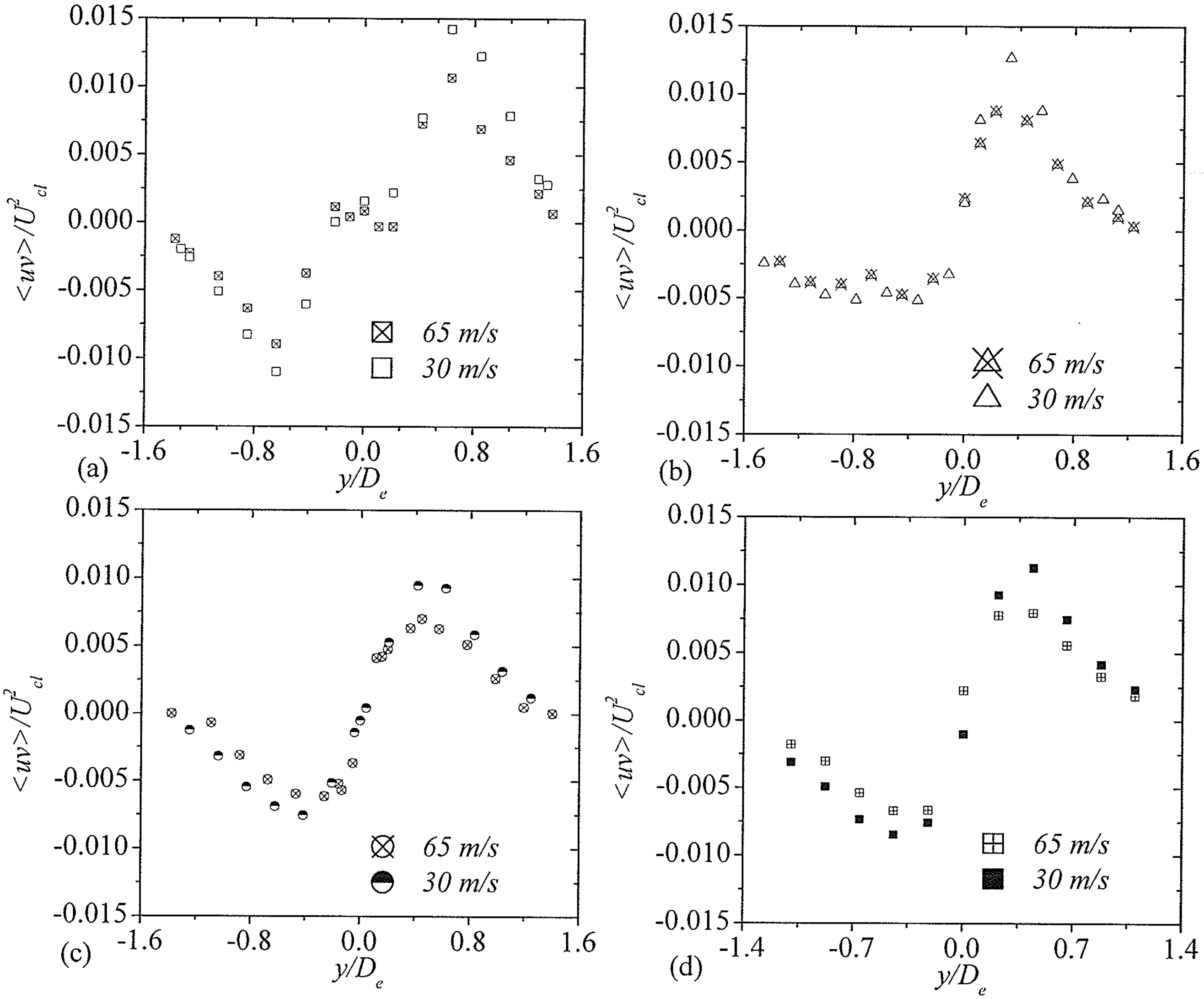

Figure 4.38: Radial distribution of Reynolds shear stress for various geometries without quarl at $x/D_e = 5$- (a) Rectangle, (b) Triangle, (c) Contracted circular, and (d) Square.

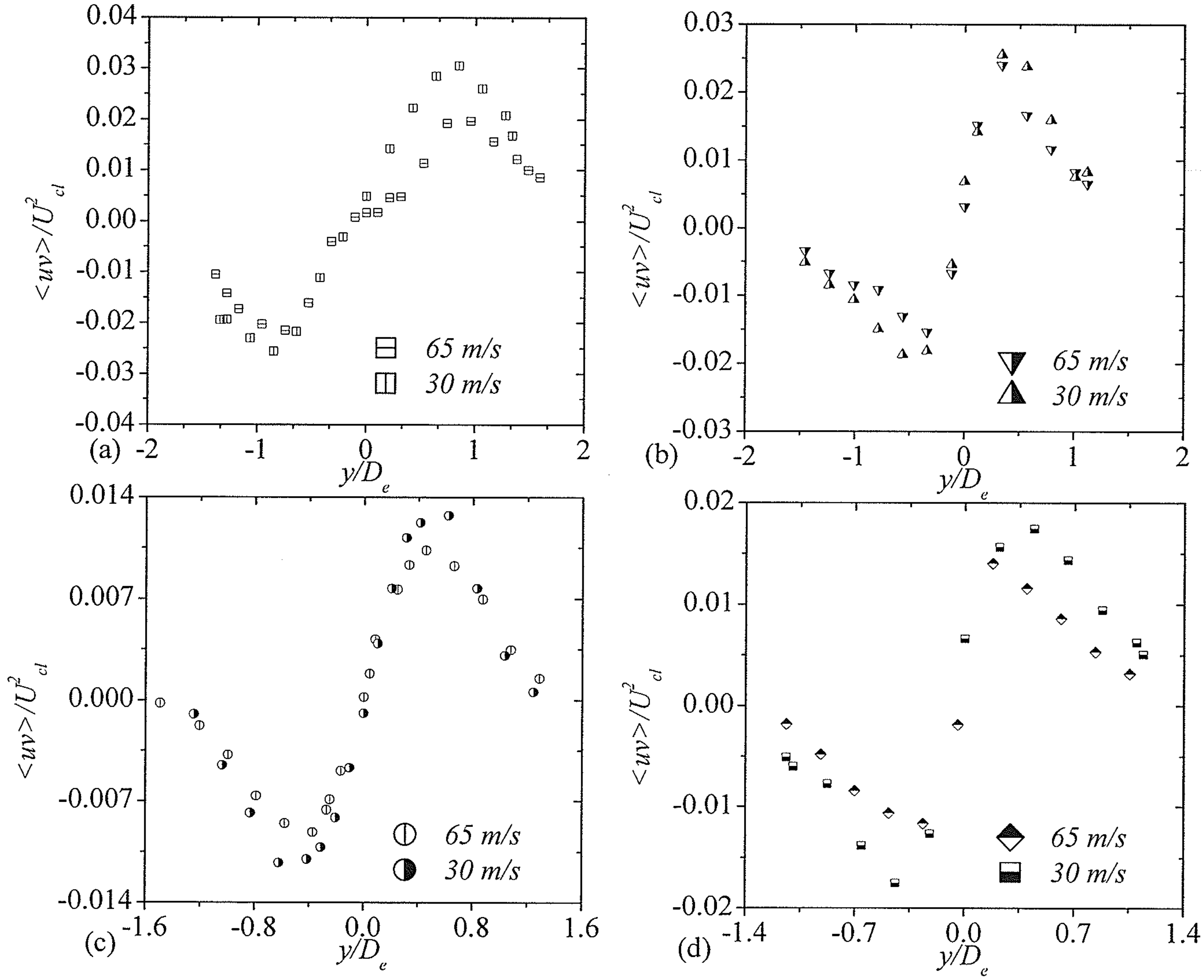

Figure 4.39: Radial distribution of Reynolds shear stress for various geometries with quarl at $x/D_e = 5$- (a) Rectangle, (b) Triangle, (c) Contracted circular, and (d) Square.

4.1.2.5 Axial Development of Turbulence Intensity

The axial distribution of the normalized centerline mean fluctuating velocity profiles (i.e. u/U_{cl} and v/U_{cl}) is shown in Fig. 4.40 and 4.41. Figure 4.40 compares the normalized turbulence intensities (i.e. u/U_{cl} and v/U_{cl}) profiles of all nozzles without quarl at 30 m/s and 65 m/s, while

Fig. 4.41 compares the turbulence intensities profiles of each individual nozzle at 30 m/s and 65 m/s for the same geometries but with sudden expansion. Figure 4.40 shows that for the two exit velocities, the values of u/U_{cl} and v/U_{cl} are higher for the asymmetric nozzles compared with their contracted circular counterpart both in the near- and far-field, but more prominent in the near-field which is consistent with earlier findings reported in this thesis (Iyogun and Birouk, 2009a). That is, there is a faster development of the turbulence intensities for the asymmetric nozzles such that their near-field turbulence is higher than those of the contracted circular nozzle. However, the level of turbulence, u/U_{cl}, at the jet centreline exit (i.e. $y/D_e = 0$, $x = 2$ mm) for all the nozzles are quite similar (i.e. $\approx$ 3%) but generally lower for the asymmetric nozzles. This higher turbulence level at the jet exit could imply that the contracted circular nozzle induces a wider range of turbulence length scales compared with those generated by the asymmetric nozzles which may ultimately suppress the development of coherent structures in the far-field of the contracted circular nozzle jet (Mi *et al.*, 2007). This scenario according to Mi *et al.* (2007) could cause the large scale interaction between the coherent structures themselves or between the structures and the ambient fluid to be weaker, thereby causing lower entrainment and spreading of the jet. Note, however, that the near-field growth rate of u/U_{cl} is higher for the asymmetric nozzles compared to the contracted circular nozzle. The advantage of this near-field turbulence is that it has a potential of increasing near-field mixing which ultimately could be of immense benefit to combustion stability. Consequently, this increased development of the turbulence intensities could be partly responsible for greater entrainment and spreading rates of jets issuing from asymmetric nozzles. Overall, these observations strengthen the role of turbulence in jet entrainment and spreading. Furthermore, Fig. 4.40 shows that for all nozzles, the axial development of the turbulence intensity levels decreases in the near-field (i.e. $x/D_e < 20$) as the exit velocity increases from 30 m/s to 65 m/s. Consequently, there is a good correlation between the development of axial turbulence and jet entrainment or spreading which is consistent with the findings of Warda *et al.* (1999). Figure 4.41, on the other hand, re-emphasizes the influence of sudden expansion on u/U_{cl} and v/U_{cl} consistent with initial finding reported earlier in this thesis. That is, at any given streamwise flow location, u/U_{cl} and v/U_{cl} are higher for jets issuing from nozzles with sudden expansion compared to without. However, this difference is more pronounced for jets issuing from asymmetric nozzles. These observations are noticeable when comparing Fig. 4.40 with Fig. 4.41. In addition, Figure 4.40 shows clearly that the near-field turbulence intensity decrease when the exit velocity is increased from 30 m/s to 65 m/s. The same figure shows also that the hump observed by Mi *et al.* (2000) is not easily discernible in the present experiment for the triangular and rectangular jets at the exit velocity of 30 m/s but becomes apparent at the higher exit velocity of 65 m/s. However, Fig. 4.41 shows that, at both exit velocities, this hump is easily discernible for the triangular and rectangular jets with quarl at $x/D_e = 5$. In fact, the peak is much larger than that observed for the corresponding 65 m/s jets issuing from nozzles without quarl. This hump has been reported by Mi *et al.* (2000) to be likely caused by the axis-switching phenomenon that occurs in both the triangular and rectangular nozzles. Though this assertion is not sufficiently proved here, the figures provide an evidence of the effect of exit velocity on the formation of the hump. Finally, the good correlation between the axial development of the turbulence intensity and entrainment and spreading for each nozzle is a clear indication of the effect of turbulence on jet entrainment and spreading.

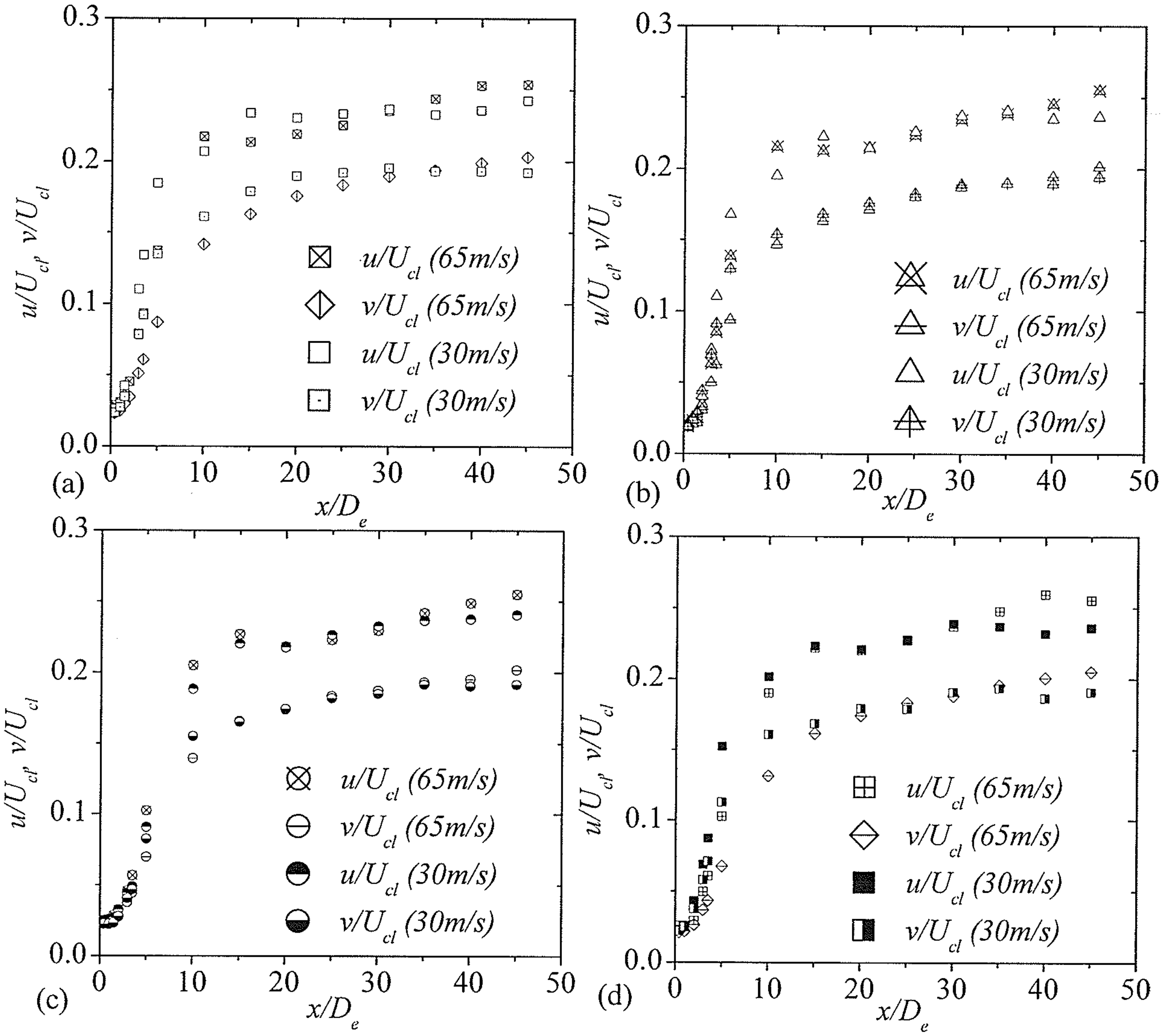

Figure 4.40: Axial development of turbulence intensities for various nozzle geometries without quarl- (a) Rectangle, (b) Triangle, (c) Contracted circular, and (d) Square.

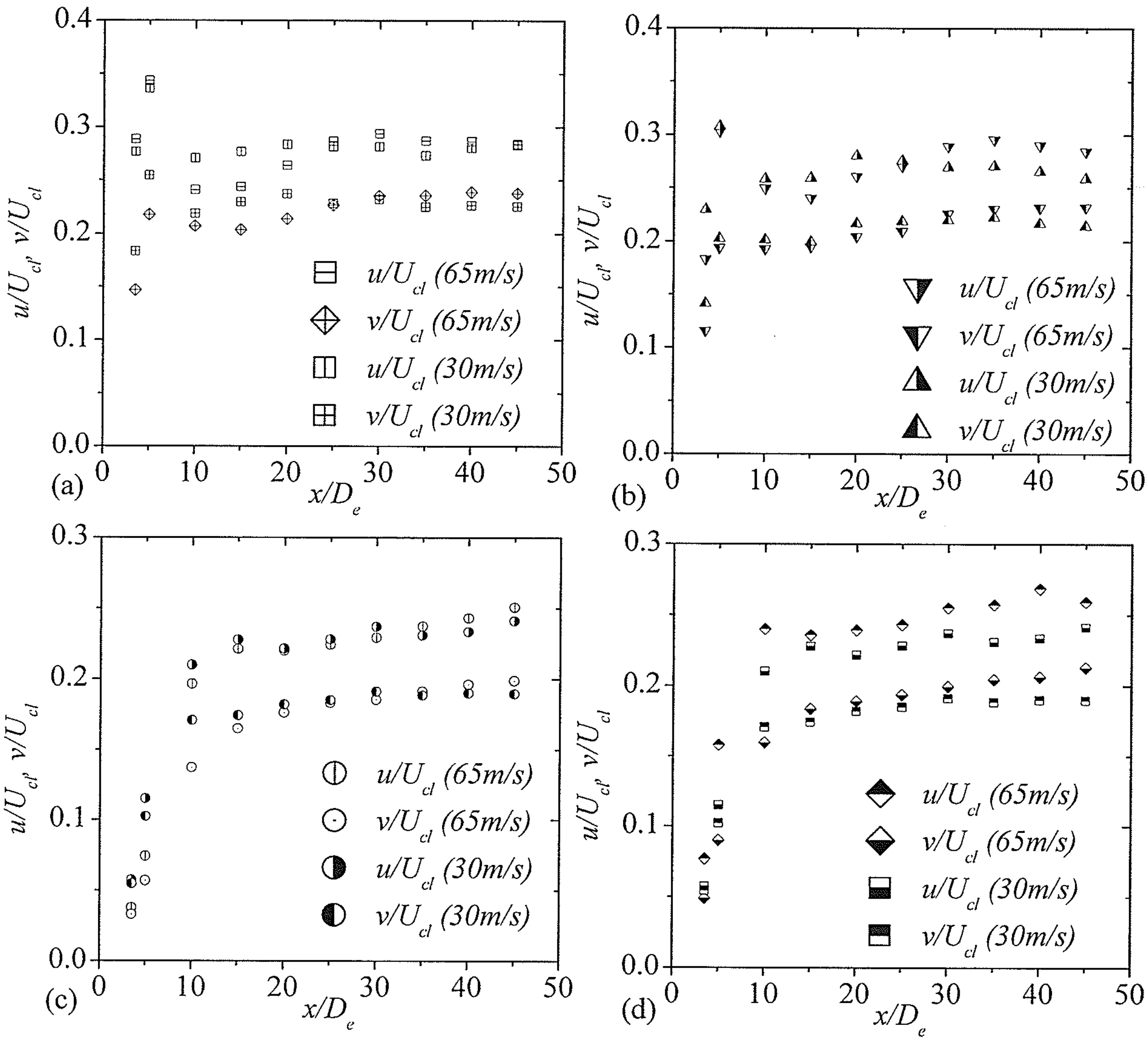

Figure 4.41: Axial development of turbulence intensities for various nozzle geometries with quarl- (a) Rectangle, (b) Triangle, (c) Contracted circular, and (d) Square.

4.2 Reacting Jet Flow

4.2.1 Effect of Nozzle Geometry on the Stability of Turbulent Jet Methane Flame

The reacting flow results presented here are investigations that reveal the effect of nozzle geometry on the stability of a turbulent methane flame. To accomplish this objective, the flame liftoff height and velocity, as well as flame reattachment and blowout are presented and discussed below for the five nozzle geometries (i.e. triangular, pipe with 4.45 mm diameter, contracted circular, rectangular, and square). The discussion of the reacting jet flow results is aided by the corresponding non-reacting jet airflow results.

4.2.1.1 Liftoff Height

The liftoff height, as a function of the jet exit velocity for the five different nozzle geometries tested in the present study, is shown in Fig. 4.42. Figure 4.43 presents a comparison of the present data for the pipe and contracted circular nozzle with the liftoff data of Kalghatgi (1984). The present lowest and highest exit velocities used for liftoff height determination are based on the liftoff and blowout velocities of the jet diffusion methane flame. Kalghatgi's (1984) flame liftoff height correlation is expressed as follows:

$$\frac{hS_u}{\nu_e} = C\frac{U}{S_u}\left(\rho_e/\rho_\infty\right)^{1.5} \tag{4.3}$$

where h is the flame liftoff height, S_u is the laminar flame speed (S_u = 0.39 m/s according to Kalghatgi (1984)), ν_e is the kinematic viscosity of the fuel at the nozzle exit, U is the exit velocity of the reacting jet, C is a constant, ρ_e is the density of the fuel at the nozzle exit and, ρ_∞ is the density of the ambient air. From Fig. 4.43 it can be seen that the pipe nozzle tested in the present study produces flame liftoff height data that are in fair agreement with that of Kalghati (1984). In addition, Fig. 4.42 and 4.43 exhibit no significant difference between the liftoff height of the contracted circular nozzle and that of the pipe. This is in good agreement with the findings of Coats and Zhao (1989), but not in agreement with those of Langman *et al.* (2007) who reported significant differences in the liftoff height between the contracted circular nozzle and the pipe. These discrepancies may be attributed to the difference in the total mass of ambient air that each jet is able to entrain. For example, in the present study, the near-field centreline mean-velocity decay of the pipe jet and that of the contracted circular jet are nearly identical (as shown in the discussion section below), which might justify why they also exhibit similar lift-off heights. Nevertheless, Langman *et al.* (2007) reported different entrainment rate between the pipe and contracted circular jets. In fact, Langman *et al.* (2007) did not provide conclusive evidence about the reasons behind the discrepancies between the liftoff height of the pipe and contracted circular nozzle, as well as with published data of Coats and Zhao (2007).

Furthermore, Fig. 4.42 shows clearly that the asymmetrical nozzles' flame liftoff heights are, in general, lower than those of the pipe and the contracted circular nozzle. The rectangular nozzle has the lowest liftoff height at exit velocities beyond 43 m/s. In addition, the square and triangular nozzles have relatively lower liftoff heights compared to their circular counterparts (i.e. the pipe and the contracted circular nozzle). Apart from the axisymmetric nozzles (i.e. pipe and contracted circular) and the square nozzle, the triangle and rectangle nozzles exhibit two distinct flame liftoff regions. One region spans up to an exit velocity of around 43 m/s, while the other region occurs for an exit velocity of around 48 m/s and above. These two regions are separated by a transition region or a step change for the rectangular nozzle. In the first region (i.e. U = 27– 43 m/s), the triangular nozzle has the lowest flame liftoff height, however, in the second region (i.e. at $U = 48$ m/s and above), the flame liftoff height of the rectangular nozzle is the lowest. For exit velocities greater than approximately of 48 m/s, the trend of the asymmetrical nozzles' liftoff heights can be fairly described by Kalghatgi's (1984) correlation but with different values of the constant C of Eq. (4.3) than the value of C = 50 reported in Kalghatgi (1984). However, in the lower range of the exit velocity, i.e. below approximately 43 m/s, the Kalghatgi's correlation fails to completely describe the flame liftoff height trend of the triangle and rectangle nozzles without changing the value of the constant C. A complete analysis of the effect of asymmetric nozzles on the flame liftoff height is discussed later on in Section 4.2.1.3.

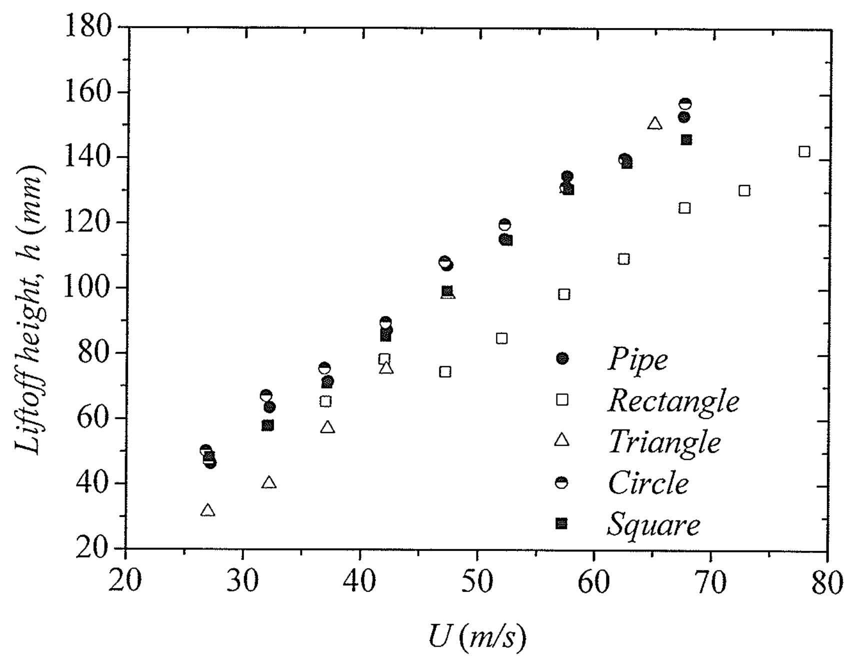

Figure 4.42: Flame liftoff height versus jet exit velocity for different nozzle geometries tested with no quarl.

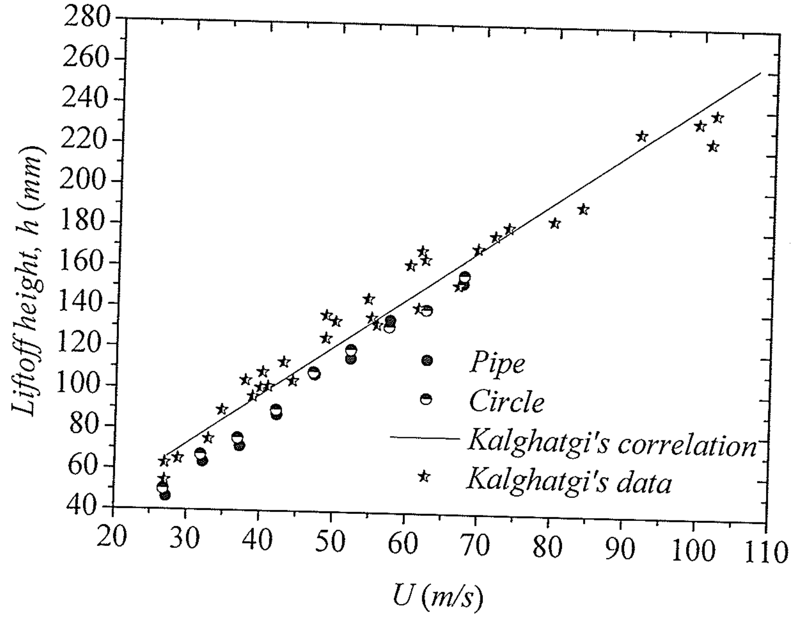

Figure 4.43: Comparison of the present liftoff height with that of Kalghatgi (1984).

Figure 4.44 presents an attempt to compare the present flame liftoff heights with the extinction theory of Peters and Williams (1983). This theory, which scales the instantaneous scalar dissipation at quenching with the global residence time; D_e/U, is formulated as

$$X_{qu}^{*} = X_{qu}\left(D_e/U\right) \tag{4.4}$$

Peters and Williams (1983) derived three analytical expressions using the extinction theory to account for the liftoff height. The three analytical formulation differ based on the manner the analytical non-dimensional scalar dissipation rate was analyzed. Note, however, that the third expression for liftoff height (i.e. X_{lb3}) was formulated purely for the purpose of achieving better agreement with experimental liftoff height data. The three formulated methods relate the non-dimensional average rate of the scalar dissipation to the liftoff height and nozzle diameter, as follows:

$$X^{*}_{qu} = X_{tb1} = 0.24(D_e/h)^{1.5}\left(1 - 0.096\sqrt{h/D_e}\right) \tag{4.5}$$

$$X^{*}_{qu} = X_{tb2} = 0.46(D_e/h)^{2}\left(1 - 0.039(h/D_e)^{1/1.4}\right) \tag{4.6}$$

$$X^{*}_{qu} = X_{tb3} = 0.018(D_e/h) \tag{4.7}$$

According to Peters and Williams (1983), the presumed liftoff criterion is when $X_{st} = X_{qu}$ where X_{st} is the rate of scalar dissipation at stoichiometry and X_{qu} is the instantaneous scalar dissipation rate at extinction or quenching. Figure 4.44 presents the evolution of X^{*}_{qu} versus h/D_e with Eq. (4.4) through (4.7) for the five different nozzles tested in the present study. The ultimate goal is to adjust X_{qu} by trial and error, for each nozzle, to enable the collapse of Eq. (4.4) with one or more of the three Eq. (4.5) through (4.7). Among the three expressions, i.e. Eq. (4.5) through (4.7), it is found that Eq. (4.7) has the best agreement with the theory of extinction described by Eq. (4.4). It is important to mention that, for each nozzle's geometry, the value of X_{qu} of Eq. (4.4) should normally be obtained experimentally or solved for analytically. Nevertheless, the instantaneous scalar dissipation rate at extinction or quenching, X_{qu}, is found (by trial and error) to be 7.8 s^{-1}, 8.0 s^{-1}, 8.1 s^{-1}, 8.3 s^{-1}, and 10.1 s^{-1} for the contracted circular, pipe, triangular, square, and rectangular nozzles, respectively. The fact that $X_{qu} \sim 8.1$ s^{-1} for the triangular nozzle is lower than that of the square nozzle may be attributed to the presence of two distinct liftoff regions for the triangular nozzle, as shown in Fig. 4.42. In the lower jet exit velocity region, that is, for $U < 43$ m/s, the triangular nozzle has the lowest flame liftoff height. However, in the higher exit velocity region, i.e. for $U > 48$ m/s, its liftoff height increases significantly and almost levels off with the other nozzles, except the rectangular which produces a flame with the lowest liftoff height. This trend suggests that the instantaneous scalar dissipation rate somehow would depend on the jet exit velocity, as the value of 8.1 s^{-1} appears adequate only for the second liftoff region. Nonetheless, the differences in the strain rate between the different nozzle geometries are in accordance with Peters and Williams (1983) proposition that turbulence intensity has a significant effect on the strain rate. Consequently, the difference in turbulence intensity between the different nozzles could possibly be the cause for the difference between their strain rates. The liftoff data of the present study, shown in Fig. 4.44, are in fair agreement with the third method (i.e. X_{tb3} or Eq. (4.7)) of Peters and Williams (1983). The reason for finding a good agreement between Eq. (4.7) for determining the non-dimensional average rate of scalar dissipation rate and the present liftoff data might be due to the way Eq. (4.7) has been formulated. This equation is derived purely for the purpose of producing better agreement with experimental liftoff data, and does not include the assumption of quenching in its formulation (Peters and Williams, 1983). It is, therefore, not surprising why this method of Peters and Williams (1983) describes fairly well the liftoff trend of all the tested nozzle's geometries.

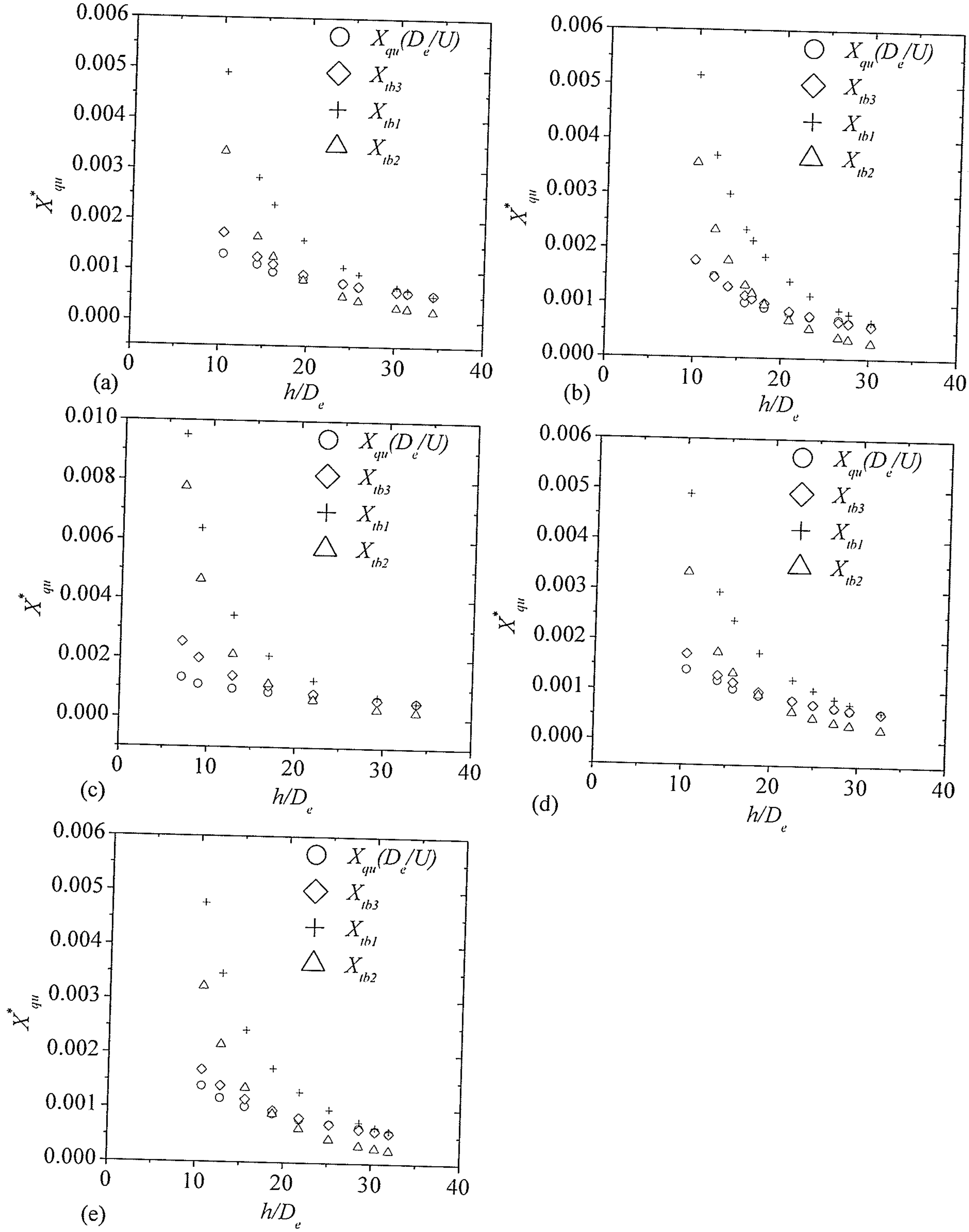

Figure 4.44: Comparison of the present liftoff height with the theory of Peters and Williams (1983)- (a) Pipe, (b) Rectangle, (c) Triangle, (d) Contracted circular and (e) Square.

It is demonstrated above that the correlation of Kalghatgi (1984) can, in general, be used to describe the liftoff heights of the present data but with a value of the constant, C of Eq. (4.3) different for each nozzle. The correlation of Kalghatgi (1984) simply states that the flame liftoff height is proportional to the jet bulk exit velocity, as for a given hydrocarbon fuel, all the remaining terms in Eq. (4.3) are constant. Equating Eq. (4.4) and (4.7) results in the following equation

$$X_{qu}(D_e/U) = 0.018(D_e/h) \quad (4.8)$$

knowing that X_{qu} is a constant for a particular nozzle and fuel type, Eq.(4.8), therefore, reveals that $h \propto U$, which is the same as the correlation of Kalghtagi (1984). However, the other methods represented by Eq. (4.5) (e.g. X_{tb1}) and Eq. (4.6) (e.g. X_{tb2}), which rely less on empirical data, have poor agreement with the present flame liftoff data, as illustrated in Fig. 4.44. The foregoing indicates that the laminar flamelet extinction theory of Peters and Williams (1983) gives about the same scale of liftoff height as the experimental data of the present study. However, it falls short of predicting the right liftoff height trend. This demonstrates that the theory of Peters and Williams (1983) is not fully developed to account for the liftoff height and, therefore, cannot in its present form be used as a stabilization mechanism of a jet diffusion flame. This is what led to the development of the triple flame concept by Peters (2000) in which the flame base is partially-premixed; however, this theory still needs additional experimental/empirical data before it becomes fully exploitable.

4.2.1.2 Blowout, Liftoff, and Reattachment Velocities

The blowout, liftoff, and reattachment velocities of the diffusion methane flame issuing from the five different nozzles tested in the present study are summarized in Table 4.10. The flame stability limits are determined by the liftoff and blowout velocities. The lower flame stability limit is the velocity at which the flame lifts off the nozzle exit; whereas the blowout velocity is the upper stability limit at which the flame ceases to exist. Liftoff is attained only when the flame completely detaches from the nozzle exit. Note that the liftoff velocity is achieved by gradually increasing the fuel jet exit velocity until the flame lifts off the nozzle exit. The blowout velocity, on the other hand, is attained by gradually increasing the jet exit velocity of the already lifted flame until the flame blows out or ceases to exist, whereas the reattachment velocity is the velocity at which the lifted flame suddenly re-attaches itself to the nozzle. The reattachment velocity is achieved by gradually reducing the exit velocity of the lifted flame until the flame re-attaches again to the nozzle. It is worth mentioning that each measurement was repeated at least three time for each set conditions to ensure the repeatability and hence the reliability of the data. An order of magnitude of the variability of these measurements is reported in Table 4.10. As shown in Table 4.10, the flame blowout velocity of the rectangular nozzle is the highest, followed by the contracted circular nozzle, the squarer nozzle, the triangular nozzle, and the pipe which has the lowest. This indicates that the rectangular nozzle has the highest flame stability limit compared to all other nozzles tested here. However, the surprising result concerns the triangular nozzle which is found to have a lower blowout velocity than the contracted circular nozzle. An attempt to explain this unexpected finding is provided below in the discussion section.

Table 4.10: Blowout, liftoff, and reattachment velocities for different nozzle geometries without sudden expansion and no co-flow

Nozzle geometry	Pipe	Contracted circular	Rectangle	Triangle	Square
Blowout velocity (m/s)	69.3	81.1	90.3	73.4	80.1
Liftoff velocity (m/s)	18.0	24.7	27.0	19.5	24.2
Reattachment velocity (m/s)	6.3	6.8	6.9	7.1	6.5

The flame liftoff velocity, on the other hand, is found different for all the nozzle's geometries. The rectangular nozzle has the highest liftoff velocity followed by the contracted circular, the square, the triangular, and lastly the pipe, with the lowest value. However, the behaviour of the flame during transition from attached to lifted is very similar for all the tested nozzles except for the pipe. For all nozzles with the exception of the pipe, shortly before the occurrence of the liftoff, sort of "holes" are formed in the flame front which tends to completely disconnect the "neck" of the flame from the rest of the flame. Figures 4.45(a) to (c) illustrates the evolution of the jet diffusion flame from attached to lifted. Figure 4.45(a) shows the pipe's flame during transition from attached to a lifted flame while Fig. 4.45(b) to (c) present that of the rectangular nozzle, which is also representative of the flame liftoff event of all the other nozzles (i.e. asymmetric, including the contracted circular, nozzles). Figures 4.45(b) to (c) show the holes that are formed during transition to liftoff for all these nozzles except the pipe. However, for the pipe, the flame during transition has no such holes as it lifts cleanly from the exit plane of the nozzle and stabilizes at a new height above the nozzle exit plane. This finding is consistent with those of Langman *et al.* (2007) and Coats and Zhao (1989) who both investigated lifted flame from a pipe and a contracted circular nozzle. Nevertheless, the initial stabilization height which corresponds to the onset of liftoff is very similar for all nozzles except the triangular nozzle and pipe. For all nozzles, except the triangular nozzle and pipe, the lifted flame stabilizes at a height of about 10 nozzle diameters above the nozzle exit. In fact, there are different explanations in the open literature that purportedly clarify the liftoff process (transition from anchored to lifted flame). For example, Coats and Zhao (1989) showed that the liftoff is initiated as a result of invasion of the initial laminar flame base by turbulence that originates from the gaseous fuel jet. For the pipe nozzle, Coats and Zhao (1989) reported that the pipe's flame liftoff height is approached when the initial laminar base of the flame is invaded directly by the pipe's core flow turbulence. However, for the contoured (i.e. contracted circular) nozzle, the corresponding flame liftoff height approaches when holes develop in the flame sheet as a result of selective quenching of the diffusion flame at the point of interference between the inner gaseous jet's high frequency vortices and the flame front (Eickhoff *et al.*, 1984). According to Coats and Zhao (1989), as the holes appear, the part of the flame, which is still attached to the nozzle, becomes increasingly more turbulent until the flame finally lifts off the nozzle.

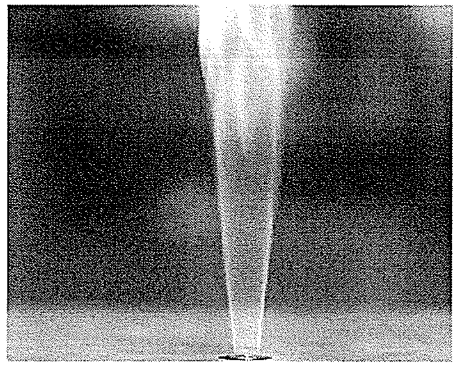

Figure 4.45(a): Attached pipe flame during transition to lifted flame.

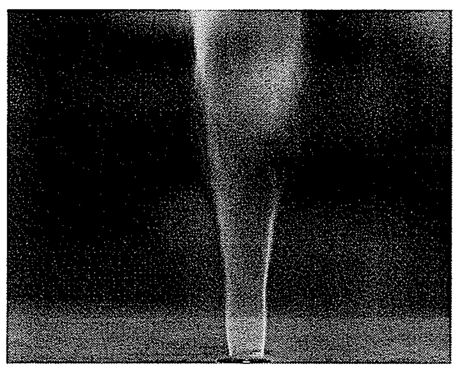

Figure 4.45(b): Attached rectangular nozzle jet flame before transition to lifted flame.

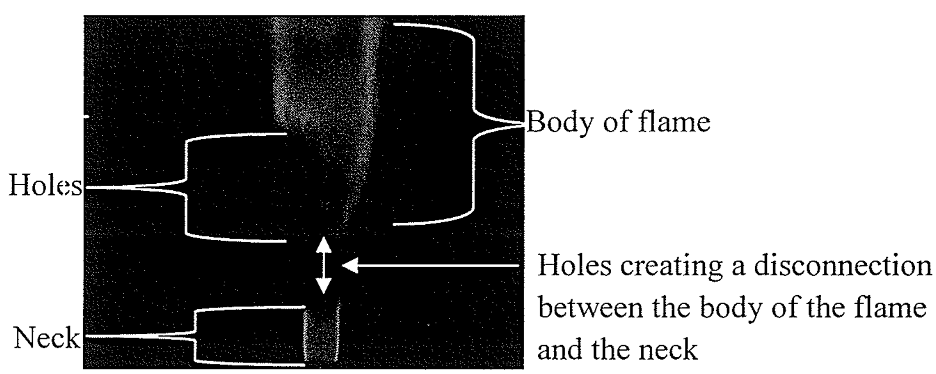

Figure 4.45(c): Attached rectangular nozzle jet flame during transition to lifted flame

Consequently, the transition from attached to lifted flame is fairly similar for all the nozzles (except the pipe) as they have similar velocity profiles, near top-hat shape in the near-field (Iyogun and Birouk, 2009a). There is a so-called "necking" and holes present in the flame sheet before the onset of liftoff for all the nozzles except for the pipe's flame (See Figures 4.45(a) through (c)). In addition, the appearance of "holes" seems to reduce the damping effect of the flame on the growth of the vortical structures in the jet shear- layer zone. As breakdown of vortices increases, the part of the flame below its neck becomes increasingly more turbulent until liftoff is initiated. However, the conclusions of Gollahalli *et al.* (1986) and Takahashi *et al.* (1984) regarding the factors responsible for the flame liftoff are not completely in line with those of Scholefield and Garside (1949), Coats and Zhao (1989), and Eickoff *et al.* (1984). However, it has not been confirmed in the present study if molecular diffusion is primarily responsible for the liftoff process according to Gollahalli *et al.* (1986). Scholefield and Garside (1949) reported that diffusion, heat release, and velocity profiles could all be key factors. On the other hand, the present study reveals that turbulence and flow structures are very likely to have an effect. The influence of the growth/reduction of organized vortical structures as the jet exit velocity is increased could explain why the flame issuing from nozzles characterised by nearly a top-hat velocity profile have different liftoff velocities. In addition, the influence of the turbulence profiles in the center region of the pipe could be responsible for the lowest liftoff velocity of the pipe which is similar to the findings of Coats and Zhao (1989) and Langman *et al.* (2007). Nevertheless, the flame base is seen to be located away from the shear-layer zones. This, in fact, seems to corroborate the findings of Gollahalli *et al.* (1986) and Takahashi *et al.* (1984) that the flame base is laminar at liftoff. However, the conclusion of Gollahalli *et al.* (1986) concerning the mechanism of liftoff does not address the differences in the liftoff velocity of the various nozzles used in the present study. The explanation of Eickhoff *et al.* (1984) might be appropriate for this apparent liftoff velocity differences. For example, local extinction regarded as holes in the flame front, according to Eichkoff *et al.* (1984), might be caused by the interference of the vortical structures with the flame front in which significant heat release could be diffused by the small-scale turbulence structures. This explanation of Eichkoff *et al.* (1984) also seems to make sense as holes are absent in the pipe jet flame during transition to liftoff.

The liftoff velocity for the contracted circular nozzle in the present study is slightly different from that of Gollahalli *et al.* (1986) who found a liftoff velocity of 29.0 m/s for a contoured nozzle with a diameter of 5.53 mm. However, the present flame liftoff velocities of the pipe and contracted circular nozzle are in good agreement with the findings of Coats and Zhao (1989) who reported 18 m/s and 24 m/s, respectively, for a 6 mm in diameter tube and a contracted circular nozzle, as well as with those of Langman *et al.* (2007) who reported 28 ± 0.8 m/s and 20 ± 0.6 m/s for a 5 mm diameter contracted circular nozzle and pipe, respectively.

The reattachment velocity, on the other hand, is nearly identical, within experimental errors, for all the tested nozzles, as shown in Table 4.10. This finding seems to be in line with the conclusion of Gollahalli *et al.* (1986), that the reattachment process is governed primarily by the dynamics of the organized structures for nozzles which have uniform velocity profiles at the exit. Consequently, the flame reattachment velocity is not significantly influenced by the nozzle geometry except the pipe which has a distinct velocity profile at the nozzle exit. Subsequently, from Table 4.10, it appears that the higher the growth of the organized structures of the shear layer, the higher the reattachment velocity. In addition, the reattachment velocities are significantly lower than the liftoff velocities for all the tested nozzles (see Table 4.10). This finding of hysteresis is consistent with the hysteresis phenomenon observed by Coats and Zhao (1989) and Gollahalli *et al.* (1986). Consequently, asymmetry of the nozzle does not seem to have an influence on the hysteresis.

4.2.1.3 Discussion

Why does a jet diffusion flame issuing from asymmetric nozzles have lower liftoff heights and largely higher blowout velocities compared to their conventional circular counterparts? In this section, experimental data of turbulent non- reacting air jet presented in section 4.1.1 are used to shed light on issues surrounding this question. In fact, non-reacting air jet is used instead of jet flame to measure the axial mean-velocity and turbulence profiles for two exit velocities which represent the two distinct liftoff regions, which are shown in Fig. 4.42. It is more economical to use air, although combustion may alter the free jet characteristics. However, a non-reacting turbulent free jet has been shown to still give a good trend and representation of the flow dynamics in the presence of chemical reactions (Gollahalli *et al.*, 1986; Gutmark and Co-workers, 1989a, 1989b, 1991; Langman *et al.*, 2007).

The streamwise centreline mean velocity decay and jet half-velocity width of the non-reacting free turbulent air jet presented earlier gives a good representation of the entrainment rates of the nozzles used. Consequently, the results are believed to be indicative of how stable the flame produced would be. The streamwise centreline mean velocity decay and jet half-velocity width of the non-reacting free turbulent air jet at an exit velocity of 30 m/s shown in Fig. 4.2 and 4.3 show that, in general, the asymmetric nozzles have higher centerline mean velocity decay and jet half-velocity width compared to the circular nozzles counterparts. This is in accordance with published reports (see, for example, Gutmark and Co-workers, 1989a, 1989b, 1991; Mi *et al.*, 2000; Quinn, 2005) in which it was observed that asymmetric nozzles induce higher streamwise centerline mean velocity decay rate compared to their axisymmetric counterparts. These higher rates of the streamwise centerline mean velocity decay and jet half-velocity width of the asymmetric nozzles is an indication of increased entrainment and jet spreading, which in turn are an indication of improved mixing. These figures also show that at an exit velocity of 30 m/s, the triangular nozzle has the highest rates of entrainment and spreading followed by the rectangular nozzle with the pipe having the lowest near-field centerline mean-velocity decay and spreading rates. Figure 4.5(a) and 4.5(b) also reflect the same scenario. Figures 4.21 and 4.23 which compared, respectively, the centerline velocity decay and jet half-velocity width at an exit velocity of 30 m/s with those at 65 m/s showed that the streamwise centerline mean velocity decay of all nozzles decrease as the jet exit velocity increases from 30 m/s to 65 m/s. The difference in entrainment might be a factor why we have two distinct liftoff regions for the rectangular and triangular nozzle. Note that the jet half-velocity width shown in Fig. 4.23 and 4.24 for the 30 m/s and 65 m/s jets mirrors the effect of exit velocity on the streamwise centerline mean velocity decay for all nozzles except for the rectangular nozzle where the reverse is the case. That is for the rectangular jet as the exit velocity increases the jet half-velocity width in the major plane increases especially in the far-field. The phenomenon of axis switching is responsible for this 'anomaly' and it appears exit velocities also affect the onset or frequencies of axis switching. Consequently, axis switching might be responsible for the two liftoff trends observed for the rectangular and triangular nozzle. Quinn (2005) showed that axis switching takes place at x/D_e = 3 and 30 for the triangular jet. This earlier occurrence of axis switching for the triangular jet compared to its location for the rectangular jet (Quinn, 1995) may explain the two distinct liftoff regions shown in Fig. 4.42. That is, the rectangular nozzle's liftoff height is lower than that of the triangular nozzle in the second liftoff region (i.e. $U > 48$ m/s) but the inverse scenario happens in the first liftoff region (i.e. $U < 43$ m/s). In addition, by comparing the near-field centerline mean-velocity decay trend of the contracted circular and pipe jets, at an exit velocity of 30 m/s, with their corresponding liftoff heights, it can be seen that they generally do correlate. That is, the two jets exhibit almost similar lift-off height as they have nearly identical near-field centreline mean-velocity decay. In brief, the above discussion leads to believe that the flame liftoff height, as shown in Fig. 4.42, may be governed primarily by local mixing rate, which is indicated by the streamwise centerline mean velocity decay and jet spreading rates.

From the blowout results shown in Table 4.10 and the entrainment and spreading rates discussions above, it can be concluded that the blowout is not only influenced by streamwise centerline mean velocity decay but it is also affected by other factors. For example, the jet entrainment results show that the near-field centerline mean-velocity decay of the contracted circular nozzle is lower than most nozzles tested here but its blowout is only second to the rectangular nozzle. In fact, there have been several attempts in the literature aimed at understanding the blowout mechanism. For example, some studies reported that flame front instabilities play a significant role in the blowout process. The kind of instabilities and how they affect blowout process have not yet been investigated thoroughly. The work of Dahm and Mayman (1990) identifies two distinct mechanisms which are responsible for liftoff and blowout. They emphasize that the extinction theory of Peters (1983) governs the liftoff process while local molecular mixing rate is the mechanism that determines the blowout. However, this mechanism of blowout reported by Dahm and Mayman (1990) seems to contradict the findings of Langman *et al.* (2007), which concluded that the mixing rate of the pipe is higher than that of the contracted circular nozzle. Consequently, based on the conclusion of Langman *et al.* (2007)

and the findings of Dahm and Mayman (1990) (i.e. local mixing rate governs blowout); the blowout of the pipe should be higher than that of the contracted circular nozzle which is, however, not the case. It has to be acknowledged that while Langman *et al.* (2007) refers to global molecular mixing rate, Dahm and Mayman (1990) calls it local molecular mixing rate which could possibly resolve the apparent contradiction. Consequently, if the molecular mixing rates of the various nozzles used in the present study would have been measured, they might have reinforced the authenticity of the blowout mechanism of Dahm and Mayman (1990). Nonethless, the present findings overall seem to support the assertion of Dahm and Mayman (1990) that the local molecular mixing rates primarily govern the blowout phenomenon, despite the fact that the present non-reacting jet flow data do not have a perfect correlation with the measured blowout velocities for the different nozzles tested here. It has to be acknowledged that the only nozzles whose flame blowout velocity has no good correlation with the non-reacting flow entrainment rates are the triangular and the contracted circular nozzles. Nevertheless, their turbulence profiles in the shear-layer zones of the jet far-field may give a hint on the near and far-field mixing and hence provide additional credence to the local molecular mixing rate mechanism of Dahm and Mayman (1990). In addition, these profiles may show the importance of organized structures in determining the blowout velocity. Figures 4.8(a) and 4.8(b) which presented the radial profiles of the turbulence intensities, u/U_{cl} and v/U_{cl}, respectively, at an exit velocity of 30 m/s taken at x = 2 mm, clearly show that in the shear-layer zones where the u/U_{cl} and v/U_{cl} are the highest, the triangular nozzle has the highest turbulence intensity whereas the pipe and the contracted circular nozzle have identical turbulence intensities, which are the lowest. This shows that the higher near-field entrainment and mixing of the asymmetric nozzles compared to their circular counterparts may be due to their higher turbulence intensity level at the mixing layer. Consequently, higher mixing rate implies lower liftoff height which is generally the case for the asymmetric nozzles. The trend shown by these results indicate that the higher the shear layer turbulence intensity, the higher the growth rate of streamwise vortices which increases the rate of the formation of a combustible mixture closer to the nozzle exit.

4.2.2 Effect of Sudden Expansion (Quarl) on Flame Stability

Using the same nozzle geometries in Section 4.2.1, the effect of quarl on the flame liftoff height as well as the liftoff, blowout, and reattachment velocities are presented and discussed. Note again that the discussion that follows after the presentations of flame stability characteristics is based on the corresponding non-reacting jet flow's mean and turbulent velocities profiles already discussed above in Section 4.2.1.

4.2.2.1 Effect of Quarl on the Liftoff Height

Figure 4.46 presents the flame liftoff height as a function of the jet exit velocity for five different nozzles with quarl. This figure shows that the flame liftoff height of each nozzle increases with the jet exit velocity in accordance with published findings (Kalghatgi, 1984; Peters and Williams, 1983; Iyogun and Birouk, 2008). Furthermore, this figure shows clearly that the asymmetrical nozzles with quarl have flame liftoff heights lower than those of the pipe and the contracted circular nozzle. The rectangular nozzle with quarl has the lowest flame liftoff height for jet exit velocities greater than approximately 43 m/s, followed by the triangle nozzle with quarl while the pipe with quarl has the highest flame liftoff height. In addition, the square nozzle with quarl has relatively lower flame liftoff height when compared to their circular counterparts with quarl. Apart from the axisymmetric nozzles (i.e., pipe and contracted circular) and the square nozzle, which display overall a linear relationship with the jet exit velocity, the triangle and rectangle nozzles with quarl exhibit two distinct liftoff regions. In the region which spans up to an exit velocity of about 43 m/s, the flame liftoff height of the rectangular nozzle with sudden expansion shows almost unchanged liftoff height as the exit velocity increases, whereas the triangular nozzle exhibits only a slight increase. However, in the second region (i.e. for U approximately >47 m/s for the rectangle and U approximately >42 m/s for the triangle), both flame liftoff heights of the rectangular and triangular nozzles increase linearly with the jet exit velocity where the rectangular nozzle has the lowest flame liftoff height. An attempt to discuss these scenarios is provided in the discussion subsection below.

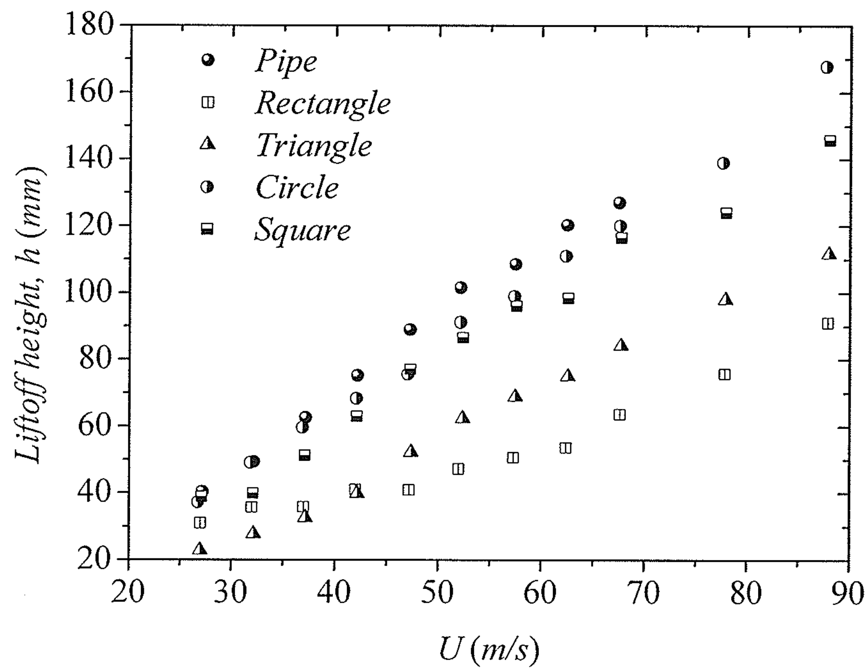

Figure 4.46: Flame liftoff height of different nozzle geometries with quarl.

Figure 4.47 compares the flame liftoff height of each nozzle with and without quarl (sudden expansion). Note that the results of these nozzles without quarl are reported above. From this figure, it is apparent that quarl reduces the flame liftoff height for all the different nozzles geometries tested in the present study. However, overall the effect of quarl is more pronounced for the flame issuing from the asymmetric nozzles as compared to their circular counterparts. Furthermore, the two flame liftoff distinct regions which occur with triangular and rectangular nozzles without quarl become even marked in the presence of quarl.

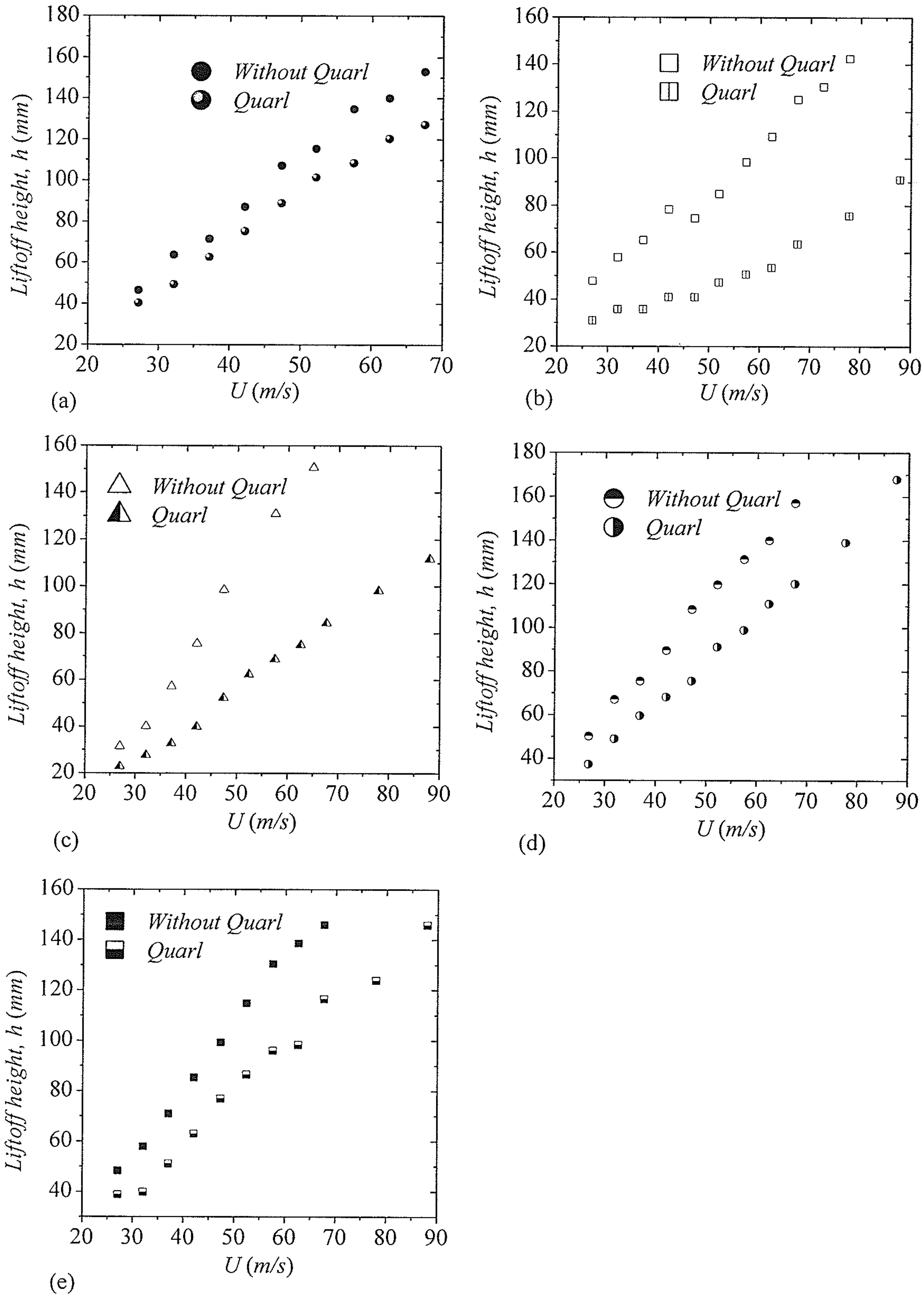

Figure 4.47: Comparison of the flame liftoff height between the various nozzles geometries with and without quarl- (a) Pipe, (b) Rectangle, (c) Triangle, (d) Circle, and (e) Square.

4.2.2.2 Effect of Quarl on the Blowout, Liftoff, and Reattachment Velocities

The turbulent diffusion jet flame's liftoff, reattachment and blowout velocities for the five different nozzles with and without sudden expansion are reported in Table 4.11. Note that the data for the five nozzles without quarl are presented and discussed above, and their usage here is strictly for comparison purposes. The lifted flame stability limits are determined by the liftoff and blowout velocities. The liftoff velocity, blowout velocity, and reattachment velocity are already defined in Section 4.2.1.2. The measurements of the liftoff, blowout, and reattachment velocities are repeated several times for each nozzle geometry configuration to ensure the repeatability and hence reliability of their values.

Table 4.11 illustrates that for the nozzle geometries with quarl configuration, the flame blowout velocity of the rectangular nozzle is the highest followed by the triangular nozzle, the square nozzle, the contracted circular nozzle, and the pipe has the lowest. The data indicate that the flame issuing from the rectangular nozzle with quarl has the highest upper stability limit compared to all other nozzle's geometries. Indeed, as indicated in Table 4.11, the use of sudden expansion (quarl) results in an increase in the blowout velocity for all nozzle geometries tested here. However, the increase in the flame blowout velocity is more significant for the asymmetric nozzles compared to their axisymmetric counterparts (pipe and contracted circular). For example, the quarl results in an increase of 74% in flame blowout velocity for the triangle nozzle, and 45% increase for the rectangle, 36% for the square nozzle. Whereas, there is only around 14 % and 13% increase for the contracted circular nozzle and pipe, respectively. Another important observation is the correlation between the blowout velocity and the far-field liftoff height, as presented in Fig. 4.46 and 4.47. That is, the higher the far-field liftoff height, the lower the blowout velocity and vice versa. Further discussion of the effect of sudden expansion based on the corresponding non-reacting jet velocity profiles is provided in the discussion section.

Table 4.11: Blowout, liftoff, and reattachment velocities of the different nozzle geometries with and without quarl

Nozzle Geometries	Blowout Velocity	Liftoff Velocity	Reattachment Velocity
Pipe with quarl	78.4	10.2	8.5
Pipe without quarl	69.3	18	6.3
Rectangle with quarl	131.2	20.9	6.8
Rectangle without quarl	90.3	27	6.9
Triangle with quarl	127.8	14.6	7.5
Triangle without quarl	73.4	19.5	7.1
Contracted circular with quarl	92.6	18.5	15.3
Contracted circular without quarl	81.1	24.7	6.8
Square with quarl	109.5	19.8	13
Square without quarl	80.7	24.2	6.5

On the other hand, the quarl affects differently the flame liftoff and blowout velocities. That is, for each nozzle the flame blowout velocity increases, whereas the flame liftoff velocity decreases. However, likewise without quarl, the rectangle nozzle with quarl still has the highest flame liftoff velocity, and the pipe with quarl maintains the lowest flame liftoff velocity. Furthermore, the order of the flame liftoff velocity with respect to the different nozzles geometries with quarl differs from that of the same nozzles without quarl. For example, the contracted circular nozzle without sudden expansion has the second highest flame liftoff velocity, whereas the same nozzle with sudden expansion has the third highest flame liftoff velocity. However, the contracted circular and square nozzles have nearly identical flame liftoff velocities, as the difference is within the experimental uncertainties. The behavior of the flame at transition from attached to lifted flame (e.g., a flame issued from a sudden expanded nozzle) is very similar for all nozzles except for the pipe. This is also true for flames issuing from similar nozzles but without quarl presented earlier. Note also that the flame issuing from a nozzle with sudden expansion anchors to the quarl exit not to the nozzle exit plane as shown in Fig. 4.48(a) to 4.48(e).

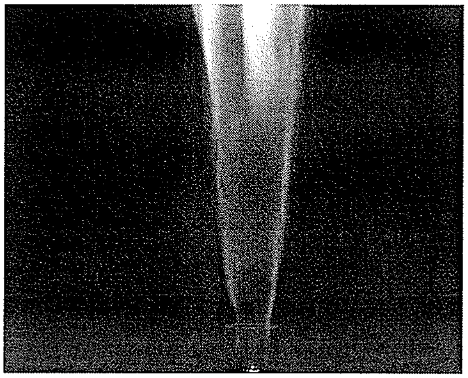

(a)

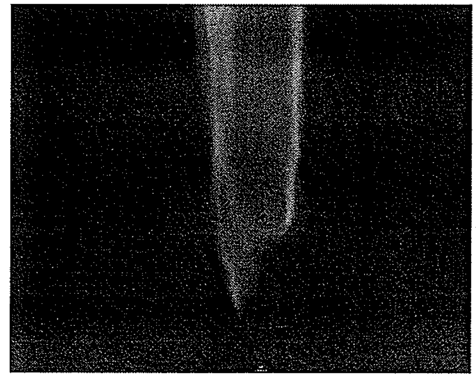

(b)

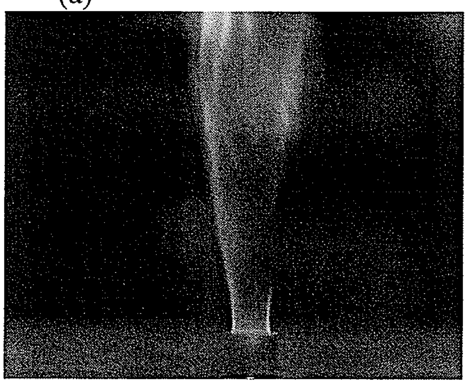

(c)

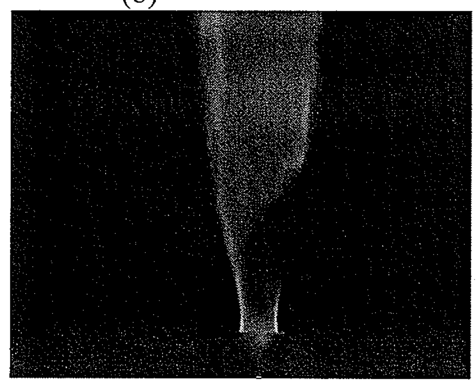

(d)

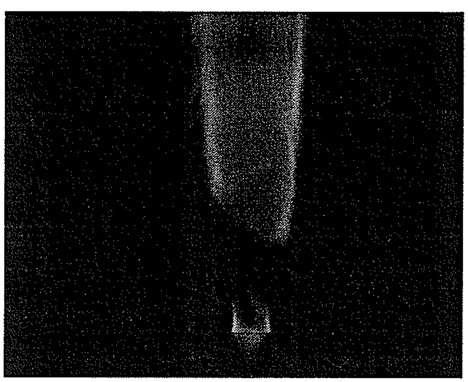

(e)

Figure 4.48: (a) transition of pipe (with quarl) flame from attached to lifted, (b) lifted pipe (with quarl) flame, (c) Onset of "necking or holes" in the flame zone from the rectangular nozzle with quarl, (d) holes developing in a rectangular nozzle (with quarl) flame, and (e) rectangular nozzle (with quarl) flame's transition from attached to lifted.

Figures 4.48(a)-4.48(b) show the liftoff event/sequence of the flame issuing from the pipe with quarl. Figure 4.48(a) shows that during transition to liftoff, the flame anchored to the quarl exit flashes back into the pipe mouth. It is found that the flashback phenomenon does not happen for the rest of the nozzles. Figure 4.48(b) shows the lifted flame from the pipe. Figures 4.48(c) to 4.48(e) present the evolution of the flame liftoff issuing from the rectangular nozzle with quarl, which is chosen as a typical representation of all asymmetric nozzles (including the contacted circular nozzle). Figure 4.48(c) is an illustration of the "necking" which takes place whereby the neck of the flame becomes increasingly thinner. Figure 4.48(d) shows the onset of "holes" within the flame sheet as the liftoff is gradually approached. Figure 4.48(e) shows the transition to lifted flame, during which the formed holes within the flame sheet tend to disconnect the upper flame from its neck. However, there are no such holes within the flame being lifted from a pipe with quarl. Several attempts were made in the literature to clarify the liftoff process of flames issuing from axisymmetric nozzles (such as pipe without quarl). For example, it was reported that the liftoff initiates as a result of the invasion of the initial laminar flame base by turbulence which is a characteristics of gaseous jet (Coats and Zhao, 1989). In the present experiment, it is found that, for any nozzle geometry, the liftoff velocity is reduced as a result of sudden expansion. The non-reacting jet results above demonstrated that, regardless of the nozzle geometry, quarl increases the turbulence intensities compared with the same geometry without quarl. This increase in the turbulence intensity induced by quarl appears to lift the flame from the quarl exit quicker compared to the same flame ensuing from the same nozzle without sudden expansion (see Fig. 4.47 and Table 4.11). Coats and Zhao (1989) mentioned that the flame liftoff from a pipe (no sudden expansion is used in their study) initiates when the initial laminar base of the flame is invaded directly by the pipe's jet flow turbulence. As shown in Iyogun and Birouk

(2009a), the higher core turbulence in the pipe jet (which is higher than that of all the nozzles tested), which is further increased by the presence of quarl, could be the reason why the flame issuing from the pipe has the lowest liftoff velocity for both cases with and without quarl configuration. This occurs particularly in the very near field at $x = 2$ mm as reported in Section 4.1.1.5. However, for the contoured (i.e. contracted circular) nozzle, its liftoff takes place when holes develop in the flame sheet as a result of selective quenching of the diffusion flame at the point of interference between the inner gaseous jet high frequency vortices and the flame front (see Eickhoff *et al.*, 1984). According to Coats and Zhao (1989), as the holes appear, part of the flame, which still attaches to the nozzle, becomes increasingly more turbulent until the flame completely lifts from the nozzle exit plane. Accordingly, except for the pipe's flame, the transition from attached to lifted flame is fairly similar for all the nozzles having identical streamwise mean-velocity profiles (i.e. top-hat shape) both for the quarl and the no-quarl configuration. In fact, except for the pipe, for all the other nozzles there is necking involved before liftoff, which is followed by the appearance of holes that seem to reduce the damping effect of the flame on the growth of the vortical structures in the jet shear layer. As breakdown of vortices increases, the flame below the neck of the flame becomes increasingly more turbulent and hence more susceptible to liftoff. In addition, local extinction regarded as holes in the flame front, according to Eichkoff *et al.* (1984), is believed to result from interference of the vortical structures with the flame due to excessive heat diffusion by the small-scale turbulence structures. This explanation of Eichkoff *et al.* (1984) seems to make a sense, as holes are absent in the pipe jet flame during its transition from anchored to lifted.

The reattachment velocity with quarl, which is presented in Table 4.11, is lower than its corresponding liftoff velocity without quarl. This finding of hysteresis is consistent with the hysteresis phenomenon reported in the literature (see, for example, Coats and Zhao, 1989; Gollahalli *et al.*, 1986). However, the reattachment velocities of the flame issuing from a nozzle with quarl are, in general, higher than their corresponding no-quarl configurations. This finding generally implies that the quarl does affect (although only slightly) hysteresis by increasing the reattachment velocity. However, earlier explanation for nozzles without sudden expansion defies the effect of the quarl. Nonetheless, it appears that the alteration of the velocity profile by the presence of the quarl, in the near field, is probably responsible for the change in the reattachment velocity. The only consistent finding from Table 4.11 concerning the reattachment process is that the two nozzles with the lowest liftoff height are those with the lowest reattachment velocities. Nevertheless, the trend of the liftoff velocity for the nozzles with quarl does not give any hint to help understanding the reattachment process. Therefore, additional work may be required to find further evidence.

4.2.2.3 Discussion

One may ask the question why asymmetric nozzles with quarl produce flames with lower liftoff heights and higher blowout velocities compared with their corresponding geometries without quarl. In an attempt to shed light on these issues, the non-reacting turbulent free air jet mean velocity and turbulence profiles measured and discussed above are highlighted.

The streamwise centreline mean velocity decay at exit velocities of 30 m/s and 65 m/s for the different nozzle geometries with and without quarl presented in section 4.12(a) shows that the presence of quarl increases the streamwise centerline mean velocity decay which translates into a significant decrease in the flame liftoff height, as shown in Fig. 4.47. Consequently, this indicates that the presence of quarl enhances further the mixing which in turn results in a lower flame liftoff height compared to their corresponding geometry without quarl. It supports the finding of Kalghatgi (1984) that the base of a lifted jet diffusion flame is mainly premixed. However, it was also discussed in section 4.1.2.1 that the quarl's impact is more pronounced for the streamwise centreline mean velocity decay of the jets issuing from the rectangular and triangular nozzles. Consequently, these two nozzle geometries have a more pronounced quarl effect.

Section 4.1.2.4 shows the effect of quarl on the turbulence intensity (u/U_{cl}) at the near-field for the free air jet exit velocities of 30 m/s and 65 m/s. That is, for each nozzle, the presence of quarl considerably increases the turbulence intensity which serves to increase the local rate of molecular mixing. Note that the increased turbulence is also a good indicator of the growth rate of streamwise vortices (Ho and Gutmark, 1989). Consequently, as the molecular mixing is increased, the liftoff height is reduced. It can also be seen from the same figure that the increase in turbulence is more pronounced for the asymmetric nozzles, which is why they have a marked lower flame liftoff height compared with their circular counterparts.

According to Table 4.11, the effect of quarl is generally seen to increase the blowout velocity for each nozzle flame. Consequently, the significant high local rate of molecular mixing (especially in the far-field, as indicated by the jet velocity decay profiles) induced by the quarl is believed to be responsible for the increase in the flame blowout velocity and hence the flame upper stability limit. However, the same trend is not observed for the same nozzles geometries without quarl. This is mainly due to the inability of the asymmetric nozzles without quarl to significantly increase the rate of molecular mixing in the far-field compared to those of their circular counterparts. However, the addition of the quarl appears to increase significantly the rate of mixing due to an increase in the growth rate of the streamwise vortices. Consequently, this assertion supports the work of Dahm and Mayman (1990) which identifies the local molecular mixing rate as the mechanism that governs the blowout process.

4.2.3 Effect of Swirling/Non-Swirling Air Co-flow and Nozzle Geometry on Flame Stability

Blowout and liftoff velocities as well as the liftoff height and length of a swirling non-premixed methane jet flame issuing from rectangular nozzle (also called RN) and contracted circular nozzle (also called CCN) are presented below. The aim was to examine the effect of the central nozzle geometry in conjunction with the co-flow swirl intensity. The effect of nozzle asymmetry on these elements of stability of a swirling or non-swirling (zero-swirl) flame is discussed using the LDV measurements of the reacting flow velocity profiles along the nozzle's centerline plane.

4.2.3.1 Flame Length

Flame length was taken to be the maximum height of the visible flame from the nozzle exit. Figures 4.49(a) and 4.49(b) present the flame length versus the gas fuel (jet/nozzle) exit velocity. The comparison made in each of these two figures is between two different nozzle's geometries (i.e, rectangular nozzle and contracted circular nozzle) for two typical co-flow exit velocities and swirl strengths. In Fig. 4.49(a) the flame length for the two nozzles is plotted for the same co-flow exit velocity (U_a = 0.58 m/s) and the same swirl strength (S = 0). In the same figure, the contracted circular nozzle flame length is also compared between two different swirl strengths (S = 0 and 1.15). In Fig. 4.49(b), the flame length of the two nozzles is presented for the same co-flow swirl strength (S = 1.15) and exit velocity (U_a = 3.02 m/s). The data presented in these figures show that the rectangular nozzle flame has a shorter flame length compared to the contracted circular nozzle flame for identical test conditions. Overall the difference in the flame length between the two fuel nozzles becomes more apparent at higher co-flow momentum (i.e. inlet velocity) and stronger swirl number, S = 1.15, as shown in Fig. 4.49(b). In addition, Fig. 4.49(a) shows that there is no significant difference in the flame length of the contracted circular nozzle as the co-flow swirl strength changes from 0 to 1.15 at low exit velocity, i.e. U_a = 0.58 m/s. However, comparing Fig. 4.49(a) with 4.49(b), for the same co-flow swirl number S = 1.15, reveals that as the co-flow exit velocity U_a increases to 3.02 m/s, the flame length decreases. These observations show that the flame length is also influenced by the fuel nozzle geometry in addition to both the co-flow exit velocity and swirl strength (i.e. increase in co-flow tangential velocity). These figures show that on average the flame length does not exhibit a very clear dependence on the central exit velocity (at least with the range tested here), as the flame length seems to fluctuate around an average height/length. However, the flame length does seem to depend on the nozzle geometry at least for the present conditions presented in Fig. 4.49. These findings at first seem to be in contradiction with those of Al-Abdeli and Masri (2007) who showed that as U_j increases flame length increases accordingly. Al-Abdeli and Masri (2007) attributed this increase in the flame length to increased jet momentum, as they quoted that this is 'less surprising'. In fact, Al-Abdeli and Masri (2007) obtained flame length for only two distinct fuel jet exit velocities, i.e. U_j = 40 m/s and 60 m/s, which might not be sufficient enough to make this categorical conclusion.

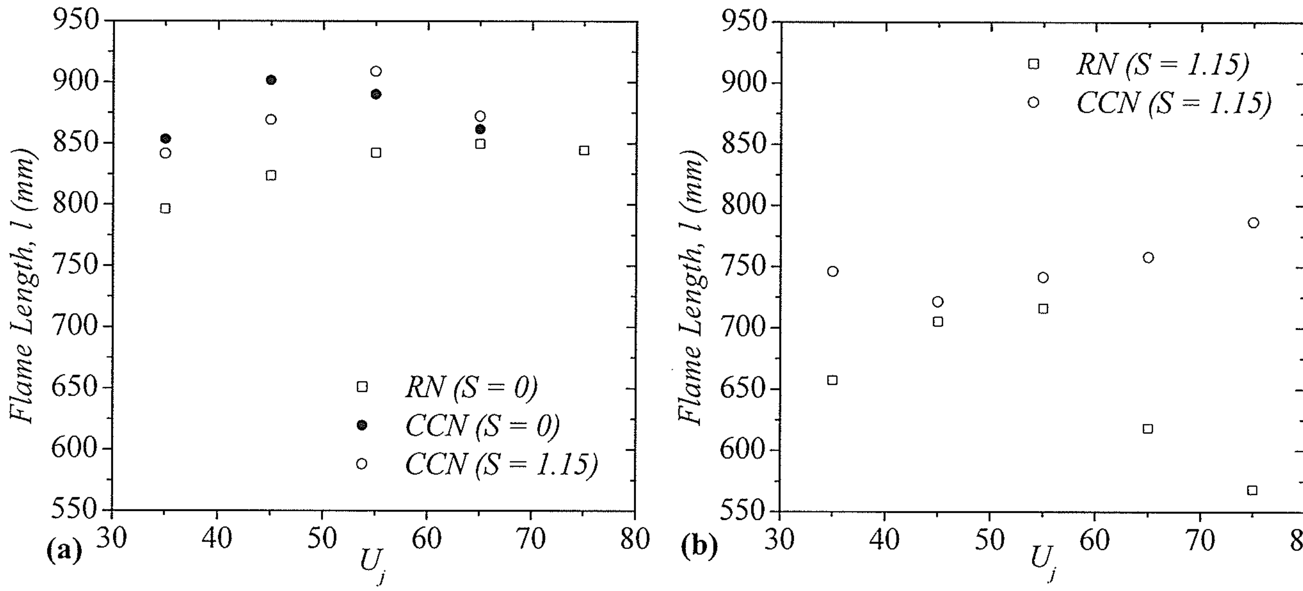

Figure 4.49: Comparison of the flame length of rectangular nozzle and contracted circular nozzle nozzles- (a) contracted circular nozzle flame (U_a = 0.58 m/s and S = 0); contracted circular nozzle flame (U_a = 0.58 m/s and S = 1.15); and rectangular nozzle flame (U_a = 0.58 m/s and S = 0), (b) contracted circular nozzle and rectangular nozzle flame (U_a = 3.02 m/s and S = 1.15).

However, concerning the influence of U_a on the flame length, Al-Abdeli and Masri (2007) suggested that as U_a increases, a stronger rate of flow recirculation takes place which thereby causes higher entrainment of the central jet. As a result of this higher entrainment, the central jet exit velocity decays faster thereby making the flame shorter. Al-Abdeli and Masri (2007) also suggested that other factors that could be responsible for the shorter flame length might be the transition to unsteady behavior or the breakdown of vortices. After careful analysis of LDV data, Al-Abdeli and Masri (2007) found that along with U_a, the most likely cause of the change in flame length is the transition into unsteady behaviour. They found that the start of the decrease in flame length as well as the overall increase in flame stability coincides with the transition to unsteady behavior. The swirl number before the transition to unsteady behavior was found to be highly dependent on U_a but not on U_j. Nevertheless, Syred and Beer (1974) attributed the reason why flames exposed to a co-flow with high swirl strength above 0.6 becomes more stable, to the ability of the high swirl co-flow to induce a toroidal recirculation zone which acts as a heat reservoir thereby contribute to recirculating hot products. Recently published results showed that the rectangular nozzle induces larger and stronger turbulence structures than the contracted circular nozzle (Iyogun and Birouk, 2009a). This may explain why the flame length decreases in Fig. 4.49(b) compared to Fig. 4.49(a). It is believed that the enhanced entrainment and mixing close to the rectangular nozzle exit with the intensification of the swirl strength resulted in a shorter rectangular nozzle flame compared to that of the contracted circular nozzle which induces less turbulence structures close to the exit. In conclusion, it is clear that the effect of fuel nozzle geometry does have a noticeable influence on the flame length especially when the co-flow swirl strength becomes relatively significant.

4.2.3.2 Liftoff Height

Figures 4.50(a) and 4.50(b) show, respectively, the liftoff heights of the rectangular nozzle and contracted circular nozzle flames for the cases with no co-flow and with a weak co-flow (i.e., U_a = 0.58 m/s and S = 0). These two figures show that the liftoff height of the rectangular nozzle flame is lower than that of the contracted circular nozzle flame for the same test conditions. This apparent decrease in the flame liftoff associated with the nozzle geometry is attributed to the significant increase in entrainment and mixing induced by the rectangular nozzle (Iyogun and Birouk, 2008, 2009a). These two figures, however, show that there is no significant difference in the flame liftoff height with and without a weak co-flow (i.e. U_a = 0.58 m/s) regardless of the nozzle geometry. This observation is an indication that the jet momentum is the driving factor in determining the flame liftoff as the weak co-flow does not seem to exercise any impact.

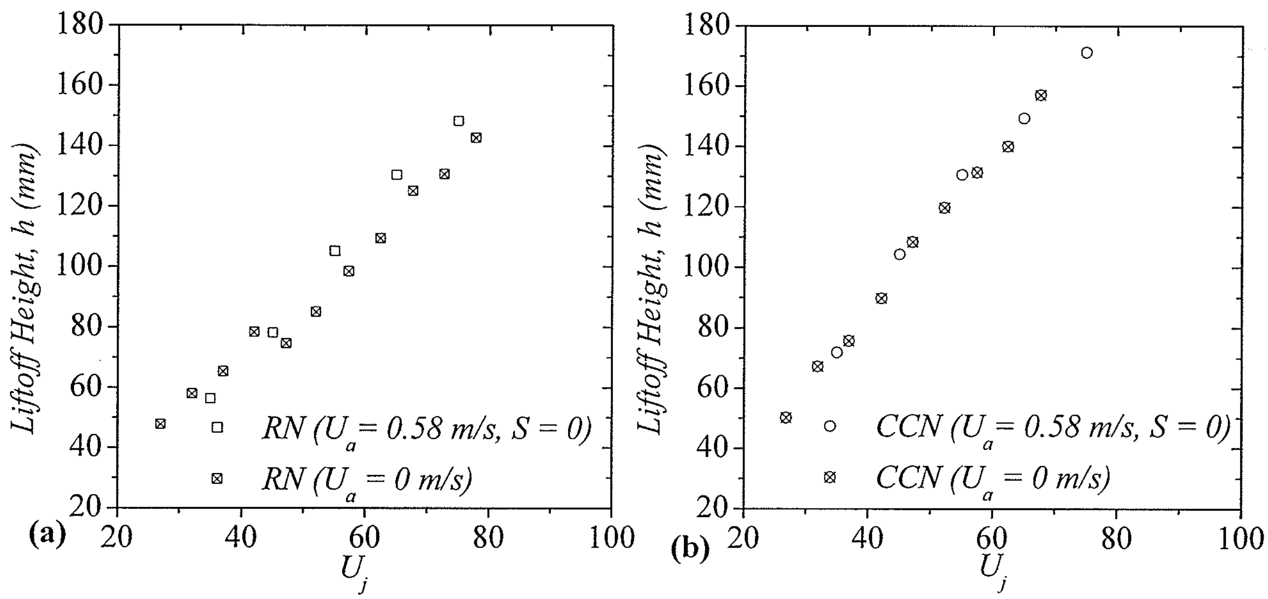

Figure 4.50: Comparison of the flame liftoff height with and without co-flow of (a) rectangular nozzle flame and (b) contracted circular nozzle flame.

Figure 4.51(a) presents the flame liftoff for both rectangular nozzle and contracted circular nozzle for the same co-flow velocity as in Fig. 4.50 but with a stronger tangential velocity component (as indicated by the swirl strength, S = 1.15). Figure 4.51(b) presents the flame liftoff for both rectangular nozzle and contracted circular nozzle for the same co-flow swirl strength as in Fig. 4.51(a), (S = 1.15), but with a relatively stronger co-flow exit velocity. Figure 4.51(a) reveals that overall the swirl strength has an effect on the flame liftoff though still weak. However, as the co-flow inlet velocity is increased from U_a = 0.58 m/s to 2.65 m/s, the flame liftoff height decreases considerably, as revealed in Fig. 4.51(b). Therefore, two important remarks might be drawn from the foregoing. Firstly, the co-flow swirl strength becomes more influential only when the co-flow momentum becomes relatively significant with respect to the jet (flow issuing from the nozzle) momentum. Secondly, the rectangular nozzle nozzle's flame has exhibited always shorter liftoff height compared to that of the contracted circular nozzle for the same test conditions; though the difference in the liftoff heights between the two flame nozzles seem to become more apparent with stronger co-flow swirl strength. This is an indication that the rectangular nozzle still has a better entrainment compared with the contracted circular nozzle under these conditions of the swirling co-flow. In conclusion, the fuel nozzle geometry seems to have a significant role on the liftoff height of swirling non-premixed flame.

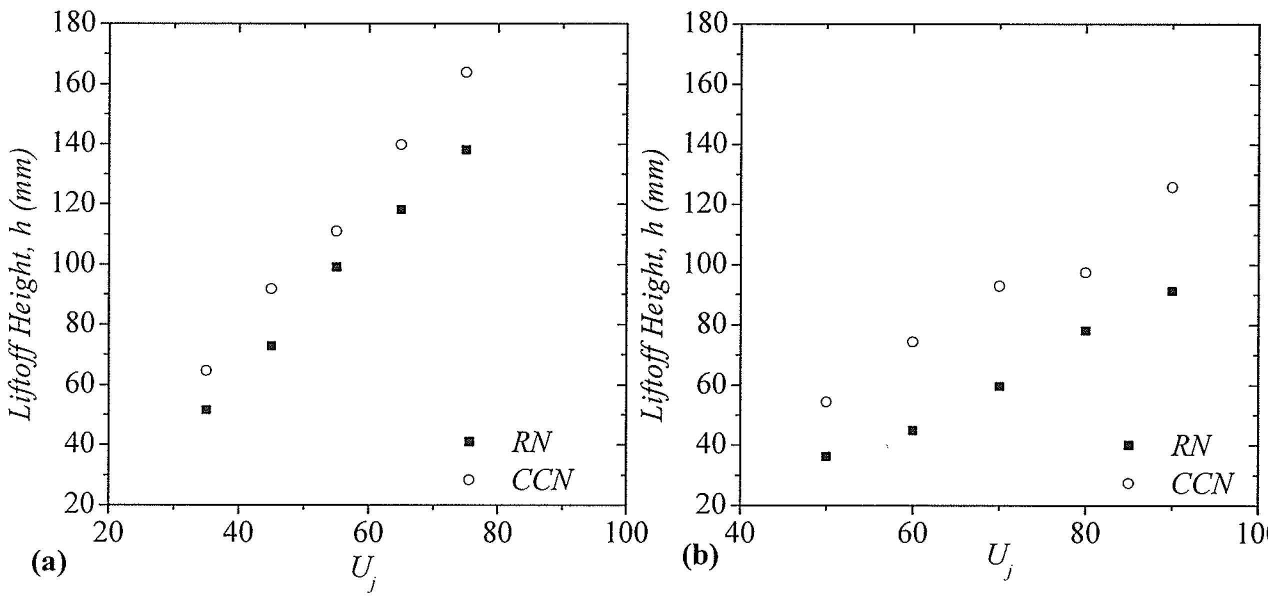

Figure 4.51: Comparison of the liftoff height between the rectangular nozzle and contracted circular nozzle flames- (a) $U_a = 0.58$ m/s and $S = 1.15$, (b) $U_a = 2.65$ m/s and $S = 1.15$.

4.2.3.3 Blowout Velocity

Flame blowout was determined visually. The earlier definition of "blowout" is also used here. It is obtained by fixing the nozzle geometry, and co-flow exit velocity and swirl strength, and then gradually increasing the jet exit velocity until the flame blows off as a lifted or as an attached flame. Figure 4.52 presents a map of the non-premixed methane flame blowout velocity, for both contracted circular nozzle and the rectangular nozzle nozzles, versus the co-flow exit velocity for different co-flow swirl strength. Figures 4.52(a) and (b) show that, for swirl strength in the range up to 0.31 (i.e., vane angles in the range between 0° and 25°), the blowout of the lifted non-premixed methane flame decreases slightly as the co-flow exit velocity, U_a, increases from around 0.58 m/s up to around 2 m/s, as shown in Fig. 4.52(a) and 4.52(b). However, further increase in the co-flow exit velocity, say around 2.5 m/s, the flame blows out as an attached flame at relatively very low jet exit velocities. In addition, Fig. 4.52(a) and 4.52(b) show that the blowoff velocity of the attached flame is similar in value for both the contracted circular nozzle and rectangular nozzle in the range of the co-flow exit velocity, U_a, employed here, which are in accordance with the observations reported by Wierzba and Oladipo (1994) for an attached axisymmetric flame. However, for co-flow exit velocity ranging below 3 m/s, the blow out velocity of the rectangular nozzle flame is relatively higher for both swirl strengths (i.e., $S = 0$ and 0.31). It is also important to mention here that the flame blowout trend observed in Fig. 4.52(a) is similar to that of Fig. 4.52(b) indicating that weak swirl strength would not really play any additional role when compared to zero-swirl co-flow, which is in accordance with the findings of Al-Abdeli and Masri (2007).

However, Fig. 4.52(c) and 4.52(d) show that for swirl strength between 0.80 and 1.15 (i.e. for vanes angle of 50° and 60°, respectively), the flame remains always lifted before it blows off for both nozzles. In addition, these figures show that, for the co-flow exit velocity U_a in the range between 0.58 m/s and 1.5 m/s, the flame blowout velocity decreases slightly especially for the contracted circular nozzle. Note that the maximum co-flow exit velocity which could be attained with the present experimental set-up was U_a = 4.56 m/s. The same figure reveals also that the flame blowout velocity increases as the co-flow swirl strength increases from S = 0.80 to 1.15 especially at high co-flow exit velocities. For example, for a co-flow exit velocity U_a = 3 m/s, the 60° swirling rectangular nozzle flame still does not blow out even by increasing the jet flowrate (fuel) to its maximum attained value in the present study (i.e., U_j = 137 m/s), whereas the 50° swirling rectangular nozzle flame blows out at about 130 m/s. More importantly these figures reveal that the blowout velocity of the swirling non-premixed methane flame is increased remarkably for the rectangular nozzle in comparison with its counterpart contracted circular nozzle.

In summary, Fig. 4.52 demonstrates that the blow out limit of swirling non-premixed methane flame increases with the rectangular nozzle (Iyogun and Birouk, 2008, 2009b). That is, the rectangular nozzle flame still has a higher blowout limit than the contracted circular nozzle even in the presence of a swirling co-airflow. It is also shown that the blowout limit of the rectangular nozzle flame can be further increased by increasing the co-flow swirl strength. It is believed that the increase in blowout as a result of using co-flow with high swirl number in conjunction with rectangular nozzle is caused by the high rate of mixing induced by large scales generated by both the swirler and the asymmetrical nozzle (i.e. the flat sides of the rectangular nozzle orifice), and the small scales generated by the asymmetric nozzle (at the corners).

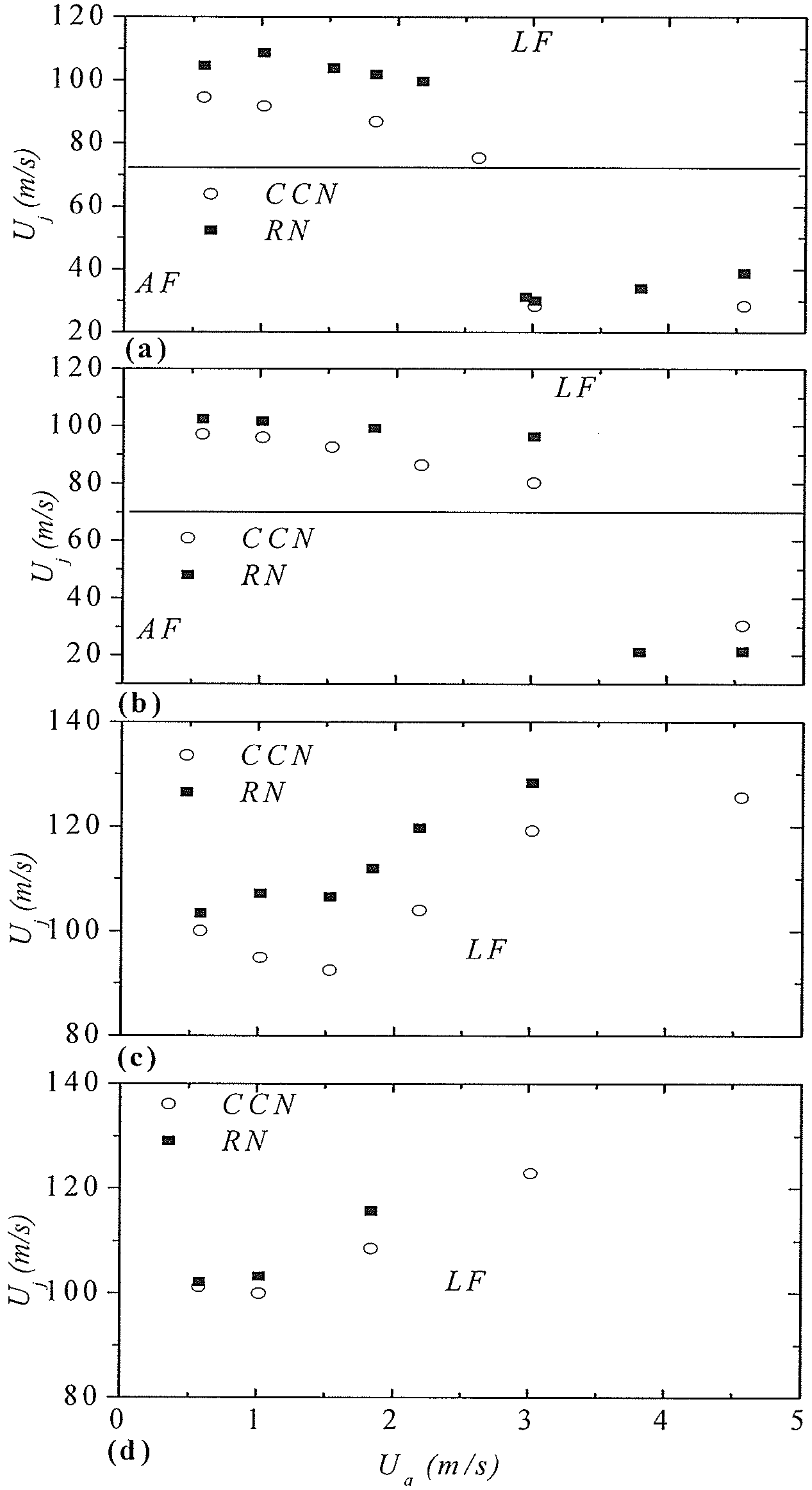

Figure 4.52: Comparison of the blowout of lifted and attached rectangular nozzle and contracted circular nozzle flames for various degrees of swirl- (a) 0° ($S = 0$), (b) 25° ($S = 0.31$), (c) 50° ($S = 0.79$), and (d) 60° ($S = 1.15$) vane angles. LF and AF denote lifted and attached flame, respectively.

4.2.3.4 Liftoff Velocity

The liftoff velocity is measured visually by slightly increasing the (central/nozzle) jet exit velocity, while keeping all other parameters (e.g. nozzle geometry and, co-flow exit velocity and swirl strength) fixed, until the flame detaches completely from the nozzle. Figure 4.53 presents the flame lift-off velocity as a function of the co-flow exit velocity for the contracted circular nozzle and rectangular nozzle nozzles for various swirl numbers/strengths. It is important to mention here that the flame lift-off velocity corresponds to the jet exit velocity at which the flame lifts off. One can notice that the trends displayed in these figures are similar to those observed in Fig. 4.52 for the flame blow-out velocity. Figures 4.53(a) and 4.53(b) show that, for both nozzle geometries, the flame lift-off velocity decreases as the co-flow exit velocity increases for a swirl number ranging up to 0.31 (i.e., swirler vane angles ranging between 0° and 25°). While the lift-off velocity of the same flame increases with the co-flow exit velocity for a swirl number ranging from 0.80 up to 1.15 (i.e. swirler vanes angle of 50° and 60°, respectively), as shown in Fig. 4.53(c) and 4.53(d). The flame lift-off velocity increases with the co-flow exit velocity at relatively high swirl numbers (i.e., swirler vanes angle of 50° and 60°) can be attributed to the flow reversal/recirculation which would occur at sufficiently high swirl numbers (e.g., Lefebvre, 1983; Aref and Gollahalli, 1990; Mathur and Maccallum, 1967). For instance, Mathur and Maccallum (1967) reported that a flow with a swirler having vane angles of 45° and greater would induce reverse velocity (i.e. recirculation), which increases in strength as the vanes angle increases. The flow reversal, therefore, makes it increasingly difficult for the flame base to lift off from the nozzle as a result of increasing toroidal vortex. More importantly these figures show that contrary to the blow-out scenario, the lift-off velocity of the contracted circular nozzle flame is generally greater than that of the rectangular nozzle flame regardless of the co-airflow swirl strength. The stability theory proposed in (Vanquickenborne and Van Tiggelen, 1966) which suggests that a lifted diffusion flame is stabilized when the turbulent burning velocity is identical to the local flow mean-velocity, and the assertion of Coats and Zhao (1989) that liftoff is initiated as a result of invasion of the initial laminar flame base by turbulence that is present in the gaseous fuel jet could possibly explain why the lift-off velocity of the contracted circular nozzle flame is higher than that of the rectangular nozzle flame. In other words, the increase in the jet turbulence in the near-field and higher rate of jet decay (which will be shown in the next section of the paper) as a result of using an asymmetric nozzle (i.e. rectangular nozzle) instead of contracted circular nozzle could explain why the lift-off velocity of the rectangular nozzle flame is generally lower than that of the contracted circular nozzle flame.

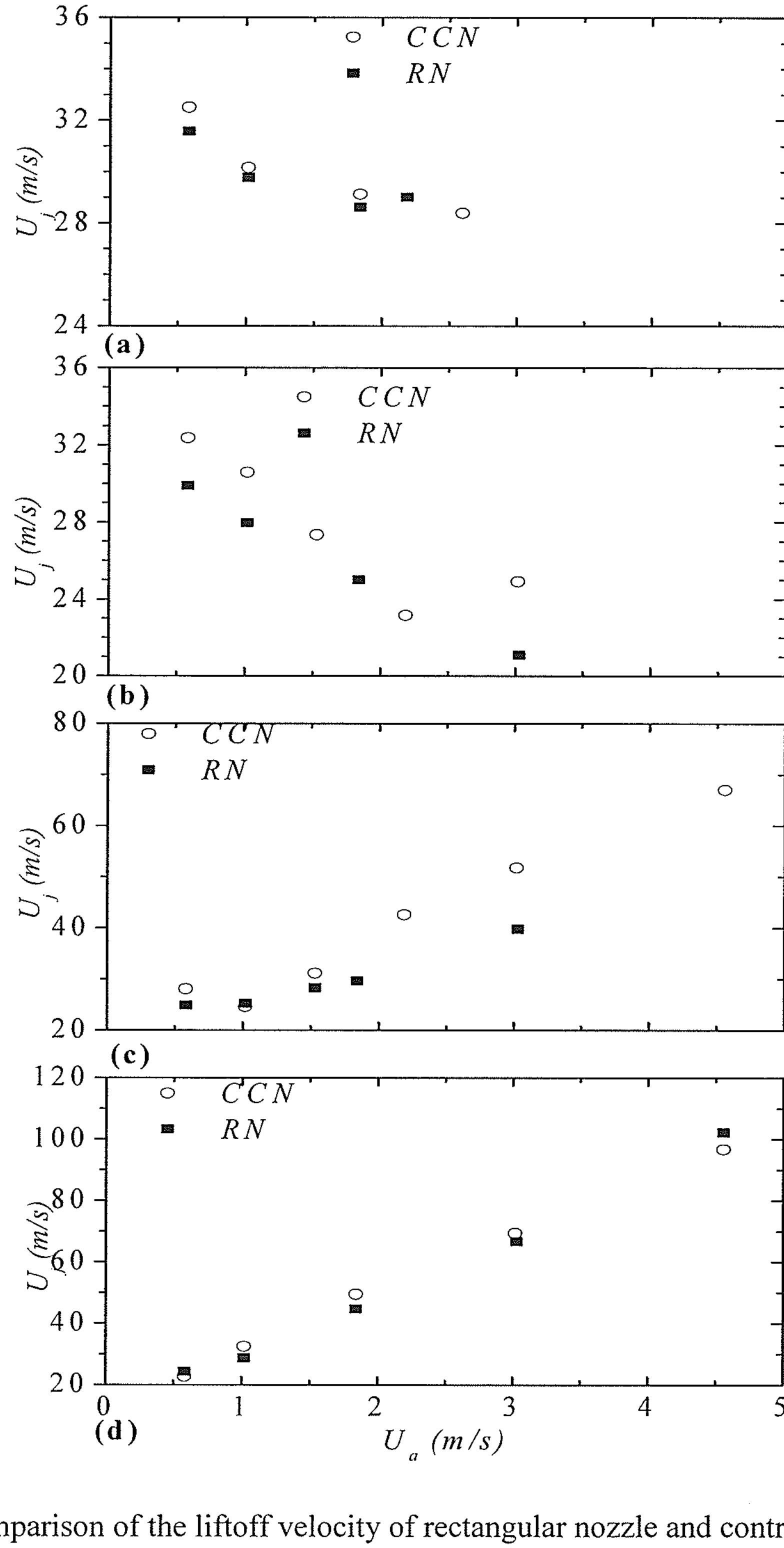

Figure 4.53: Comparison of the liftoff velocity of rectangular nozzle and contracted circular nozzle flames for various swirler vane angles- (a) 0° (S = 0), (b) 25° (S = 0.31), (c) 50° (S = 0.79), and (d) 60° (S = 1.15).

4.2.3.5 LDV Measurements

The LDV measurements of the reacting flow were undertaken as an attempt to help in explaining the flame blowout, flame length, and liftoff phenomena. These measurements were taken at two distinct typical test conditions: U_j = 20 m/s and U_a = 1.84 m/s, and U_j = 60 m/s and U_a = 3.02 m/s. All measurements were limited to two swirl numbers: S = 0 and 1.15. Figure 4.54 shows the normalized streamwise mean velocity profile, U/U_{cl}, of the rectangular nozzle flame across the central radial plane at a jet exit velocity of 20 m/s and co-airflow with an exit velocity of 1.84 m/s at three typical streamwise locations, x/D_e = 5, 10, and 15. The velocity U is the mean-velocity at any radial flow location and U_{cl} is the centerline mean-velocity. Figure 4.55 presents the corresponding mean turbulence intensity profiles (i.e. u/U_{cl}) at the same streamwise locations. Figure 4.54 shows that in the near-field (i.e. x/D_e = 5), the 60° swirling flame has a negative U/U_{cl} and reaches a minimum at the interface between the co-flow and the methane jet flow. This is caused by the high swirl strength which causes recirculation according to Mathur and Maccallum (1967), thereby making the momentum of the core jet flow weaker. This recirculation is an indication of higher entrainment of the core jet flame with the surrounding ambient (i.e. co-airflow). The higher entrainment, which is induced by the stronger swirl, is more apparent at farther streamwise locations (i.e., at x/D_e = 10 and 15). It can be seen that at these downstream flow locations the 60° swirling rectangular nozzle flame spreads faster than its zero-swirling flame counterpart. This is why flame blowout increases for the 60° swirling RN flame while both flame liftoff height and length decrease. It also helps to explain why the liftoff velocity of the 60° swirling rectangular nozzle flame increases as the co-airflow exit velocity increases. That is, as the co-airflow exit velocity increases, the swirl strength gains momentum and hence the recirculation zone increases which prolongs the near-field flame extinction because of the weakening of the core jet momentum (e.g., Syred and Beer, 1974). Figure 4.55 shows that in the near-field (i.e. $x/D_e = 5$), the turbulence intensity of the 60° swirling rectangular nozzle flame is higher than that of the zero-swirling rectangular nozzle flame. It underscores the importance of turbulence intensity to blowout. Figure 4.55 also shows that downstream of the reacting jet, the turbulence intensity significantly increases for the 60° swirling flame compared to the zero-swirl flame. As a result, the blowout of the 60° swirling flame is increased because of the increase in both near and far-field molecular mixing caused by the increased turbulence intensities, which is consistent with the findings of Syred and Beer (1974). The Reynolds shear stresses (not shown here) also support the assertion that the high swirl number causes an increase in molecular mixing in the far-field. As a result of this increase, the blowout for the 60° swirling flame is much higher than that of the 0° counterpart. This assertion is further supported by the streamwise centerline mean-velocity decay, $U_{x/De\ =5}/U_{cl}$ shown in Table 4.12. The first and maximum streamwise mean-velocity at this test condition was obtained at $x/D_e = 5$. This figure (Fig. 4.55) clearly re-emphasizes that the 60° swirling flame has much higher rates of entrainment compared to the 0° swirling flame which is in accordance with the findings of Syred and Beer (1974). Consequently, it seems that far-field molecular mixing is increased, leading to higher blowout velocity.

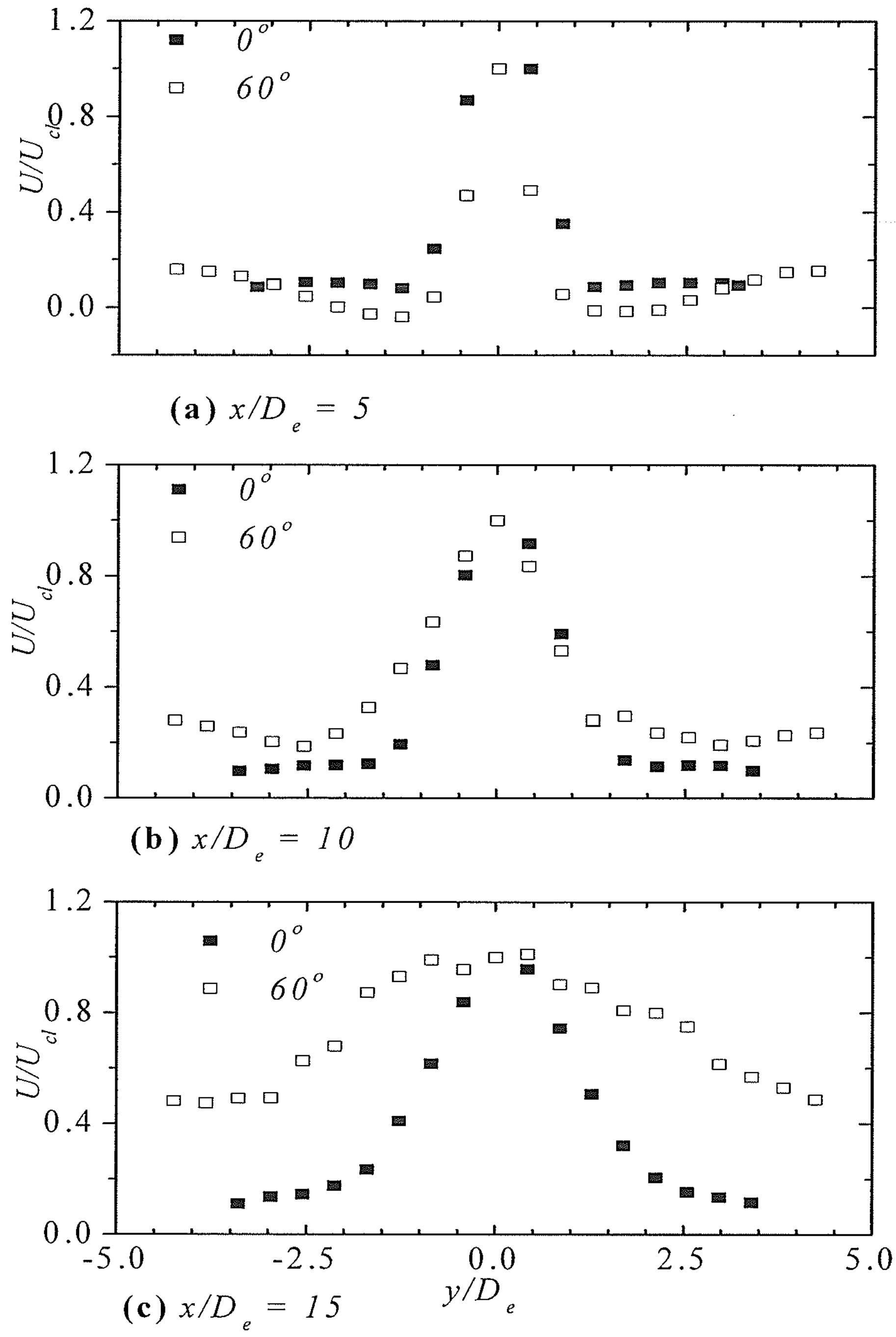

Figure 4.54: Comparison of the streamwise mean-velocity profiles of the 0° swirling and 60° swirling rectangular nozzle flame for typical exit conditions (U_j = 20 m/s, U_a = 1.84 m/s).

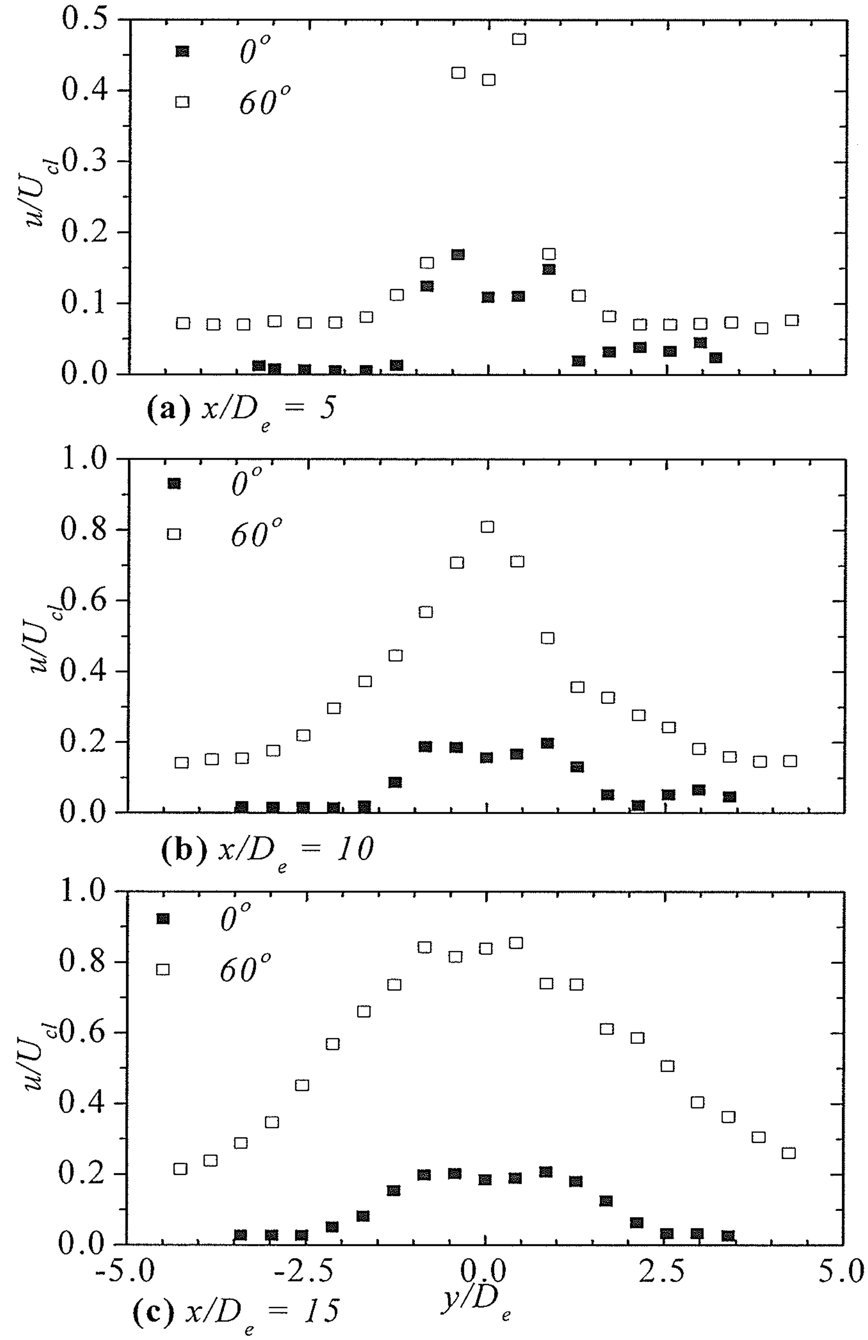

Figure 4.55: Comparison of the mean turbulence intensity radial profiles of the zero-swirling and 60° swirling rectangular nozzle flames for typical exit test conditions (U_j = 20 m/s, U_a = 1.84 m/s).

Table 4.12: Comparison of the centerline mean-velocity decay of rectangular nozzle flame for typical inlet conditions ($U_j = 20$ m/s and $U_a = 1.84$ m/s) between two different swirl strengths

0° ($S = 0$)		**60°($S = 1.15$)**	
x/D_e	$U_{@x/De=5}/Ucl$	x/D_e	$U_{@x/De=5}/Ucl$
5	1	5	1
10	1.18	10	2.50
15	1.49	15	4.73

Figure 4.56 shows a comparison of the normalized mean velocity profiles, U/U_{cl}, of the rectangular nozzle and contracted circular nozzle flames across the central radial plane for a typical jet exit velocity of 60 m/s and a co-flow exit velocity of 3.02 m/s with S =1.15. Figures 4.57 and 4.58 present the corresponding turbulence intensity and Reynolds shear stresses profiles, respectively. Only two streamwise measurement locations, x/D_e = 5 and 10 were chosen to further elucidate the reason why the blowout of the swirling rectangular nozzle flame is higher than that of the contracted circular nozzle flame, whereas the liftoff velocity, liftoff height, and flame lengths are lower for identical test conditions. It can be seen that contrary to Fig. 4.54 where negative co-flow velocities were observed as a result of the strong influence of the swirl strength, S =1.15, Fig. 4.56 shows positive mean velocity profiles across the central radial plane; because of the stronger momentum of the core jet flow (i.e. U_j = 60 m/s). Therefore, the interplay between the central (jet) and surrounding (co-flow) flows also plays a part in the liftoff phenomena as reported by Takahashi *et al.* (1996). In fact, for relatively higher co-flow exit velocities, say, U_a = 3.02 m/s with S = 1.15, the central jet exit velocity must be increased

substantially before liftoff occurs, whereas the liftoff occurs at relatively lower jet exit velocities for U_a = 1.84 m/s for the same co-flow swirl strength. However, for lower jet exit velocities, there is more tendency of reverse flow to occur because of the strong momentum of the co-airflow. This explains why the 60° swirling flame at U_a = 3.02 m/s has more tendency to flashback into the nozzle mouth which can cause damage of the burner (e.g., Tangirala *et al.*, 1987). However, at higher jet exit velocities, the flame stabilizes at the nozzle exit and further increase in the central/nozzle jet velocity eventually leads to flame liftoff. Figure 4.56 shows that at x/D_e = 10, the mean velocity of the rectangular nozzle flame is wider than that of the contracted circular nozzle counterpart. This is an indication of higher entrainment which is further supported by the turbulence intensity profiles shown in Fig. 4.57. Figure 4.57 reveals also that the turbulence mean intensity profiles of the rectangular nozzle flame show larger values than those of the contracted circular nozzle flame, especially at x/D_e = 10, which is an indication of higher molecular mixing induced by the rectangular nozzle geometry. The higher turbulence intensity of the rectangular nozzle flame also explains why its liftoff velocity is lower than that of the contracted circular nozzle flame at identical test conditions. The Reynolds shear stress profiles which are shown in Fig. 4.58 further accentuate the assertion that the rectangular nozzle has a higher rate of molecular mixing. This figure shows that the Reynolds shear stresses of the rectangular nozzle flame are overall higher than those of the contracted circular nozzle flame especially in the mid-field (i.e. x/D_e = 10). The centerline mean velocity decay, U_{max}/U_{cl} presented in Fig. 4.59 further enhances the earlier assertion of higher entrainment for the rectangular nozzle flow. U_{max} is the maximum streamwise centerline mean velocity. It is worth noting that this figure shows that the flow far-field (i.e., for x/D_e beyond around 30) exhibits no change in U_{max}/U_{cl}. Nevertheless, this figure reveals clearly that the centerline mean velocity decay of the rectangular nozzle swirling flame is significantly higher than that of the contracted circular nozzle flame. This is a good illustration of the suspected increase in mixing caused by using non-symmetric central fuel nozzle (i.e., rectangular nozzle). The enhanced mixing with the use of rectangular nozzle is believed to be due to the presence of large and small turbulent structures generated by the three-dimensional geometry of the nozzle's orifice where small structures are generated at the corners and large structures at the flat sides of the nozzle's orifice.

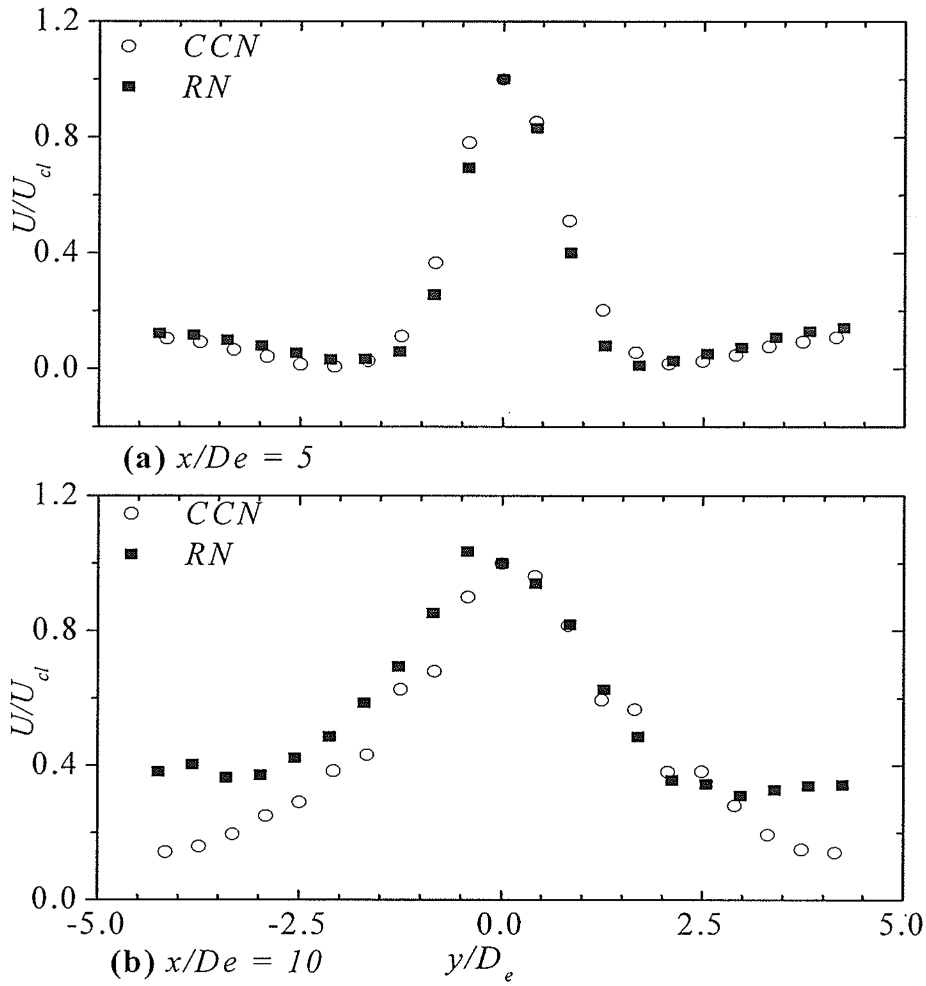

Figure 4.56: Comparison of the centerline mean-velocity radial profiles of the rectangular nozzle and contracted circular nozzle flames for typical test conditions (U_j = 60 m/s, U_a = 3.02 m/s, and S = 1.15).

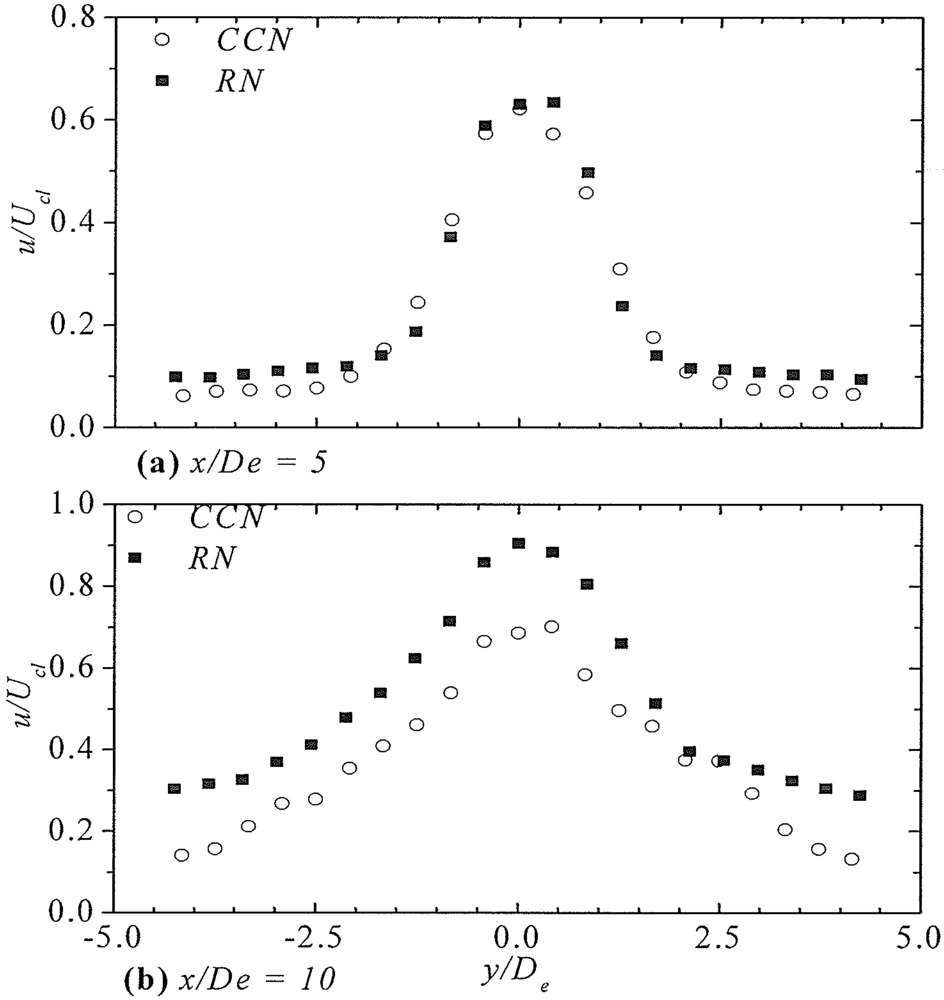

Figure 4.57: Comparison of the mean turbulence intensity radial profiles of the rectangular nozzle and contracted circular nozzle flames for typical test inlet conditions (U_j = 60 m/s, U_a = 3.02 m/s, and S = 1.15).

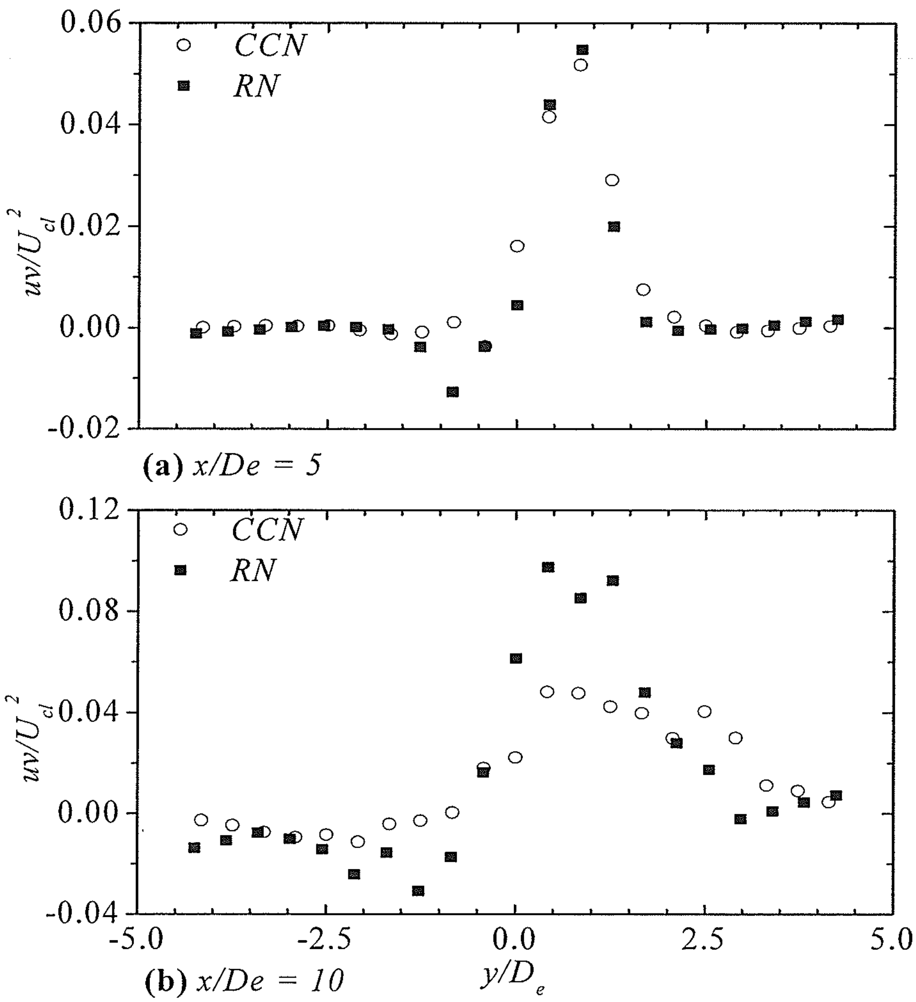

Figure 4.58: Comparison of the mean Reynolds shear stress radial profiles of the rectangular nozzle and contracted circular nozzle flame for typical test initial conditions (U_j = 60 m/s, U_a = 3.02 m/s, and S = 1.15).

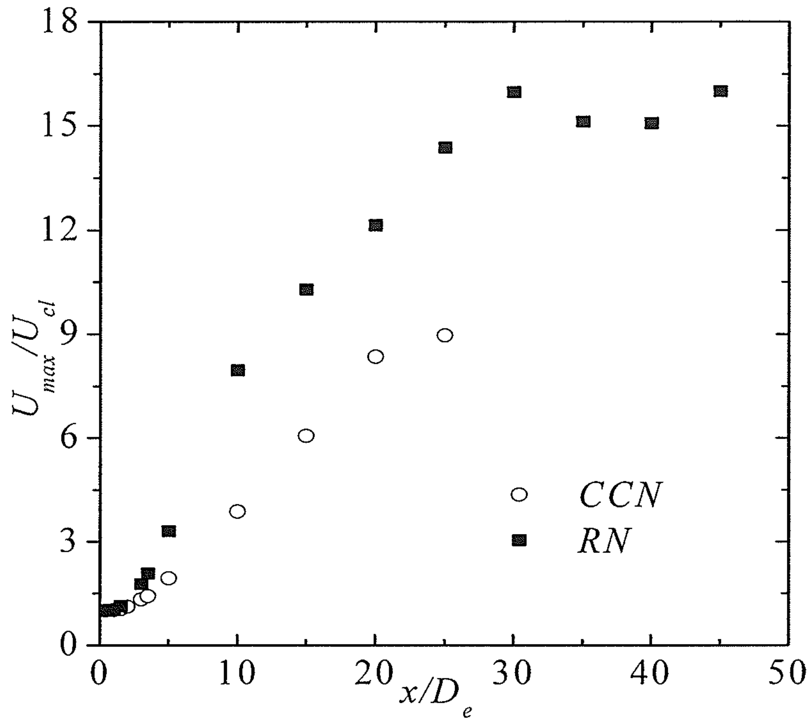

Figure 4.59: Comparison of the streamwise centerline mean-velocity decay of the rectangular nozzle and contracted circular nozzle flames for typical test conditions (U_j = 60 m/s, U_a = 3.02 m/s, and S = 1.15).

CHAPTER 5: CONCLUSIONS AND RECOMMENDATIONS

5.1 Summary and Conclusions

5.1.1 Effect of Nozzle Geometry on Entrainment and Spreading Rates of Free Turbulent Non-Reacting Jets

Five nozzles with different geometries (i.e. nozzle's orifice); a contracted circular, a square, a rectangular, a triangular, and a pipe with and without quarl were tested to study their effect on jet entrainment and spreading rates. The jet bulk exit velocity used was kept 30 m/s for all the nozzles. For the nozzle configurations without quarl (i.e. no sudden expansion was used), it was found that the jet flows issuing from asymmetric nozzles exhibited higher entrainment and jet spreading rates compared with their axisymmetric counterparts which is in agreement with published findings. Moreover, it was demonstrated here that the use of quarl further improved the jet entrainment and spreading rates compared with the nozzle configuration without quarl. The results revealed that entrainment and spreading rates of jets issuing from the triangular and rectangular nozzles were more affected by the presence of quarl compared with the other nozzles (i.e. contracted circular and square), while the contracted circular nozzle was only mildly affected. This higher entrainment from these geometries with quarl is attributed to the strong counter-rotating vortices which are believed to be produced as a result of the sudden expansion brought about by the quarl. The improved entrainment and spreading rates of the asymmetric nozzles without quarl which becomes even higher with quarl are also seen to be directly related to the increased level of turbulence. Overall, it is found that the triangular nozzle without quarl exhibits the highest rate of entrainment and spreading while the rectangular nozzle with quarl has the highest rate of entrainment.

5.1.2 Effect of Exit Velocity on the Entrainment and Spreading Rates of Free Turbulent Non-Reacting Jet Issuing from Asymmetric Nozzles

The same nozzle geometries described above, except the pipe, were used to examine the effect of exit velocity on the spreading and entrainment rates of the ensuing turbulent free jet. Two exit velocities i.e. 30 m/s and 65 m/s, were tested. For the nozzle configurations without sudden expansion at the same exit velocity, it was found that the jet issuing from asymmetric nozzles exhibited higher entrainment and spreading rates compared with the contracted circular nozzle, which is in accordance with previous published results. In addition, for the same nozzle configuration with and without sudden expansion, it was found that increasing the exit velocity from 30 m/s to 65 m/s reduces the rate of entrainment and spreading of the jet. This applies to all nozzle configurations examined here. Furthermore, at both exit velocities of 30 m/s and 65m/s, the present results of the nozzle geometries without sudden expansion agree with published findings, that is the triangular nozzle have higher rate of entrainment compared with that of the rectangular nozzle. However, the rectangular nozzle showed higher entrainment and spreading rates compared with the triangular nozzle with sudden expansion regardless of the exit velocity. In addition, it was found that though the jet exit velocity may not affect the decay constant of the contracted circular nozzle, it however changes its virtual origin. More importantly, varying the exit velocity altered the value of the decay constant and the virtual origins of the asymmetric nozzles. Jet entrainment and spreading was also seen to be directly correlated with the corresponding axial turbulence especially in the near-field and in the shear-layer of the jet. Reynolds stresses also correlated well with the entrainment and spreading rates. That is, the higher the turbulence in the shear-layer, the axial development of turbulence intensities, and the Reynolds shear stresses, the higher the tendency to have increased jet entrainment and spreading rates. Consequently, 30 m/s jets were seen to exhibit higher turbulence intensities and Reynolds shear stresses compared with their counterpart jets at 65 m/s.

5.1.3 Effect of Nozzle Geometry on the Stability of Turbulent Jet (Diffusion) Methane Flame

The present findings reveal that asymmetric nozzles overall, have lower flame liftoff heights than their axisymmetric counterparts. The results show that the far-field liftoff height varies linearly with the exit velocity for all the nozzles. However, the triangular and rectangular nozzles have two distinct liftoff regions separated by a transition. In the first liftoff region, the triangular nozzle has the lowest liftoff height while the rectangular nozzle has the lowest flame liftoff height in the second liftoff region. However, the rectangular nozzle is overall found to have a much lower flame liftoff height than the other nozzles. The liftoff height appears to be primarily governed by local rate of molecular mixing. The increase in molecular mixing, induced by the asymmetry of the nozzle, is believed to create a more combustible mixture closer to the nozzle exit which then helps the flame to stabilize itself closer to the nozzle exit. An attempt was made to assess the underlying theories which Kalghtagi (1984) and, Peters and Williams (1983) based their liftoff height data. It showed that only Kalghatgi's (1984) empirical correlation had good agreement with the present study. However, only one expression for correlating liftoff height prescribed by Peters and Williams (1983) agrees fairly well with the present data. Nevertheless, this agreement is due to the empirical determination of this expression and does not support the assumption of flamelet quenching being responsible for diffusion flame stabilization mechanism.

Furthermore, nozzle geometry was found to influence the blowout and liftoff velocities. The blowout is higher for the asymmetric nozzles as compared with their axisymmetric counterparts.

Conversely, the reattachment velocity is fairly similar for all nozzles, which is an indication that nozzle geometry does not significantly influence the reattachment process. On the other hand, the liftoff process is seen to be fairly similar for the nozzles with approximately top-hat velocity profile shape and different for the pipe jet with a fully developed turbulent velocity profile, meaning that the velocity profile at the nozzle exit plays a significant role in the liftoff process.

5.1.4 Effect of Nozzle's Sudden Expansion on the Stability of Turbulent Jet (Diffusion) Methane Flame

The presence of quarl at the exit of the nozzle appears to increase further the rate of mixing which results in even lower liftoff height compared with the corresponding geometry without quarl. Furthermore, the effect of quarl on the flame liftoff height is more pronounced for the asymmetric nozzles than their axisymmetric counterparts. In addition, with the exception of the very low end of the exit velocity at which the flame liftoff height is nearly constant, the liftoff height increases nearly linearly with the exit velocity for all nozzles with quarl configuration. The rectangular nozzle with and without quarl has the lowest liftoff height. It appears that an increase in mixing as a result of quarl creates a much better combustible mixture closer to the burner which could be the main reason why the flame stabilizes closer to the nozzle exit plane. Furthermore, asymmetric nozzles with quarl are found to influence further the blowout, reattachment, and liftoff velocities. It increases the blowout and reattachment velocities, whereas it decreases the liftoff velocity. The level of increase in flame blowout velocity for the asymmetric nozzles with quarl is much more significant than that of their axisymmetric counterparts. The blowout is believed to be primarily controlled by the rate of molecular mixing in the far-field of the jet. Succinctly, the most significant effect of quarl is the increase in the lifted flame stability velocity range. Therefore, the use of asymmetric nozzles with quarl seems to be very beneficial for industrial applications where a lifted flame operating within a wide stability range may be needed.

5.1.5 Effect of Swirling/Non-Swirling Co-flow and Nozzle Geometry on a Non-Premixed Methane Flame

The effect of swirling/non-swirling co-airflow on some of the stability features of a methane jet flame issuing from a rectangular and a contracted circular nozzle was also examined. The major outcome of this experimental work is that the blowout of the rectangular nozzle swirling methane diffusion flame is higher than that of the contracted circular nozzle for identical test conditions, and all the liftoff velocity, liftoff height, and flame length are lower (though not to the same extent) than those of the corresponding contracted circular nozzle flame. These observations clearly indicate that asymmetric fuel (central fuel jet) nozzle has an apparent impact on enhancing stability of swirling non-premixed flame which is in agreement with the trend of the results without swirling co-flow shown in previous sections. More importantly, the blowout of the rectangular nozzle flame seems to increase as the co-flow swirl strength increases. The LDV measurements of the reacting flow revealed that the far-field local mixing plays a prominent role in the blowout phenomena. The enhanced mixing is believed to result from the interplay between the turbulent structures induced by both the swirl strength and the asymmetric nozzle geometry. The present data showed that as swirl number/strength increases, all the turbulence intensity and Reynolds shear stress levels increase, and the streamwise mean-velocity radial profiles become wider. Also, the rectangular nozzle flame has higher turbulence levels as well as Reynolds shear stresses compared with the contracted circular nozzle flame. All the aforementioned contributed to increased rectangular nozzle swirling flame stability.

5.2 Recommendations for Further Studies

The experimental work carried out in this study provides new and helpful information about the effect of asymmetric fuel nozzles on jet mixing and hence flame stability. However, the present work needs to be extended in order to develop a more comprehensive examination on the relationship between asymmetric nozzle geometry and the ensuing reacting or non-reacting jet. The following suggestions can be made for future investigations:

- There is, for example, a need to measure the whole velocity field of the asymmetric jets with and without sudden expansion in order to completely analyze the flow dynamics. This will give a better understanding of the entire flow field and hence give a detailed radial and streamwise development of the mean velocity, turbulence intensities, and Reynolds stresses. These detailed data will also serve as data bank for validating numerical simulations.
- In addition, the sudden expansion (quarl) used which is cylindrical in shape should be varied. There is a need to see what impact changing the length as well as the diameter would have on jet entrainment and spreading rates. The shape of the sudden expansion could also be changed to assess its impact on jet characteristics (e.g. entrainment and spreading rates).
- Measuring the pollutant formation and emission in conjunction with temperature field would provide information about the relationship between fuel nozzle geometry and flame emissions.
- Burner aerodynamic (nozzle geometry) effects on the combustion performance of other types of conventional as well as renewable fuels (e.g. hydrogen and syngas) should also be examined.

REFERENCES

Ahuja, K.K. and Brown, W.H. (1989) Shear Flow Control by Mechanical Tabs, *AIAA Paper* 89-0994.

Al-Abdeli, Y.M. and Masri, A.R. (2007) Turbulent Swirling Natural Gas Flames: Stability Characteristics, Unsteady Behavior and Vortex Breakdown, *Combust. Sci. Technol.,* **179** 207-225.

Antonia, R.A., Satyaprakash, B.R., and Hussain, A.K.M.F. (1980) Measurements of Dissipation Rate and some other Characteristics of Turbulent Plane and Circular Jets, *Phys. Fluids* **23** 695-700.

Antonia, R.A. and Zhao, Q. (2001) Effect of Initial Conditions on a Circular Jet, *Exp. Fluids,* **31** 319-323.

Aref, A.A. and Gollahalli, S.R. (1995) Effects of Secondary Air Swirling on the Lift-Off and Combustion Characteristics of a Burning Jet-A Fuel Spray, *Proc. of the Emerging Energy Techn. Conf. ASME,* **66** 1-9.

Belovich, V.M., Samimy, M. and Reeder, M.F. (1996) Dual Stream Axisymmetric Mixing in the Presence of Axial Vorticity, *J. Prop. Power,* **12** 178-185.

Birouk, M. And Gupta, A.K. (2001) Structure of Lean Premixed Swirling Flames Using PLIF Imaging, *J. Flow Visualization and Image Processing,* **8** 341-353.

Boersma, B.J., Brethouwer, G., and Nieuwstadt, F.T.M. (1998) A Numerical Investigation on the Effect of the Inflow Conditions on the Self-Similar Region of a Round Jet, *Phys. Fluids,* **10** 899-909.

Boulanger, J., Vervisch, L., Reveillon, J., and Ghosal, S. (2003) Effects of Heat Release in Laminar Diffusion Flames Lifted on Round Jets, *Combust. Flame*, **134** (4), 355-368.

Broadwell, J.E., Dahm, W.J.A., and Mungal, M.G. (1984) Blowout of Turbulent Diffusion Flames, *Proc. Combust. Inst.*, **20** 303-310.

Buckmaster, J. and Weber, R. (1996) Edge-Flame Holding, *Proc. Combust. Inst.*, **26** 1143-1149.

Capp, S.P., Hussein, H.J., and George, W.K. (1990) Velocity Measurements in a High Reynolds Number Momentum-Conserving, Axisymmetric, Turbulent Jets, *Tech. Rep.,* **123,** Turbulence Research Laboratory, University at Buffalo, SUNY.

Chang, Y; Lee, H., and Tseng, H. (2007) The Formation of Incense Smoke, *J. Aerosol Science,* **38** 39-51.

Cheng, Y. S., Bechtold, W. E., Yu, C. C., and Hung, I. F. (1995) Incense Smoke: Characterization and Dynamics in Indoor Environments, *Aerosol Science and Technology,* **23** 271-281.

Chigier, N.A. and Chervinsky, A. (1967) Experimental Investigation of Swirling Vortex Motion in Jets, *J. Appl. Mech.*, **34** 443-451.

Coats, C.M. and Zhao, H. (1989) Transition and Stability of Turbulent Jet Diffusion Flames, *Proc. Combust. Inst.*, **22** 685-692.

Corrsin, S. (1943) Investigation of Flow in an Axially Symmetrical Heated Jet of Air, *NACA Wartime Report* **94.**

Corrsin, S. and Uberoi, M.S. (1949) Further Experiments on the Flow and Heat transfer in a Heated Turbulent Air Jet, *NACA TN-1865.*

Corrsin, S. and Uberoi, M.S. (1951) Spectra and Diffusion in a Round Turbulent Jet, *NACA-Report-1040.*

Corrsin, S. and Kistler, A. (1955) The Free-Stream Boundaries of Turbulent Flows, *NACA-Report-1040.*

Dahm, W.J.A. and Mayman, A.G. (1990) Blowout Limits of Turbulent Jet Diffusion Flames for Arbitrary Source Conditions, *AIAA J.,* **28**, 1157-1161.

Dold, J.W. (1989) Flame Propagation in a Nonuniform Mixture: Analysis of a Slowly Varying Triple Flame, *Combust. Flame,* **76**, 71-88.

Eickhoff, H., Lenze, B., and Leuckel, W. (1984) Experimental Investigation on the Stabilization Mechanism of Jet Diffusion Flames, *Proc. Combust. Inst.,* **20** 311-318.

Feikema, D., Chen, R.-H., and Driscoll, J.F. (1991) Blowout of Nonpremixed Flames: Maximum Coaxial Air Velocities Achievable with and without Swirl, *Combust. Flame,* **86** 347-358.

Ferdman, E., Otugen, M.V., and Kim, S. (2000) Effect of Initial Velocity Profile on the Development of Round Jets, *J. Prop. Power*, **16** 676-686.

Foss, J.K. and Zaman, K.B.M.Q. (1999) Large and Small Scale Vortical Motions in a Shear Layer Perturbed by Tabs, *J. Fluid Mech.,* **382** 307-329.

Fricker, N. and Leuckel, W. (1976) The Characteristics of Swirl Stabilized Natural Gas Flames. Part 3: The Effect of Swirl and Burner Mouth Geometry on Flame Stability, *J. Inst. Fuel,* **49** 152-158.

Gollahalli, S.R., Khana, T., and Prabhu, N. (1992) Diffusion Flames of Gas Jets Issued from Circular and Elliptic Nozzles, *Comb. Sci. Techn.,* **86**, 267-288.

Gollahalli, S.R., Savas, O., Huang, R.F., and Rodriguez-Azara, J.L. (1986) Structure of Attached and Lifted Gas Jet Flames in Hysteresis Region, *Proc. Combust. Inst*, **21** 1463-1471.

Gutmark, E., Schadow, K.C., and Wilson, K.J. (1989a) Noncircular Jet Dynamics in Supersonic Combustion, *J. Prop. Power,* **5**(5), 529-533.

Gutmark, E., Schadow, K.C., Parr, T.P., Hanson-Parr, D.M., and Wilson, K.J. (1989b) Noncircular Jets in Combustion Systems, *Exp. Fluids,* **7**, 248-258.

Gutmark, E., Schadow, K.C., and Wilson, K.J. (1989c) Subsonic and Supersonic Combustion Using Noncircular Injectors, *J. Prop. Power,* 7(2), 240-249.

Gutmark, E., Schadow, K.C., and Wilson, K.J. (1991) Subsonic and Supersonic Combustion Using Noncircular Injectors, *J. Prop. Power,* **27** (2), 240-249.

Hinze, J.O. (1959) Turbulence, New York: McGraw-Hill.

Ho, C. and Gutmark, E. (1987) Vortex Induction and Mass Entrainment in a Small-Aspect-Ratio Elliptic Jet, *J. Fluid Mech.,* **179** 383-405.

Holman, J.P. (1994) Experimental Methods for Engineers, McGraw-Hill, Inc. New York.

Hussain, F. and Husain, H. (1989) Eliiptic Jets. Part 1. Characteristics of Unexcited and Excited Jets, *J. Fluid Mech.*, **208** 257-320.

Hussein, H.J., Capp, S.P., and George, W.K. (1994) Velocity Measurements in a High-Reynolds-Number, Momentum-Conserving, Axisymmetric, Turbulent Jet, *J. Fluid Mech.*, **258** 31-75.

Hussein, A.K.M.F. and Zedan, M.F. (1978) Effects of Initial Condition on the Axisymmetric Free Shear Layer: Effects of Initial Momentum Thickness, *Phys. Fluids,* **21** 1100-1112.

Iyogun, C.O. and Birouk, M. (2008) Effect of Fuel Nozzle Geometry on the Stability of a Jet Turbulent Diffusion Methane Flame, *Combust. Sci. Technol.*, **180**, 2186-2209.

Iyogun, C.O. and Birouk, M., (2009a) Effects of Sudden Expansion on Entrainment and Spreading Rates of a Jet Issuing from Asymmetric Nozzles, *Flow, Turbulence, Combust.*, **82** 287-315.

Iyogun, C.O. and Birouk, M. (2009b) Stability of Turbulent Jet Diffusion Methane Flame Issuing from an Asymmetrical Nozzle with Sudden Expansion, *Combust. Sci. Technol.*, **181** 1-17.

Kalghatgi, G.T. (1981) Blowout Stability of Gaseous Jet Diffusion Flames, Part 1: In Still Air, *Combust. Sci. Techn.*, **26** 233-239.

Kalghatgi, G.T. (1984) Lift-Off Heights and Visible Flame Lengths of Vertical Turbulent Jet Diffusion Flames in Still Air, *Combust. Sci. Technol.*, **41**, 17-29.

Kamal, A. and Gollahalli, S.R., (2001) Effects of Jet Reynolds Number on the Performance of Axisymmetric and Nonaxisymmetric Gas Burner Flames, *J. Energy Resources Technol.*, Transactions of ASME, **123** 167-172.

Karbasi, M. and Wierzba, I. (1995) Prediction of the Blowout of Jet Diffusion Flames in a Coflowing Stream of Air, *Proc. of ASME Energy and Environmental Expo. Emerging Energy Technology Symposium,* **66** 21-27.

Koshigoe, S., Gutmark, E., and Schadow, K.C. (1989) Initial Development of Noncircular Jets Leading to Axis Switching, *AIAA J.,* **27**(4), 411-419.

Langman, A.S., Nathan, G.J., Mi, J., and Ashman, P.J. (2007) The Influence of Geometric Nozzle Profile on the Global Properties of a Turbulent Diffusion Flame, *Proc. Combust. Inst.* **31**, 1599-1607.

Lefebvre, A.H. (1983) *Gas Turbine Combustion, Hemisphere Publishing Corporation,* New York, NY, 129-131.

Lyons, K.M. (2007) Toward an Understanding of the Stabilization Mechanisms of Lifted Turbulent Jet Flames: Experiments, *Prog. Energ. Combust. Sci.,* **33**, 211-231.

Malmstrom, T.G., Kirkpatrick, A.T., Christensen, B., and Knappmiller, K.D. (1997) Centerline Velocity Decay Measurements in Low-Velocity Axisymmetric Jets, *J. Fluid Mech.,* **346** 363-377.

Masri, A.R. and Dally, B.B. (1999) Flow Field Structure of a Methane Diffusion Flame Stabilized on a Swirl Burner, *1999 Australian Symp. on Combust. and the 6th Australian Flame Days,* Newcastle, Australia, 150-153.

Mathur, M.M.L. and Maccallum, N.R.L. (1967) Swirling Air Jets Issuing From Vane Swirlers, Part 1: Free Jets. *Fuel,* **40** 214-225.

McCormick, D.C. and Bennett, J.C. (1993) Vortical and Turbulent Structure of a Lobed Mixer Free-Shear Layer, *AIAA Paper* 93-0219.

Melling, A. (1997) Tracer Particles and Seeding for Particle Image Velocimetry, *Meas. Sci. Techn.,* **8** 1406-1416.

Mi, J., Kalt, P., Nathan, G.J., and Wong, C.Y. (2007) PIV Measurement of a Turbulent Jet Issuing From Round Sharp-Edged Plate, *Exp. Fluids,* **42** 625-637.

Mi, J., Nathan, G.J., and Luxton, R.E. (2000) Cenetreline Mixing Characteristics of Jets from Nine Differently Shaped Nozzles, *Exp. Fluids* (Short Communication), **28**, 93-94.

Mi, J., Nathan, G.J. and Nobes, D.S. (2001a) Influence of Jet Conditions on the Passive Scalar Field of an Axisymmetric Free Jet, *J. Fluid Mech.,* **432** 91-125.

Mi, J., Nathan, G.J., and Nobes, D.S. (2001b) Mixing Characteristics of Axisymmetric Free Jets from a Contoured Nozzle, an Orifice Plate and a Pipe, *J. Fluid Eng.,* **123** 878-883.

Miake-Lye, R.C. and Hammer, J.A. (1988) Lifted Turbulent Jet Flames: A Stability Criterion Based on the Jet Large-Scale Structure, *Proc. Combust. Inst.,* **22**, 817-824.

Miller, R.S., Madnia, C.K., and Givi, P. (1995) Numerical simulation of Non-Circular Jets, *Comput. Fluids* **24** 1-25.

Nakao, S. (1986) Turbulent Flow in Square Ducts after an Expansion, *AIAA J.,* **24** 979-982.

Nathan, G.J., Mi, J., Alwahabi, Z.T., Newbold, G.J.R., and Nobes, D.S. (2006) Impacts of a Jet's Exit Flow Pattern on Mixing and Combustion Performance, *Prog. Energy Combust. Sci.,* **32** 496-538.

New, T.H; Tan, K.S; and Tsai, H.M. (2007) Effects of Noncircular Collars on an Axisymmetric Jet, *Phys. Fluids,* **19** 084104.

Panchapakesan, N.R. and Lumley, J.L. (1993) Turbulence Measurements in Axisymmetric Jets of Air and Helium. 1. Air jet, *J. Fluid Mech.,* **246** 197-223.

Panda, J. and McLaughlin, D.K. (1994) Experiments on the Instabilities of a Swirling Jet. *Phys. Fluids,* **6** 263-276.

Patrick, R. W. (1987) Flowfield Measurements in a Separated and Reattached Flat Plate Turbulent Boundary Layer, *NASA CR-4052*, March.

Peters, N. (1983) Local Quenching Due to Flame Stretch and Non-Premixed Turbulent Combustion, *Combust. Sci. Technol.,* **30**(1), 1-17.

Peters, N. (2000) Turbulent Combustion, Cambridge, Cambridge University Press.

Peters, N. and Williams, F.A. (1983) Liftoff Characteristics of Turbulent Jet Diffusion Flames, *AIAA J.,* **21** (3), 423-429.

Phillips, H. (1965) Flame in a buoyant layer, *Proc. Combust. Inst.*, **10**, 1277-1283.

Philips, T.M., An Experimental Study of the Effects of Asymmetric Fuel Nozzles on the Stability of Turbulent Diffusion Flames, *M.Sc. thesis, University of Manitoba, Canada*, 2006.

Pitts, W. M. (1988) Assessment of Theories for the Behavior and Blowout of lifted Turbulent Jet Diffusion Flames, *Proc. Combust. Inst.*, **22**, 809-816.

Quinn, W.R. (1989) On Mixing in an Elliptic Turbulent Free Jet, *Phys. Fluids A,* **1** 1716-1722.

Quinn, W.R. (1991) Passive Near-Field Mixing Enhancement in Rectangular Jet Flows, *AIAA J.*, **29** 515-519.

Quinn, W.R. (1994) Development of a Large-Aspect-Ratio Rectangular Turbulent Free Jet, *AIAA J.*, **32** 547-554.

Quinn, W.R. (1995) Turbulent Mixing in a Free Jet Issuing from a Low Aspect Ratio Contoured Rectangular Nozzle, *The Aeronautical J.*, **99** 337-342.

Quinn, W.R. (2005) Measurements in the Near Flow Field of an Isosceles Triangular Free Jet, *Exp. Fluids*, **39** 111-126.

Rabinowicz, E. (1970) An Introduction to Experimentation, Addison-Wesley Publishing Company, Philippines.

Reeder, M.F. and Samimy, M. (1996) The Evolution of a Jet with Vortex-Generating Tabs: Real-Time Visualization and Quantitative Measurements, *J. Fluid Mech.*, **311** 73-118.

Reeder, M.F. and Zaman, K.B.M.Q (1996) The Impact of Tab Location Relative to the Nozzle Exit on Jet Distortion *AIAA J.*, **34** 197-199.

Riopelle, G., Stubley, G.D., and Strong, A.B. (1994) Numerical Study of the Influence of the Ambient Pressure Field on Free Plane Turbulent Vertical Jets and Plumes, *Numerical Heat Transfer, Part A*, **26** 273-286.

Rodi, W. (1975) A New Method of Analyzing Hot-Wire Signals in Highly Turbulent Flow and its Evaluation in a Round Jet, *DISA Information*, **17**.

Ruetsch, G.R. and Broadwell, J.E. (1995) Effects of Confinement on Partially Premixed Flames *Annual Research Briefs*, Center for Turbulence Research, 323-333.

Sau, A. (2002) Vortex Dynamics and Mass Entrainment in a Rectangular Channel with a Suddenly Expanded and Contracted Part, *Phys. Fluids,* **14** 3280-3308.

Sau, A. (2004) Generation of Streamwise Vortices in Square Sudden-Expansion Flows, *Phys. Rev. E, **69**, 056304,* 1-10.

Scholefield, D.A. and Garside, J.E. (1949) The Structure and Stability of Diffusion Flames, *Proc. Combust. Inst.*, **3**, 102-110.

Sheen, H.J., Chen, W.J., and Jeng, S.Y. (1996) Recirculation Zones of Unconfined and Confined Annular Swirling Jets, *AIAA J.,* **34** 572-579.

Syred, N. and Beer, J.M. (1974) Combustion in Swirling Flows: A Review, *Combust. Flame,* **23** 143-201.

Takahashi, F., Mizomoto, M., Ikai, S., and Futaki, N. (1984) Lifting Mechanism of Free Jet Diffusion Flames, *Proc. Combust. Inst.*, **20**, 295-302.

Takahashi, F. and Schmoll, W.J. (1990) Lifting Criteria of Jet Diffusion Flames, *Proc. Combust. Inst.,* **23** 677-683.

Takahashi, F., Schmoll, W.J., Trump, D.D., and Goss, L.P. (1996) Vortex-Flame Interactions and Extinction in Turbulent Jet Diffusion Flames, *Proc. Combust. Inst.,* **26** 145-152.

Tangirala, V., Chen, R.-H., and Driscoll, J.F. (1987) Effect of Heat Release and Swirl on the Recirculation within Swirl-Stabilized Flames, *Combust. Sci. Technol.,* **51** 75-95.

TSI LDV/PDPA System Instruction Manual (2001) Combustion Laboratory, Room E3-340 Engineering building, University of Manitoba, Winnipeg.

Upatnieks, A., Driscoll, J.F., Rasmussen, C.C., and Ceccio, S.L. (2004) Lift-off of Turbulent Jet Flames-Assessment of Edge Flame and other Concepts Using Cinema-PIV, *Combust. Flame*, **138**, 259-272.

Vanquickenborne, L. and Van Tiggelen, A. (1966) The Stabilization Mechanism of Lifted Diffusion Flames, *Combust. Flame,* **10,** 59-69.

Veynante, D., Vervisch, L., Poinsot, T., Linan, A., and Ruetsch, G.R. (1994) Triple Flame structure and diffusion Flame Stabilization, *Summer Program Proceedings,* Center for Turbulence Research, NASA Ames/Stanford Univ., 55-73.

Warda, H.A., Kassab, S.Z., Elshorbagy, K.A., and Elsaadawy, E.A. (1999) An Experimental Investigation of the Near-Field Region of Free Turbulent Round Central and Annular Jet, *Flow Measurement and Instrumentation,* **10** 1-14.

Wierzba, I., and Oladipo, A.B., Blowout of Jet Diffusion Flames in Co-Flowing Air Stream, *Proc. of 24th ASME Energy-Sources Tech. Conf.,* PD-Vol. **57**, 1994, 29-33.

Wohl, K., Gazley, C., and Kapp, N. (1949) Diffusion Flames, *3rd Symposium on Combustion and Flame and Explosion Phenomena,* Baltimore, MD, **288**.

Wu, C.-Y., Chao, Y.-C., Cheng, T.-S., Li, Y.-H., Lee, K.-Y., and Yuan, T. (2006) The Blowout Mechanism of Turbulent Jet Diffusion Flames, *Combust. Flame,* **145**, 481-494.

Wu, H.L. and Fricker, N.J. (1976) The Characteristics of Swirl Stabilized Natural Gas Flames. Part 2: The Behavior of Swirling Jet Flames in a Narrow Cylindrical Furnace, *J. Inst. Fuel,* **49** 144-151.

Wygnanski, I. and Fiedler, H. (1969) Some Measurements in the Self-Preserving Jet, *J. Fluid Mech.,* **38** 577-612.

Xu, G. and Antonia, R.A. (2002) Effect of Different Initial Conditions on a Turbulent Round Free Jet, *Experiments in Fluids* **33** 677-683.

Yap, L.T. and Pourkashanian, M. (1996) Low-NOx Oxy-Fuel Flames for Uniform Heat Transfer, *Light Metals1996*, W. Hale, Ed., Minerals, Metals & Materials Society, 655-660.

Zaman, K.B.M.Q. (1996) Axis Switching and Spreading of an Asymmetric Jet: The Role of Coherent Structure Dynamics, *J. Fluid Mech.,* **316** 1-27.

Zaman, K.B.M.Q. (1997) Entrainment and Spreading Characteristics of Jets from Asymmetric Nozzles, *AIAA Paper* 97-1878.

Zaman, K.B.M.Q. (1999) Spreading Characteristics of Compressed Jets from Nozzles of Various Geometries, *J. Fluid Mech.,* **383** 197-228.

Zaman, K.B.M.Q., Reeder, M.F. and Samimy, M. (1994) Control of an Axisymmetric Jet using Vortex Generators, *Phys. Fluids A* **6** 778-793.

APPENDIX A: FREQUENCY RESPONSE EQUATIONS

Melling (1997) formulated a set of equations that describes the frequency response of tracer particles to the instantaneous motion of the continuous phase (air or methane in the present study). These equations are based on the assumptions that the turbulent flow is homogeneous and stationary as well as the tracer particles being smaller than the smallest turbulence eddies. In addition, the particle ambient must consist of the same fluid molecules and there can only be insignificant relative motion between a particle and the carrier fluid. The solution was expressed either as the relative amplitude, η, and phase response of the instantaneous particle, β, or as the ratio of fluctuation energies of the time-averaged particle and fluid motions, $\overline{u_p^2}/\overline{u_f^2}$. For a high density ratio (i.e. ratio of particle density to ambient fluid density), the solution of the equations proposed reduces to

$$C = \frac{18\mu}{\rho_p d_p^2} \tag{A.1}$$

$$\eta = \left(1 + \frac{\omega_c^2}{C^2}\right)^{-1/2} \tag{A.2}$$

where C is a characteristic frequency of the particle motion. Note that $\omega_c = 2\pi f_c$ is the highest turbulence frequency of interest and f_c is the maximum frequency response of the particle. ρ_p and d_p is the particle density and diameter, respectively, while μ is the fluid dynamic viscosity. Note that η was taken to be 0.99, which indicates the amplitude of the particle instantaneous velocity was assumed to be 99% of the fluid instantaneous velocity. This is the recommendation given by Melling (1997).

For example, the incense particles used had a density of 1060 kg/m^3 and a mass median aerodynamic diameter of 0.3 μm (this is taken to be the average particle diameter) while the air dynamic viscosity, was 1.7796×10^{-5} Pas,

Therefore,

$$C = \frac{18\mu}{\rho_p d_p^2} = \frac{18 \times 1.7796 \times 10^{-5}}{1060 \times (0.3 \times 10^{-6})^2} = 3357735.85 s^{-1}$$

and

$$\eta = \left(1 + \frac{\omega_c^2}{C^2}\right)^{-1/2} = \left(1 + \frac{(2\pi f_c)^2}{C^2}\right)^{-1/2}$$

$$\left(1 + \frac{(2\pi f_c)^2}{C^2}\right) = \frac{1}{\eta^2}$$

if η is taken to be 99%,

$$\left(1 + \frac{(2\pi f_c)^2}{C^2}\right) = \frac{1}{0.99^2} = 1.02$$

$$\frac{(2\pi f_c)^2}{C^2} = 0.02$$

$$(2\pi f_c)^2 = 0.02 \times C^2 = 0.02 \times 3357735.85^2$$

$$f_c \approx 76\, KHz$$

APPENDIX B: MATLAB CODES FOR IMAGE PROCESSING

B.1 Matlab Code for Determining the Flame Liftoff Height

```
clear all
close all
clc
threshold = 42;
Path = '.\75(3)';
maxFiles = 814;
yLength = 115.3; %the physical length of the image in mm
xLength = floor(yLength*1280/1024);
xvec = linspace(0,xLength,1280);
yvec = linspace(0,yLength,1024);
 xCutoff = 25;%str2num(char(inputdlg('Select the minimum X value to search','User
Input',1,{'0'})));
yCutoff = 114.5;%str2num(char(inputdlg('Select the maximum Y value to search','User
Input',1,{'0'})));
for (n = 1:maxFiles)
  if (n < 10)
     endfile = ['00000' num2str(n)];
  end
  if (n>9 & n<100)
     endfile = ['0000' num2str(n)];
  end
  if (n>99 & n< 1000)
     endfile = ['000' num2str(n)];
  end
  filename = ['ImgA' endfile '.tif'];
  %there are a total of 1024 pixels in the y direction,
  %1280 in the x direction, therefore
  %load in the image
  IMG = imread([Path '\' filename],'tiff');
  IMG(IMG<threshold) = 0;
  IMG(IMG>=threshold) = 1;
  IMG = bwareaopen(IMG,1000);
%     figure
%     %plot the image
%     imagesc(xvec,yvec,IMG);
%     colorbar
%     title(['Image of ' [Path '\' filename] 'Before Thresholding']);
%     xlabel('X - [mm]');
%     ylabel('Y - [mm]');
  % pause
  % BW = EDGE(IMG,'sobel');
  % figure
```

```
    % imagesc(BW);
    % % pause
    iX = find(xvec<xCutoff);
    [dummy,iX] = max(iX);
    iY = find(yvec<yCutoff);
    [dummy,iY] = max(iY);
    %Threshold the image (based on the threshold value at top of code)
    IMG(end,:) = 0;
    %zero out the two boxes
    IMG(:,1:iX) = 0;
    IMG(iY:end,:) = 0;
    iX = find(xvec<105);
    [dummy,iX] = max(iX);
    IMG(:,iX:end) = 0;
%    figure
%    %plot the image
%    imagesc(xvec,yvec,IMG);
%    colorbar
%    title(['Image of ' [Path '\' filename] 'After Thresholding']);
%    xlabel('X - [mm]');
%    ylabel('Y - [mm]');
%    pause
    %Find the pixel locations where the thresholded image is non-zero
    indices = find(IMG~=0);
    % indices = find(BW~=0);
    [I,J] = ind2sub(size(IMG),indices);
    %%%% This may be used to determine the exact locations of
    %%% the non-zero pixels
%    figure
%    scatter(I,J)
%    title('Scatter Plot of thresholded values');
    %determine the location of the lowest flame/pixel
    [maxY,yIndex] = max(I);
    maxYinMM(n) = yvec(maxY);
    %determine the x location of the lowest pixel
    maxX = J(yIndex);
    maxXinMM(n) = xvec(maxX);
end
%adjust so that y length is from bottom of image
maxYinMM = yLength - maxYinMM;
maxYinMM = maxYinMM';
maxXinMM = maxXinMM';
figure
scatter(maxXinMM,maxYinMM);
axis([min(xvec) max(xvec) min(yvec) max(yvec)]);
title('Scatter Plot of values found for start of flame');
```

```
xlabel('X - [mm]');
ylabel('Y - [mm]');
yAvg = mean(maxYinMM)
xAvg = mean(maxXinMM)
```

B.2 Matlab Code for Determining Flame Length

```
clear all
close all
clc
% subplot(221)
% threshold = 90;
Path = '.\45-length';
maxFiles =815;
yLength = 320; %the physical length of the image in mm
yLength1 = yLength/1024;
% xvec = linspace(0,xLength,1280);
% yvec = linspace(0,yLength,1024);


% xCutoff = 20;%str2num(char(inputdlg('Select the minimum X value to search','User
Input',1,{'0'})));
% yCutoff = 96;%str2num(char(inputdlg('Select the maximum Y value to search','User
Input',1,{'0'})));
skipcount = 0;
fileNumbersMissed = [];
for (n = 1:maxFiles)
   if (n < 10)
      endfile = ['00000' num2str(n)];
   end
   if (n>9 & n<100)
      endfile = ['0000' num2str(n)];
   end
   if (n>99 & n< 1000)
      endfile = ['000' num2str(n)];
   end
   filename = ['ImgA' endfile '.tif'];
a = imread([Path '\' filename],'tiff');
a = imread('ImgA000815.tif');
a = 256*a/max(max(a));
imagesc(a);
colormap(hsv(256));
(a<threshold) = 0;
a(a>=threshold) = 1;
subplot(222)
      level = graythresh(a);
      level = 0.7813;
```

```
        amax = max(max(a));
        level = 0.15*double(amax)/256; % <------------------- Threshold
        BW = im2bw(a,level);
 imagesc(BW)
 colormap gray
 subplot(223)
 BW2 = bwareaopen(BW,100); % <------------------- Threshold
 imagesc(BW2)
 colormap gray
 [s1 s2] = size(BW2);
 salir = 0;
 conta = 0;
 [s1 s2] = size(a);
 while salir == 0
    conta = conta+1;
      many = sum(BW2(conta,:));
      if many >0
        salir =1;
      end
    if conta == s1
        salir = 1;
    end
 end
 salir = 0;
 conta2 = 0;
 while salir == 0
    conta2 = conta2+1;
     if BW2(conta,conta2) > 0
        salir =1;
     end
     if conta2 == s2
        salir = 1;
     end
 end
 results(n)= conta;
 results2(n)= conta2;
 end
 results = floor(results*yLength1);
 results2= floor(results2*yLength1);
 results = (320-results)+665;
 results = results';
 results2 = results2';
 Yaverage = mean(results)
 Xaverage = mean(results2)
 results2=results2';
 % save results.txt results results2 -ASCII
```

```
figure
imagesc(BW2)
colormap(gray)
 title(num2str(conta))
```

APPENDIX C: EQUATIONS FOR LDV PROBE VOLUME

Waist, D_f

$$D_f = \frac{4F\lambda}{\pi E D_l} \quad \text{(C.1)}$$

Length:

$$\delta_z = \frac{D_f}{sin(\phi_2|2)} \quad \text{(C.2)}$$

Width:

$$\delta_y = D_f \quad \text{(C.3)}$$

Height:

$$\delta_x = \frac{D_f}{cos(\phi_2|2)} \quad \text{(C.4)}$$

Fringe Separation:

$$\delta = \frac{\lambda}{2sin(\phi_2|2)} \quad \text{(C.5)}$$

Number of Fringes:

$$N_f = \frac{\delta_x}{\delta} = \frac{8Ftan(\phi_2|2)}{\pi E D_L} \quad \text{(C.6)}$$

In the present LDV set-up we have the following: E = Beam Expander Ratio = 1.00, F = Lens Focal Length= 363 mm, ϕ_2 = Angle between the two input laser beams, and D_L = Laser Beam diameter = 2.80 mm.

APPENDIX D: UNCERTAINTY ANALYSIS

An uncertainty analysis, which involves systematic procedures for calculating error estimates for the experimental data was carried out. There are two broad sources of error in experimental measurements, namely bias and precision errors. Consequently, the total uncertainty can be found by combining precision and bias errors as: $\sigma_{\text{total}} = \pm(B+tP)$, where B is the bias error, P is the precision error, and t known as the confidence coefficient, which is 2 for a 95% confidence level (Holman, 1994).

D.1 Uncertainty Analysis for LDV Measurements

The method of uncertainty analysis used by Schwarz (1998) for LDV measurements was employed in this study. The primary sources of bias uncertainties according to Patrick (1987) are errors due to the laser beam geometry, signal processor errors and seeding bias errors, while the precision errors are affected by the ensemble size and the variation from the population mean. Note that the velocity bias error is corrected using transit time weighting, while frequency shifting was used to minimize angle bias. Consequently, Schwarz (1998) suggested that most of the bias errors can be completely eliminated or very minimal due to improvements in LDV, except the beam-crossing angle. Consequently, Schwarz (1998) ascribes a value of ±0.4% for the error in determining the uncertainty in the beam-crossing angle, which is the same value taken in this study.

The combined uncertainties of the streamwise and radial mean velocities according to Schwarz (1998) are as follows:

$$\frac{\sigma_U}{U} = \left[(\sigma_o)^2 + \frac{1}{N}\left(\frac{u}{U}\right)^2\right]^{\frac{1}{2}} \tag{D.1}$$

$$\frac{\sigma_V}{U} = \left[(\sigma_o)^2 + \frac{1}{N}\left(\frac{v}{U}\right)^2\right]^{\frac{1}{2}} \tag{D.2}$$

The corresponding equations for the turbulence intensities and Reynolds shear stress are:

$$\frac{\sigma_u}{u} = \left[(\sigma_o)^2 + \frac{1}{2N}\right]^{\frac{1}{2}} \tag{D.3}$$

$$\frac{\sigma_v}{v} = \left[(\sigma_o)^2 \left(\frac{\langle uv\rangle}{v^2}\right)^2 + \frac{1}{2N}\right]^{\frac{1}{2}} \tag{D.4}$$

$$\frac{\sigma_{\langle uv\rangle}}{\langle uv\rangle} = \left[(\sigma_o)^2 \left(1 + \frac{u^2}{\langle uv\rangle}\right)^2 + \frac{1}{N}\left(\frac{2}{R}\right)^2\right]^{\frac{1}{2}} \tag{D.5}$$

where σ_o is the uncertainty in the determination of the beam crossing angle (taken as 0.4%), N is the number of samples, and R is the shear stress correlation coefficient. U and V are the streamwise and radial mean velocity, respectively while u and v are the corresponding streamwise and radial mean turbulence intensities, respectively. Finally, $<uv>$ is the Reynolds shear stress.

Applying the equations above to a typical flow characteristic indicated in Table D.1, we have the following combined errors indicated in the same table. Note that this typical flow shown in Table D.1 concern a 30 m/s contracted circular jet without sudden expansion. This values shown in Table D.1 are for x = 2 mm and y/D_e = 0.45 (i.e. the shear-layer) location.

Table D.1: Uncertainties for a typical 30 m/s contracted circular jet at a particular location.

	U_j (m/s) 41.07956	**u (m/s)** 4.988396	**V_j (m/s)** 0.755367	**v (m/s)** 1.251853	**<uv>** -1.27399
$\frac{\sigma_U}{U}$	0.4%	-	-	-	-
$\frac{\sigma_V}{U}$	-	-	0.4%	-	-
$\frac{\sigma_u}{u}$	-	0.7%	-	-	-
$\frac{\sigma_v}{v}$	-	-	-	0.6%	-
$\frac{\sigma_{\langle uv\rangle}}{\langle uv\rangle}$	-	-	-	-	8.9%

D.2 Uncertainty Analysis for Flame Liftoff Height, Length, Blowout and Liftoff Velocities

The primary sources of bias uncertainties are due to the camera's resolution, calibration, and errors due to measurements of fundamental quantities. These errors are difficult to obtain and are therefore not included in the error analysis. Precision errors arise as a result of flame unsteadiness. They are reduced by increasing the number of measurement samples. The method outlined by Holman (1994) and Rabinowicz (1970) was used to calculate the precision uncertainties.

A Precision error is given by

$$P = \frac{t\sigma}{N} \tag{D.6}$$

where σ is the standard deviation of the sample of N images, which is defined as

$$\sigma = \sqrt{\frac{\sum_{k=1}^{N}[(x)_k - \bar{x}]^2}{N-1}} \tag{D.7}$$

where x could be liftoff height, h, flame length, l, blowout velocity or liftoff velocity. The mean, $\bar{x}$ is defined by the following equation

$$\bar{x} = \frac{1}{N}\sum_{k=1}^{N} x_k \tag{D.8}$$

Calculating the precision error in the liftoff height of a 65 m/s contracted circular nozzle flame exposed to a 0.58 m/s co-flow with no swirl for example; we start by applying the standard deviation, σ equation above. The equation produced σ of 12.09 mm. Since $N = 815$ images (i.e. the number of images used to obtain the average liftoff height) and $t = 1.96$, we have the precision error

$$P = \frac{t\sigma}{N}$$

$$P = \frac{1.96 \times 12.09}{815}$$

$$P = 0.83 \text{ mm}$$

This implies that with an average liftoff height of 149.36 mm obtained for this kind of flame described above, the precision error is about 0.6%.